Numerical Investigation of Thermochemical Nonequilibrium Inductively Coupled Plasma Flow

喻, 明浩

https://doi.org/10.15017/1543967

出版情報：九州大学, 2015, 博士（工学）, 課程博士
バージョン：

Numerical Investigation of Thermochemical Nonequilibrium Inductively Coupled Plasma Flow

By
Minghao YU

Department of Aeronautics and Astronautics
Kyushu University, Fukuoka, Japan
April, 2015

Contents

List of Figures

List of Tables

Nomenclature

A	=	area, m^2 , or magnetic vector potential, V. sec/m
$\boldsymbol{A}$	=	Jacobian matrix, or area, or magnetic vector potential
B	=	blackbody function, W/m^3, or magnetic flux density, T
$\boldsymbol{B}$	=	magnetic flux density vector
c	=	speed of sound, or speed of light, m/sec
$\boldsymbol{C}$	=	mass fraction, or model constant
C_p	=	specific heat at constant pressure, J/(kg. K)
C_v	=	specific heat at constant volume, J/(kg. K)
C_j	=	jth component of thermal velocity, m/sec
d	=	distance, m
D	=	electric flux density, C/m^2, or, effective diffusion coefficient, m^2/sec, or diameter, m
$\boldsymbol{D}$	=	electric flux density vector, or vector of destruction terms
e	=	electric charge, C, or energy per unit mass, J/kg
E	=	internal energy, J/m^3, or electric field, V/m
$\boldsymbol{E}$	=	electric field vector
f	=	mass fraction, or model function
F	=	external force or Lorentz force, N/m^3
$\mathbf{F}$	=	vector of inviscid terms
$\mathbf{F}_v$	=	vector of viscous terms
g	=	relatively velocity, m/sec
h	=	enthalpy, J/kg, or Planck constant, m^2 kg/sec
Δh^0	=	enthalpy of formation, J/kg
H	=	magnetic field , A/m
$\mathbf{H}$	=	magnetic field vector, or vector of axisymmetric source terms
I	=	current, A
$\mathbf{I}$	=	identity matrix
j	=	current density, A/m^2
J_s	=	diffusion flux of species s, $kg/(m^2 \cdot sec)$, or Jacobian
$\boldsymbol{J}$	=	current-density vector
k	=	Boltzmann constant, J/K, or reaction-rate coefficient, m^3/(mole. sec), or turbulence energy, J/kg
K_n	=	Knudsen number
K^{eq}	=	equilibrium constant
L	=	Length, m
m	=	mass, kg ,or mass flux, $kg/(m^2 \cdot sec)$
M	=	Mach number
$\dot{m}$	=	mass-flow rate, kg/sec
n	=	number density, $1/m^3$
nm	=	number of molecular species
ns	=	number of species
p	=	pressure, Pa
Pr_t	=	turbulent Prandtl number
$\mathbf{P}$	=	vector of production terms
q	=	heat flux, W/m^2
$\bar{Q}$	=	collision cross section, m^2

Q	=	internal energy-exchange rate, W/m^3
$\mathbf{Q}$	=	vector of conservative variables
r	=	radial coordinate, m
R	=	gas constant, J/(kg. K), or, radius, m
Re	=	Reynolds number
$\mathbf{R}$	=	residual vector
S_{int}	=	internal energy-exchange rate, W/m^3
S_{joule}	=	Joule-heating rate, W/m^3
t	=	time, sec
T	=	temperature, K
$\mathbf{T}$	=	eigenvector matrix
u	=	velocity, m/sec
U	=	magnitude of velocity, m/sec
v	=	mass average velocity, m/sec
v_{s}	=	average velocity of species s, m/sec
V	=	volume, m^3, or diffusion velocity, m/sec
$\dot{\omega}$	=	mass-production rate, kg/(m^3.sec)
$\mathbf{W}$	=	vector of source terms
x	=	axial coordinate, m
$\boldsymbol{X}$	=	mole fraction
y	=	radial coordinate, m
y_{wd}	=	distance from wall, m
Z_{i}	=	number of charges of species *i*
α	=	degree of ionization
β	=	interaction parameter, coil current parameter, relaxation parameter
γ	=	specific heat ratio, or reduced velocity
δ_{ij}	=	Kronecker delta
ε	=	dissipation rate of turbulence energy, W/kg
ε_0	=	vacuum permittivity, 8.85×10^{-12} F/m
η	=	heat efficiency
Θ	=	characteristic temperature, K
λ	=	thermal conductivity, W/(K. m), or Mean free path, m, or wavelength, m, or eigenvalue
λ_D	=	Debye length, m
Λ	=	eigenvector
μ	=	molecular viscosity, N. sec/m^2
$\mu_{s,k}$	=	reduced mass of species s and k, kg
μ_t	=	turbulent viscosity, N. sec/m^2
μ_0	=	magnetic permeability, 1.26×10^{-6} V. sec / (A. m)
ν	=	collision frequency, 1/sec, or kinematic viscosity, m^2/sec
$\nu_{s,r}$	=	stoichiometric coefficient of reaction *r* of species *s*
ρ	=	density, kg/ m^3
ρ_e	=	charge density, C/ m^3
σ	=	electrical conductivity, S/m, or model constant, or spectral radius
$\sigma_{i,j}$	=	differential scattering cross section for species i and j
σ_{sb}	=	Stefan-Boltzmann constant, W/(K$^{4.}$ m^2)
τ	=	stress, N/m^2, or relaxation time, sec
τ^t	=	Reynolds stress, N/m^2
$\langle\varphi_s\rangle$	=	average quantity per unit particle

χ = angle of deflection
Ω = collision integral, m^2

Subscripts

av = mass-averaged
B = magnetic
b = backward
CFL = Courant-Friedrichs-Lewy condition
D = dissociation, or Debye
e = electron
ex = electronic excitation
E = electric
f = forward
k = turbulence energy
I = ionization, imaginary part
in = inflow
int = internal
L = left, Lorentz force
M = molecular
p = p^{th} control volume
R = real part, or rotation, or right
rad = radiation
ref = reference
rot = rotation
s = species
t = turbulent
T = translation
tr = translation
V = vibration
v = viscous
vib = vibration
w = wall
ε = dissipation rate of turbulence energy
λ = wavelength
θ = tangential component
1 = cell next to wall surface
1/2 = cell interface

Superscripts

a = ambipolar
conv = convection
e = electron
j = component in jth direction
n = time step
rad = radiation
rot = rotation
t = turbulent
T = temperature
vib = vibration

Chapter 1 Introduction

1.1 Research Background

As a spacecraft entries or re-entries the atmosphere of planet such as Earth, Mars, Jupiter etc., its surface will be subjected to the strong aerodynamic heating due to the dramatic deceleration from several km/s to the lowest possible velocity. To ensure safe landing of the vehicle, it is necessary to load the thermal protection system (TPS) such as light ablator and heat-shield ceramics on the spacecraft to prevent it being damaged. As is indicated by M. Auweter-Kurtz [1], the material of TPS should have following characteristics: (1) be able to withstand the strong convective and radiative heat fluxes; (2) with small mass, and a smooth surface; (3) the material catalycity should be as low as possible to avoid the activation of surface recombination reactions or nitrogen oxide formation; (4) the emissivity of material must be as high as possible to promote the radiation cooling. To research and develop TPS, a lot of efforts have been made in past decades to model the reentry conditions of spacecraft by using the ground-based facilities. The common characteristic of these facilities is that all of them can generate high-enthalpy flows to reproduce planet-entry environment on the ground.

The representatives of such facilities are as following: shock tunnel, arc-heated wind tunnel, inductively coupled plasma wind tunnel etc. The characteristics of each facility are described respectively as following: (1) the shock tunnels are very useful devices to produce supersonic and hypersonic flow to simulate reentry condition on the ground. However, these facilities have disadvantages that they can maintain high speed flow only for very short time because of their intermittent working. (2) The arc-heated wind tunnel is capable to generate the high-enthalpy flow stably and continuously, while the electrode erosions of arc is apt to contaminate the high-enthalpy flow. Therefore it cannot be used to study the catalytic effects of TPS materials, because the electrode erosions may also participate or play as the catalytic agent in the chemical reactions. (3) The inductively coupled plasma wind tunnel (ICPWT) is also one of important high-enthalpy facilities in the aerospace industry. It can produce stable and continuous high-enthalpy flows with peak temperatures of approximate 10000 K by means of the radio-frequency (RF) inductive discharge of operating gases. Because there is no contact between the heating element and working gas in the heating process, the produced inductively coupled plasma (ICP) flow is highly pure. This advantage and the high-enthalpy property make ICP flows being preferred sources to develop the thermal protection systems of reentry vehicles. Thus many researchers pay their attention and interests to construct ICP wind tunnels in the past three decades.

1.2 Inductively Coupled Plasma Wind Tunnel

In the worldwide, there are various power-scale inductively coupled plasma wind tunnels. Table 1.1 illustrates the examples of ICP wind tunnels. Generally, The ICP wind tunnel is composed of inductive coil, quartz tube and vacuum chamber. According to the heating type of the inductive coil, the inductively coupled plasma wind tunnel (or called inductively coupled plasma heaters) is clarified into two types: helical and planar type. Fig. 1.1(a) and (b) show the helical and planar coil inductively coupled plasma

heaters, respectively. In the materials processing industries, the planar coil inductively coupled plasma heater is preferred. It is widely used to modify the surface properties of materials such as plasma etching, preparing nanoparticles of silicon base intermetallic compounds [2], plasma synthesis of ultrafine nanostructure powders [3] etc. Usually, the working pressure of the planar coil inductively coupled plasma heater is relatively low, and is about 1.0 – 500 Pa.

On the other hand, in the aerospace industry the helical coil type inductively coupled plasma heater is more common. This may be contributed to the advantage that it can work in wide-range and high pressure conditions, even in the atmospheric pressure condition. This advantage makes the helical coil ICP heaters an adaptable and convenient means to study the catalytic effects of TPS materials, model thermal and chemical phenomena on the surfaces of heat shields of reentry spacecraft, and develop high-performance materials of flare-type membrane aeroshells in the aerospace industry. In this study, we focus on studying the helical coil type inductively coupled plasma heaters in the following parts.

Table 1.1 Examples of inductively coupled plasma heaters

Country	Affiliation	Coil type	Total power (kW)	Pressure (kPa)	Frequency (MHz)	Refs.
Belgium	VKI	helical	1200.0	101.0	0.40	[4]
Japan	ISAS/JAXA	helical	110.0	10.0	1.78	[5]
Japan	ISAS/JAXA	helical	10.0	4.0	4.00	[6]
Japan	Univ. Tokyo	helical	2.0	0.1	13.56	[7]
Russia	IPM RAS	helical	100.0	10.0	1.76	[8]
China	CARDC	helical	500.0	5.0	0.44	[9]
China	CAS	helical	15.0	50.0	3.00	[10]
German	IRS	helical	375.0	100.0	1.45	[11]
USA	Univ.Houston	planar	2.0	0.001	13.56	[12]
Korea	KAIST	planar	0.5	0.001	13.56	[13]

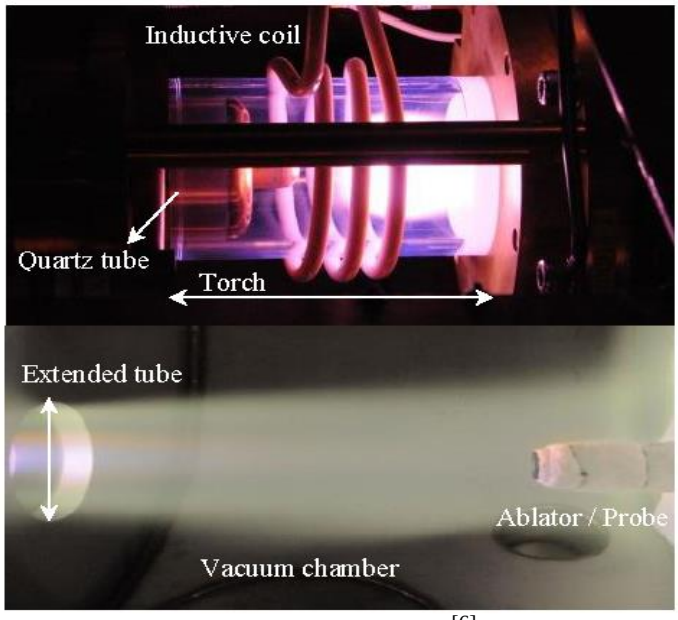

(a) helical coil type [6]

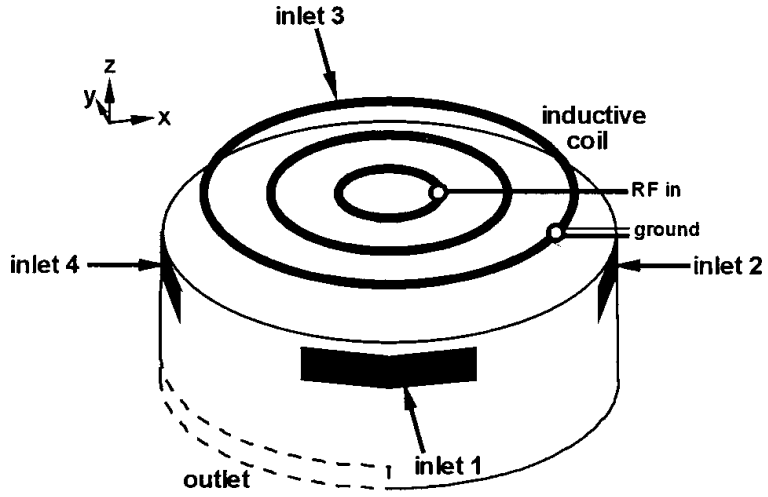

(b) planar coil type [12]

Fig. 1.1 Inductively coupled plasma heater: (a) helical coil type ; (b) planar coil type

1.3 Historical Studies and Current Trends

In past decades, numerical investigation using computational fluid dynamics is an attractive approach to understand the heating mechanism, examine the flow and temperature fields, optimize structural parameters of ICP heaters [14], etc. Thus far, many numerical simulations have been performed for argon ICP flows [15-20]. For the pure nitrogen ICP flow, Barnes and Nikdel [21] first applied a linearized energy-balance equation to obtain the temperature and velocity distributions for an ICP discharge. Punjabi et al. [22] comprehensively examined the flow fields of an ICP torch using several test gases including nitrogen under the assumption of local thermal and chemical equilibrium. This LTE hypothesis is very useful for studying the transport of mass, momentum and energy as well as the gas flow and the temperature fields in the ICPWTs but limited to some restricted operating conditions such as atmospheric pressure working conditions. Tanaka et al [23] numerically studied the chemical nonequilibrium nitrogen ICP flows by using Dunn-Lordi's chemical kinetic model [24] to simulate the chemical nonequilibrium process under the local thermal equilibrium assumption. A departure from chemical equilibrium in the distribution of the particle composition was found when the chemical kinetic model was considered. About the chemical kinetic model, compared with Dunn-Lordi's chemical reaction model, an improved chemical kinetic model was developed later by Dunn and Kang through experimental and theoretical studies [25]. Park also made some improvements for the development of chemical-kinetic model for nonequilibrium plasma flows [26]. Several dissociation reactions (e.g., $N_2+e^- \rightleftharpoons N+N+e^-$) were found playing important roles in predicting chemical compositions of plasma simulations [27, 28].

As for air ICP simulations, because it is difficult to model thermodynamic and transport phenomena for multicomponent air, a few studies have attempted to predict the flow properties of air plasma inside ICP torches in the last decade. Vasil'evskii and Kolesnikov [29] simulated inductive air and argon plasma flow in a cylindrical discharge plasmatron channel by approximating chemical and thermodynamic equilibrium. Their calculations revealed two types of complex plasma vortexes in the channel. However, there were no adequate air chemical models to describe the ionization and dissociation

processes of air at high temperature in their works. Degrez et al. [30] take into account a chemical-kinetic model by using two different finite-rate chemistry models for ICP flows in air. The chemical-kinetic model was found to play an important role in predicting temperature distributions and concentrations of species. Sumi et al. [5] performed numerical studies of air flow inside the 110 kW-class ICP wind tunnel. They solved Navier-Stokes (N-S) equations coupled with Park's two-temperature model considering Dunn-Kang's 11 species and 32 chemical reactions of air. Although their work was encouraging, the flow was limited to in the ICP torch. In a practical situation, the plasma will flow from the torch exit into a larger vacuum chamber for experiments and applications such as plasma diagnosis, spectroscopic analysis, and ablation experiments of TPS materials. On one hand, because there is sufficient space and a stable environment in the vacuum chamber, precision measuring instruments can easily be set up in it and reliable experimental data can be acquired there for validation of numerical methods. On the other hand, if detailed flow properties inside the vacuum chamber can be obtained, they will be very useful for tentative analysis and determining correct flow parameters for further studies such as investigation of nitridation reactions occurring at a graphite surface [31] and simulation of thermal response of an ablator [32].

Recently, in order to predict the flow properties more accurately, the numerical simulation coupled with an thermal nonequilibrium model is an interesting subject for many researchers. Previously, Park's two-temperature model is widely used to study thermal nonequilibrium phenomena of arc-heated and ICP flows. For more accurately prediction of internal energy exchanges between translational, vibrational, rotational, and electronic mode of chemical particles, a four-temperature model considering the internal energy transfer such as electron-vibration, electron-rotation, vibration-translation, vibration-rotation, and rotation-translation was developed and used to study the thermal nonequilibrium process of an arc-heated flow [33]. Note that for the electron-vibrational energy relaxation time, Lee's previous theoretical data [34] was used in this four-temperature model. According to Bourdon's work [35], more accurate vibrational-electron relaxation time was available in the temperature range of 3000–20000 K. Beyond this temperature range, Kim et al [36] recently proposed a method to assess the vibrational-electron relaxation time for nitrogen molecular in modeling electron-vibration energy exchange.

Radio-frequency inductive discharge is one of important characteristics for ICP flows. Maxwell's electromagnetic equations need to be solved to describe this phenomenon and obtain the Joule heating rate distribution. Previously, Mostaghimi and Boulos [37] proposed a standard electromagnetic model to describe the inductive discharge for ICP flows. Although this model is quite accurate and physically relevant. However, because of the point-by-point integral boundary conditions on the torch wall, this method requires a lengthy iterative process to realize a converged solution of the electromagnetic equations [19]. In addition, this method can be used for high-pressure ICP flows. While for low-pressure ICP flows, it is apt to lose the effectiveness and accuracy [19]. Based on this standard electromagnetic model, Xue et al [38] proposed a far-field electromagnetic model to reduce the computational time. The computational domain was generally divided into three zones as: plasma torch, inductive coils and far-field region. This far-field model is quite efficient and physical correct, while the computational method which is needed to update the electromagnetic field or coil current was not given in their work.

As for an ICP simulation, transport properties of the working gas serve as important and indispensable components in the modeling procedure. In the last decade, for simplicity the first-order formula of Chapman-Enskog approximation was widely used

to calculate the transport properties such as electrical conductivity and electron thermal conductivity for ICP flows [20, 23, 39]. because of the tight coupling between aerodynamic and electromagnetic fields in an ICP simulation, the electrical conductivity will affect the distributions of Joule heating rate and Lorentz force significantly. Therefore, it is better to compute the electron transport properties using the high-order perturbation technique of Chapman-Enskog theory [40]. While the calculation with this high-order technique needs much more collision integral data and is complex. With development of molecular and atom theory, recently Ghorui et al [41] gave a method to calculate different kinds of collision integrals for interactions of charged-charged species. Laricchiuta et al [42] also tabulated some transport coefficients to evaluate collision cross-sections for interactions of electron-neutral species. Therefore, the high-order accuracy electron transport properties for nitrogen and air became achievable through their works.

As a summary, in this study the four-temperature model with a modified electron-vibration relaxation time is adopted to study thermal nonequilibrium properties of an ICP flow. It is the first time applied to ICP simulations. Moreover, Xue *et al*'s far-field electromagnetic model is introduced to describe the radio-frequency discharge. A stable and efficient method is proposed to update the coil current for the control of that electromagnetic-field calculation. Besides, a relatively simple but accurate method is developed to compute the third-order-accuracy electron transport properties of nitrogen and air. This method and the computed high-accuracy results are applied to present ICP simulations.

1.4 Objective and Scope of the Present study

Because complex heating phenomena occur in ICP wind tunnels, it is difficult to measure all of the flow properties, such as spatial distributions of temperature, velocity, and concentration of chemical species. Numerical investigations using computational fluid dynamics methods are an attractive approach to study the flow fields and heating process of ICP wind tunnels. Therefore, it is necessary to establish effective computational code to predict basic flow properties of an inductive plasma.

As for the purposes of this study: (1) the final goal is to supply accurate flow-field properties (e.g. flow temperature, pressure, number density of chemical species etc.) for the study of TPS such as investigation of nitridation reactions occurring on the TPS materials, simulation of thermal response of an ablator. (2) Another objective is to develop effective computation code for the optimum design of ICP wind tunnels. (3) The direct purpose of present study is to make clear the flow and electromagnetic fields of the 10-kW ICP wind tunnel. To clearly understand the inductive discharge, it is necessary to reveal the heating process and the interactions between electromagnetic and flow fields.

About the scope of present study, the flow fields inside the 10-kW and 110-kW ICP wind tunnels are studied by solving two-dimensional axisymmetric compressible N-S equations tightly coupled with the electromagnetic-field calculation. To accurately determine the temperature field a four-temperature model with chemical-kinetic reactions is employed to determine the temperature field and study the thermochemical state of plasma flows. Since the radio-frequency (RF) inductive discharge plays an important role in the coil region, we introduce a far-field electromagnetic model to describe the heating process by the RF discharge. The interactions between the electromagnetic and flow fields in the induction torch are studied and discussed. Taking

into account the effects of turbulent heat transfer in ICP flows, the low Renolds-number turbulence model AKN k-ε model is also used.

In addition, the third-order-accuracy electron transport properties for nitrogen and air are computed in wide pressure and temperature ranges and applied to the present simulations. A relatively simple approach to calculate the electron transport properties is summarized and given in this study with the latest available collisional integral data. To validate the method, the calculated electron transport properties for air and nitrogen under the atmospheric pressure condition are compared with the corresponding experimental and theoretical results in literatures.

In summary, as the first step, we numerically simulate nitrogen and air ICP flows by using the abovementioned equations and models in the 10-kW and 110-kW ICPWTs. Their basic flow properties are shown and discussed in detail. Thereafter, to validate the numerical methods used presently, comparisons of the numerical and experimental results are performed for the 10-kW and 110-kW ICPWTs, respectively. Next, we compare the numerical results obtained under the local thermal equilibrium and thermal nonequilibrium assumptions. Finally, the effects of electron transport properties with the first-order and third-order accuracies on the temperature field are investigated.

1.5 Outline of Thesis

The outline of thesis is given here. Generally, the thesis includes five parts:

First, the research background, physical model, objectives and study scope are discussed in the Chapter 1.

In Chapter 2, the description of facility and key physical features of an ICP flow are given first. Second, the governing equations and models used to describe the flow and electromagnetic fields e.g. N-S equations, magnetic vector potential equations and chemical reactions model are constructed and discussed. Third, the basic theories for computing gas transport properties and internal energy exchanges are addressed.

Numerical methods used to solve abovementioned equations are mainly described in Chapter 3. The governing equations are solved using a finite volume approach. The numerical fluxes of the flow-field and electromagnetic-field equations are evaluated using proper schemes, respectively. The time integration is performed implicitly. The boundary conditions for solving abovementioned equations are also given in this chapter.

Chapter 4 gives the numerical results of the flow and electromagnetic fields for the 10-kW and 110-kW ICP wind tunnels. In order to validate the present numerical methods, the simulated results are compared with the corresponding experimental data first. Then, flow properties such as thermochemical nonequilibrium, interactions between flow and electromagnetic fields, and effects of detailed electron transport properties model are discussed in detail.

Finally, some conclusions obtained from the present study are denoted in Chapter 5.

Chapter 2 Flow Characteristics and Governing Equations

2.1 Analysis Objects

In the present study, we focus on flow fields in the following two ICP wind tunnels: the 10-kW and 110-kW ICP wind tunnels in Japan Aerospace Exploration Agency (JAXA). Table 2.1 shows comparison of the facility feature, e.g., driving frequency of the coil current *f*, lengths of the torch L_{ch}, diameters of the coil d_c. In addition, the three operating parameters, i.e., the typical input power *P*, operating pressure p_{ch} in chamber, and the mass flow rate $\dot{m}$ are also shown in this table. These facilities working-pressure and power-scale are quite different and the characteristics of the flow field are expected to be greatly different. For example, as the operating pressure is higher, the inductive plasma flow field tends to be thermochemically in equilibrium and the effect of thermal nonequilibrium model is thought to become important.

Table 2.1 Comparison of 10 kW and 110-kW ICPWTs

Facility	f (MHz)	L_{ch} (mm)	d_c (mm)	P (kW)	p_{ch} (kPa)	$\dot{m}$ (g/s)	Refs.
10-kW	4.00	200.0	8.0	10.0	1.0-5.0	0.3–1.5	[6]
110-kW	1.78	250.0	8.0	90.0	2.0-10.0	1.0-2.5	[5, 43]

2.2 Facility Description

The ICP wind tunnel system usually consists of double quartz tube, inductive coil, radio frequency generator, test chamber, vacuum system, gas and power supply system, and water cooling system.

2.2.1 10-kW ICP Wind Tunnel

Overview and geometry of the 10 kW inductively coupled plasma wind tunnel is illustrated in Fig. 2.1. The inductive coil and quartz tube are the key components of an ICP wind tunnel. Specifically, the 10 kW inductively coupled plasma heater consists of five parts: the gas inlet, inductive coil, quartz tube, extended tube, and the vacuum chamber. The inductive coil turns three times around the discharge torch (quartz tube) with an interval of 17.5 mm. The diameter of the coil is 8 mm. The axial and radial positions of the first coil center is x = 90.0, y = 52.5 mm. The total length and diameter of the torch are 200.0 and 75.0 mm, respectively. The frequency of the alternative current that runs through the coil is 4.0 MHz. Because of narrow space in the torch, it is difficult to carry on experimental studies in the torch, therefore, an extended tube is connected to the torch exit to lead the plasma flow into the spacious vacuum chamber. Sometimes in the experiment of generating an air ICP flow, the flow tends to be unstable in the vacuum chamber in the radial direction [6]. Thus, a thin orifice plate with an inner radius of 25 mm and wall thickness of 1.5 mm is assembled in the extended tube to stabilize the air plasma flow. Finally, the produced high-enthalpy flow spreads into the large vacuum chamber for various industrial applications.

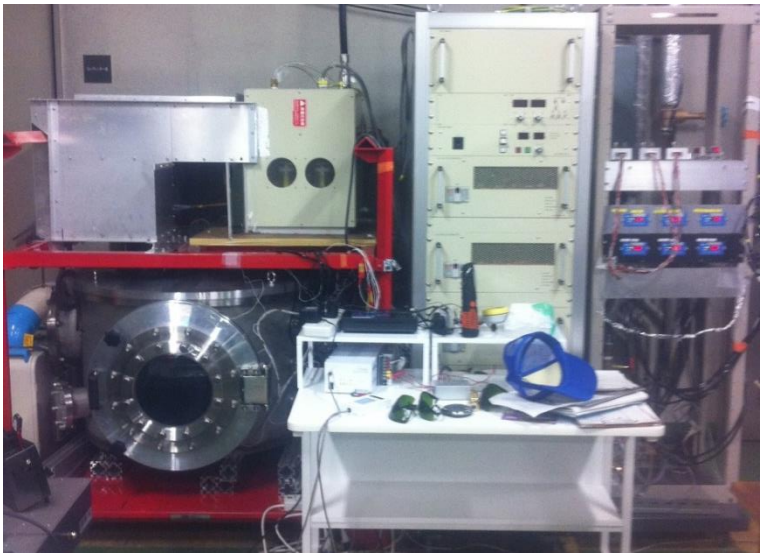

(a)

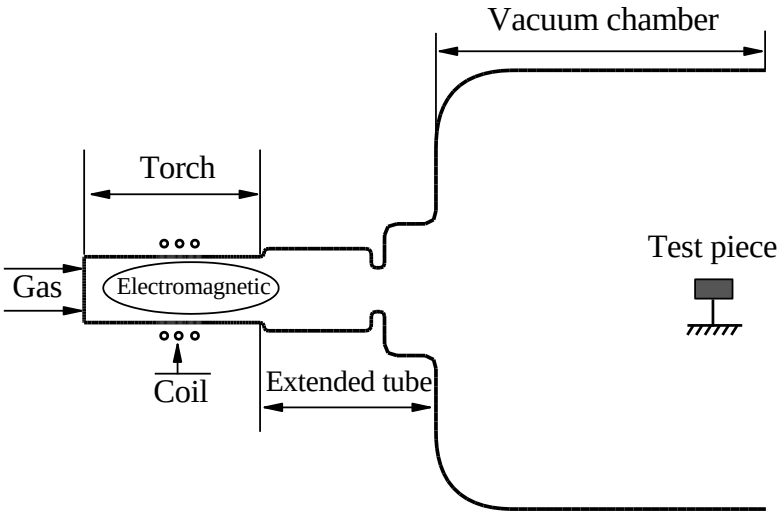

(b)

Fig. 2.1 Schematic of the 10-kW inductively coupled plasma wind tunnel: (a) overview, (b) detailed components

2.2.2 110 kW ICP Wind Tunnel

Schematic view of the 110 kW inductively coupled plasma wind tunnel is illustrated in Fig. 2.2. The test gas such as nitrogen, air and carbon dioxide is injected from a narrow opening near the wall at the beginning of the torch. The width of the inlet is about 2.4 mm in the radial direction [5]. The total length and diameter of the torch are 250.0 and 75.0 mm, respectively. The coil also turns three times around the quartz tube. The interval between each coil center is 16.5 mm. The axial and radial positions of the first coil center is x=51.0, y=51.0 mm. Compared with the 10-kW inductively coupled plasma wind tunnel, the discharge region of this wind tunnel is closer to the torch inlet. It seems that the effects of the turbulence and gas movements near the inlet would be stronger than those of the 10-kW ICP wind tunnel.

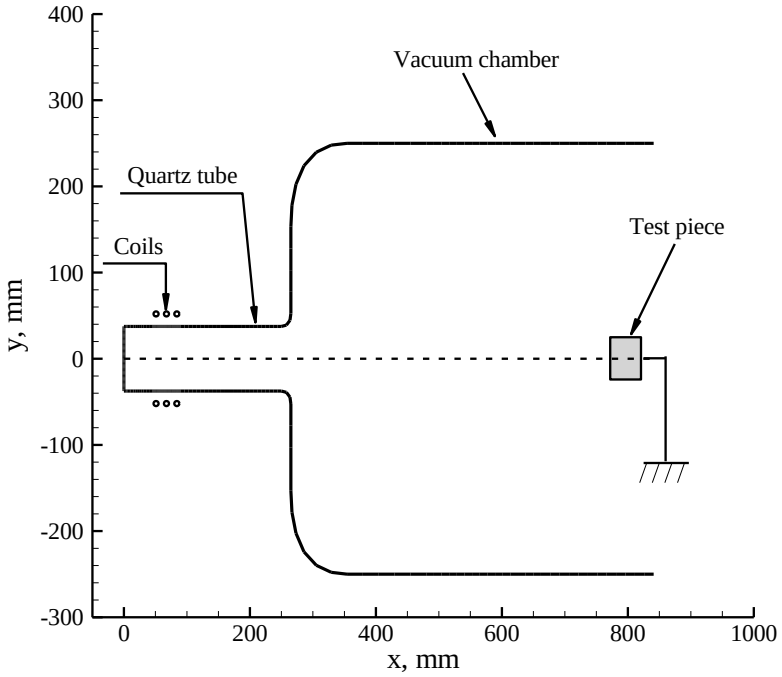

(a)

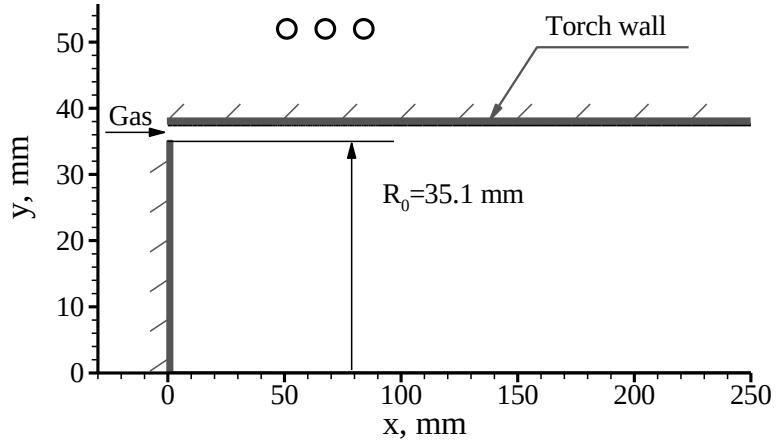

(b)

Fig. 2.2 Schematic of the 110-kW inductively coupled plasma wind tunnel

2.3 Physical Phenomena in an ICP wind tunnel

Although the structure of an ICP torch as shown in Fig. 2.3 is relatively simple, physical phenomena in the torch are very complicated. The working gas is injected from the inlet with a subsonic speed, and then heated up dramatically by the intense electromagnetic-field which is induced by the RF alternative coil current. Because of large Joule heating deposition in the coil region, the working gas begin dissociating and ionizing, and then forms a high-temperature, and high-enthalpy flow in this region. Because of light mass and active property of electrons, much Joule heating energy is preferentially absorbed by them. Through elastic collisions between electrons and other heavy particles, they exchange internal energy between each other. In the condition of

relatively high-pressure but low input power, the generated inductive plasma flow may be weakly ionized. It means that compared with the number density of heavy particles, the amount of electron existing in the flow is much fewer than that of heavy particles. Therefore the internal energy exchange between electron and heavy particles may be insufficient. It results in the possibility that the ICP flow stays in thermochemical nonequilibrium.

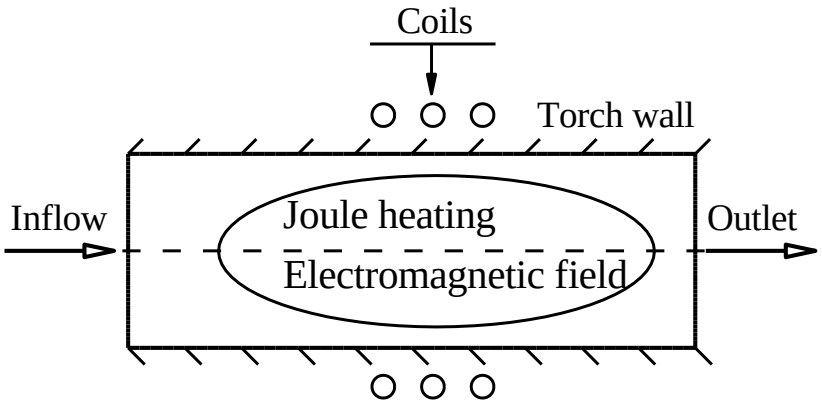

Fig. 2.3 Structure of inductively coupled plasma torch

2.3.1 Radio Frequency Inductive Discharge

Inductive discharge is nearly as old as the invention of electric power, with the first report of an "electrodeless ring discharge" by Hittorf [44]. He wrapped a coil around an evacuated tube and observed a discharge when the coil was excited with Leyden jar. Plasma in an inductive discharge is created by application of radio-frequency power to a non-resonant inductive coil. Inductive sources have potential advantages over high density wave-heated sources, including simplicity of concept, no requirement for dc magnetic fields, and radio frequency rather than microwave source power.

The inductive coil is commonly driven at 1.0 – 13.56 MHz through a capacitive matching network. The coil can also be driven by using a balanced transformer which places a virtual ground in the middle of the coil and reduces the maximum coil-to-plasma voltage. This reduces the undesired capacitively coupled RF current flowing from coil to plasma. In an inductively coupled plasma, power is transferred from the electric fields to the plasma electrons within a skin depth layer of thickness δ near the plasma surface by collisional dissipation and by a collisionless heating process in which bulk plasma electrons collide with the oscillating inductive electric fields within the layer. Electrons are accelerated and subsequently thermalized by the Joule heating process. The collisional skin depth of an inductive discharge can be roughly written in the forms:

$$\delta_{\text{skin}} = \sqrt{\frac{1}{\pi f \mu_0 \sigma}} \,. \tag{2.1}$$

where f, μ_0, and σ are the current frequency, vacuum permeability, and electrical conductivity of plasma.

2.3.2 Dissociation and Ionization Process

The working gas is dissociated and ionized by the severe Joule heating in the inductive coil section. The dissociation and ionization process is thus one of the important phenomena in an inductively coupled plasma wind tunnel.

There are processes of dissociation and ionization by various events in a discharge field. Some types of dissociation, recombination and ionization reactions are described here.

(1) Collision dissociation:

Molecules can be dissociated to form atoms through elastic collisions with heavy particles which possess enough energy. The molecule AB denotes N_2, O_2 and NO for nitrogen and air.

$$AB + C \rightleftharpoons A + B + C \tag{2.2}$$

(2) Inelastic collision - Third body recombination:

An inelastic collision occurs between a particle A and another B which has enough high kinetic energy.

$$A + B \rightleftharpoons A^+ + e^- + B \tag{2.3}$$

In starting process of ionization, the next two reactions (3) and (4) are important.

(3) Photoionization - Radiative recombination:

In a very high-temperature region, gas radiation may become predominant. In such field, it is sufficiently thought that an atom absorbs a photon which has high frequency and it ionizes.

$$A + h\nu \rightleftharpoons A^+ + e^- \tag{2.4}$$

where h and ν represent the Planck constant and frequency, respectively.

(4) Field ionization:

An electron is extracted from the atom by a strong electric field.

$$E(A) \rightleftharpoons A^+ + e^- \tag{2.5}$$

(5) Charge exchange ionization:

As moving electron from a particle, charge exchange occurs.

$$A + B^+ \rightleftharpoons A^+ + B \tag{2.6}$$

Near the torch wall where the temperature is relatively low, the above reaction becomes important to transfer the discharge.

(6) Electron-impact Ionization:

This ionization process caused performed by electron collision is very important in the discharge region.

$$A + e^- \rightleftharpoons A^+ + e^- + e^- \tag{2.7}$$

Through the electron-impact ionization reaction, two electrons are generated by one collision. When temperature and number density of the electron reach certain values, the above reaction can rapidly proceed. This torrential ionization is referred to as “Electron Avalanche (also Avalanche Ionization)” and it is one of the key mechanisms to maintain a discharge in an ICP facility.

2.3.3 Joule Heating

A working gas such as argon, nitrogen, air, oxygen or carbon dioxide is injected into a quartz tube from the inlet of the ICP torch, and is vigorously heated by an alternating electromagnetic field induced by a radio-frequency current. This heating process is the Joule-heating (or called Ohmic heating) and is one of the most important mechanisms in the ICP wind tunnel. The electric energy is transformed into the test gas by the Joule-heating process in the heating section. It is thought that the gas in the inductive coil region is dissociated/ionized, forming high temperature and high enthalpy flow. On the other hand, in the outer flow around the plasma core, the gas forms low temperature flow due to cooling water on the quartz tube wall. Hence, the chemical composition in the outer flow is expected to be molecules.

Because of intense electromagnetic-field induced by the alternative coil current, the interaction and coupling between this electromagnetic-field and the electrons in an ICP flow is strong. Therefore the effect of electromagnetic-field induced by the plasma current should be also considered i.e., the Lorentz force should be considered. In performing the ICP simulation, it seems that not only the Joule heating need to be solved with the flow field equations, but also the Lorentz forces should be considered in the momentum equations. Additionally, to take into account the phase difference of the electromagnetic-fields induced by the coil current and plasma current, the complex form of Maxwell electromagnetic equations is usually used to figure out the distributions of the electric and magnetic fields in the ICP torch.

2.3.4 Nonequilibrium Process

In general, the nonequilibrium process of a plasma flow usually includes two aspects: chemical nonequilibrium and thermal nonequilibrium. (1) the chemical equilibrium or nonequilibrium state of a flow highly relates to the number density of the gas considered. Because the chemical reaction rate mainly determined by the number density of the chemical species participating in the dissociation/ionization reactions. The rate of chemical reaction increases rapidly with increasing of the number density at a given temperature. Therefore, we may encounter circumstances where the characteristic time of chemical reactions τ_c is the same order with that of the flow field τ_f due to low density. In this case, it is usually referred as chemical nonequilibrium flow. However, if $\tau_f \gg \tau_c$, in this case, it indicates that the chemical reactions complete instantaneously so that local chemical compositions of gas can be determined only by thermodynamic properties at that location. Then, the flow can be thought in chemical equilibrium, or called chemical equilibrium flow. (2) To explain the thermal equilibrium and nonequilibrium processes, First we explain internal energy modes of a gas here. For dissociated/ionized gases, a diatomic molecule has several modes of internal energy as: translational, rotational, vibrational and electronic excitation energy modes which are shown in Fig. 2.4. For a monoatomic molecule, atom and electron, there exist the translational degree of freedom. The atom as well as the molecule also include the electronic excitation degree of freedom. Furthermore, the property 'temperature' can be defined for each internal degree of freedom as translational, rotational, vibrational and electronic excitation temperatures. If there is no sufficient time or chance to relax the internal energies between chemical species. It means the temperatures hardly relax for each other. Then, the flow is referred to as "thermal nonequilibrium flow". On the other hand, if the energy relaxation between internal energies proceeds fast and cause energy equilibrium for each internal energy mode. In such a situation, all temperatures are almost the same and the flow is referred to as "thermal equilibrium flow.

In the high pressure such as atmospheric pressure condition, it is thought that the flow field of an inductive plasma is close to be in equilibrium due to the frequent collisions between particles. On the other hand, as the pressure decreases in the torch, there tend to be less particle collisions. The internal energy exchange and chemical reaction by the particle collisions may be hardly occur. As a result, the ICP flow is far from thermochemical equilibrium. Thus, in order to predict the flow properties accurately, nonequilibrium analysis may be required in the present inductively coupled plasma flow calculation.

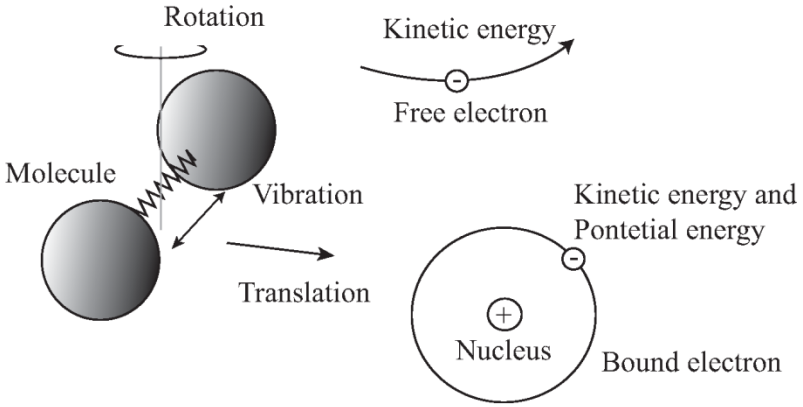

Fig. 2.4 Internal energy-mode

2.4 Numerical Modeling of Nonequilibrium ICP Flow

So far, the main physical phenomena in the inductively coupled plasma wind tunnel were described in the previous sections. In this section, some key phenomena are discussed in order to introduce an appropriate numerical model into the present inductively coupled plasma flow simulation.

2.4.1 Flow Field

In experimental studies, commonly, a steady inductive coupled plasma flow is desired and useful to carry on ablating or spectroscopic investigations. Although three-dimension flow simulation is preferable, its numerical procedure will cost much computation time and is difficult. Since the inductive coil and quartz tube are cylindrical and axisymmetric, it is reasonable to adopt the axisymmetric two dimensional assumption in the present simulations. Thus, the flow-field computations are carried out under the two-dimensional, axisymmetric and steady state assumptions.

To approximately evaluate whether the flow is continuous or not, it is available to calculate the Knudsen number as:

$$K_n = \frac{\lambda}{L} \tag{2.8}$$

where λ denotes the mean free pass and L shows the characteristic length in a flow field. The mean free pass is expressed as follows:

$$\lambda = \frac{1}{\sqrt{2}\pi d^2 n} \tag{2.9}$$

where d is the diameter of the particle (i.e., d=0.375 nm for molecular nitrogen) and n represents the number density. With the characteristic length L and the mean free path λ, the Knudsen number can be calculated. If the Knudsen number is smaller than 0.01, the flow field can be assumed to be continuous and it is possible to utilize the Navier-Stokes equations to analyze the flow field. To approximately evaluate number density, the following gas state equation is used:

$$n = p / kT \tag{2.10}$$

where k is Boltzmann constant. For the 10 kW and 110 KW ICPWTs, their typical operating conditions are 4000 Pa and 10000 Pa, respectively. the maximum temperature of an ICP flow is about 10000 K. Using above equations and constants, the Knudsen numbers can be approximately calculated, which are shown in Table 2.2. For the 10 kW and 110 KW ICPWTs, the evaluated Knudsen numbers under their typical working conditions are 0.0014 and 0.0058. Thus, the Navier-Stokes equations can be used to analyze the flow fields of 10 kW and 110 KW ICPWTs.

Table 2.2 Knudsen numbers

Facility	λ(m)	L(m)	d(nm)	p(Pa)	n(1/m^3)	K_n
10-kW ICPWT	5.3×10^{-5}	0.0375	0.375	4000	3.0×10^{22}	0.0014
110-kW ICPWT	2.2×10^{-5}	0.0375	0.375	10000	7.5×10^{22}	0.0058

2.4.2 Electromagnetic Field

For an inductively coupled plasma flow, the electromagnetic fields induced by a radio-frequency coil current controls heating process of the flow. The working gas such as nitrogen and air is vigorously heated and dissociated/ionized by this alternating electromagnetic field. In order to make clear the heating mechanism and the interactions between electromagnetic and flow fields, Maxwell's equations need to be solved to figure out the Joule heating rate and electromagnetic fields in the ICP torch.

The complete Maxwell's equations which consists of the Faraday, Ampere and Gauss laws are written as

$$\nabla \cdot \boldsymbol{D} = \rho_c, \tag{2.11}$$

$$\nabla \cdot \boldsymbol{B} = 0, \tag{2.12}$$

$$\nabla \times \boldsymbol{E} = -\mu_0 \frac{\partial \boldsymbol{H}}{\partial t}, \tag{2.13}$$

$$\nabla \times \boldsymbol{H} = \boldsymbol{J} + \frac{\partial \boldsymbol{D}}{\partial t}. \tag{2.14}$$

where ρ_c, $\frac{\partial D}{\partial t}$, ε_0, μ_0, $\boldsymbol{E}$, $\boldsymbol{H}$, $\boldsymbol{J}$ denote the total electric charge density, displacement current density, permittivity of free space, permeability of free space, electric-field intensity, magnetic-field intensity, and total current density respectively. The electric flux density $\boldsymbol{D}$ and magnetic flux density $\boldsymbol{B}$ are proportional to the electric field and the magnetic field as:

$$\boldsymbol{D} = \varepsilon_0 \boldsymbol{E}, \tag{2.15}$$

$$\boldsymbol{B} = \mu_0 \boldsymbol{H}. \tag{2.16}$$

Because plasma flow can be thought being electric neutrality, so the total electric charge density ρ_c can be assumed to be zero. On the other hand, because the physical essence of the displacement current ($I_d = \oint \frac{\partial D}{\partial t} dS$) is the variation of electric field. It cannot contribute to generate Joule heating or other chemical effects [45]. Moreover, in this study the evaluated displacement current density ($J_d = \partial D/\partial t = i2\pi f \varepsilon_0 E \approx 2\pi \times 4.0 \times 10^6 \times 8.85 \times 10^{-12} \times 5000 \approx 1.1\ \mathrm{A/m^2}$) seems much smaller than the coil current density ($J_c = I/(\pi R_{coil}^2) \approx 100/(\pi \times 0.004^2) \approx 2.0 \times 10^6\ \mathrm{A/m^2}$). So the displacement current density $\frac{\partial D}{\partial t}$ can be neglected for an ICP simulation. Then, abovementioned complete Maxwell equations are simplified as following for the ICP simulations:

$$\nabla \cdot \boldsymbol{E} = 0, \tag{2.17}$$

$$\nabla \cdot \boldsymbol{H} = 0, \tag{2.18}$$

$$\nabla \times \boldsymbol{E} = -\mu_0 \frac{\partial \boldsymbol{H}}{\partial t}, \tag{2.19}$$

$$\nabla \times \boldsymbol{H} = \boldsymbol{J}. \tag{2.20}$$

If these four equations can be solved out, the electromagnetic field of an ICP flow can be clearly understood.

2.4.3 Thermochemical Nonequilibrium

In the inductive coil region, it is possible that the generated plasma flows stays in thermal and chemical nonequilibrium states in some extent. Thermochemical nonequilibrium strongly affects evaluations of chemical reactions and solutions of electromagnetic field. Particularly, rotational and vibrational temperatures are important factors in dissociation/recombination processes, while the electron temperature will have influence on ionization/de-ionization reactions and evaluation of electrical conductivity which is involved in the magnetic vector potential equations, Joule heating rate, and Lorentz forces. In an ICP flow simulation, these chemical reaction processes and Joule heating are expected to play important roles. Thus, it will be better and more proper to consider thermochemical nonequilibrium in the numerical modeling.

For nonequilibrium plasma simulation, previously, Park's two-temperature model was widely used to study thermal nonequilibrium phenomena of arc-heated and ICP flows. For more accurately prediction of the internal energy exchange between translational, vibrational, rotational, and electronic mode of chemical particles, recently a four-temperature model considering the internal energy transfer such as electron-vibration, electron-rotation, vibration-translation, vibration-rotation, and rotation-translation was developed and used to study the thermal nonequilibrium process of an arc-heated flow [33]. Note that for the electron-vibrational energy relaxation time, Lee's previous theoretical data [34] were used in this four-temperature model. According to Bourdon's work [35], however, more accurate vibrational-electron relaxation time was available in the temperature range of 3000–20000 K. Beyond this temperature range, Kim et al [36] recently proposed a method to assess the vibrational-electron relaxation time for nitrogen molecular in modeling electron energy phenomena.

2.4.4 Assumptions

Based on the above discussions, the following assumptions are introduced in this study:

(1) The flow is continuum, steady, and axisymmetric.
(2) Nitrogen and air are used as the working gas.
(3) The flow field is in thermochemical nonequilibrium and the temperature is separated into translational T_{tr}, rotational T_{rot}, vibrational T_{vib} and electron T_e temperatures. The electronic excitation temperature is assumed to be equilibrated with the electron temperature. On the other hand, the electronic-excitation energy and the electron energy are assumed to be equilibrated $T_{ex} = T_e$.
(4) The placement current and total free charge density in free space are neglected.
(5) The Lorentz force, magnetic field induced by plasma, and gravity are considered.
(6) Turbulence is considered

2.5 Flow-Field Equations

As the first step of a numerical computation, derivations of the governing equations should be performed correctly. On the basis of the assumptions introduced in the previous sections, we derive flow-field equations in the present section. As for a thermochemical equilibrium flow simulation, it is reasonable to use the total mass, momentum and total energy conservations only to describe the flow field. However, if the interest exists in the simulation of thermochemical nonequilibrium flow, it is necessary to also consider the species mass and species energy conservations e.g., rotation, vibration and electron-energy conservations in the system of governing equations. Thus, in this section the derivations of the flow-field equations including total mass, momentum, total energy, rotational, vibrational and electron energy conservations are discussed here. The present formulation derivations owe substantially to the Ref. [46].

The conservation equations can be derived according to the Boltzmann equation. Multiplying the average quantity per unit particle $\langle \varphi_s \rangle$, the Boltzmann equation becomes

$$\frac{\partial}{\partial t}\left(n_s \langle \varphi_s \rangle\right) + \frac{\partial}{\partial x_j}\left(n_s \langle \varphi_s u_s^j \rangle\right) = S\left(\langle \varphi_s \rangle\right), \tag{2.21}$$

where $\langle\ \rangle$ represents the averaged value of a quantity, and n_s, v_s^j are the number density of species *s* and *j*th component of particle velocity, respectively. In addition, $S\left(\langle \varphi_s \rangle\right)$ shows the variation rate by interactions among species.

2.5.1 Mass Conservation

Taking $\varphi_s = m_s$ in Eq. (2.21), we can obtain the mass conservation for species *s*. First, the mass density is written by, $n_s \langle m_s \rangle = \rho_s$ and the *j*th component of the thermal velocity is defined as follows:

$$C_s^j \equiv u_s^j - u_0^j, \tag{2.22}$$

where u_0^j is the *j*th component of the mass-averaged velocity, which is given by:

$$u_0^j = \frac{\sum_s^{ns} \rho_s u_s^j}{\sum_s^{ns} \rho_s}. \tag{2.23}$$

Thus, replacing the thermal velocity C_s^j by the diffusion velocity V_s^j, the mass conservation for species *s* is written by:

$$\frac{\partial \rho_s}{\partial t} + \frac{\partial}{\partial x_j}\left[\rho_s\left(u_0^j + V_s^j\right)\right] = \dot{w}_s, \tag{2.24}$$

where $\dot{w}_s$ represents the mass production rate due to collisions. The summation of Eq. (2.24) over all the species yields

$$\frac{\partial}{\partial t}\sum_s^{ns}\rho_s + \frac{\partial}{\partial x_j}\left[\sum_s^{ns}\rho_s u_0^j + \sum_s^{ns}\rho_s V_s^j\right] = \sum_s^{ns}\dot{w}_s. \tag{2.25}$$

Since $\sum_s^{ns}\rho_s V_s^j$ and $\sum_s^{ns}\dot{w}_s$ are zero by definition, we obtain the total mass conservation as follows:

$$\frac{\partial \rho}{\partial t} + \frac{\partial(\rho u_0^j)}{\partial x_j} = 0, \tag{2.26}$$

where

$$\rho = \sum_s^{ns}\rho_s. \tag{2.27}$$

2.5.2 Momentum Conservation

The momentum conservation equation for the species *s* can be obtained by replacing the quantity φ_s by the momentum $m_s u_s^i$. Here, the production rate term $S\left(\langle m_s u_s^i\rangle\right)$ consists of the following three external forces: the interaction force due to collision of species $F_{\text{int},s}^i$ the electric field force $F_{\text{E},s}^i$ and the magnetic field force. The second term on the left hand side of Eq. (2.21) in identifying $\varphi_s = m_s u_s^j$ is expressed by:

$$n_s\langle m_s u_s^i u_s^j\rangle = \rho_s\left(\langle u_0^i u_0^j\rangle + \langle u_0^i C_s^j\rangle + \langle C_s^i u_0^j\rangle + \langle C_s^i C_s^j\rangle\right) = \rho_s\left(u_0^i u_0^j + \langle C_s^i C_s^j\rangle\right). \tag{2.28}$$

The viscous stress tensor τ^{ij} is defined as:

$$\tau_s^{ij} \equiv -\left(\rho_s\langle C_s^i C_s^j\rangle - p_s\delta^{ij}\right), \tag{2.29}$$

where δ^{ij} is the Kronecker delta. As a result, the momentum conservation can be obtained as follows:

$$\frac{\partial}{\partial t}\left(\rho_s u_s^i\right)+\frac{\partial}{\partial x^j}\left(\rho_s u_0^i u_0^j+p_s\delta^{ij}\right)-\frac{\partial \tau_s^{ij}}{\partial x^j}=F_{\mathrm{int},s}^i+F_{\mathrm{E},s}^i+F_{\mathrm{B},s}^i. \tag{2.30}$$

Taking all plasma species s as an integer, the internal force $F_{\mathrm{int},s}^i$ between chemical species can be thought as 0. Therefore, the total momentum conservation equation is obtained by summation over all the species as:

$$\frac{\partial}{\partial t}\left(\rho u_0^i\right)+\frac{\partial}{\partial x^j}\left(\rho u_0^i u_0^j+p\delta^{ij}\right)-\frac{\partial \tau^{ij}}{\partial x^j}=\sum_s^{ns}F_{\mathrm{E},s}^i+\sum_s^{ns}F_{\mathrm{B},s}^i. \tag{2.31}$$

According to Hirschfelder, Curtiss and Bird [47] the viscous stress tensor is given by:

$$\tau^{ij}=\mu\left(\frac{\partial u_0^i}{\partial x^j}+\frac{\partial u_0^j}{\partial x^i}-\frac{2}{3}\frac{\partial u_0^k}{\partial x^k}\delta^{ij}\right), \tag{2.32}$$

where μ is the viscosity for a gas mixture. Due to strong interactions between the electromagnetic field and the ionic species of an inductively coupled plasma flow, the electric and magnetic forces are considered in this study. The summation of the electric and magnetic forces are usually called as the Lorentz force F_{Li}. Consequently, the total momentum conservation equation is expressed by

$$\frac{\partial}{\partial t}\left(\rho u_0^i\right)+\frac{\partial}{\partial x^j}\left(\rho u_0^i u_0^j+p\delta^{ij}\right)=\frac{\partial}{\partial x^j}\left[\mu\left(\frac{\partial u_0^i}{\partial x^j}+\frac{\partial u_0^j}{\partial x^i}\right)-\frac{2}{3}\mu\frac{\partial u_0^k}{\partial x^k}\delta^{ij}\right]+F_{Li}. \tag{2.33}$$

2.5.3 Energy Conservation

The energy conservation equation for species s is obtained by setting $\langle\varphi_s\rangle=\langle\frac{1}{2}m_s u_s^i u_s^i\rangle+\langle\epsilon_{\mathrm{int}}\rangle$, where the $\langle\frac{1}{2}m_s u_s^i u_s^i\rangle$ and $\langle\epsilon_{\mathrm{int}}\rangle$ are the average densities of translational energy and internal energy of rotation, vibration, electron and chemical energy mode, respectively. First, we transform the translational energy density as

$$\langle\frac{1}{2}m_s u_s^i u_s^i\rangle=\frac{1}{2}m_s\sum_i^3\langle u_s^i u_s^i\rangle, \tag{2.34}$$

where

$$\langle u_s^i u_s^i\rangle=\langle\left(u_0^i+C_s^i\right)^2\rangle=u_0^i u_0^i+\langle C_s^i C_s^i\rangle. \tag{2.35}$$

Hence, the energy becomes

$$n_s\langle\frac{1}{2}m_s u_s^i u_s^i\rangle+n_s\langle\epsilon_{\mathrm{int}}\rangle=\rho_s\left(\frac{1}{2}u_0^i u_0^i+\frac{1}{2}\langle C_s^i C_s^i\rangle+e_{\mathrm{int},s}\right)=\rho_s\left(\frac{1}{2}u_0^i u_0^i+e_s\right), \tag{2.36}$$

where e_s represents the total energy per unit mass. Then, the translational energy flux $\langle u_s^i u_s^i u_s^j\rangle$ is transformed as follows:

$$\langle u_s^i u_s^i u_s^j\rangle=\left[\sum_i^3\left(u_0^i+C_s^i\right)^2\right]\left(u_0^j+C_s^j\right)$$

$$= \left(u_0^i u_0^i + \langle C_s^i C_s^i \rangle \right) u_0^j + 2\langle C_s^i C_s^j \rangle u_0^i + \langle C_s^i C_s^i C_s^j \rangle \,. \tag{2.37}$$

The heat flux component due to random motion is defined by

$$q_s^j \equiv \frac{1}{2} \rho_s \langle C_s^i C_s^i C_s^j \rangle + \rho_s \langle \epsilon_{\text{int}} C_s^j \rangle. \tag{2.38}$$

The energy flux term in Eq. (2.21) is here described with Eqs. (2.29) and (2.38) as follows:

$$n_s \langle \frac{1}{2} m_s u_s^i u_s^i u_s^j \rangle + n_s \langle \epsilon_{\text{int}} u_s^j \rangle = \rho_s u_0^j \left(\frac{1}{2} u_0^i u_0^i + e_s \right) + \rho_s \left(-\tau_s^{ij} + p_s \right) + q_s. \tag{2.39}$$

The production rate term $S\left(\langle m_s u_s^i u_s^i \rangle \right)$ consists of the power done by the electric and magnetic forces $\left(F_{\text{E},s}^i + F_{\text{B},s}^i \right) u_s^i$ the rate of energy supplied by elastic and inelastic collisions S_{int} and the Joule-heating rate by the electric field S_{joule}. Thus, the energy conservation equation for species *s* is expressed as

$$\frac{\partial}{\partial t}\left[\rho_s \left(\frac{1}{2} u_0^i u_0^i + e_s \right) \right] + \frac{\partial}{\partial x^j}\left[\rho_s u_0^j \left(\frac{1}{2} u_0^i u_0^i + e_s \right) \right] + \frac{\partial}{\partial x^j}\left(p_s u_0^j \right) - \frac{\partial}{\partial x^j}\left(\tau_s^{ij} u_0^j \right) + \frac{\partial q_s^j}{\partial x^j}$$

$$= \left(F_{\text{E},s}^j + F_{\text{B},s}^j \right) u_s^j + S_{\text{int},s} + S_{\text{joule}}. \tag{2.40}$$

Similarly, the total energy conservation equation is obtained by summation over all the species:

$$\frac{\partial}{\partial t}\left[\rho \left(\frac{1}{2} u_0^i u_0^i + e \right) \right] + \frac{\partial}{\partial x^j}\left[\rho u_0^j \left(\frac{1}{2} u_0^i u_0^i + e \right) \right] + \frac{\partial}{\partial x^j}\left(p u_0^j \right) - \frac{\partial}{\partial x^j}\left(\tau^{ij} u_0^j \right) + \frac{\partial q^j}{\partial x^j}$$

$$= \sum_s^{ns} \left(F_{\text{E},s}^j + F_{\text{B},s}^j \right) u_s^j + S_{\text{joule}} \,. \tag{2.41}$$

where *e* is the total energy per unit mass and q^j is the *j*th component of the total heat flux. The summation of the rate of energy by elastic and inelastic collisions $\sum_s^{ns} S_{\text{int},s}$ is zero by definition. When the Chapman-Enskog approximation is applied to a gas mixture [46] the total heat flux is expressed as summation of translational, rotational, vibrational and electron temperature gradients and diffusion, that is,

$$q_j = \lambda_{tr} \frac{\partial T_{tr}}{\partial x_j} + \lambda_{rot} \frac{\partial T_{rot}}{\partial x_j} + \lambda_{vib} \frac{\partial T_{vib}}{\partial x_j} + \lambda_e \frac{\partial T_e}{\partial x_j} + \sum_s^{ns} \rho_s h_s V_s^j \,. \tag{2.42}$$

where h_s shows the enthalpy per unit mass for species *s*. In addition, $\lambda_{tr}, \lambda_{rot}, \lambda_{vib}, \lambda_e$ are the translational, rotational, vibrational and electron components of the frozen thermal conductivity, respectively. Consequently, under the assumption that the plasma is macroscopically neutral, the total energy conservation equation is obtained as the following form:

$$\frac{\partial}{\partial t}\left[\rho \left(\frac{1}{2} u_0^i u_0^i + e \right) \right] + \frac{\partial}{\partial x^j}\left[\rho u_0^j \left(\frac{1}{2} u_0^i u_0^i + e \right) + p u_0^j \right]$$

$$= \frac{\partial}{\partial x^j}\left(\lambda_{tr}\frac{\partial T_{tr}}{\partial x_j} + \lambda_{rot}\frac{\partial T_{rot}}{\partial x_j} + \lambda_{vib}\frac{\partial T_{vib}}{\partial x_j} + \lambda_e\frac{\partial T_e}{\partial x_j} + \sum_s^{ns}\rho_s h_s V_s^j \right)$$

$$+ \frac{\partial}{\partial x^j}\left[u_0^j \mu\left(\frac{\partial u_0^i}{\partial x^j} + \frac{\partial u_0^j}{\partial x^i}\right) - \frac{2}{3}u_0^j \mu \frac{\partial u_0^k}{\partial x_0^k}\delta_{ij} \right] + S_{\text{joule}}. \quad (2.43)$$

In the same way, each internal energy conservation is obtained for the rotational energy conservation,

$$\frac{\partial(\rho e_{\text{rot}})}{\partial t} + \frac{\partial(\rho e_{\text{rot}} u_0^j)}{\partial x^j} = \frac{\partial}{\partial x^j}(\lambda_{rot}\frac{\partial T_{rot}}{\partial x^j}) + \frac{\partial}{\partial x^j}(\rho\sum_{s=M}^{nm} h_{rot,s}V_s) + S_{\text{int},rot}, \quad (2.44)$$

and for the vibrational energy conservation,

$$\frac{\partial(\rho e_{\text{vib}})}{\partial t} + \frac{\partial(\rho e_{\text{vib}} u_0^j)}{\partial x^j} = \frac{\partial}{\partial x^j}(\lambda_{vib}\frac{\partial T_{vib}}{\partial x^j}) + \frac{\partial}{\partial x^j}(\rho\sum_{s=M}^{nm} h_{vib,s}V_s) + S_{\text{int},vib}, \quad (2.45)$$

finally, for the electron energy conservation,

$$\frac{\partial(\rho e_{\text{e}})}{\partial t} + \frac{\partial(\rho e_{\text{e}} u_0^j)}{\partial x^j} = -\frac{\partial(p_{\text{e}} u_0^j)}{\partial x^j} + \frac{\partial}{\partial x^j}(\lambda_e\frac{\partial T_e}{\partial x^j}) + \frac{\partial}{\partial x^j}(\rho h_e V_e) + S_{\text{int},e} + S_{\text{joule}}. \quad (2.46)$$

where e_{rot}, e_{vib}, e_e are the rotational, vibrational and electron energies per unit mass, respectively. Additionally, h_{rot}, h_{vib}, h_e represent the enthalpies per unit mass for each energy. The production terms due to collisions $S_{\text{int, rot}}$, $S_{\text{int, vib}}$, $S_{\text{int, e}}$ and S_{joule} will be discussed later.

2.5.4 AKN *k*-ε Turbulence Model

For the arc-heated flow simulation it was reported that the turbulence model played an important role in the heat transfer process [27]. Therefore, in this study the turbulence model is also considered to model the turbulent energy transfer. In order to predict the effect of turbulence properly, the AKN *k*-ε model [48], a low-Reynolds-number two-equation turbulence model, is used in this study. The turbulence transport equations for the turbulent kinetic energy *k* and its dissipation rate ε can be written as

$$\frac{\partial\rho k}{\partial t} + \frac{\partial}{\partial x_j}\left(\rho k u_j\right) = \frac{\partial}{\partial x_j}\left\{\left(\mu + \frac{\mu_{\text{t}}}{\sigma_k}\right)\frac{\partial k}{\partial x_j}\right\} + \tau_{ij}^{\text{t}}\frac{\partial u_j}{\partial x_j} - \rho\varepsilon, \quad (2.47)$$

$$\frac{\partial\rho\varepsilon}{\partial t} + \frac{\partial}{\partial x_j}\left(\rho\varepsilon u_j\right) = \frac{\partial}{\partial x_j}\left\{\left(\mu + \frac{\mu_{\text{t}}}{\sigma_\varepsilon}\right)\frac{\partial\varepsilon}{\partial x_j}\right\} + C_{\varepsilon 1}f_1\frac{\varepsilon}{k}\tau_{ij}^{\text{t}}\frac{\partial u_j}{\partial x_j} - C_{\varepsilon 2}f_2\rho\frac{\varepsilon^2}{k}. \quad (2.48)$$

The turbulent eddy viscosity can be obtained from:

$$\mu_{\text{t}} = C_\mu f_\mu \rho\frac{k^2}{\varepsilon}. \quad (2.49)$$

The model constants in Eqs. (2.47), (2.48) and (2.49) are given by:

$$C_\mu = 0.09,\quad \sigma_k = 1.4,\quad \sigma_\varepsilon = 1.4,\quad C_{\varepsilon 1} = 1.5,\quad C_{\varepsilon 2} = 1.9$$

and the model functions are denoted as

$$f_\mu = \left\{1-\exp\left(-\frac{y^*}{14}\right)\right\}^2\left[1+\frac{5}{R_t^{3/4}}\exp\left\{-\left(\frac{R_t}{200}\right)^2\right\}\right],$$

$$f_1 = 1,$$

$$f_2 = \left\{1-\exp\left(-\frac{y^*}{3.1}\right)\right\}^2\left[1-0.3\exp\left\{-\left(\frac{R_t}{200}\right)^2\right\}\right],$$

where

$$y^* = \frac{(\nu\varepsilon)^{1/4} y_{wd}}{\nu}, \tag{2.50}$$

$$R_t = \frac{k^2}{(\nu\varepsilon)}. \tag{2.51}$$

Here, ν represents the kinematic molecular viscosity.

2.6 Electromagnetic-Field Equations

In order to enhance the computational efficiency and reduce the complexity of the electromagnetic equations, the aforementioned Maxwell's equations are rewritten here and simplified further as following:

$$\nabla \cdot \boldsymbol{E} = 0, \tag{2.52}$$

$$\nabla \cdot \boldsymbol{H} = 0, \tag{2.53}$$

$$\nabla \times \boldsymbol{E} = -\mu_0 \frac{\partial \boldsymbol{H}}{\partial t}, \tag{2.54}$$

$$\nabla \times \boldsymbol{H} = \boldsymbol{J}. \tag{2.55}$$

where $\boldsymbol{E}$, $\boldsymbol{H}$, $\boldsymbol{J}$ are the electric-field intensity, magnetic-field intensity, and total current density, respectively. Considering that the magnetic-field intensity can be expressed by the magnetic vector potential $\boldsymbol{A}$ that satisfies [37]:

$$\mu_0 \boldsymbol{H} = \nabla \times \boldsymbol{A}. \tag{2.56}$$

Substituting equation (2.56) into (2.54) yields:

$$\boldsymbol{E} = -\frac{\partial \boldsymbol{A}}{\partial t}. \tag{2.57}$$

Since the vector potential $\boldsymbol{A}$ is oscillating with the angular frequency of a coil current ω, $\boldsymbol{A}$ can be expressed in a Flourier mode, and equation (2.57) becomes:

$$\boldsymbol{E} = -\frac{\partial \boldsymbol{A}}{\partial t} = -i\omega A_0 e^{i\omega t} = -i\omega \boldsymbol{A}, \tag{2.58}$$

where $\omega=2\pi f$. f, A_0, i respectively denote the driving frequency of the coil current, amplitude of the vector potential, and complex factor ($i=\sqrt{-1}$). Substituting equation (2.56) into (2.55) as well as using the Coulomb's gauge $\nabla \cdot \boldsymbol{A} = 0$, we obtain:

$$\nabla^2 \boldsymbol{A} = -\mu_0 \boldsymbol{J}. \tag{2.59}$$

For the cylindrical induction plasma torch, the coil and plasma current can be assumed to be composed of parallel rings. So it is reasonable to assume the vector potential has only the tangential component [38] i.e., $\boldsymbol{A} = (A_r, A_\theta, A_z) = (0, A_\theta, 0)$. To take into account the phase differences between the electromagnetic field generated by the coil current and that induced by the plasma, the tangential vector potential A_θ stands for a complex variable, i.e., $A_\theta = A_R + iA_I$. Finally, the magnetic vector-potential equation is expressed as:

$$\nabla^2 A_\theta = -\mu_0 J_\theta . \tag{2.60}$$

2.6.1 Standard Electromagnetic Model

To solve the magnetic vector potential governed by Eq. (2.60), Mostaghimi and Boulos [37] proposed a mathematically elegant model to deal with this issue. In this model, the electromagnetic field in the ICP torch is only considered. The coil current is out of the computational domain. The effect of vector potential generated by the coil current is equivalently transformed and considered through the torch wall. In the ICP torch, because there only exist plasma current, so J_θ in Eq. (2.60) denotes plasma current density. Taking into account the Ohm's law and using Eq. (2.58), the plasma current density can be expressed as:

$$J_\theta = \sigma E_\theta = -i\omega\sigma A_\theta = -i\omega\sigma(A_R + iA_I), \tag{2.61}$$

Substituting the Eq. (2.61) into Eq. (2.60), then we get:

$$\nabla^2 A_R + \omega\mu_0\sigma A_I = 0, \tag{2.62}$$

$$\nabla^2 A_I - \omega\mu_0\sigma A_R = 0. \tag{2.63}$$

The vector potential in the torch can be solved by these two equations. While the vector potential A_R and A_I on the torch wall are defined as following:

$$A_R = \frac{\mu_0 I}{2\pi}\sum_{j=1}^{n}\sqrt{\frac{y_j}{y_0}}G(k_j) + \frac{\mu_0\omega}{2\pi}\sum_{p=1}^{C.V.}\sqrt{\frac{y_p}{y_0}}\sigma_p A_{I,p} S_p G(k_p), \tag{2.64}$$

$$A_I = -\frac{\mu_0\omega}{2\pi}\sum_{p=1}^{C.V.}\sqrt{\frac{y_p}{y_0}}\sigma_p A_{R,p} S_p G(k_p), \tag{2.65}$$

$$G(k) = \left(\frac{2}{k} - k\right)K(k) - \frac{2}{k}E(k), \tag{2.66}$$

$$k_j = \sqrt{\frac{4y_j y_0}{(y_j + y_0)^2 + (x_j - x_0)^2}}, \text{ and } k_p = \sqrt{\frac{4y_p y_0}{(y_p + y_0)^2 + (x_p - x_0)^2}}. \tag{2.67}$$

where (x_j, y_j), (x_0, y_0), (x_p, y_p), which are shown in Fig. 2.5, denote the position coordinates of the j^{th} coil current, torch wall and the p^{th} control volume. *K(k)* and *E(k)* are the first and the second kinds of complete elliptic integrals. The symbols I and S_p denote the amplitude of a coil current and the cross section area of p^{th} control volume in the torch. Note that in the Eq. (2.64), A_R includes two parts $A_R = A_{R1} + A_{R2}$:

$$A_{R1}=\frac{\mu_0 I}{2\pi}\sum_{j=1}^{n}\sqrt{\frac{y_j}{y_0}}G(k_j);\ A_{R2}=\sum_{p=1}^{C.V.}A_{R2,p}=\frac{\mu_0\omega}{2\pi}\sum_{p=1}^{C.V.}\sqrt{\frac{y_p}{y_0}}\sigma_p A_{I,p}S_p G(k_p). \quad (2.68)$$

A_{R1} is the vector potential generated by the coil current. A_{R2} is integrated from the flow field and denotes the vector potential produced plasma current.

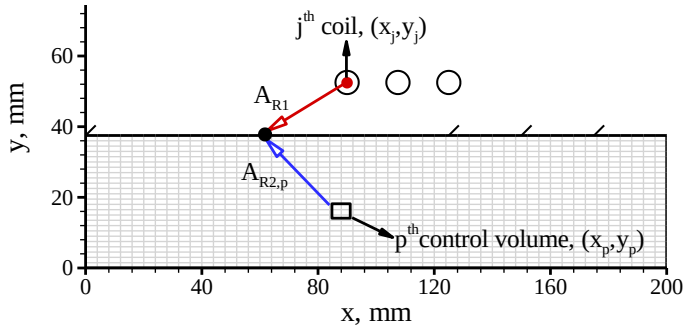

Fig. 2.5 Illustration of the vector potential on torch wall

The advantage of this electromagnetic model is that vector potential induced by an coil current or plasma current ring can be analytically computed by Biot-Savart law [49], which is explained and expanded from cylindrical to Cartesian coordinate system in the Appendix A. This model is mathematically elegant, physical correct and indicated as the standard model for ICP simulations in the past [38]. It has been introduced into my computational code, and is useful to study physical properties for the high-pressure ICP flow [50]. However, under the relatively low-pressure ICP flow (e.g., p=3.9 kPa) this standard model tends to be incorrect due to its ignorance of coil current diameter and failed to reproduce plasma flow in the simulation. The assumption of this standard model that current carry rings of the coil is infinite thin seems tending to be ineffective in the low-pressure condition for the ICP simulation. To remedy this, a far-field electromagnetic model is also introduced in the computational code.

2.6.2 Far-field Electromagnetic Model

To properly solve the electromagnetic field for the low-pressure ICP flow, Xue *et al*'s far-field electromagnetic model [38] is introduced into this study to describe the radio-frequency discharge. The computational domain of electromagnetic field is extended from the ICP torch to a farther field. The current carrying rings are not assumed to be infinitely thin. The diameter of the coil current is taken into account in the computation.

Thus, the current density J_θ in Eq. (2.60) is thought to be composed of two parts: $J_\theta = J_c + J_{ind}$, where J_c is the current density in the coil, and J_{ind} is the current density in the plasma. Similarly, considering the simplified Ohm's law, and then using Eq. (2.58), we obtain:

$$J_{ind}=\sigma E_\theta=-i\omega\sigma A_\theta, \quad (2.69)$$

Then the Eq. (2.60) becomes:

$$\nabla^2 A_\theta - i\mu_0\omega\sigma A_\theta=-\mu_0 J_c, \quad (2.70)$$

If an amplitude of sinusoidal coil current I is given, the amplitude of the current density J_c can be calculated by $J_c=I/(\pi R_c^2)$, where R_c is the radius of the coil. Finally, the far-field magnetic vector-potential equations are expressed as:

$$\nabla^2 A_R + \omega\mu_0\sigma A_I = -\mu_0 J_c, \tag{2.71}$$

$$\nabla^2 A_I - \omega\mu_0\sigma A_R = 0. \tag{2.72}$$

When solve these two equations on the far-field grids, the coil current density J_c is set zero outside the inductive coils. Outside plasma torch, the electrical conductivity σ is set to be zero. Different from Xue et al's work [38], no additional source terms for momentum and energy equations are used to counteract the inertia forces between interfaces and achieve a no flow situation outside the torch in this study. In addition, the computational method which is needed to update the electromagnetic field or coil current was not described in their work. Therefore, we supplement a method to control the electromagnetic-field calculation when solving the equations (2.71) and (2.72). This method is described in Section 3.8 in Chapter 3.

Finally, once the equations (2.71) and (2.72) are solved out, then the electric field and magnetic field can be calculated by vector potential A_θ as:

$$E_\theta = E_R + iE_I = -i\omega A_\theta = -i\omega(A_R + iA_I) = \omega A_I - i\omega A_R, \tag{2.73}$$

$$\mu_0 H_x = \frac{\partial A_\theta}{\partial y}, \tag{2.74}$$

$$\mu_0 H_y = -\frac{\partial A_\theta}{\partial x}. \tag{2.75}$$

And then, the bridge terms of the electromagnetic and flow fields such as the Joule heating rate S_{joule} and Lorentz forces F_{Li} (e.g., F_{Lx}, F_{Ly}) terms can be obtained. The Joule heating rate that is derived from Ohm's law is defined as:

$$S_{\text{joule}} = \frac{1}{2}\sigma\omega^2\left(A_R^2 + A_I^2\right), \tag{2.76}$$

The axial and radial Lorentz forces can be expressed as:

$$F_{Lx} = \frac{-\mu_0\sigma}{2}\text{Re}\left[E_\theta H_y^*\right] = \frac{-\mu_0\sigma}{2}(E_R H_{R,y} + E_I H_{I,y})$$
$$= -\frac{\sigma\omega}{2}\left(A_R\frac{\partial A_I}{\partial x} - A_I\frac{\partial A_R}{\partial x}\right), \tag{2.77}$$

$$F_{Ly} = \frac{\mu_0\sigma}{2}\text{Re}\left[E_\theta H_x^*\right] = \frac{\mu_0\sigma}{2}(E_R H_{R,x} + E_I H_{I,x})$$
$$= -\frac{\sigma\omega}{2}\left(A_R\frac{\partial A_I}{\partial y} - A_I\frac{\partial A_R}{\partial y}\right). \tag{2.78}$$

where Re[ ] denotes the real part of the term in the bracket. The tangential electric field is expressed as $E_\theta = E_R + iE_I$. H^* represents the complex conjugate of magnetic field intensity H.

2.7 Chemical Reaction Model

2.7.1 Reaction Rate

For the simulation of a chemical equilibrium flow, chemical compositions are locally determined by temperature and density because the reactions instantaneously accomplish due to frequent collisions between chemical species. However, in treating chemical nonequilibrium that chemical reaction rate has finite value, the chemical species equations must be solved and the source term need to be evaluated. When there are n_s chemical species and n_r reactions in reaction system, an equation of the chemical reaction is expressed as follows:

$$\nu_{1,r}X_1 + \cdots + \nu_{ns,r}X_{ns} \rightleftharpoons \nu'_{1,r}X_1 + \cdots + \nu'_{ns,r}X_{ns}, \quad r = 1, \cdots, nr, \tag{2.79}$$

where $\nu_{s,r}$ and $\nu'_{s,r}$ represent the stoichiometric coefficients of reactants and productions of a reaction *r* of a chemical species *s*, respectively. Mass production and reaction rates of the chemical species *s* in forward and backward reaction *r* are expressed by

$$\left(\frac{d[X_s]}{dt}\right)_{\mathrm{f},r} = \nu'_{s,r} k_{\mathrm{f},r} [X_{1,r}]^{\nu_{1,r}} [X_{2,r}]^{\nu_{2,r}} \cdots [X_{ns,r}]^{\nu_{ns,r}}, \tag{2.80}$$

$$\left(\frac{d[X_s]}{dt}\right)_{\mathrm{b},r} = \nu_{s,r} k_{\mathrm{b},r} [X_{1,r}]^{\nu'_{1,r}} [X_{2,r}]^{\nu'_{2,r}} \cdots [X_{ns,r}]^{\nu'_{ns,r}}. \tag{2.81}$$

Here $k_{\mathrm{f},r}$ and $k_{\mathrm{b},r}$ show the reaction rate constants of the forward and backward reactions. Mole concentration of species *s* is defined as: $[X_s] \equiv \rho_s / M_s$. The production rate $\dot{w}_s$ is obtained by summing Eqs. (2.80) and (2.81) over all the reactions:

$$\dot{w}_s = M_s \sum_{r=1}^{nr} (\nu'_{s,r} - \nu_{s,r})(L_{\mathrm{f},r} - L_{\mathrm{b},r}), \tag{2.82}$$

where

$$L_{\mathrm{f},r} = k_{\mathrm{f},r} \prod_{j=1}^{ns} \left(\frac{\rho_j}{M_j}\right)^{\nu_{j,r}}, \tag{2.83}$$

$$L_{\mathrm{b},r} = k_{\mathrm{b},r} \prod_{j=1}^{ns} \left(\frac{\rho_j}{M_j}\right)^{\nu'_{j,r}}. \tag{2.84}$$

Assuming forward or backward reaction rate *k* to be a function of temperature, the reaction rate is written with an Arrhenius type form as

$$k = CT^n \exp(-\theta_r / T). \tag{2.85}$$

The reaction-rate coefficients *C*, *n*, and θ depend on temperature. In particular, θ_r is referred to as characteristic temperature of reaction *r*. In equilibrium state $\dot{w}_s = 0$, the mass production and reaction rate is equal in Eq. (2.82), $L_{\mathrm{f},r} = L_{\mathrm{b},r}$, hence,

$$\frac{k_{\mathrm{f},r}}{k_{\mathrm{b},r}} = K_r^{\mathrm{eq}}, \tag{2.86}$$

where K_r^{eq} is the equilibrium constant, which can be obtained as

$$K_r^{\mathrm{eq}} = \frac{\prod_{j=1}^{ns}\left(\frac{\rho_j}{M_j}\right)^{\nu_{j,r}}}{\prod_{j=1}^{ns}\left(\frac{\rho_j}{M_j}\right)^{\nu'_{j,r}}}. \tag{2.87}$$

2.7.2 Reaction Type

There are many reaction types in chemical reaction in high-temperature gas. Here, the following reactions are treated and modeled:

1) Heavy-particle impact dissociation,

$$\mathrm{A}_2 + M \rightleftharpoons \mathrm{A} + \mathrm{A} + M, \tag{2.88}$$

2) Electron impact dissociation,

$$\mathrm{A}_2 + \mathrm{e}^- \rightleftharpoons \mathrm{A} + \mathrm{A} + \mathrm{e}^-, \tag{2.89}$$

3) Associative ionization,

$$\mathrm{A}+\mathrm{A} \rightleftharpoons \mathrm{A}_2^+ + \mathrm{e}^-, \tag{2.90}$$

4) Electron impact ionization,

$$\mathrm{A} + \mathrm{e}^- \rightleftharpoons \mathrm{A}^+ + \mathrm{e}^- + \mathrm{e}^-, \tag{2.91}$$

5) Charge exchange reaction,

$$\mathrm{A}_2 + \mathrm{B}^+ \rightleftharpoons \mathrm{A}_2^+ + \mathrm{B}, \tag{2.92}$$

where *M* shows the heavy particle such as N_2 and O.

For chemical reactions in high-temperature air, the test gas was assumed to consist of 11 air species (N_2, O_2, NO, N_2^+, O_2^+, NO^+, N, O, N^+, O^+ and e^-) and 49 chemical reactions which are summarized in Table 2.3. Note that when nitrogen is considered as the test gas, 5 species (N_2, N_2^+, N, N^+, and e^-) and 8 chemical reactions summarized in Table 2.4 are used. The chemical reaction rate was determined with an Arrhenius type form as

$$k_{f,r}\left(T_f\right) = C_r T_f^n \exp\left(-\theta_r / T_f\right). \tag{2.93}$$

The coefficients of the reaction rate C_r, n, and θ_r were taken from Park's and Dunn-Kang's work [25, 26, 51, 52]. The backward reaction rate $k_{b,r}$ was evaluated from the corresponding equilibrium constant K^{eq}:

$$k_{b,r}(T_b) = k_f(T_b)/K^{eq}(T_b). \tag{2.94}$$

The effective temperatures T_f and T_b are determined from T_{tr} and T_e or the geometric average of T_{tr}, T_{vib} and T_e. Note that the rotational temperature is not used when calculating the effective temperatures in the present study because it is unclear how it contributes to the above chemical reactions.

Recent studies (reported in Ref. [53]) have employed the rotational temperature by a state-to-state approach and have focused on the contribution of the rotational temperature to dissociation reactions. However, these data are considered to be inadequate for determining the contribution of rotation in multi-temperature models. The equilibrium constants, which are functions of only temperature, are calculated by the curve-fitting formula given in Ref. [26] as

$$K_r^{\mathrm{eq}} = \exp\left[A_{1,r} / Z_{\mathrm{P}} + A_{2,r} + A_{3,r} \ln Z_{\mathrm{P}} + A_{4,r} Z_{\mathrm{P}} + A_{5,r} Z_{\mathrm{P}}^2 \right], \tag{2.95}$$

where $Z_{\mathrm{P}} = 10^4 / T_{\mathrm{b},r}$. Note that there exist no available data in the above reference for a charge-exchange reaction between molecular nitrogen and ionized one ($\mathrm{N_2} + \mathrm{N^+} \rightleftharpoons \mathrm{N_2^+} + \mathrm{N}$) as

$$K_r^{\mathrm{eq}} = \exp\left[B_{1,r} Z_{\mathrm{G}}^5 + B_{2,r} Z_{\mathrm{G}}^4 + B_{3,r} Z_{\mathrm{G}}^3 + B_{4,r} Z_{\mathrm{G}}^2 + B_{5,r} Z_{\mathrm{G}} + B_{6,r} \right], \tag{2.96}$$

where $Z_{\mathrm{G}} = \ln(10^4 / T_{\mathrm{b},r})$. We use the parameters for this reaction reported in Ref. [28], though several models for this reaction have been reported in previous studies [54, 55].

Table 2.3 Chemical reactions of air

r	Reactants		Products	T_f	T_b	C_r	n	θ_r
1-6	N_2+M_1	⇌	$N+N+M_1$	$\sqrt{T_{tr}T_{vib}}$	T_{tr}	7.0×10^{21}	-1.60	113,200
7-10	N_2+M_2	⇌	$N+N+M_2$	$\sqrt{T_{tr}T_{vib}}$	T_{tr}	3.0×10^{22}	-1.60	113,200
11	N_2+e^-	⇌	$N+N+e^-$	T_e	$\sqrt{T_{tr}T_e}$	3.0×10^{24}	-1.60	113,200
12-17	O_2+M_1	⇌	$O+O+M_1$	$\sqrt{T_{tr}T_{vib}}$	T_{tr}	2.0×10^{21}	-1.50	59,500
18-21	O_2+M_2	⇌	$O+O+M_2$	$\sqrt{T_{tr}T_{vib}}$	T_{tr}	1.0×10^{22}	-1.50	59,500
22-25	$NO+M_3$	⇌	$N+O+M_3$	$\sqrt{T_{tr}T_{vib}}$	T_{tr}	5.0×10^{15}	0.00	75,500
26-31	$NO+M_4$	⇌	$N+O+M_4$	T_{tr}	T_{tr}	1.1×10^{17}	0.00	75,500
32	$NO+O$	⇌	$N+O_2$	T_{tr}	T_{tr}	8.4×10^{12}	0.00	19,450
33	N_2+O	⇌	$NO+N$	T_{tr}	T_{tr}	6.4×10^{17}	-1.00	38,400
34	$N+N$	⇌	$N_2^+ + e^-$	T_{tr}	T_{tr}	4.4×10^{7}	1.50	67,500
35	$O+O$	⇌	$O_2^+ + e^-$	T_{tr}	T_{tr}	7.1×10^{2}	2.70	80,600
36	$N+O$	⇌	$NO^+ + e^-$	T_{tr}	T_{tr}	8.8×10^{8}	1.00	31,900
37	$N+e^-$	⇌	$N^+ + e^- + e^-$	T_e	T_e	2.5×10^{34}	-3.82	168,600
38	$O+e^-$	⇌	$O^+ + e^- + e^-$	T_e	T_e	3.9×10^{33}	-3.78	158,500
39	$NO^+ + O$	⇌	$N^+ + O_2$	T_{tr}	T_{tr}	1.0×10^{12}	0.50	77,200
40	$O_2^+ + N$	⇌	$N^+ + O_2$	T_{tr}	T_{tr}	8.7×10^{13}	0.14	28,600
41	$O^+ + NO$	⇌	$N^+ + O_2$	T_{tr}	T_{tr}	1.4×10^{5}	1.90	26,600
42	$O_2^+ + N_2$	⇌	$N_2^+ + O_2$	T_{tr}	T_{tr}	9.9×10^{12}	0.00	40,700
43	$O_2^+ + O$	⇌	$O^+ + O_2$	T_{tr}	T_{tr}	4.0×10^{12}	-0.09	18,000
44	$NO^+ + N$	⇌	$O^+ + N_2$	T_{tr}	T_{tr}	3.4×10^{13}	-1.08	12,800
45	$NO^+ + O_2$	⇌	$O_2^+ + NO$	T_{tr}	T_{tr}	2.4×10^{13}	0.41	32,600
46	$NO^+ + O$	⇌	$O_2^+ + N$	T_{tr}	T_{tr}	7.2×10^{12}	0.29	48,600
47	$O^+ + N_2$	⇌	$N_2^+ + O$	T_{tr}	T_{tr}	9.1×10^{11}	0.36	22,800
48	$NO^+ + N$	⇌	$N_2^+ + O$	T_{tr}	T_{tr}	7.2×10^{13}	0.00	35,500
49	N_2+N^+	⇌	$N_2^+ + N$	T_{tr}	T_{tr}	1.0×10^{12}	0.50	12,200

Note: M_1=N_2, O_2, NO, N_2^+, O_2^+, NO^+; M_2=N, O, N^+, O^+; M_3=N_2, O_2, N_2^+, O_2^+; M_4=NO, N, O, NO^+, N^+, O^+

Table 2.4 Chemical reactions of nitrogen

r	Reactants		Products	T_f	T_b	C_r	n	θ_r
1	N_2+N_2	⇌	$N+N+N_2$	$\sqrt{T_{tr}T_{vib}}$	T_{tr}	4.700×10^{17}	-0.50	113,200
2	$N_2+N_2^+$	⇌	$N+N+N_2^+$	$\sqrt{T_{tr}T_{vib}}$	T_{tr}	7.000×10^{21}	-1.60	113,200
3	N_2+N	⇌	$N+N+N$	$\sqrt{T_{tr}T_{vib}}$	T_{tr}	4.085×10^{22}	-1.50	113,200
4	N_2+N^+	⇌	$N+N+N^+$	$\sqrt{T_{tr}T_{vib}}$	T_{tr}	3.000×10^{22}	-1.60	113,200
5	N_2+e^-	⇌	$N+N+e^-$	T_e	$\sqrt{T_{tr}T_e}$	3.000×10^{24}	-1.60	113,200
6	$N+N$	⇌	$N_2^+ + e^-$	T_{tr}	T_e	1.400×10^{13}	0.00	67,800
7	$N+e^-$	⇌	$N^+ + e^- + e^-$	T_e	T_e	1.100×10^{32}	-3.14	169,000
8	N_2+N^+	⇌	$N_2^+ + N$	$\sqrt{T_{tr}T_{vib}}$	$\sqrt{T_{tr}T_{vib}}$	2.020×10^{11}	0.81	13,000

2.8 Thermodynamic Model

2.8.1 Thermodynamic Properties

For a diatomic molecule, internal energies per unit mass are described as follows:

$$e_s = e_{tr} + e_{rot} + e_{vib,s} + \Delta h_s^0, \tag{2.97}$$

$$h_s = e_s + R_s T_{tr}, \tag{2.98}$$

$$e_{tr,s} = \frac{3}{2} R_s T_{tr}, \tag{2.99}$$

$$e_{rot,s} = R_s T_{rot}, \tag{2.100}$$

$$e_{vib,s} = \frac{R_s \Theta_{vib,s}}{\exp\left(\Theta_{vib,s} / T_{vib,s}\right) - 1}. \tag{2.101}$$

Hence, specific heats of the diatomic molecule are expressed as follows:

$$C_{\upsilon,s} = C_{\upsilon,tr,s} + C_{\upsilon,rot,s} + C_{\upsilon,vib,s}, \tag{2.102}$$

$$C_{p,s} = C_{\upsilon,s} + R_s, \tag{2.103}$$

$$C_{\upsilon,tr,s} = \frac{\partial e_{tr,s}}{\partial T_{tr}} = \frac{3}{2} R_s, \tag{2.104}$$

$$C_{\upsilon,rot,s} = \frac{\partial e_{rot,s}}{\partial T_{rot}} = R_s, \tag{2.105}$$

$$C_{\upsilon,vib,s} = \frac{\partial e_{vib,s}}{\partial T_{vib}} = R_s \left[\frac{\left(\Theta_{vib,s} / 2T_{vib,s}\right)}{\sinh\left(\Theta_{vib,s} / 2T_{vib,s}\right)} \right]^2. \tag{2.106}$$

On the other hand, for a monoatomic molecule, since there exit no rotational and vibrational freedoms, the internal energies per unit mass and the specific heats are given by

$$e_s = e_{tr} + \Delta h_s^0 = \frac{3}{2} R_s T_{tr} + \Delta h_s^0, \tag{2.107}$$

$$h_s = e_s + R_s T_{tr} = \frac{5}{2} R_s T_{tr} + \Delta h_s^0, \tag{2.108}$$

$$C_{\upsilon,s} = C_{\upsilon,tr,s} = \frac{3}{2} R_s, \tag{2.109}$$

$$C_{p,s} = C_{\upsilon,s} + R_s = \frac{5}{2} R_s. \tag{2.110}$$

For electrons,

$$e_e = e_{tr,e} = \frac{3}{2} R_e T_e, \tag{2.111}$$

$$h_e = e_e + R_e T_e = \frac{5}{2} R_e T_e, \tag{2.112}$$

$$C_{\upsilon,e} = C_{\upsilon,tr,e} = \frac{3}{2} R_e, \tag{2.113}$$

$$C_{p,e} = C_{\upsilon,e} + R_e = \frac{5}{2} R_e. \tag{2.114}$$

Chemical data of each species, such as the molar mass M_s, the vibrational characteristic temperature $\Theta_{vib,s}$, the enthalpy of formation Δh_s^0, the dissociation energy $E_{\mathrm{D},s}$ and the ionization energy $E_{\mathrm{I},s}$, are shown in Table 2.5.

Table 2.5 Chemical species data

Species	M_s (kg/mole)	$\Theta_{vib,s}$ (K)	Δh_s^0 (J/kg)	$E_{D,s}$ (J/kg)	$E_{I,s}$ (J/kg)	Ref.
N_2	28×10^{-3}	3353	0	3.365×10^{7}	-	[26]
O_2	32×10^{-3}	2239	0	1.545×10^{7}	-	[26]
NO	30×10^{-3}	2699	2.995×10^{6}	2.267×10^{7}	-	[26]
N_2^+	28×10^{-3}	3129	5.372×10^{7}	-	-	[26]
O_2^+	32×10^{-3}	2652	3.639×10^{7}	-	-	[26]
NO^+	30×10^{-3}	3373	3.282×10^{7}	-	-	[26]
N	14×10^{-3}	-	3.364×10^{7}	-	1.002×10^{8}	[26]
O	16×10^{-3}	-	1.543×10^{7}	-	8.218×10^{7}	[26]
N^+	14×10^{-3}	-	1.339×10^{7}	-	-	[26]
O^+	16×10^{-3}	-	9.787×10^{7}	-	-	[26]
e^-	5.486×10^{-7}	-	0	-	-	[26]

2.8.2 Equation of State

Partial pressure of each chemical species is expressed as

$$p_s = \rho_s R_s T_{tr}. \tag{2.115}$$

For electron, electron pressure is given in the same fashion by

$$p_e = \rho_e R_e T_e. \tag{2.116}$$

Total pressure is obtained by summation of the partial pressure of each species:

$$p = \sum_{s}^{ns} p_s = \sum_{s\neq e}^{ns} \rho_s R_s T_{tr} + \rho_e R_e T_e = \rho \hat{R} T_{tr} + p_e. \tag{2.117}$$

The gas constant $\hat{R}$ except the electron is defined as

$$\hat{R} = \sum_{s\neq e}^{ns} \frac{\rho_s}{\rho} R_s. \tag{2.118}$$

For the specific heats and the specific heat ratio of the mixture gas,

$$\hat{C}_v = \sum_{s\neq e}^{ns} \frac{\rho_s}{\rho} C_{v,s},\ \hat{C}_p = \sum_{s\neq e}^{ns} \frac{\rho_s}{\rho} C_{p,s},\ \hat{\gamma} = \hat{C}_p / \hat{C}_v. \tag{2.119}$$

Since $\hat{C}_p - \hat{C}_v = \hat{R}$ the pressure is also written as follows:

$$p = (\hat{\gamma} - 1)\rho \hat{C}_v T_{tr} + p_e. \tag{2.120}$$

The total energy per unit volume is given by summation of each internal energy and the kinetic energy as

$$\begin{aligned} E &= \sum_{s}^{ns} \rho_s e_s + \frac{1}{2}\rho u_i u_i + \rho k \\ &= \rho \hat{C}_v T_{tr} + \sum_{s=M}^{nm} \rho_s e_{rot,s} + \sum_{s=M}^{nm} \rho_s e_{vib,s} + \rho_e e_e + \sum_{s}^{ns} \rho_s \Delta h_s^0 + \frac{1}{2}\rho q^2 + \rho k \\ &= E_{tr} + E_{rot} + E_{vib} + E_e + \sum_{s=1}^{ns} \rho_s \Delta h_s^0 + \frac{1}{2}\rho q^2 + \rho k\ . \end{aligned} \tag{2.121}$$

where $q^2 = u_i u_i$. With Eqs. (2.120) and (2.121) the total pressure is given again by

$$p = (\hat{\gamma} - 1)\left[E - E_{rot} - E_{vib} - E_e - \sum_{s}^{ns} \rho_s \Delta h_s^0 - \frac{1}{2}\rho q^2 - \rho k \right] + p_e. \tag{2.122}$$

Moreover, the total energy *E* can be also written with the pressure *p* as

$$E = \frac{p - p_e}{\hat{\gamma} - 1} + E_{rot} + E_{vib} + E_e + \sum_{s}^{ns} \rho_s \Delta h_s^0 + \frac{1}{2}\rho q^2 + \rho k. \tag{2.123}$$

The expressions are utilized in differentiating partially the pressure.

2.9 Transport Properties

The transport properties were calculated by using the Chapman-Enskog theory [56] in the present study. The kinetic theory of gases is based on the Boltzmann equation, which describes the behaviour of atoms and molecules in dilute gases using a statistical approach.

To accurately evaluate the electron transport properties such as electrical conductivity and electron thermal conductivity, the third-order formula of Sonine polynomial terms were used to determine them [40]. The required several kinds of collision cross sections were referred from the works of Laricchiuta et al [42], Capitelli et al [57], and Ghorui et al [41]. To validate the numerical methods used in calculating the electron transport properties, the computed electron transport properties under the atmospheric pressure condition will be presented and compared with other researcher's experimental and theoretical data. Last, because the ICP flow was usually operating under the pressure conditions p = 0.01 – 1.0 atm [19, 58], so we also give the computed electron transport properties under the representative pressure conditions such as p = 0.01, 0.1, 0.5, 1.0 atm. The variation tendency of the electron transport properties under different pressure conditions will be also studied.

Moreover, the viscosity μ and translational, rotational, vibrational thermal conductivity were calculated according to the Yos' formula [59], which is based on the Chapman-Enskog approximation. The collision integrals required to compute the viscosity and the abovementioned thermal conductivities were evaluated using the methods and data in Ref. [28]. For a nonequilibrium plasma, Fertig et al. [60, 61] gave an improved value of the collision integral data for N-e and O-e. Therefore we adopted their data in the present calculation. The diffusion coefficients were given by the formula of Curtiss and Hirschfelder [62]. Ambipolar diffusion was assumed for charged species, $D_s^a = (1 + T_e / T_{tr}) D_s$, where D_s is the effective diffusion coefficient of the ionic species.

2.9.1 Collision Cross Section

In order to determine the transport properties of high-temperature air and nitrogen, we need to calculate the collision cross sections. Strictly, the accurate collision cross sections $\overline{Q}_{i,j}^{(l,s)}$ should be calculated by:

$$\overline{Q}_{i,j}^{(l,s)} = \frac{4(l+1)}{(s+1)!\left[2l+1-(-1)^l\right]} \times \int_0^\infty \exp\left(-\gamma_{i,j}^2\right) \gamma_{i,j}^{2s+3} Q^l(g) d\gamma, \tag{2.124}$$

where the cross section is given as:

$$Q^{(l)} = 2\pi \int_0^\pi \left[1 - \cos^l(\chi)\right] b db, \tag{2.125}$$

The angle of deflection is :

$$\chi = \pi - 2b \int_{r_m}^\infty \frac{dr}{r^2 \sqrt{1 - b^2/r^2 - 2\varphi(r)/\mu_{i,j} g^2}}, \tag{2.126}$$

where b is the impact parameter; $\gamma_{i,j} = \sqrt{\mu_{i,j} g^2 / 2kT}$ is the reduced relative velocity of particles; $\mu_{i,j} = \dfrac{m_i m_j}{m_i + m_j}$ is the reduced mass of both colliding particles; g is the relative velocity of both particles at infinity; and r_m is the distance of closest approach. $\varphi(r)$ is the interaction potential between species such as the Screened Coulomb potential between charged-charged species.

Ghorui's method

To accurately determine the collision cross section for the interactions between charged and charged species such as $N_2^+ - e^-$, $e^- - e^-$, recently Ghorui et al [41] gave an improved method to evaluate the collision integral under screened coulomb potential for nonequilibrium plasmas. The simple expressions of collision integrals $\Omega_{i,j}^{(l,s)}$ (l=1-2, s=1-5) are written as:

$$\Omega_{i,j}^{(1,s)} = \sqrt{\frac{2\pi k T_{ij}^*}{m_{ij}^*}} \beta^2 b_0^2 \Gamma(s) \left[\ln(\Lambda) - 0.5 - 2\bar{\gamma} + \psi(s)\right], \tag{2.127}$$

$$\Omega_{i,j}^{(2,s)} = 2\sqrt{\frac{2\pi kT_{ij}^*}{m_{ij}^*}}\beta^2 b_0^2 \Gamma(s)\left[\ln(\Lambda) - 1.0 - 2\bar{\gamma} + \psi(s)\right]. \tag{2.128}$$

Then, the collision cross sections $\overline{Q}_{i,j}^{(l,s)}$ can be expressed as:

$$\overline{Q}_{i,j}^{(l,s)} = \frac{4(l+1)}{(s+1)![2l+1-(-1)^l]} \frac{\Omega_{ij}^{(l,s)}}{\sqrt{\frac{kT_{ij}^*}{2\pi m_{ij}^*}}}. \tag{2.129}$$

where the reduced temperature T_{ij}^*, and the reduced mass m_{ij}^* are expressed as

$$T_{ij}^* = \frac{m_i T_j + m_j T_i}{m_i + m_j}, \tag{2.130}$$

$$m_{ij}^* = \frac{m_i m_j}{m_i + m_j}. \tag{2.131}$$

Here the subscript *i* and *j* denote the pair of mutual collision species.

$$\Lambda = \frac{2\lambda_D}{\beta b_0}, \tag{2.132}$$

$$b_0 = \frac{\Delta}{2\beta}, \tag{2.133}$$

where the distance of closet approach Δ is expressed as

$$\Delta = \beta\left[\frac{1}{4\pi\varepsilon_0}\frac{e^2}{kT_{ij}^*}\right]. \tag{2.134}$$

A value of β equal 1.03 is used in this study. The Euler constant $\bar{\gamma}$ is equal 0.5772. λ_D is the Debye length. The accurate form of λ_D, which considers the effect of ions on Debye Shielding, is expressed as:

$$\lambda_D = \left[\frac{e^2}{\varepsilon_0 k}\left(\frac{n_e}{T_e} + \sum_{\substack{i=1 \\ i\neq e}}^{ns-1}\frac{n_i}{T_i}\right)\right]^{-1/2}. \tag{2.135}$$

$$\psi(s) = \sum_{\substack{n=1 \\ s\neq 1}}^{s-1}\frac{1}{n},\ \psi(1) = 0. \tag{2.136}$$

The value of the Gamma function $\Gamma(s)$ is given as $\Gamma(1)$=1.0, $\Gamma(2)$=1.0, $\Gamma(3)$=2.0, $\Gamma(4)$=6.0, $\Gamma(5)$=24.0.

Laricchiuta's curve-fittings

Since the calculation of the collision cross sections requires much computational cost, Curve-fitting of the collision cross sections have been carried out by many researchers for the interactions between heavy particles. It is effective to use those fitting data to reduce the computation cost, if they are available.

According to the recent work of Laricchiuta et al, the collision cross section for electron-neutral interactions are expressed as a function of temperatures as the following formula:

$$\overline{Q}_{e,j}^{(l,s)} = \frac{g_3 x^{g_6} \exp\left[\left(x-g_1\right)/g_2\right]}{\exp\left[\left(x-g_1\right)/g_2\right]+\exp\left[-\left(x-g_1\right)/g_2\right]} + g_7 \exp\left[-\left(\frac{x-g_8}{g_9}\right)^2\right] + g_4 + g_{10} x^{g_5}. \tag{2.137}$$

where $x = \ln\left(T_e\right)$, $g_1 \sim g_{10}$ are the tabulated transport coefficients given in Ref. [42]

Gupta's curve-fittings

According to Gupta, Yos, Thompson and Lee [28], the diffusion-type $\overline{Q}_{i,j}^{(1,1)}$ and the viscosity-type $\overline{Q}_{i,j}^{(1,1)}$ collision cross sections are expressed as a function of temperatures as the following formula:

$$\overline{Q}_{i,j}^{(1,1)} = \left[\exp\left(D_{\overline{Q}_{i,j}^{(1,1)}}\right)\right] T^{\left[A_{\overline{Q}_{i,j}^{(1,1)}}(\ln T)^2 + B_{\overline{Q}_{i,j}^{(1,1)}}\ln T + C_{\overline{Q}_{i,j}^{(1,1)}}\right]}, \tag{2.138}$$

$$\overline{Q}_{i,j}^{(2,2)} = \left[\exp\left(D_{\overline{Q}_{i,j}^{(2,2)}}\right)\right] T^{\left[A_{\overline{Q}_{i,j}^{(2,2)}}(\ln T)^2 + B_{\overline{Q}_{i,j}^{(2,2)}}\ln T + C_{\overline{Q}_{i,j}^{(2,2)}}\right]}. \tag{2.139}$$

where the constants $A_{\overline{Q}_{i,j}^{(l,s)}}$, $B_{\overline{Q}_{i,j}^{(l,s)}}$, $C_{\overline{Q}_{i,j}^{(l,s)}}$ and $D_{\overline{Q}_{i,j}^{(l,s)}}$ are obtained by Gupta's works [28], If collision particle pair consists of ions or electron,

$$\overline{Q}_{i,j}^{(1,1)} = \overline{Q}_{i,j}^{(1,1)} \times \ln \Lambda\left(p_e\right), \quad \overline{Q}_{i,j}^{(2,2)} = \overline{Q}_{i,j}^{(2,2)} \times \ln \Lambda\left(p_e\right). \tag{2.140}$$

Specifically, if collision particle pair consists of ions,

$$\ln \Lambda(p_e) = \frac{1}{2}\ln\left[2.09\times10^{-2}\left(\frac{T_{tr}}{1000\,p_e^{1/4}}\right)^4 + 1.52\left(\frac{T_{tr}}{1000\,p_e^{1/4}}\right)^{8/3}\right], \tag{2.141}$$

where p_e is the electron pressure in atmospheres. For the pair of collision which consists of electrons, the collision cross section is corrected by multiplying the following factor:

$$\ln \Lambda(p_e) = \frac{1}{2}\ln\left[2.09\times10^{-2}\left(\frac{T_e}{1000\,p_e^{1/4}}\right)^4 + 1.52\left(\frac{T_e}{1000\,p_e^{1/4}}\right)^{8/3}\right]. \tag{2.142}$$

Since it is reported that the collision cross section data for N-e and O-e in the Gupta model are not accurate in low temperature region according to Ref. [63], those data should be particularly replaced by another model.

Fertig's curve-fittings

Fertig, Dohr and Früuhauf [60, 61] have performed new curve-fitting of the diffusion-type $\bar{Q}_{i,j}^{(1,1)}$ and the viscosity-type $\bar{Q}_{i,j}^{(1,1)}$ for the interactions between electron-neutral species in air nonequilibrium plasma. Their fitting expressions can be written as:

$$\bar{Q}_{i,j}^{(1,1)} = \pi \exp\left[A_{\bar{Q}_{i,j}^{(1,1)}} (\ln T)^4 + B_{\bar{Q}_{i,j}^{(1,1)}} (\ln T)^3 + C_{\bar{Q}_{i,j}^{(1,1)}} (\ln T)^2 + D_{\bar{Q}_{i,j}^{(1,1)}} (\ln T) + E_{\bar{Q}_{i,j}^{(1,1)}} \right], \quad (2.143)$$

$$\bar{Q}_{i,j}^{(2,2)} = \pi \exp\left[A_{\bar{Q}_{i,j}^{(2,2)}} (\ln T)^4 + B_{\bar{Q}_{i,j}^{(2,2)}} (\ln T)^3 + C_{\bar{Q}_{i,j}^{(2,2)}} (\ln T)^2 + D_{\bar{Q}_{i,j}^{(2,2)}} (\ln T) + E_{\bar{Q}_{i,j}^{(2,2)}} \right], \quad (2.144)$$

where the constants $A_{\bar{Q}_{i,j}^{(l,s)}}$, $B_{\bar{Q}_{i,j}^{(l,s)}}$, $C_{\bar{Q}_{i,j}^{(l,s)}}$, $D_{\bar{Q}_{i,j}^{(l,s)}}$ and $E_{\bar{Q}_{i,j}^{(l,s)}}$ are obtained by Fertig et al's works [60, 61]. If the pair of species consists of ions, the collision cross sections should be corrected by use of the Debye radius λ_D. The modified collision cross section is expressed as

$$\bar{Q}_{i,j}^{(l,s)} = (\lambda_D / T^*)^2 \bar{Q}_{i,j}^{(l,s)*}(T^*). \quad (2.145)$$

The dimensionless temperature T^* is defined by

$$T^* = \lambda_D \left(\frac{e^2}{4\pi\varepsilon_0 k T_{tr}} \right)^{-1} \quad \text{or} \quad T^* = \lambda_D \left(\frac{e^2}{4\pi\varepsilon_0 k T_e} \right)^{-1}. \quad (2.146)$$

Abbreviations

Finally, to simplify the equations developed hereafter, we introduce the abbreviations as

$$\Delta_{i,j}^{(1)}(T) = \frac{8}{3}\left[\frac{2 m_i m_j}{\pi k T (m_i + m_j)} \right]^{1/2} \bar{Q}_{i,j}^{(1,1)}, \quad (2.147)$$

$$\Delta_{i,j}^{(2)}(T) = \frac{16}{5}\left[\frac{2 m_i m_j}{\pi k T (m_i + m_j)} \right]^{1/2} \bar{Q}_{i,j}^{(2,2)}, \quad (2.148)$$

$$A_{i,j}^* = \frac{\bar{Q}_{i,j}^{(2,2)}}{\bar{Q}_{i,j}^{(1,1)}}, \quad (2.149)$$

$$B_{i,j}^* = \frac{5\pi \bar{Q}_{i,j}^{(1,2)} - 4\pi \bar{Q}_{i,j}^{(1,3)}}{\bar{Q}_{i,j}^{(1,1)}}. \quad (2.150)$$

The mole fraction is defined by

$$X_i = \frac{\frac{\rho_i}{M_i}}{\sum_j^{ns} \frac{\rho_j}{M_j}}. \tag{2.151}$$

2.9.2 High-Order Electron Transport Properties

Devoto [40] have pointed out that for weakly or partially ionized plasma simulations the high-order formulas of Chapman-Enskog approximations are necessary to be used for calculating the electron transport properties of the test gas. Therefore, in the present study, we use the third-order formulas of Sonine polynomial terms to evaluate the electrical conductivity and electron thermal conductivity.

Electrical conductivity

According to the Chapman-Enskog theory, the expression of the third-order and the first-order electrical conductivity can be written as following respectively [40]:

$$\sigma = \sigma^{3\text{rd}} = \frac{3e^2 n_e^2}{2kT_e} \sqrt{\frac{2\pi kT_e}{m_e}} \frac{\begin{vmatrix} q^{11} & q^{12} \\ q^{21} & q^{22} \end{vmatrix}}{\begin{vmatrix} q^{00} & q^{01} & q^{02} \\ q^{10} & q^{11} & q^{12} \\ q^{20} & q^{21} & q^{22} \end{vmatrix}}, \tag{2.152}$$

$$\sigma = \sigma^{1\text{st}} = \frac{3e^2}{8kT_e} \frac{n_e}{\sum_{i \neq e} n_i \left[\frac{2m_e m_i}{\pi kT_e (m_e + m_i)} \right]^{\frac{1}{2}} \overline{Q}_{ei}^{(1,1)}} \tag{2.153}$$

where n_e, n_i, m_e, m_i are the number density and mass of electron and chemical species, $\overline{Q}_{ei}^{(1,1)}$ is the collision integral of the momentum transfer cross section between the electron and chemical species, and *e*, *k* respectively denote the electric charge and Boltzmann constant.

In addition, q^{mn} (*m*, *n*=0-2) are functions of number density of species and several kinds of collision cross sections $\overline{Q}_{ei}^{(l,s)}$ (*l*=1-2, *s*=1-5) between electron and chemical species [40]. q^{mn} has the symmetric property i.e., $q^{mn} = q^{nm}$. According to the Devoto's work, q^{mn} are expressed as following:

$$q^{00} = 8 \sum_{i \neq e} n_e n_i \overline{Q}_{ei}^{(1,1)}, \tag{2.154}$$

$$q^{01} = 8 \sum_{i \neq e} n_e n_i \left(\frac{5}{2} \overline{Q}_{ei}^{(1,1)} - 3\overline{Q}_{ei}^{(1,2)} \right), \tag{2.155}$$

$$q^{11} = 8\sqrt{2} n_e^2 \overline{Q}_{ee}^{(2,2)} + 8 \sum_{i} n_e n_i \left(\frac{25}{4} \overline{Q}_{ei}^{(1,1)} - 15\overline{Q}_{ei}^{(1,2)} + 12\overline{Q}_{ei}^{(1,3)} \right), \tag{2.156}$$

$$q^{02} = 8\sum_{i\neq e} n_e n_i \left(\frac{35}{8}\overline{Q}_{ei}^{(1,1)} - \frac{21}{2}\overline{Q}_{ei}^{(1,2)} + 6\overline{Q}_{ei}^{(1,3)} \right), \tag{2.157}$$

$$q^{12} = 8\sqrt{2}n_e^2 \left(\frac{7}{4}\overline{Q}_{ee}^{(2,2)} - 2\overline{Q}_{ee}^{(2,3)} \right) +$$

$$8\sum_{i} n_e n_i \left(\frac{175}{16}\overline{Q}_{ei}^{(1,1)} - \frac{315}{8}\overline{Q}_{ei}^{(1,2)} + 57\overline{Q}_{ei}^{(1,3)} - 30\overline{Q}_{ei}^{(1,4)} \right), \tag{2.158}$$

$$q^{22} = 8\sqrt{2}n_e^2 \left(\frac{77}{16}\overline{Q}_{ee}^{(2,2)} - 7\overline{Q}_{ee}^{(2,3)} + 5\overline{Q}_{ee}^{(2,4)} \right) +$$

$$8\sum_{i} n_e n_i \left(\frac{1225}{64}\overline{Q}_{ei}^{(1,1)} - \frac{735}{8}\overline{Q}_{ei}^{(1,2)} + \frac{399}{2}\overline{Q}_{ei}^{(1,3)} - 210\overline{Q}_{ei}^{(1,4)} + 90\overline{Q}_{ei}^{(1,5)} \right). \tag{2.159}$$

Electron thermal conductivity

Similarly, the expression of the third-order electron thermal conductivity can be written as:

$$\lambda_e = \lambda_{\mathrm{e}}^{3\mathrm{rd}} = \frac{75 n_e^2 k}{8 k T_e} \sqrt{\frac{2\pi k T_e}{m_e}} \frac{q^{22}}{\begin{vmatrix} q^{11} & q^{12} \\ q^{21} & q^{22} \end{vmatrix}}. \tag{2.160}$$

where q^{11}, q^{12} and q^{22} are the same as are given above. On the other hand, the first-order electron thermal conductivity can be given by

$$\lambda_{\mathrm{e}} = \frac{15}{4} k \left[\frac{X_{\mathrm{e}}}{\sum_{j}^{ns} \alpha_{\mathrm{e}j} X_j \Delta_{\mathrm{e},j}^{(2)}(T_{\mathrm{e}})} \right], \tag{2.161}$$

where

$$\alpha_{ej} = 1 + \frac{\left[1 - \left(m_e / m_j\right)\right]\left[0.45 - 2.54\left(m_e / m_j\right)\right]}{\left[1 + \left(m_e / m_j\right)\right]^2}. \tag{2.162}$$

.

2.9.3 Validation of Electron Transport Properties

Because the procedure of calculating the electron transport properties with abovementioned formulas and curve-fitting methods is a little complex, it may be easy making some mistakes in programing that computational code. To eliminate any mistake in that procedure and validate above methods, we calculated the electron transport properties under the atmosphere pressure condition, and compared our results with experimental and theoretical data in literatures.

To perform this validation, first we calculated chemical composition of air and nitrogen under the atmospheric pressure. Here, Saha equation [64] and Guldberg–Waage equation [65] were used to figure out the number density of species for the ionization and

dissociation reactions, respectively. The internal partition functions of species involved in these two equations and equilibrium constant for a chemical reaction were computed according to Park's work [26]. The mass conservation law of species and Dalton's law (electric neutrality principle) were also taken into account. Thereafter, we compared our computed chemical compositions with Colona's accurate data [66, 67]. Finally, we compared the our computed electron transport properties with other researcher's data.

Equilibrium Compositions of Nitrogen and Air

To calculate the chemical compositions of air and nitrogen plasmas, 11 species (N_2, O_2, NO, N_2^+, O_2^+, NO^+, N, O, N^+, O^+ and e^-) 8 chemical reactions of air, and 5 species (N_2, N_2^+, N, N^+ and e^-) 3 chemical reactions of nitrogen (r = 1, 4, 6 in Table 2.6) were used to figure out the mole fractions of air and nitrogen species under the local thermodynamic equilibrium condition. The required parameters for calculating the chemical compositions such as chemical reaction rates, partition functions, and characteristic temperatures of air and nitrogen were summarized in Table 2.6.

Fig. 2.6(a) and Fig. 2.6(b) show the calculated mole fractions of chemical species under the atmospheric pressure condition for nitrogen and air, respectively. To validate the methods used presently, our results are also compared with the accurate chemical composition data of Colonna et al [66, 67]. As is shown in Fig. 2.6, they show good agreements for the dominant chemical species in the temperature range T=300 – 20000 K, although a few deviation is found for the species N_2^+. This deviation may be caused by the neglected reactions for the excited atomic species N^{++} and N^{+++} in our calculations. While the mole fraction of N_2^+ is always several order of magnitudes smaller than other species. So it is thought that this deviation hardly affect the following calculation of transport properties.

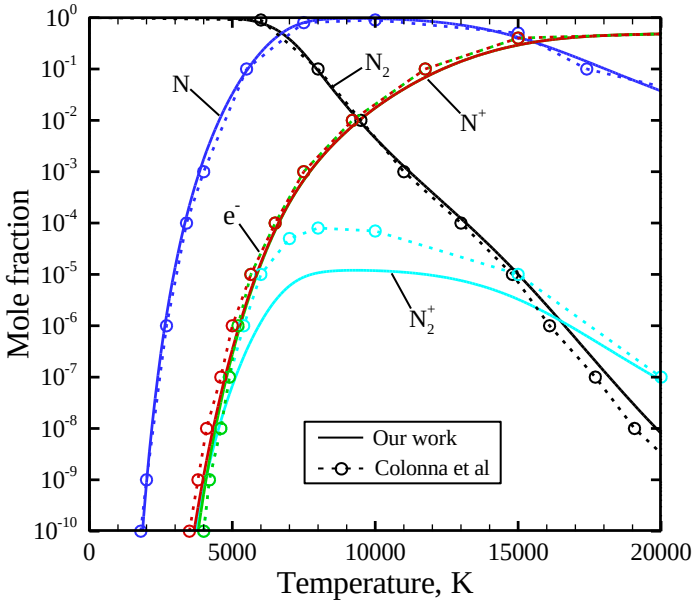

(a)

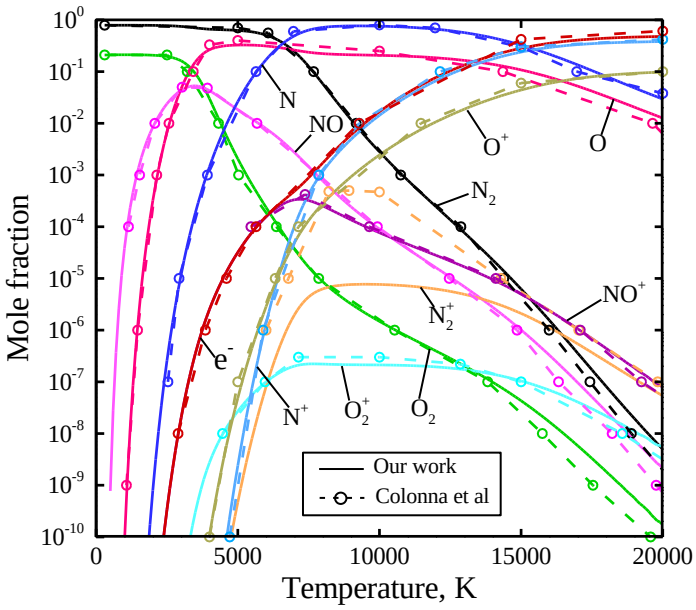

(b)

Fig. 2.6 Mole fraction of chemical species under the atmospheric pressure condition, (a) nitrogen; (b) air

Table 2.6 Required parameters for the computation of chemical compositions

r	Reactants		Products	E_r (J)	Species	Θ_{rot} (K)	Θ_{vib} (K)
1	N_2	⇌	$N+N$	1.565×10^{-18}	N_2	2.879	3353
2	O_2	⇌	$O+O$	8.210×10^{-19}	O_2	2.069	2239
3	$2NO$	⇌	N_2+O_2	-1.492×10^{-19}	NO	2.440	2699
4	N_2	⇌	$N_2^+ + e^-$	2.665×10^{-18}	N_2^+	2.879	3129
5	O_2	⇌	$O_2^+ + e^-$	1.934×10^{-18}	O_2^+	2.069	2652
6	N	⇌	$N^+ + e^-$	2.329×10^{-18}	N, N^+	-	-
7	O	⇌	$O^+ + e^-$	2.183×10^{-18}	O, O^+, e^-	-	-
8	NO	⇌	$NO^+ + e^-$	1.486×10^{-18}	NO^+	2.440	3373

Comparisons of electron transport properties

In this section, the computed electron transport properties under the atmospheric pressure condition are compared with other researchers' experimental and theoretical results. Fig. 2.7(a) shows the comparison of electrical conductivity for nitrogen between the works of Colombo et al [68], Asinovsky et al [69], Capitelli and Devoto [70], Gupta et al [28], and our work. It can be seen that the obtained electrical conductivity in this study shows good agreement with the recent work of Colombo et al [68] and the theoretical data of Capitelli and Devoto [70], although it seems a little higher than the experimental data of Asinovsky et al, the relative deviation between our result and the experimental data is within 3.5%. One the other hand, as can be seen from Fig. 2.7(a), the frequently-used Gupta's work [28], which were computed by the first-order formula of Chapman-

Enskog approximation with relative old collision cross-section data, seems underestimate the value obviously as the temperature is higher than 9000 K.

Fig. 2.7(b) shows the comparison of electrical conductivity for air between the works of Murphy A. B. [71], Asinovsky et al [69], Capitelli et al [72], D'Angola et al [73], Gupta et al [28], and our work. It can be seen that in the temperature range 500 – 12000 K, our work shows good agreements with the recent work of D'Angola et al and the experimental data of Asinovsky et al [69]. In the higher temperature range 12000 – 15000, a few percent differences are seen among our work, the works of Murphy A. B., D'Angola et al, and the experimental data. The maximum differences between our work and the works of Murphy A. B., D'Angola et al are within 4.8% and 5.9%. These deviations may be caused by the uncertainties of collision integral data between electron and neutral particles in the molecular and atomic theory under the high temperature condition. In this study, we used the tabulated collision cross section data given by Laricchiuta et al for the electron-neutral collisions. Although their collision integrals used in calculating the transport coefficients are more accurate than the values used in previous theoretical studies, the uncertainties of collision integrals for e-N and e-O interactions still remain according to the study of Wright et al [74]. Thus, these uncertainties may be the reason why different researchers gave different electrical conductivity for air, as is indicated in the Fig. 2.7(b), in the higher temperature range T=12000 – 15000.

Fig. 2.8 shows the comparison of electron thermal conductivity between our work and the works of Murphy A. B. [71, 75] for air and nitrogen. As is shown in the Fig. 2.8, good agreements can be seen between our computed electron thermal conductivity and Murphy's work. The first order accuracy electron thermal conductivities computed by Gupta's collision cross section data for air and nitrogen are still smaller than Murphy's and our results in the high-temperature range.

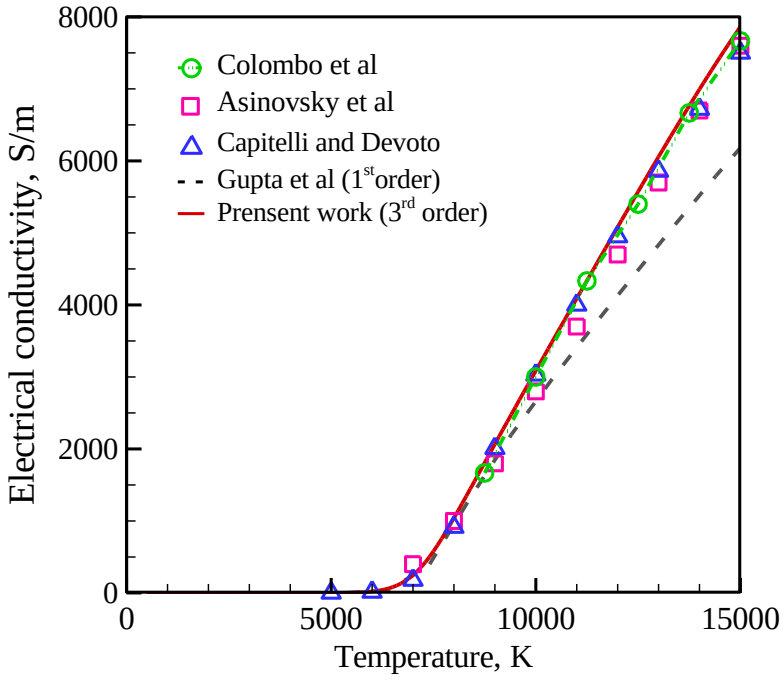

(a)

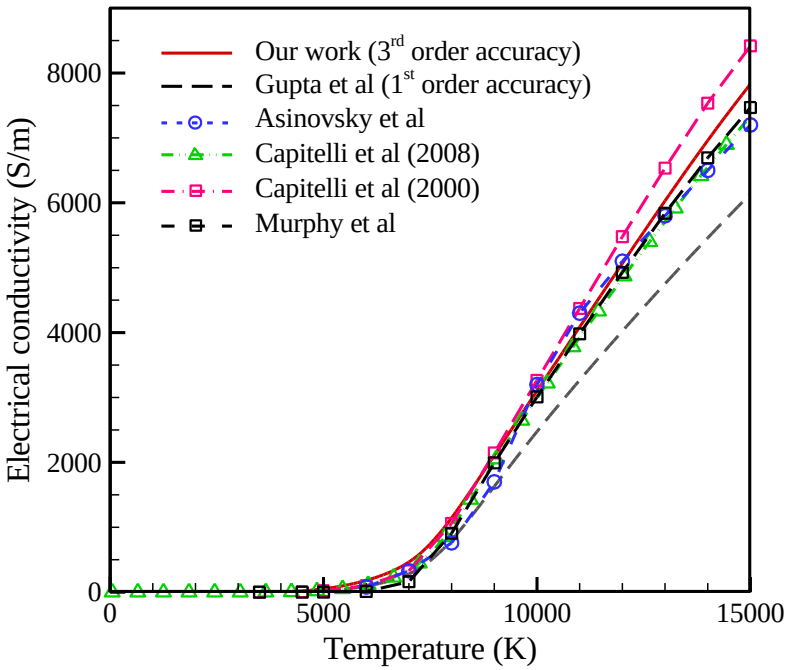

(b)

Fig. 2.7 Comparison of the computed electrical conductivity with experimental and theoretical results in literatures: (a) nitrogen; (b) air

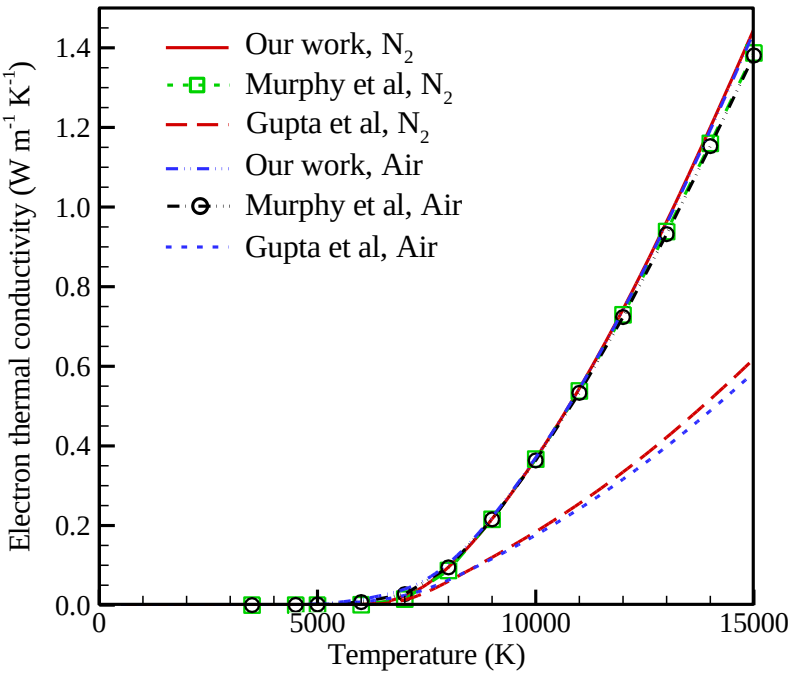

Fig. 2.8 Comparison of electron thermal conductivity for nitrogen and air

2.9.4 Electron Transport Properties in Various Pressure Conditions

As is known, according to different industrial applications, ICP wind tunnels commonly work under different pressure conditions. While they are usually operating under the pressure conditions such as p = 0.01 – 1.0 atm [19, 58]. As an extension work, here we also give the computed electron transport properties under the different pressure conditions such as p = 0.01, 0.1, 0.5, 1.0 atm. The variation tendency of the electron transport properties under different pressure conditions is studied here.

Fig. 2.9 shows the computed electron transport properties of nitrogen and air in the pressure and temperature ranges p=0.01 – 1.0 atm, T= 300 – 15000 K. Fig. 2.9(a) and Fig. 2.9(b) show the influence of pressure on the electrical conductivity and electron thermal conductivity of nitrogen, respectively. As can be seen from Fig. 2.9: (1) when the temperature is lower than 5000 K, because the ionization degree of the test gas is very small i.e., a few number of electrons, the electron transport properties are very small; (2) in the temperature range (T=5000 – 9000 K), because the mole fraction of electron increase dramatically with the increase of temperature as is seen from Fig. 2.6. It means the ionization reactions begin to proceed fast in this temperature range. Therefore, the electron transport properties are increasing gradually from T = 5000 K. And also, the electron transport properties seem increasing with the decrease of the pressure there; (3) in the higher temperature range T = 9000 – 15000, ions and atomic nitrogen become the dominant chemical species. Abundant electrons and ions lead to fast growths of the electron transport properties in this temperature range. However, with the decrease of the pressure the electron transport properties are decreasing. It shows inverse trend with that in the temperature range 5000 – 10000 K. This seems caused by less amount of electrons and less collision frequencies between electron and other species under the lower pressure condition.

Fig. 2.10(a) and Fig. 2.10(b) show the influence of pressure on the electrical conductivity and electron thermal conductivity of air. They showed similar variation trends with those of nitrogen mentioned above. While because of active chemical properties of Oxygen, the value of electrical conductivity and electron thermal conductivity of air are a little higher than those values of nitrogen under the same pressure condition in the temperature range 5000 – 9000 K. In the rest of temperature ranges, the differences of the electron transport properties between air and nitrogen are quite small.

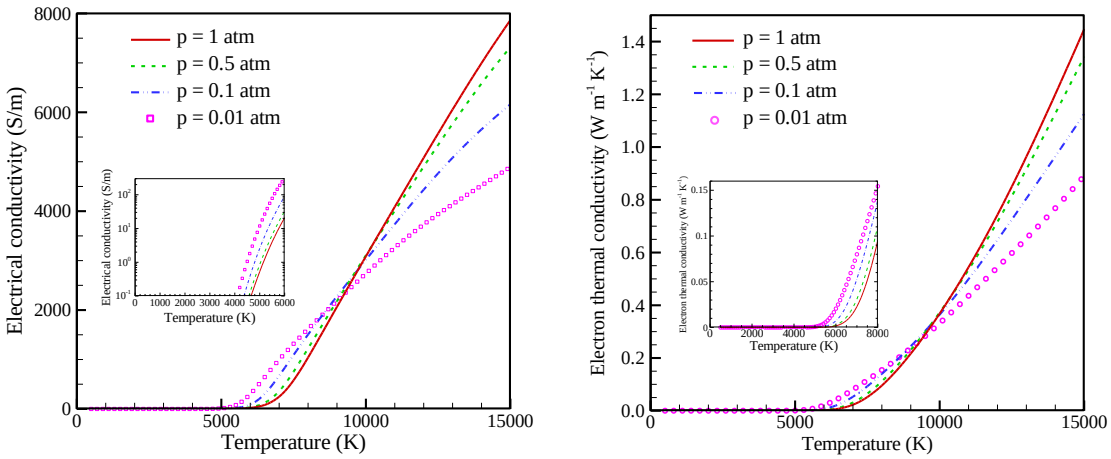

(a) (b)

Fig. 2.9 Electron transport properties of nitrogen under different pressure conditions, (a) electrical conductivity; (b) electron thermal conductivity

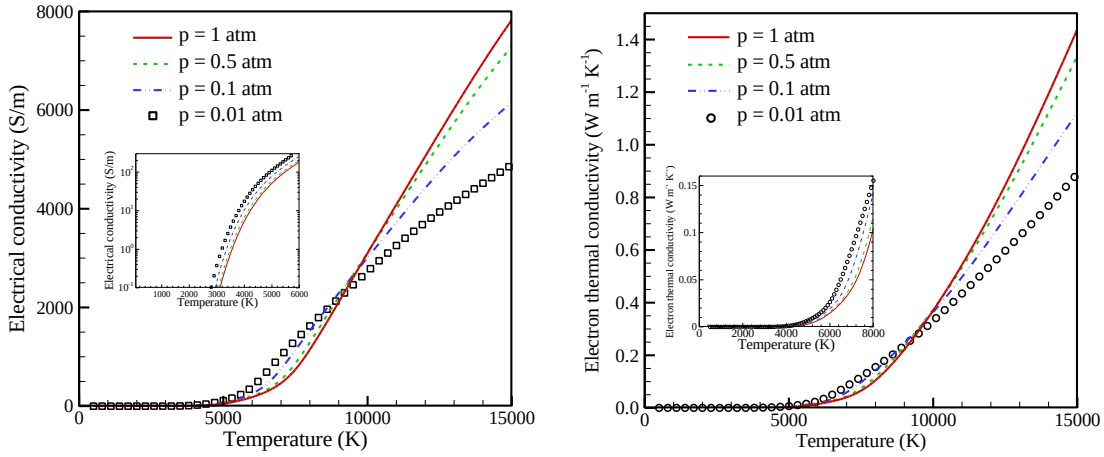

Fig. 2.10 Electron transport properties of air under different pressure conditions, (a) electrical conductivity; (b) electron thermal conductivity

2.9.5 Viscosity

According to Hirschfelder, Curtiss and Bird [46], the viscosity for mixture gas is given with rigorous first order kinetic theory by,

$$\mu = -\frac{\begin{vmatrix} H_{1,1} & H_{1,2} & \cdots & H_{1,ns} & X_1 \\ H_{1,2} & H_{2,2} & \cdots & H_{2,ns} & X_2 \\ \vdots & \vdots & \ddots & \vdots & \vdots \\ H_{1,ns} & H_{2,ns} & \cdots & H_{ns,ns} & X_{ns} \\ X_1 & X_2 & \cdots & X_{ns} & X_0 \end{vmatrix}}{\begin{vmatrix} H_{1,1} & H_{1,2} & \cdots & H_{1,ns} \\ H_{1,2} & H_{2,2} & \cdots & H_{2,ns} \\ \vdots & \vdots & \ddots & \vdots \\ H_{1,ns} & H_{2,ns} & \cdots & H_{ns,ns} \end{vmatrix}}, \tag{2.163}$$

where

$$H_{i,i} = \frac{X_j^2}{\mu_i} + \sum_{j \neq i}^{ns} \frac{2X_i X_j}{m_i + m_j} \frac{RT}{pD_{i,j}} \left[1 + \frac{3}{5} \frac{m_j}{m_i} A_{i,j}^* \right], \tag{2.164}$$

$$H_{i,j} = -\frac{2X_i X_j}{m_i + m_j} \frac{RT}{pD_{i,j}} \left[1 - \frac{3}{5} A_{i,j}^* \right], \; i \neq j. \tag{2.165}$$

The viscosity of the pure species μ_i is expressed in the self-diffusion coefficient $D_{i,i}$ as

$$\mu_i = \frac{5}{6} \frac{\rho D_{i,i}}{A_{i,i}^*}. \tag{2.166}$$

Compared with the diagonal elements $H_{i,i}$ the off-diagonal elements $H_{i,j}$ are small. Primary contributions of the viscosity are born by $H_{i,i}$. Assuming that $A^*_{i,j} = 5/3$, the off-diagonal elements $H_{i,j}$ are exactly vanished. The viscosity μ for the multicomponent gas can be expressed by only $H_{i,i}$. The approximate expression is given by Yos [59] as

$$\mu = \sum_{i}^{ns} \left[\frac{m_i X_i}{\sum_{j}^{ns} X_j \Delta^{(2)}_{i,j}(T)} \right]. \tag{2.167}$$

2.9.6 Thermal Conductivity

Translational Degree of Freedom

The translational component of the thermal conductivity is given by

$$\lambda_{tr} = -\frac{\begin{vmatrix} L_{1,1} & L_{1,2} & \cdots & L_{1,ns} & X_1 \\ L_{1,2} & L_{2,2} & \cdots & L_{2,ns} & X_2 \\ \vdots & \vdots & \ddots & \vdots & \vdots \\ L_{1,ns} & L_{2,ns} & \cdots & L_{ns,ns} & X_{ns} \\ X_1 & X_2 & \cdots & X_{ns} & X_0 \end{vmatrix}}{\begin{vmatrix} L_{1,1} & L_{1,2} & \cdots & L_{1,ns} \\ L_{1,2} & L_{2,2} & \cdots & L_{2,ns} \\ \vdots & \vdots & \ddots & \vdots \\ L_{1,ns} & L_{2,ns} & \cdots & L_{ns,ns} \end{vmatrix}}, \tag{2.168}$$

where

$$L_{i,i} = -\frac{4X_i^2}{\lambda_{i,\mathrm{tr,mono}}} - \frac{16}{25}\frac{T}{p}\sum_{j\neq i}^{ns}\left[\frac{X_i X_j \left(\frac{15}{2} m_i^2 + \frac{25}{4} m_j^2 - 3m_i^2 B^*_{i,j} + 4m_i m_j A^*_{i,j} \right)}{\left(m_i + m_j \right)^2 D_{i,j}} \right], \tag{2.169}$$

$$L_{i,j} = \frac{16}{25}\frac{T}{p}\frac{X_i X_j m_i m_j}{\left(m_i + m_j \right)^2 D_{i,j}} \left[\frac{55}{4} - 3B^*_{i,j} - 4A^*_{i,j} \right] \quad i \neq j. \tag{2.170}$$

The translational contribution of the thermal conductivity of the pure species $\lambda_{i,\mathrm{tr,mono}}$ is expressed as

$$\lambda_{i,\mathrm{tr,mono}} = \frac{15}{4} R \mu_i. \tag{2.171}$$

The translational component of the thermal conductivity can be simplified in the same fashion with the viscosity for multicomponent gas mixture. The approximate expression is given by Yos [59] as

$$\lambda_{\mathrm{tr}} = \frac{15}{4} k \sum_{i \neq e}^{ns} \left[\frac{X_i}{\sum_{j}^{ns} \alpha_{ij} X_j \Delta_{i,j}^{(2)}(T)} \right], \tag{2.172}$$

where

$$\alpha_{ij} = 1 + \frac{\left[1 - \left(m_i / m_j\right)\right]\left[0.45 - 2.54\left(m_i / m_j\right)\right]}{\left[1 + \left(m_i / m_j\right)\right]^2}. \tag{2.173}$$

Internal Degree of Freedom

The contribution of the internal degree to the thermal conductivity λ_{int}, such as the rotational and vibrational, is given by

$$\lambda_{\mathrm{int}} = \sum_{i}^{nm} \frac{X_i \left(\lambda_{i,\mathrm{int}} - \lambda_{i,\mathrm{tr,mono}}\right)}{D_{i,i} \sum_{j}^{ns} \frac{X_j}{D_{i,j}}}. \tag{2.174}$$

Hirschfelder et al. expressed $\lambda_{i,\mathrm{int}}$ as the following form:

$$\lambda_{i,\mathrm{int}} = \frac{1}{4} \left[\left(15 - 6\frac{\rho_i D_{i,i}}{\mu_i}\right) C'_{p,\mathrm{int},i} - \left(15 - 10\frac{\rho_i D_{i,i}}{\mu_i}\right) C'_{v,\mathrm{int},i} \right] \mu_i, \tag{2.175}$$

where

$$C'_{p,\mathrm{int},i} = C_{p,tr} + C_{p,\mathrm{int},i}, C'_{v,\mathrm{int},i} = C_{v,tr} + C_{v,\mathrm{int},i}. \tag{2.176}$$

With Eqs. (2.166) and (2.175), we obtain the following expression as

$$\lambda_{i,\mathrm{int}} - \lambda_{i,\mathrm{tr,mono}} = \rho_i D_{i,i} C_{v,\mathrm{int},i}. \tag{2.177}$$

Substituting Eq. (2.177) with Eq. (2.166) into Eq. (2.174) one obtains

$$\lambda_{\mathrm{int}} = k \sum_{i}^{nm} \left[\frac{\left(\frac{C_{v,\mathrm{int},i}}{R_i}\right) X_i}{\sum_{j}^{ns} X_j \Delta_{i,j}^{(1)}(T)} \right]. \tag{2.178}$$

2.9.7 Diffusion

Multicomponent Diffusion Model

The diffusion velocity V_s^j is defined with the species-averaged velocity v_s^j as

$$V_s^j = v_s^j - v^j, \tag{2.179}$$

where the mass-averaged velocity v is given by

$$v^j = \sum_{s=1}^{ns} \frac{\rho_s}{\rho} v_s^j. \tag{2.180}$$

With Eqs. (2.179) and (2.180), one obtains the following relation:

$$\sum_{s=1}^{ns} \rho V_s^j = 0. \tag{2.181}$$

Following Hirschfelder, Curtiss and Bird [46], the diffusion velocity is given by

$$V_s^j = \frac{n^2}{n_s} \sum_{k=1}^{ns} m_k D_{s,k} d_k^j - \frac{D_s^T}{\rho} \frac{\partial \ln T}{\partial x^j}, \tag{2.182}$$

$$d_s^j \equiv \frac{\partial}{\partial x^j}\left(\frac{n_s}{n}\right) + \left(\frac{n_s}{n} - \frac{\rho_s}{\rho}\right)\frac{\partial \ln p}{\partial x^j} - \frac{\rho_s}{p}\left(F_s^j - \sum_{k=1}^{ns} \frac{\rho_k}{\rho} F_k^j\right), \tag{2.183}$$

where $D_{s,k}$ and D_s^T are the multicomponent mass diffusion coefficient and the thermal diffusion coefficient, respectively. In addition, F_s^j in d_s^j represents the external force acting on the species s. Equation (2.182) involves four components of the diffusion velocity caused by different ways: (1) the gradient in the concentration (ordinary diffusion), (2) the pressure gradient (pressure diffusion), (3) the external force gradient (forced diffusion) (4) the temperature gradient (thermal diffusion). In the present study, the effects of the pressure, the forced and thermal gradients are neglected because those terms are small compared with that of the ordinary diffusion. Hence, Eq. (2.182) can be expressed by

$$V_s^j = \frac{n^2}{n_s} \sum_{k}^{ns} m_k D_{s,k} \frac{\partial}{\partial x^j}\left(\frac{n_s}{n}\right). \tag{2.184}$$

According to Hirschfelder, Curtiss and Bird [46], the binary diffusion coefficient $D_{s,k}$ is given by

$$D_{s,k} = \frac{kT}{p\Delta_{s,k}^{(1)}(T)}. \tag{2.185}$$

Following Curtiss and Hirschfelder [62], it is possible to simplify the Eq. (2.184) by a rearrangement as

$$\sum_{k=1}^{ns} \frac{n_s n_k}{D_{s,k}} \left(V_s^j - V_k^j\right) = -n^2 \frac{\partial}{\partial x^j}\left(\frac{n_s}{n}\right). \tag{2.186}$$

Based on Eq. (2.186), assuming that $V_s^j = \text{const}$ for $s \neq k$, the diffusion velocity V_s^j for multicomponent mixtures is given by Yos [59] as the following form:

$$V_s^j = -\frac{1 - C_s}{\sum_{k \neq s}^{ns} X_k / D_{s,k}} \frac{1}{X_s} \frac{\partial X_s}{\partial x^j}, \tag{2.187}$$

where the effective diffusion coefficient is defined as

$$D_s \equiv \frac{1-C_s}{\sum_{k\neq s}^{ns} X_k / D_{sk}} \frac{C_s}{X_s}. \tag{2.188}$$

Thus, the mass flux is expressed by

$$\rho_s V_s^j = -\rho D_s \frac{\partial X_s}{\partial x^j}. \tag{2.189}$$

Ambipolar diffusion

Since electron's mass is very small compared with the heavy particle (atom, molecule, and their ions), the electrons tend to diffuse faster than the heavy particle species. An ambipolar electric field is formed in the plasma, when the electrical potential drop between the diffused electrons (negative charge) and the remaining charged species (positive) is caused. The positive charged species are forced and accelerated by the electric field, while the electrons are decelerated. Thus, the ambipolar diffusion should be considered in the partially or fully multicomponent plasma. In the present study, the effect of the ambipolar diffusion for charged species is approximately evaluated by

$$D_s^a = \left(1+\frac{T_e}{T_{tr}}\right) D_s. \tag{2.190}$$

where D_s is the effective diffusion coefficient of the ionic species in the absence of the ambipolar electric field.

Electron diffusion coefficient

The effective diffusion coefficient of the electron is given by

$$D_e = \frac{m_e \sum_{s=I}^{ns} D_s^a X_s}{\sum_{s=I}^{ns} m_s X_s}. \tag{2.191}$$

2.9.8 Summary of Transport Properties

When the electron temperature is largely different from the translational temperature of the heavy species, presence of the electrons should be considered in the transport properties calculation. The transport properties for gas mixture in thermochemical nonequilibrium are summarized here.

Electric Conductivity

The third-order electrical conductivity:

$$\sigma = \sigma^{3\text{rd}} = \frac{3e^2 n_e^2}{2kT_e}\sqrt{\frac{2\pi kT_e}{m_e}}\frac{\begin{vmatrix} q^{11} & q^{12} \\ q^{21} & q^{22} \end{vmatrix}}{\begin{vmatrix} q^{00} & q^{01} & q^{02} \\ q^{10} & q^{11} & q^{12} \\ q^{20} & q^{21} & q^{22} \end{vmatrix}}, \tag{2.152}$$

The first-order electrical conductivity:

$$\sigma = \sigma^{1\text{st}} = \frac{3e^2}{8kT_e}\frac{n_e}{\sum\limits_{i\neq e} n_i \left[\frac{2m_e m_i}{\pi kT_e\left(m_e + m_i\right)}\right]^{\frac{1}{2}} \bar{Q}_{ei}^{(1,1)}}. \tag{2.153}$$

Electron Thermal Conductivity

The third-order electron thermal conductivity

$$\lambda_e = \lambda_{\text{e}}^{3\text{rd}} = \frac{75n_e^2 k}{8kT_e}\sqrt{\frac{2\pi kT_e}{m_e}}\frac{q^{22}}{\begin{vmatrix} q^{11} & q^{12} \\ q^{21} & q^{22} \end{vmatrix}}. \tag{2.160}$$

The first-order electron thermal conductivity:

$$\lambda_e = \frac{15}{4}k\sum_{j\neq e}^{ns}\left[\frac{X_e}{\sum\limits_{j\neq e}^{ns} 1.45X_j\Delta_{e,j}^{(2)}(T_e) + X_e\Delta_{e,e}^{(2)}(T_e)}\right]. \tag{2.192}$$

Viscosity for mixture gas

$$\mu = \sum_{i\neq e}^{ns}\left[\frac{m_i X_i}{\sum\limits_{j\neq e}^{ns} X_j\Delta_{i,j}^{(2)}(T_{tr}) + X_e\Delta_{i,e}^{(2)}(T_e)}\right] + \frac{m_e X_e}{\sum\limits_{j}^{ns} X_j\Delta_{e,j}^{(2)}(T_e)}. \tag{2.193}$$

Thermal conductivity of heavy particles

Translational contribution of thermal conductivity in a multicomponent gas mixture except for electrons:

$$\lambda_{\text{tr}} = \frac{15}{4}k\sum_{i\neq e}^{ns}\left[\frac{X_i}{\sum\limits_{j\neq e}^{ns}\alpha_{ij}X_j\Delta_{i,j}^{(2)}(T_{tr}) + 3.54X_e\Delta_{i,e}^{(2)}(T_e)}\right]. \tag{2.194}$$

Rotational contribution of thermal conductivity in a multicomponent gas mixture:

$$\lambda_{rot} = k\sum_{i=\mathrm{M}}^{nm}\left[\frac{X_i}{\sum_{j\neq e}^{ns} X_j\Delta_{i,j}^{(1)}(T_{tr}) + X_e\Delta_{i,e}^{(1)}(T_e)}\right]. \tag{2.195}$$

Vibrational contribution of thermal conductivity in a multicomponent gas mixture:

$$\lambda_{vib} = k\sum_{i=\mathrm{M}}^{nm}\left[\frac{\left(\frac{C_{\upsilon,vib,i}}{R_i}\right)X_i}{\sum_{j\neq e}^{ns} X_j\Delta_{i,j}^{(1)}(T_{tr}) + X_e\Delta_{i,e}^{(1)}(T_e)}\right]. \tag{2.196}$$

Binary diffusion coefficient

$$D_{ij} = \frac{kT_{tr}}{p\Delta_{i,j}^{(1)}(T_{tr})}, \quad \text{for } i\neq e \text{ and } j\neq e, \tag{2.197}$$

$$D_{ij} = \frac{kT_e}{p\Delta_{i,j}^{(1)}(T_e)}, \quad \text{for } i = e \text{ or } j = e, \tag{2.198}$$

where

$$\Delta_{i,j}^{(1)}(T) = \frac{8}{3}\left[\frac{2m_im_j}{\pi kT(m_i+m_j)}\right]^{1/2}\bar{Q}_{i,j}^{(1,1)}, \tag{2.199}$$

$$\Delta_{i,j}^{(2)}(T) = \frac{16}{5}\left[\frac{2m_im_j}{\pi kT(m_i+m_j)}\right]^{1/2}\bar{Q}_{i,j}^{(2,2)}, \tag{2.200}$$

$$\alpha_{ij} = 1+\frac{\left[1-\left(m_i/m_j\right)\right]\left[0.45-2.54\left(m_i/m_j\right)\right]}{\left[1+\left(m_i/m_j\right)\right]^2}. \tag{2.201}$$

2.10 Internal Energy Exchange Model

Internal energy transfer due to elastic and inelastic collisions among electrons, molecules, and atoms were modelled and added to the corresponding electron, vibrational, and rotational energy equations. The internal energy-exchange rates, S_{int}, in the source-term vector, $\boldsymbol{W}$, are expressed as follows:

$$S_{\mathrm{int},rot} = Q_{T-R} - Q_{R-V} - Q_{R-e} + Q_D^{rot}, \tag{2.202}$$

$$S_{\mathrm{int},vib} = Q_{T-V} + Q_{R-V} + Q_{e-V} + Q_D^{vib}, \tag{2.203}$$

$$S_{\mathrm{int},e} = Q_{T-e} + Q_{R-e} - Q_{e-V} + Q_D^{e} + Q_I^{e}. \tag{2.204}$$

The chemical energy loss due to ionization and dissociation reactions (e.g., Q_D^{rot}, Q_D^{vib}, Q_D^e, Q_I^e) and energy transfer between each of the internal energy modes (i.e., translation–rotation (T–R), translation–vibration (T–V), translation–electron (T–e), rotation–vibration (R–V), and rotation–electron (R–e)) were considered and evaluated by the same formulas as were referred from Takahashi's work [33]. The vibrational-election energy exchange ($Q_{e\text{-}V}$) is modified in the present work with newly available data and methods. Detailed description of the internal energy exchange model is given below.

2.10.1 Vibrational-Electron Energy Exchange

The term $Q_{e\text{-}V}$ denotes the energy transfer between electrons and the vibrational mode of molecules, and is evaluated to be of the Landau–Teller form [76]:

$$Q_{e-V} = \frac{E_{vib,N_2}^{eq}(T_e) - E_{vib,N_2}^{eq}(T_{vib})}{\tau_{N_2-e}}, \tag{2.205}$$

where τ_{N_2-e} is the vibrational relaxation time of molecular nitrogen during collisions with electrons, derived by Lee [34]:

$$\tau_{N_2-e} = \frac{2kT_e}{p_e\left(1-e^{-\Theta_{vib}/T_e}\right)^2 \int k_{0,j}^{e-V} j^2 dj}. \tag{2.206}$$

In Eq. (2.206), $k_{0,j}^{e\text{-}V}$ is a vibrational excitation rate coefficient from the vibrational state 0 to the state *j*. Lee gave the curve-fit formula for the vibrational relaxation time $\tau_{N_2\text{-}e}$ and suggested that it could be used for highly ionized plasma simulations such as modelling of the high-power arc-heated flows [27, 34]. Alternatively, Bourdon and Vervisch [35] proposed an improved expression for calculating $\tau_{N_2\text{-}e}$ in the temperature range of 3000 – 20000 K. Good agreement between the experimental and theoretical data for $\tau_{N_2\text{-}e}$ were seen in their work. The gave the curve-fitting expression as following:

$$\tau_{N_2-e} = \left(p_e/101325\right)^{-1} 10^{\left(C_2Z^2+C_1Z+C_0\right)}, \tag{2.207}$$

where $Z = \log_{10}(T_e)$, p_e is the electron pressure in unit Pa. The coefficients $C_0 \sim C_2$ are summarized in Table 2.7. On the other hand, out of the above temperature range, recently Kim [36] modelled the rate coefficient $k_{0,j}^{e\text{-}V}$ and gave the validated fitting formula to calculate the relaxation time. The rate coefficient $k_{0,j}^{e\text{-}V}$ can be calculated by

$$k_{0,j}^{e-V} = 10^{-15}\bar{a}T_e^{-\frac{3}{2}} \exp\left(\frac{\bar{b}}{T_e} + \bar{c}\right), \tag{2.208}$$

where the vibrational state j is equal 10, and the corresponding fitting coefficients $\bar{a}$, $\bar{b}$, $\bar{c}$ are summarized in Table 2.8. And then, the vibration-electron relaxation time out of the temperature range 3000 ~ 20000 K is computed by

$$\tau_{\mathrm{N_2-e}} = \frac{2kT_e}{p_e\left[1-\exp\left(\frac{-\Theta_{vib}}{T_e}\right)^2 \int k_{0,j}^{e-V} j^2 dj\right]}$$

$$= \frac{2kT_e}{p_e}\left[1-\exp\left(\frac{-\Theta_{vib}}{T_e}\right)\sum_{j=1}^{10} k_{0,j}^{e-V} j^2\right]^{-1}. \quad (2.209)$$

Note that here the unit of T_e and p_e are electron-Volt (eV) and standard atmospheric pressure (atm). Finally, the computed vibrational-electron relaxation time in dependence of T_e is given in Fig. 2.11. The difference of the vibrational relaxation time between Lee's work and the present work is illustrated in Fig. 2.11

About air plasma flow, since the translational-electron energy coupling for O_2 and NO is slower than that for N_2 the relaxation times for O_2 and NO are used by multiplying 300 to that for N_2 as proposed by Park and Lee [77] as

$$\tau_{\mathrm{O_2\text{-}e}} = 300\tau_{\mathrm{N_2\text{-}e}}, \quad (2.210)$$

$$\tau_{\mathrm{NO\text{-}e}} = 300\tau_{\mathrm{N_2\text{-}e}}. \quad (2.211)$$

Table 2.7 Constants for electron-vibration relaxation time

Temperature range (K)	C_2	C_1	C_0
3000-7000	5.019	-38.625	64.219
7000-20000	2.448	-18.704	25.635

Table 2.8 Coefficients of the vibrational-excitation-rate coefficient model

j	$\bar{a}$	$\bar{b}$	$\bar{c}$
1	8.0340	-2.227	2.005000
2	7.9240	-2.235	1.479000
3	7.8760	-2.257	1.054000
4	7.6260	-2.334	0.649900
5	7.3260	-2.454	0.204900
6	4.9000	-2.556	0.007448
7	2.4570	-2.702	0.002952
8	1.1190	-2.865	0.001133
9	0.4681	-3.042	0.004312
10	0.1837	-3.223	0.0002219

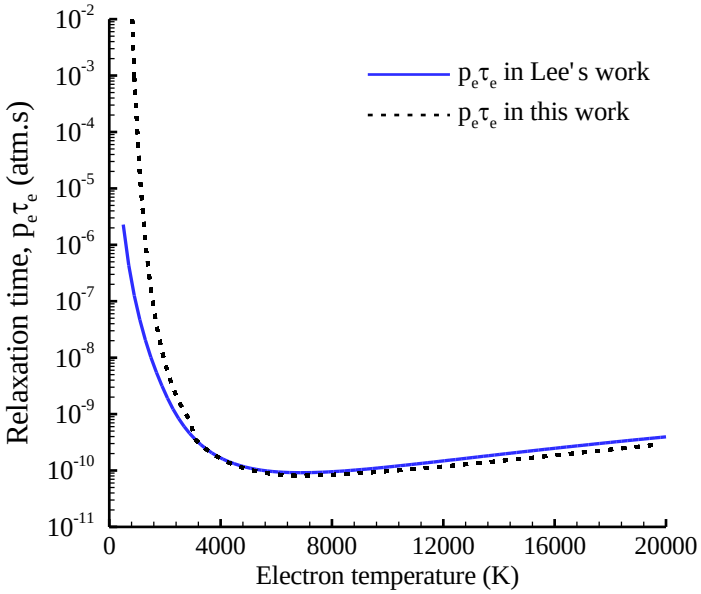

Fig. 2.11 Comparison of the electron-vibration relaxation time

2.10.2 Translational-Rotational Energy Exchange

The Parker model [78] has been widely adopted for various thermochemical nonequilibrium flow simulations, while the temperature range of the model is limited by $T \leq 1500$ K. There can be a high-temperature region where the temperature exceeds 10,000 K in the present calculations and uncertainties for an accurate prediction of such a high-temperature gas may remain. Thus, instead of the Parker model, the translational-rotational energy-exchange rate $Q_{\text{T-R}}$ proposed by Park model [79] in the present study, which is given by

$$Q_{\text{T-R}} = \sum_{s=M}^{nm} \frac{E_{rot}^{\text{eq}}(T_{tr}) - E_{rot}(T_{rot})}{\tau_{\text{T-R}}}. \tag{2.212}$$

The rotational relaxation time $\tau_{\text{T-R}}$ is obtained by the following relation:

$$\tau_{\text{T-R}} = 2.46\times10^{-14} T_{\text{tr}}^{1.692} / p. \tag{2.213}$$

where the pressure p is given in unit of the standard atmosphere (atm).

2.10.3 Translational, Rotational-Vibrational Energy Exchange

Translational-vibrational relaxation can be described by the Landau-Teller equation. According to Park [79], energy exchange between the vibrational and rotational modes also needs to be considered. The formula of Millikan and White [80] with the Park's collision-limiting correction [81] at high temperature is used for the T-V coupling. On the other hand, the rotational-vibrational relaxation time is evaluated by only the Millikan-White formula. Thus, the vibrational relaxation rate $Q_{\text{V-TR}}$ is represented as follows:

$$Q_{\text{V-TR}} = \sum_{s=M}^{nm} 0.4 \frac{E_{\text{vib}}^{\text{eq}}(T_{\text{rot}}) - E_{\text{vib}}}{\langle \tau_{\text{s}}^{\text{MW}} \rangle} + \sum_{s=M}^{nm} 0.6 \frac{E_{\text{vib}}^{\text{eq}}(T_{\text{tr}}) - E_{\text{vib}}}{\langle \tau_{\text{s}}^{\text{MW}} \rangle + \langle \tau_{\text{s}}^{\text{P}} \rangle}. \tag{2.214}$$

In the above equation, the first and second terms gives R-V and T-V energy-transfer rates, respectively. In order to conserve the total energy, the rotational energy-exchange rate $Q_{\text{R-V}}$ and the translational energy-exchange rate $Q_{\text{T-V}}$ are respectively expressed as

$$Q_{\text{R}-\text{V}} = -\sum_{s=M}^{nm} 0.4 \frac{E_{\text{vib}}^{\text{eq}}(T_{\text{rot}}) - E_{\text{vib}}}{\left\langle \tau_{\text{s}}^{\text{MW}} \right\rangle}. \tag{2.215}$$

$$Q_{\text{T}-\text{V}} = -\sum_{s=M}^{nm} 0.6 \frac{E_{\text{vib}}^{\text{eq}}(T_{\text{tr}}) - E_{\text{vib}}}{\left\langle \tau_{\text{s}}^{\text{MW}} \right\rangle + \left\langle \tau_{\text{s}}^{\text{P}} \right\rangle}. \tag{2.216}$$

Under the condition of temperature range between 300 ~ 8,000 K, the relaxation time is given by a semi-empirical equation introduced by Millikan and White as follows:

$$\tau_{s,k}^{\text{MW}} = (p/101{,}325)^{-1} \exp(A_{\text{s},k} T_{tr}^{-1/3} - B_{s,k}), \tag{2.217}$$

where

$$A_{\text{s},k} = 1.16 \times 10^{-3} \mu_{s,k}^{1/2} \Theta_{vib,s}^{4/3}, \tag{2.218}$$

$$B_{s,k} = 0.015 \mu_{s,k}^{1/4} A_{\text{s},k} + 18.42, \tag{2.219}$$

$$\mu_{s,k} = m_s m_k / (m_s + m_k). \tag{2.220}$$

Mean relaxation time of species is given by

$$\left\langle \tau_{\text{s}}^{\text{MW}} \right\rangle = \frac{\sum_{k=M}^{nm} \frac{\rho_k}{M_k}}{\sum_{k \neq e}^{ns} \frac{\rho_k}{M_k \tau_{\text{s,k}}^{\text{MW}}}}. \tag{2.221}$$

Moreover, the Park's collision-limiting correction of the relaxation time is evaluated as

$$\left\langle \tau_s^{\text{P}} \right\rangle = \left[n_s \sigma_{vib} \left(\frac{8 R_s T_{tr}}{\pi} \right)^{1/2} \right]^{-1}, \tag{2.222}$$

where σ_{vib} represents the effective collision cross section, which is set to be $\sigma_{vib} = 1.0 \times 10^{-21} \left(50{,}000 / T_{tr}\right)$ m^2 here.

2.10.4 Translational-Electron Energy Exchange

The Appleton's energy-exchange model [82] is used for coupling the translational and electron energy modes:

$$Q_{\text{T-e}} = \sum_{s \neq e}^{ns} n_e \frac{2 m_e}{m_s} \nu_{e,s} \frac{3}{2} k \left(T_{tr} - T_e\right), \tag{2.223}$$

where $\nu_{e,s}$ is the collision frequency between the electron and other species *s*, and can be expressed as

$$\nu_{e,s} = n_s \sigma_{e,s} \left(\frac{8kT_e}{\pi m_e} \right)^{\frac{1}{2}}. \tag{2.224}$$

Here $\sigma_{e,s}$ is momentum-transfer cross section between electron and heavy particles.

According to works of Park [26] and Mitchner et al [83], the effective momentum-transfer cross section between the electron and ionic species is given in SI units as

$$\begin{aligned} \sigma_{e,s} &= \frac{8\pi}{3} \frac{e^4}{\left(3kT_e\right)^2} \ln\left[1 + \frac{\lambda_D^2 \left(3kT_e\right)^2}{e^4} \right] \\ &= 5.85\times10^{-6} \ln\left(1.24\times10^7 \times T_e^{1.5} n_e^{0.5}\right). \end{aligned} \tag{2.225}$$

where $\lambda_D = \left(\frac{\varepsilon_0 kT_e}{e^2 n_e} \right)^{\frac{1}{2}}, \varepsilon_0 = 8.85\times10^{-12}$

For collisions between the electron and the neutral species, The effective cross section $\sigma_{e,s}$ is obtained from a curve-fit of Gnoffo's work [84]:

$$\sigma_{e,s} = \tilde{a}_s + \tilde{b}_s T_e + \tilde{c}_s T_e^2. \tag{2.226}$$

where the coefficients $\tilde{a}_s$, $\tilde{b}_s$, $\tilde{c}_s$ are shown in Table 2.9.

Table 2.9 Curve-fit constants for electron-neutral cross-section

Species	N_2	O_2	NO	N	O
$\tilde{a}_s$	7.5×10^{-20}	2.0×10^{-20}	1.0×10^{-19}	5.0×10^{-20}	1.2×10^{-20}
$\tilde{b}_s$	5.5×10^{-24}	6.0×10^{-24}	0	0	1.7×10^{-24}
$\tilde{c}_s$	-1.0×10^{-28}	0	0	0	-2.0×10^{-29}

2.10.5 Rotational-Electron Energy Exchange

In these nonequilibrium plasma studies [33, 85], the rate of the rotational-electron energy coupling is given as follows:

$$Q_{\text{R-e}} = \sum_{s=M}^{nm} g_{rot,s} n_e \frac{2m_e}{m_s} \nu_{e,s} \frac{3}{2} k\left(T_{rot} - T_e\right). \tag{2.227}$$

the coefficients $g_{rot,s}$ = 10 is assumed for the neutral species such as N_2, O_2, and NO. For the ionic molecules, since accurate values are unexplained, the same coefficients are used as those of the neutral species.

2.10.6 Energy Loss Due to Chemical Reactions

Energy losses of rotation and vibration (Q_D^{rot} and Q_D^{vib}) due to heavy particles' impact dissociation reactions can be given by a nonpreferential dissociation model as [84]

$$Q_D^{rot} = \sum_{s=M} e_{rot} \dot{\omega}_s^D, \tag{2.228}$$

$$Q_D^{vib} = \sum_{s=M} e_{vib}\dot{\omega}_s^D \ . \tag{2.229}$$

where $\dot{\omega}_s^D$ is the mass-production rate by the heavy particle impact dissociation reactions (reaction number in Table 2.3: r = 1–10, 12-31, and Table 2.4: r = 1–4). Moreover, e_{rot} and e_{vib} represent the rotation and vibration energies per unit mass, respectively.

On the other hand, electron energy losses due to electron impact dissociation Q_D^e and ionization Q_I^e can be given by

$$Q_D^e = E_{\mathrm{D,N_2}}\dot{\omega}_{\mathrm{N_2}}^{\mathrm{e}}, \tag{2.230}$$

$$Q_I^e = E_{\mathrm{I,N}}\dot{\omega}_{\mathrm{N}}^{\mathrm{e}} + E_{\mathrm{I,O}}\dot{\omega}_{\mathrm{O}}^{\mathrm{e}}. \tag{2.231}$$

where $\dot{\omega}_{\mathrm{N_2}}^{\mathrm{e}}$, $\dot{\omega}_{\mathrm{N}}^{\mathrm{e}}$ and $\dot{\omega}_{\mathrm{O}}^{\mathrm{e}}$ are mass-production rates by the electron-impact dissociation and ionization reactions (reaction number in Table 2.3: r = 11, 37-38, and Table 2.4: r = 5, 8), respectively. In addition, $E_{\mathrm{D,N_2}}$ shows the dissociation energy of molecular nitrogen, and $E_{\mathrm{I,N}}$ and $E_{\mathrm{I,O}}$ represents the ionization energy of the atomic nitrogen and oxygen.

2.11 Summary

In this chapter, structures and geometries of the 10-kW and 110-kW ICP wind tunnels were primarily described. The basic flow phenomena occurring in an ICP wind tunnel were depicted. The flow-field and electromagnetic-field equations such as mass, momentum, energy conservations and magnetic vector-potential equations etc. were discussed in detail. The transport properties of the test gases and the internal energy exchange between translational, rotational, vibrational and electron energy modes were also given in this chapter. The basic governing equations used in this study are summarized as following:

Mass conservation equation:

$$\frac{\partial \rho}{\partial t} + \frac{\partial}{\partial x_i}\left(\rho u_i\right) = 0. \tag{2.232}$$

Momentum equation:

$$\frac{\partial\left(\rho u_j\right)}{\partial t} + \frac{\partial}{\partial x_j}\left(\rho u_i u_j + \delta_{ij}\, p\right) =$$

$$\frac{\partial}{\partial x_j}\left[\left(\mu+\mu_t\right)\left(\frac{\partial u_i}{\partial x_j}+\frac{\partial u_j}{\partial x_i}-\frac{2}{3}\frac{\partial u_k}{\partial x_k}\delta_{ij}\right)-\frac{2}{3}\rho k\delta_{ij}\right] + F_{Li}. \tag{2.233}$$

Total energy equation:

$$\frac{\partial E}{\partial t} + \frac{\partial}{\partial x_j}\left[(E+p)u_j\right] = \frac{\partial}{\partial x_j}(\lambda_{tr}\frac{\partial T_{tr}}{\partial x_j} + \lambda_{rot}\frac{\partial T_{rot}}{\partial x_j} + \lambda_{vib}\frac{\partial T_{vib}}{\partial x_j} + \lambda_e\frac{\partial T_e}{\partial x_j} + \lambda_t\frac{\partial T_{tr}}{\partial x_j})$$

$$+\frac{\partial}{\partial x_j}(\rho\sum_{s=1}^{ns}h_s D_s\frac{\partial X_s}{\partial x_j})$$

$$+\frac{\partial}{\partial x_j}\left[(\mu+\mu_t)\left(\frac{\partial u_i}{\partial x_j}+\frac{\partial u_j}{\partial x_i}-\frac{2}{3}\frac{\partial u_k}{\partial x_k}\delta_{ij}\right)-\frac{2}{3}\rho k\delta_{ij}\right]+S_{\text{joule}}. \tag{2.234}$$

Species mass conversation equation:

$$\frac{\partial\rho_s}{\partial t}+\frac{\partial}{\partial x_j}\left(\rho_s u_j\right)=\frac{\partial}{\partial x_j}\left(\rho_s D_s\frac{\partial X_s}{\partial x_j}\right)+\dot{\omega}_s. \tag{2.235}$$

Rotational energy equation:

$$\frac{\partial E_{\text{rot}}}{\partial t}+\frac{\partial(E_{\text{rot}}u_j)}{\partial x_j}=\frac{\partial}{\partial x_j}(\lambda_{rot}\frac{\partial T_{rot}}{\partial x_j})+\frac{\partial}{\partial x_j}(\rho\sum_{s=M}^{nm}h_{rot,s}D_s\frac{\partial X_s}{\partial x_j})+S_{\text{int},rot}. \tag{2.236}$$

Vibrational energy equation:

$$\frac{\partial E_{\text{vib}}}{\partial t}+\frac{\partial(E_{\text{vib}}u_j)}{\partial x_j}=\frac{\partial}{\partial x_j}(\lambda_{vib}\frac{\partial T_{vib}}{\partial x_j})+\frac{\partial}{\partial x_j}(\rho\sum_{s=M}^{nm}h_{vib,s}D_s\frac{\partial X_s}{\partial x_j})+S_{\text{int},vib}. \tag{2.237}$$

Electron energy equation:

$$\frac{\partial E_{\text{e}}}{\partial t}+\frac{\partial(E_{\text{e}}u_j)}{\partial x_j}=-p_e\frac{\partial u_j}{\partial x_j}+\frac{\partial}{\partial x_j}(\lambda_e\frac{\partial T_{\text{e}}}{\partial x_j})+\frac{\partial}{\partial x_j}(\rho_e h_e D_e\frac{\partial X_e}{\partial x_j})+S_{\text{jolue}}+S_{\text{int},e}. \tag{2.238}$$

Turbulence energy equation

$$\frac{\partial(\rho k)}{\partial t}+\frac{\partial}{\partial x_j}\left(\rho k u_j\right)=\frac{\partial}{\partial x_j}\left\{\left(\mu+\frac{\mu_{\text{t}}}{\sigma_k}\right)\frac{\partial k}{\partial x_j}\right\}+$$

$$\left\{\mu_t\left(\frac{\partial u_i}{\partial x_j}+\frac{\partial u_j}{\partial x_i}-\frac{2}{3}\frac{\partial u_k}{\partial x_k}\delta_{ij}\right)-\frac{2}{3}\rho k\delta_{ij}\right\}\frac{\partial u_j}{\partial x_j}-\rho\varepsilon. \tag{2.239}$$

Turbulence dissipation rate equation

$$\frac{\partial(\rho\varepsilon)}{\partial t}+\frac{\partial}{\partial x_j}\left(\rho\varepsilon u_j\right)=\frac{\partial}{\partial x_j}\left\{\left(\mu+\frac{\mu_{\text{t}}}{\sigma_\varepsilon}\right)\frac{\partial\varepsilon}{\partial x_j}\right\}$$

$$+C_{\varepsilon1}f_1\frac{\varepsilon}{k}\left\{\mu_t\left(\frac{\partial u_i}{\partial x_j}+\frac{\partial u_j}{\partial x_i}-\frac{2}{3}\frac{\partial u_k}{\partial x_k}\delta_{ij}\right)-\frac{2}{3}\rho k\delta_{ij}\right\}\frac{\partial u_j}{\partial x_j}-C_{\varepsilon2}f_2\rho\frac{\varepsilon^2}{k}. \tag{2.240}$$

Far-field electromagnetic equations

$$\nabla^2 A_R+\omega\mu_0\sigma A_I=-\mu_0 J_c, \tag{2.241}$$

$$\nabla^2 A_I-\omega\mu_0\sigma A_R=0. \tag{2.242}$$

Gas state equation:

$$p=\sum_{s\neq e}^{ns-1}\rho_s R_s T_{tr}+\rho_e R_e T_e. \tag{2.243}$$

The internal energy is defined as follows:

$$E = E_{tr} + E_{rot} + E_{vib} + E_e + \sum_{s=1}^{ns} \rho_s \Delta h_s^0 + \frac{1}{2}\rho u_i u_i + \rho k . \tag{2.244}$$

Translational, rotational, vibrational and electron energy are given by:

$$E_{tr} = \sum_{s \neq e} \frac{3}{2} \rho_s R_s T_{tr} , \tag{2.245}$$

$$E_{rot} = \sum_{s=M} \rho_s R_s T_{rot} , \tag{2.246}$$

$$E_{vib} = \sum_{s=M} \frac{\rho_s R_s \Theta_{vib,s}}{exp\left(\Theta_{vib,s} / T_{vib,s}\right) - 1}, \tag{2.247}$$

$$E_e = \frac{3}{2} \rho_e R_e T_e . \tag{2.248}$$

Chapter 3 Numerical Procedure

The governing equations and models described in the previous chapters should be numerically solved to obtain flow-field and electromagnetic-field properties in the ICP facilities. The equation systems are composed of the Navier-Stokes equations, the turbulent transport equations, and the far-field electromagnetic equations. The Navier-Stokes equations involve many conservations such as density, momentum and total energy equations etc. When treating these equations, it is desirable and more efficient that these equations are solved simultaneously rather than solved separately. The time-marching method should be introduced to update the solutions at each time step. Suitable discretization manners should be selected for spatial discretization. Advection and viscous terms in the Navier-Stokes equations have respectively hyperbolic and parabolic natures. Thus, it is nature that the former fluxes are evaluated by an upwind manner and the later are calculated by a central difference method. The electromagnetic field are also evaluated by the central difference method because of an elliptic nature. The accuracy of the discretization is kept to be the second-order accuracy for all the differential equations.

In addition, the equation system tends to be unstable due to that nonlinearity such as the chemical reactions and the Joule-heating in the electromagnetic field calculation. Efficient and robust numerical methods must be introduced to overcome numerical stiffness and reduce computational cost. In this chapter, the numerical methods used in the present study will be stated in detail.

3.1 Discretization

To numerically solve the governing equations described in the previous chapters, the spatial discretization of the equations i.e., the numerical approximation of the convective and viscous fluxes as well as of the source term is one of important issues in a numerical modeling. In the pasts, many different methodologies were developed for the purpose of the spatial discretization. In order to sort them, we can divide these spatial discretization methods into three main categories: finite difference method (FDM), finite volume method (FVM) and finite element method (FEM) [86]. All these methods relies on some kinds of grid in order to discretize the governing equations. Basically, there are two types of grids: structured and unstructured grids. In this study, the finite difference and finite volume methods are used to discretize the governing equations, and the computational domain consists of the structured grids. In order to follow closely the boundaries of the physical space, we transform the Cartesian coordinate system in the physical domain (x, y, z) into the generalized coordinate system in the computational domain (ξ, η, ζ). The transforming matrix can be expressed by

$$\begin{bmatrix} dx \\ dy \\ dz \end{bmatrix} = \begin{bmatrix} x_\xi & x_\eta & x_\zeta \\ y_\xi & y_\eta & y_\zeta \\ z_\xi & z_\eta & z_\zeta \end{bmatrix} \begin{bmatrix} d\xi \\ d\eta \\ d\zeta \end{bmatrix}, \tag{3.1}$$

where the notations in the right-hand-side matrix represent differential form e.g., $x_\xi = \frac{\partial x}{\partial \xi}$, $y_\eta = \frac{\partial y}{\partial \eta}$, $z_\varsigma = \frac{\partial z}{\partial \varsigma}$ in Eq. (3.1). The inversed matrix of Eq. (3.1) is

$$\begin{bmatrix} d\xi \\ d\eta \\ d\zeta \end{bmatrix} = \begin{bmatrix} \xi_x & \xi_y & \xi_z \\ \eta_x & \eta_y & \eta_z \\ \zeta_x & \zeta_y & \zeta_z \end{bmatrix} \begin{bmatrix} dx \\ dy \\ dz \end{bmatrix}. \tag{3.2}$$

Comparing Eq. (3.1) and Eq. (3.2), we can obtain:

$$\xi_x = J\left(y_\eta z_\zeta - y_\zeta z_\eta\right), \quad \xi_y = J\left(z_\eta x_\zeta - z_\zeta x_\eta\right), \quad \xi_z = J\left(x_\eta y_\zeta - x_\zeta y_\eta\right), \tag{3.3}$$

$$\eta_x = J\left(y_\zeta z_\xi - y_\xi z_\zeta\right), \quad \eta_y = J\left(z_\zeta x_\xi - z_\xi x_\zeta\right), \quad \eta_z = J\left(x_\zeta y_\xi - x_\xi y_\zeta\right), \tag{3.4}$$

$$\zeta_x = J\left(y_\xi z_\eta - y_\eta z_\xi\right), \quad \zeta_y = J\left(z_\xi x_\eta - z_\eta x_\xi\right), \quad \zeta_z = J\left(x_\xi y_\zeta - x_\zeta y_\xi\right). \tag{3.5}$$

Here, J is the Jacobian of the coordinate transformation. The inversion of the Jacobian is given by

$$J^{-1} = x_\xi\left(y_\eta z_\zeta - y_\zeta z_\eta\right) + x_\eta\left(y_\zeta z_\xi - y_\xi z_\zeta\right) + x_\zeta\left(y_\xi z_\eta - y_\eta z_\xi\right). \tag{3.6}$$

Then, the governing equations in the generalized coordinate system can be written as

$$\frac{\Delta \tilde{\boldsymbol{Q}}}{\Delta t} + \frac{\Delta \tilde{\boldsymbol{F}}^\xi}{\Delta \xi} + \frac{\Delta \tilde{\boldsymbol{F}}^\eta}{\Delta \eta} + \frac{\Delta \tilde{\boldsymbol{F}}^\zeta}{\Delta \zeta} = \tilde{\boldsymbol{W}}, \tag{3.7}$$

where

$$\tilde{\boldsymbol{Q}} = \frac{1}{J}\boldsymbol{Q}, \tag{3.8}$$

$$\tilde{\boldsymbol{F}}^\xi = \frac{1}{J}\left(\xi_x \tilde{\boldsymbol{F}}^x + \xi_y \tilde{\boldsymbol{F}}^y + \xi_z \tilde{\boldsymbol{F}}^z\right), \tag{3.9}$$

$$\tilde{\boldsymbol{F}}^\eta = \frac{1}{J}\left(\eta_x \tilde{\boldsymbol{F}}^x + \eta_y \tilde{\boldsymbol{F}}^y + \eta_z \tilde{\boldsymbol{F}}^z\right), \tag{3.10}$$

$$\tilde{\boldsymbol{F}}^\zeta = \frac{1}{J}\left(\zeta_x \tilde{\boldsymbol{F}}^x + \zeta_y \tilde{\boldsymbol{F}}^y + \zeta_z \tilde{\boldsymbol{F}}^z\right), \tag{3.11}$$

$$\tilde{\boldsymbol{W}} = \frac{1}{J}\boldsymbol{W}. \tag{3.12}$$

The inversion of the Jacobian J^{-1} is equal to the volume of the control volume. On the other hand, the governing equation of the flow field is rewritten in an integral form as:

$$\frac{d}{dt}\iiint \boldsymbol{Q} dV + \int \boldsymbol{F}_j d\boldsymbol{A}_j = \iiint \boldsymbol{W} dV, \tag{3.13}$$

where $\boldsymbol{Q} = [\rho, \rho u_i, E, \rho_1, \cdots, \rho_{ns}, E_{rot}, E_{vib}, E_e, \rho k, \rho\varepsilon]^{\mathrm{T}}$ is the vector of the conservative variables and $\boldsymbol{F}$ shows the advection/viscous flux vector. Additionally, $\boldsymbol{W}$ represents the source term vector which includes the Lorentz force, Joule-heating rate, mass-production rate of chemical species and energy exchange rate between each internal

energy mode. Volume of the control volume is V and $\boldsymbol{A}_j$ shows the jth component of the area vector $\boldsymbol{A}_j$. Equation (3.13) is discretized by using finite volume formulation as

$$\frac{V}{\Delta t}\Delta \boldsymbol{Q} + \sum_j \left(\boldsymbol{F}_k \boldsymbol{A}_k\right)_j = V\boldsymbol{W}. \tag{3.14}$$

The conservative variables can be obtained by evaluating the numerical fluxes at each interface and the gain/loss in the control volume.

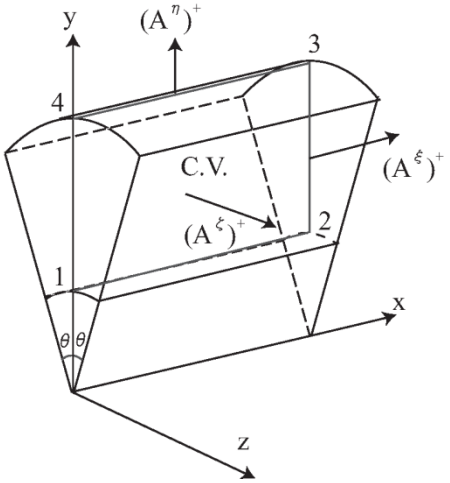

Fig. 3.1 Control volume

About the control volume, if an analysis object can be expressed as a cylindrical coordinate system, it is very effective to adopt axisymmetric two dimension. As shown in Fig. 3.1, we now consider a three-dimensional control volume. The space along the circumferential direction is assumed to be infinitely-thin. Thus, the three-dimensional governing equations are discretized in space instead of transforming the equations into axisymmetric two-dimensional form. The physical properties, such as the density, velocities and temperatures, are defined at the center of the control volume. The area vectors $(\boldsymbol{A}^{\xi})^{\pm}$, $(\boldsymbol{A}^{\eta})^{\pm}$ and $(\boldsymbol{A}^{\zeta})^{\pm}$ in ξ, η, ζ directions are defined by

$$(\boldsymbol{A}^{\xi})^{+} = (y_3 + y_2)\theta[(y_3 - y_2), -(x_3 - x_2), 0], \tag{3.15}$$

$$(\boldsymbol{A}^{\xi})^{-} = (y_4 + y_1)\theta[(y_4 - y_1), -(x_4 - x_1), 0], \tag{3.16}$$

$$(\boldsymbol{A}^{\eta})^{+} = (y_3 + y_4)\theta[-(y_3 - y_4), (x_3 - x_4), 0], \tag{3.17}$$

$$(\boldsymbol{A}^{\eta})^{-} = (y_2 + y_1)\theta[-(y_2 - y_1), (x_2 - x_1), 0], \tag{3.18}$$

$$(\boldsymbol{A}^{\zeta})^{\pm} = S[0, \theta^{\pm}, 1]. \tag{3.19}$$

where S shows the cross section of the control volume, which is evaluated by

$$S = \left|(x_3 - x_1)(y_4 - y_2) - (y_3 - y_1)(x_4 - x_2)\right| / 2. \tag{3.20}$$

The volume V is obtained by splitting of the control volume into six tetrahedrons,

$$V = \theta[\, y_4 \left|x_1 y_3 - x_1 y_4 - x_3 y_1 + x_3 y_4 + x_4 y_1 - x_4 y_3\right|$$

$$+ y_3 \left|x_1 y_3 - x_1 y_4 - x_3 y_1 + x_3 y_4 + x_4 y_1 - x_4 y_3\right|$$

$$+y_1\left|x_1y_3-x_1y_4-x_3y_1+x_3y_4+x_4y_1-x_4y_3\right|$$

$$+y_1\left|x_1y_2-x_1y_3-x_2y_1+x_2y_3+x_3y_1-x_3y_2\right|$$

$$+y_3\left|x_1y_2-x_1y_3-x_2y_1+x_2y_3+x_3y_1-x_3y_2\right|$$

$$+y_2\left|x_1y_2-x_1y_3-x_2y_1+x_2y_3+x_3y_1-x_3y_2\right|]/3\ . \tag{3.21}$$

Substituting Eqs. (3.15) - (3.19) into Eq. (3.14)

$$\frac{V}{\Delta t}\Delta\boldsymbol{Q}+(\boldsymbol{F}_k\boldsymbol{A}_k^{\xi})^{+}-(\boldsymbol{F}_k\boldsymbol{A}_k^{\xi})^{-}+(\boldsymbol{F}_k\boldsymbol{A}_k^{\eta})^{+}-(\boldsymbol{F}_k\boldsymbol{A}_k^{\eta})^{-}+(\boldsymbol{F}_k\boldsymbol{A}_k^{\zeta})^{+}-(\boldsymbol{F}_k\boldsymbol{A}_k^{\zeta})^{-}=V\boldsymbol{W}. \tag{3.22}$$

In the present study, numerical fluxes in the ζ direction in the above equation are treated as a source term, that is:

$$\frac{V}{\Delta t}\Delta\boldsymbol{Q}+(\boldsymbol{F}_k\boldsymbol{A}_k^{\xi})^{+}-(\boldsymbol{F}_k\boldsymbol{A}_k^{\xi})^{-}+(\boldsymbol{F}_k\boldsymbol{A}_k^{\eta})^{+}-(\boldsymbol{F}_k\boldsymbol{A}_k^{\eta})^{-}+H=V\boldsymbol{W}. \tag{3.23}$$

where $\boldsymbol{H}$ shows the axisymmetric source term vector as

$$\boldsymbol{H}=2\theta S\begin{bmatrix}0\\0\\-p+\tau_{yy}-\tau_{yy}\\(\tau_{yy}-\tau_{yy})\upsilon\\0\\\vdots\\0\end{bmatrix}. \tag{3.24}$$

All the terms of left and right hand sides in Eq. (3.23) are multiplied by angular θ and this angular can be cancelled in this equation.

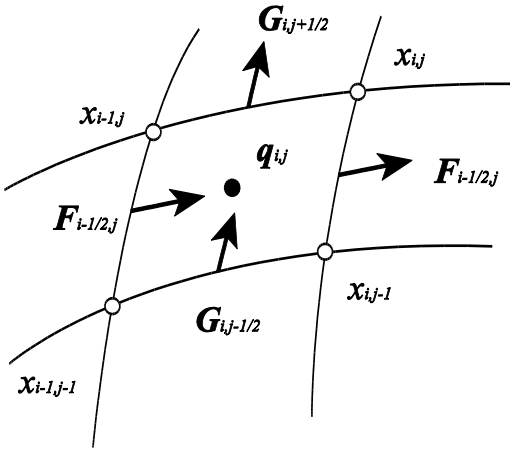

Fig. 3.2 Mesh index system of a cell

Fig. 3.2 shows a schematic view of mesh index system for a cell. Here, (i, j) is defined at the center of the cell. The cell is surrounded by the four-bordering cells, i.e., the nodes of (i, j), (i, j-1), (i-1, j) and (i-1, j-1). The area vectors of the cell in Eqs. (3.15) - (3.18) are given by

$$(\boldsymbol{A}^{\xi})^{+} = (y_{i,j} + y_{i,j-1})[(y_{i,j} - y_{i,j-1}), -(x_{i,j} - x_{i,j-1}), 0]$$

$$= [2\bar{y}(y_{\eta}, -x_{\eta}, 0)]_{i+1/2,j}, \tag{3.25}$$

$$(\boldsymbol{A}^{\xi})^{-} = (y_{i-1,j} + y_{i-1,j-1})[(y_{i-1,j} - y_{i-1,j-1}), -(x_{i-1,j} - x_{i-1,j-1}), 0]$$

$$= [2\bar{y}(y_{\eta}, -x_{\eta}, 0)]_{i-1/2,j}, \tag{3.26}$$

$$(\boldsymbol{A}^{\eta})^{+} = (y_{i,j} + y_{i-1,j})[-(y_{i,j} - y_{i-1,j}), (x_{i,j} - x_{i-1,j}), 0]$$

$$= [2\bar{y}(-y_{\xi}, x_{\xi}, 0)]_{i,j+1/2}, \tag{3.27}$$

$$(\boldsymbol{A}^{\eta})^{-} = (y_{i,j-1} + y_{i-1,j-1})[-(y_{i,j-1} - y_{i-1,j-1}), (x_{i,j-1} - x_{i-1,j-1}), 0]$$

$$= [2\bar{y}(-y_{\xi}, x_{\xi}, 0)]_{i,j-1/2}. \tag{3.28}$$

Where $\bar{y}_{i+1/2,j} = (y_{i,j} + y_{i,j-1})/2$ Substituting Eqs. (3.25) - (3.28) into Eq. (3.23), we can obtain the following system of the linear equations:

$$\frac{V_{i,j}}{\Delta t}\Delta\boldsymbol{Q}_{i,j} + \left[2\bar{y}\left(\boldsymbol{F} - \boldsymbol{F}_{v}\right)\right]_{i+1/2,j} - \left[2\bar{y}\left(\boldsymbol{F} - \boldsymbol{F}_{v}\right)\right]_{i-1/2,j} +$$

$$\left[2\bar{y}\left(\boldsymbol{G} - \boldsymbol{G}_{v}\right)\right]_{i,j+1/2} - \left[2\bar{y}\left(\boldsymbol{G} - \boldsymbol{G}_{v}\right)\right]_{i,j-1/2} + \left(\boldsymbol{H}\right)_{i,j} = \left(V\boldsymbol{W}\right)_{i,j}, \tag{3.29}$$

where

$$\boldsymbol{F} = y_{\eta}\boldsymbol{F} - x_{\eta}\boldsymbol{G}, \quad \boldsymbol{F}_{v} = y_{\eta}\boldsymbol{F}_{v} - x_{\eta}\boldsymbol{G}_{v}, \tag{3.30}$$

$$\boldsymbol{G} = -y_{\xi}\boldsymbol{F} + x_{\xi}\boldsymbol{G}, \quad \boldsymbol{G}_{v} = -y_{\xi}\boldsymbol{F}_{v} + x_{\xi}\boldsymbol{G}_{v}. \tag{3.31}$$

The numerical fluxes of inviscid and viscous terms in the Cartesian coordinates are denoted by $\boldsymbol{F}$, $\boldsymbol{G}$, $\boldsymbol{F}_{\upsilon}$ and $\boldsymbol{G}_{\upsilon}$ respectively. On the other hand, $\widetilde{\boldsymbol{F}}$, $\widetilde{\boldsymbol{G}}$, $\widetilde{\boldsymbol{F}}_{\upsilon}$ and $\widetilde{\boldsymbol{G}}_{\upsilon}$ are the numerical fluxes in the generalized coordinates. These numerical fluxes are evaluated at each interface of the control volume, which are expressed in the vector form as

$$\widetilde{\boldsymbol{F}} = \begin{bmatrix} \rho U \\ \rho u U + y_{\eta} p \\ \rho \upsilon U - x_{\eta} p \\ (E + p)U \\ \rho_1 U \\ \vdots \\ \rho_{ns} U \\ E_{rot} U \\ E_{vib} U \\ E_e U \\ \rho k U \\ \rho \varepsilon U \end{bmatrix}, \quad \widetilde{\boldsymbol{F}}_{\upsilon} = \begin{bmatrix} 0 \\ y_{\eta}(\tau_{xx} + \tau_{t,xx}) - x_{\eta}(\tau_{xy} + \tau_{t,xy}) \\ y_{\eta}(\tau_{yx} + \tau_{t,yx}) - x_{\eta}(\tau_{yy} + \tau_{t,yy}) \\ y_{\eta}\beta_x - x_{\eta}\beta_y \\ -y_{\eta}J_{1,x} + x_{\eta}J_{1,y} \\ \vdots \\ -y_{\eta}J_{ns,x} + x_{\eta}J_{ns,y} \\ -y_{\eta}q_{rot,x} + x_{\eta}q_{rot,y} \\ -y_{\eta}q_{vib,x} + x_{\eta}q_{vib,y} \\ -y_{\eta}q_{e,x} + x_{\eta}q_{e,y} \\ y_{\eta}d_{k,x} - x_{\eta}d_{k,y} \\ y_{\eta}d_{\varepsilon,x} - x_{\eta}d_{\varepsilon,y} \end{bmatrix}, \tag{3.32}$$

$$\tilde{\tilde{\boldsymbol{G}}} = \begin{bmatrix} \rho V \\ \rho u V - y_\xi p \\ \rho \upsilon U + x_\xi p \\ (E+p)V \\ \rho_1 V \\ \vdots \\ \rho_{ns} V \\ E_{rot} V \\ E_{vib} V \\ E_e V \\ \rho k V \\ \rho \varepsilon V \end{bmatrix}, \quad \tilde{\tilde{\boldsymbol{G}}}_\upsilon = \begin{bmatrix} 0 \\ -y_\xi(\tau_{xx}+\tau_{t,xx}) + x_\xi(\tau_{xy}+\tau_{t,xy}) \\ -y_\xi(\tau_{yx}+\tau_{t,yx}) + x_\xi(\tau_{yy}+\tau_{t,yy}) \\ -y_\xi \beta_x + x_\xi \beta_y \\ y_\xi J_{1,x} - x_\xi J_{1,y} \\ \vdots \\ y_\xi J_{ns,x} - x_\xi J_{ns,y} \\ y_\xi q_{rot,x} - x_\xi q_{rot,y} \\ y_\xi q_{vib,x} - x_\xi q_{vib,y} \\ y_\xi q_{e,x} - x_\xi q_{e,y} \\ -y_\xi d_{k,x} + x_\xi d_{k,y} \\ -y_\xi d_{\varepsilon,x} + x_\xi d_{\varepsilon,y} \end{bmatrix}. \tag{3.33}$$

Here, contravariant velocities U and V are respectively defined as

$$U = y_\eta u - x_\eta v, \tag{3.34}$$

$$V = -y_\xi u + x_\xi v. \tag{3.35}$$

The stress tensors are given by

$$\tau_{xx} = \frac{2}{3}\mu\left(2\frac{\partial u}{\partial x} - \frac{\partial v}{\partial y} - \frac{v}{y}\right), \tag{3.36}$$

$$\tau_{yy} = \frac{2}{3}\mu\left(2\frac{\partial v}{\partial y} - \frac{\partial u}{\partial x} - \frac{v}{y}\right), \tag{3.37}$$

$$\tau_{xy} = \tau_{yx} = \mu\left(\frac{\partial u}{\partial y} + \frac{\partial v}{\partial x}\right), \tag{3.38}$$

$$\tau_{yz} = \tau_{zy} = 2\mu\left(\frac{\partial v}{\partial y} - \frac{v}{y}\right). \tag{3.39}$$

The Reynolds stress tensors are expressed as follows:

$$\tau_{t,xx} = \frac{2}{3}\mu_t\left(2\frac{\partial u}{\partial x} - \frac{\partial v}{\partial y} - \frac{v}{y}\right) - \frac{2}{3}\rho k, \tag{3.40}$$

$$\tau_{t,yy} = \frac{2}{3}\mu_t\left(2\frac{\partial v}{\partial y} - \frac{\partial u}{\partial x} - \frac{v}{y}\right) - \frac{2}{3}\rho k, \tag{3.41}$$

$$\tau_{t,xy} = \tau_{t,yx} = \mu_t\left(\frac{\partial u}{\partial y} + \frac{\partial v}{\partial x}\right), \tag{3.42}$$

$$\tau_{t,yz} = \tau_{t,zy} = 2\mu_t\left(\frac{\partial v}{\partial y} - \frac{v}{y}\right). \tag{3.43}$$

The contributions β_x and β_y of the stress tensors are expressed by

$$\beta_x = u\left(\tau_{xx}+\tau_{t,xx}\right)+v\left(\tau_{xy}+\tau_{t,xy}\right)+\lambda_{tr}\frac{\partial T_{tr}}{\partial x}+\lambda_{rot}\frac{\partial T_{rot}}{\partial x}+\lambda_{vib}\frac{\partial T_{vib}}{\partial x}+$$
$$\lambda_e\frac{\partial T_e}{\partial x}+\lambda_t\frac{\partial T_{tr}}{\partial x}+\rho\sum_{s=1}^{ns}h_s D_s\frac{\partial X_s}{\partial x}, \tag{3.44}$$

$$\beta_y = u\left(\tau_{yx}+\tau_{t,yx}\right)+v\left(\tau_{yy}+\tau_{t,yy}\right)+\lambda_{tr}\frac{\partial T_{tr}}{\partial y}+\lambda_{rot}\frac{\partial T_{rot}}{\partial y}+\lambda_{vib}\frac{\partial T_{vib}}{\partial y}+$$
$$\lambda_e\frac{\partial T_e}{\partial y}+\lambda_t\frac{\partial T_{tr}}{\partial y}+\rho\sum_{s=1}^{ns}h_s D_s\frac{\partial X_s}{\partial y}. \tag{3.45}$$

The diffusion fluxes are expressed by

$$J_{s,x} = -\rho D_s\frac{\partial X_s}{\partial x}, \tag{3.46}$$

$$J_{s,y} = -\rho D_s\frac{\partial X_s}{\partial y}. \tag{3.47}$$

The heat fluxes are evaluated by

$$q_{rot,x} = -\lambda_{rot}\frac{\partial T_{rot}}{\partial x}-\rho\sum_{s=M}^{nm}e_{rot,s}D_s\frac{\partial X_s}{\partial x}, \tag{3.48}$$

$$q_{rot,y} = -\lambda_{rot}\frac{\partial T_{rot}}{\partial y}-\rho\sum_{s=M}^{nm}e_{rot,s}D_s\frac{\partial X_s}{\partial y}, \tag{3.49}$$

$$q_{vib,x} = -\lambda_{vib}\frac{\partial T_{vib}}{\partial x}-\rho\sum_{s=M}^{nm}e_{vib,s}D_s\frac{\partial X_s}{\partial x}, \tag{3.50}$$

$$q_{vib,y} = -\lambda_{vib}\frac{\partial T_{vib}}{\partial y}-\rho\sum_{s=M}^{nm}e_{vib,s}D_s\frac{\partial X_s}{\partial y}, \tag{3.51}$$

$$q_{e,x} = -\lambda_e\frac{\partial T_e}{\partial x}-\rho h_e D_e\frac{\partial X_e}{\partial x}, \tag{3.52}$$

$$q_{e,y} = -\lambda_e\frac{\partial T_e}{\partial y}-\rho h_e D_e\frac{\partial X_e}{\partial y}, \tag{3.53}$$

Finally,

$$d_{k,x} = \left(\mu+\frac{\mu_t}{\sigma_{t,k}}\right)\frac{\partial k}{\partial x}, \tag{3.54}$$

$$d_{k,y} = \left(\mu+\frac{\mu_t}{\sigma_{t,k}}\right)\frac{\partial k}{\partial y}, \tag{3.55}$$

$$d_{\varepsilon,x} = \left(\mu+\frac{\mu_t}{\sigma_{t,\varepsilon}}\right)\frac{\partial \varepsilon}{\partial x}, \tag{3.56}$$

$$d_{\varepsilon,y} = \left(\mu + \frac{\mu_{\mathrm{t}}}{\sigma_{\mathrm{t},\varepsilon}} \right) \frac{\partial \varepsilon}{\partial y}. \tag{3.57}$$

Components of the source term vector are shown as

$$\tilde{\boldsymbol{W}} = \begin{bmatrix} 0 \\ 0 \\ 0 \\ S_{\mathrm{joule}} \\ \dot{\omega}_1 \\ \vdots \\ \dot{\omega}_{ns} \\ S_{\mathrm{int},rot} \\ S_{\mathrm{int},vib} \\ S_{\mathrm{joule}} + S_{\mathrm{int},e} \\ \tau_{t,ij} \dfrac{\partial u_j}{\partial x_j} - \rho\varepsilon \\ C_1 f_1 \tau_{t,ij} \dfrac{\partial u_j}{\partial x_j} \dfrac{\varepsilon}{k} - C_2 f_2 \rho \dfrac{\varepsilon^2}{k} \end{bmatrix}, \tag{3.58}$$

In the computational domain, the metrics are evaluated as follows:

$$(x_\xi)_{i,j+1/2} = x_{i,j} - x_{i-1,j}, \tag{3.59}$$

$$(y_\xi)_{i,j+1/2} = y_{i,j} - y_{i-1,j}, \tag{3.60}$$

$$(x_\eta)_{i+1/2,j} = x_{i,j} - x_{i,j-1}, \tag{3.61}$$

$$(y_\eta)_{i+1/2,j} = y_{i,j} - y_{i,j-1}. \tag{3.62}$$

3.2 Inviscid Flux

For solving above N-S equations, Evaluation of inviscid numerical fluxes at the cell interfaces of the conservative law results in solving the Riemann problem. Most rigorous approach to solve the Riemann problem is known as Godunov scheme [87]. However, what we need is only evaluation of the numerical flux across the cell interface. Until now, some approximate Riemann solvers have been proposed.

3.2.1 SLAU Scheme

In the 1990s, low-diffusion flux splitting schemes have been proposed. In Ref. [88], Liou and Steffen developed a low-dissipative scheme called Advective Upwind Splitting Method (AUSM). The AUSM scheme is robust enough in calculating strong shock waves and can capture the discontinuity surface without excessive numerical

dissipation, while a slight overshoot can appear behind the shock wave. Up to now, many modified AUSM schemes have been approached.

In the present study, we focus on SLAU [89] (Simple Low-Dissipation Advection Upwind splitting) method, which is a new, parameter-free simple compressible numerical flux function of the AUSM family method. We briefly review the SLAU scheme in this section. Firstly, the numerical flux of the AUSM-family scheme including SLAU at the cell interface is given as [90]

$$\widetilde{\boldsymbol{F}} = \frac{\dot{m}+|\dot{m}|}{2}\boldsymbol{\Psi}_{\boldsymbol{L}} + \frac{\dot{m}+|\dot{m}|}{2}\boldsymbol{\Psi}_{R} + \tilde{p}\boldsymbol{N}\ , \tag{3.63}$$

where

$$\boldsymbol{\Psi} = \begin{bmatrix} 1 \\ u \\ \upsilon \\ h \\ f \\ \vdots \\ f_{ns} \\ E_{rot}/\rho \\ E_{vib}/\rho \\ E_{e}/\rho \end{bmatrix}, \boldsymbol{N} = \begin{bmatrix} 0 \\ x_n \\ y_n \\ 0 \\ 0 \\ \vdots \\ 0 \\ 0 \\ 0 \\ 0 \end{bmatrix}, \tag{3.64}$$

$$h = (E+p)/\rho\ ,\ f_s = \rho_s/\rho\ . \tag{3.65}$$

About (x_n, y_n), when evaluate the numerical flux $\widetilde{\boldsymbol{F}}$:

$$(x_n, y_n) = (y_\eta/\sqrt{x_\eta^2+y_\eta^2}, -x_\eta/\sqrt{x_\eta^2+y_\eta^2})\ . \tag{3.66}$$

when evaluate $\widetilde{\boldsymbol{G}}$:

$$(x_n, y_n) = (y_\eta/\sqrt{x_\eta^2+y_\eta^2}, -x_\eta/\sqrt{x_\eta^2+y_\eta^2})\ . \tag{3.67}$$

The mass flux function of SLAU is given as

$$\dot{m} = \frac{1}{2}\{(\rho V_n)_L + (\rho V_n)_R - |\overline{V}_n|\Delta\rho(1-g) - \frac{\chi}{2\overline{c}}\Delta p\ , \tag{3.68}$$

where $V_n = x_n u + y_n \upsilon$ is the velocity normal to the cell interface. $\Delta q = q_R - q_L$, here q indicates p, ρ, etc. In addition,

$$\chi = (1-\hat{M})^2\ , \tag{3.69}$$

$$\hat{M} = \min\left(1.0, \frac{1}{\overline{c}}\sqrt{\frac{u_L^2+\upsilon_L^2+u_R^2+\upsilon_R^2}{2}}\right), \tag{3.70}$$

$$\left|\overline{V_n}\right| = \frac{\rho_L \left|V_n\right|_L + \rho_R \left|V_n\right|_R}{\rho_L + \rho_R}, \tag{3.71}$$

$$g = -\max[\min(M_L, 0), -1] \cdot \min[\max(M_R, 0), 1]$$

$$M_{L/R} = \frac{(V_n)_{L/R}}{\bar{c}} = \frac{u_{L/R} x_n + \upsilon_{L/R} y_n}{\bar{c}}, \tag{3.72}$$

$$\bar{c} = (c_L + c_R)/2. \tag{3.73}$$

Finally, the pressure function is given by

$$\tilde{p} = \frac{p_L + p_R}{2} + \frac{\beta_+ + \beta_-}{2}(p_L - p_R) + (1-\chi)(\beta_+ + \beta_- - 1)\frac{p_L + p_R}{2}, \tag{3.74}$$

$$\beta_\pm = \begin{cases} \dfrac{1}{4}(2 \mp M_{L/R})(M_{L/R} \pm 1)^2, & \text{for } \left|M_{L/R}\right| < 1 \\ \dfrac{1}{2}[1 + \mathrm{sgn}(M_{L/R})], & \text{otherwise} \end{cases}. \tag{3.75}$$

3.2.2 MUSCL Approach

In order to prevent the generation of oscillations and spurious solutions in the region of high gradients, it is necessary to use flux limiter functions to achieve second – or higher-order upwind spatial discretisations. In the present study, this is achieved by the Monotonic Upstream-centered Scheme for Conservation Laws (MUSCL), which is proposed by van Leer [91, 92]. In the presently-used MUSCL, the physical properties at the cell interface are determined by linearly interpolating properties in neighbour cells. Thus, accuracy of the numerical fluxes is basically kept to the second order. In order to keep the monotonicity and prevent the numerical oscillations, "minmod limiter" which is a one of the flux limiter is introduced. In the present calculation, the physical properties at the call interface are expressed as follows:

$$q^-_{i+1/2} = q_i + \frac{l_i}{2}\,\mathrm{minmod}\left(\Delta^-_i, \Delta^+_i\right), \tag{3.76}$$

$$q^+_{j+1/2} = q_{j+1} - \frac{l_{j+1}}{2}\,\mathrm{minmod}\left(\Delta^+_{j+1}, \Delta^-_{j+1}\right), \tag{3.77}$$

$$\mathrm{minmod}\,(a, b) = \mathrm{sgn}(a) \cdot \max[0, \min\{0, \mathrm{sgn}(b), b \cdot \mathrm{sgn}(a)\}]. \tag{3.78}$$

$$\Delta^+_i = \frac{2(q_{i+1} - q_i)}{(l_i + l_{i+1})}, \tag{3.79}$$

$$\Delta^-_j = \frac{2(q_j - q_{j-1})}{(l_{j-1} + l_j)}, \tag{3.80}$$

where

$$l_i = \frac{1}{2}\left[\left(\sqrt{x_\xi^2 + y_\xi^2}\right)_{i,j+1/2} + \left(\sqrt{x_\xi^2 + y_\xi^2}\right)_{i,j-1/2}\right], \tag{3.81}$$

$$l_j = \frac{1}{2}\left[\left(\sqrt{x_\eta^2 + y_\eta^2}\right)_{i+1/2,j} + \left(\sqrt{x_\eta^2 + y_\eta^2}\right)_{i-1/2,j}\right]. \tag{3.82}$$

3.3 Viscous Flux

All viscous terms are calculated by the second-order central difference method. In this calculation, differential procedure is implemented as follows:

$$u_x = \xi_x u_\xi + \eta_x u_\eta = J \cdot \left(y_\eta u_\xi - y_\xi u_\eta\right), \tag{3.83}$$

$$u_y = \xi_y u_\xi + \eta_y u_\eta = J \cdot \left(-x_\eta u_\xi + x_\xi u_\eta\right). \tag{3.84}$$

The stress tensors are expressed by

$$\tau_{xx} = J \cdot \frac{2}{3}\mu\left[2\left(y_\eta u_\xi - y_\xi u_\eta\right) - \left(-x_\eta v_\xi + x_\xi v_\eta\right) - v/\left(y \cdot J\right)\right], \tag{3.85}$$

$$\tau_{yy} = J\,\frac{2}{3}\mu\left[2\left(y_\eta v_\xi - y_\xi v_\eta\right) - \left(-x_\eta u_\xi + x_\xi u_\eta\right) - v/\left(y \cdot J\right)\right], \tag{3.86}$$

$$\tau_{xy} = J\,\mu\left[-x_\eta u_\xi + x_\xi u_\eta + y_\eta v_\xi - y_\xi v_\eta\right]. \tag{3.87}$$

Then, the Reynolds stress tensors are calculated as follows:

$$\tau_{\mathrm{t},xx} = J\,\frac{2}{3}\mu_\mathrm{t}\left[2\left(y_\eta u_\xi - y_\xi u_\eta\right) - \left(-x_\eta v_\xi + x_\xi v_\eta\right) - v/\left(y \cdot J\right)\right] - \frac{2}{3}\rho k, \tag{3.88}$$

$$\tau_{\mathrm{t},yy} = J\,\frac{2}{3}\mu_\mathrm{t}\left[2\left(y_\eta v_\xi - y_\xi v_\eta\right) - \left(-x_\eta u_\xi + x_\xi u_\eta\right) - v/\left(y \cdot J\right)\right] - \frac{2}{3}\rho k, \tag{3.89}$$

$$\tau_{\mathrm{t},xy} = J\,\mu_\mathrm{t}\left[-x_\eta u_\xi + x_\xi u_\eta + y_\eta v_\xi - y_\xi v_\eta\right]. \tag{3.90}$$

Substituting Eqs. (3.85) - (3.90) into Eqs. (3.32) and (3.33), one obtains

$$\left[y_\eta\left(\tau_{xx} + \tau_{\mathrm{t},xx}\right) - x_\eta\left(\tau_{xy} + \tau_{\mathrm{t},xy}\right)\right]_{i+1/2,j} = \left\{J\left(\mu + \mu_\mathrm{t}\right)\left[\left(\gamma + \frac{y_\eta^2}{3}\right)u_\xi\right.\right.$$

$$\left.\left. - \left(\beta + \frac{y_\xi y_\eta}{3}\right)u_\eta - \frac{x_\eta y_\eta}{3}v_\xi - \left(\varepsilon - \frac{x_\xi y_\eta}{3}\right)v_\eta - \frac{2}{3}\frac{y_\eta v}{yJ}\right] - \frac{2}{3}y_\eta \rho k\right\}_{i+1/2,j}, \tag{3.91}$$

$$\left[-y_\xi\left(\tau_{xx} + \tau_{\mathrm{t},xx}\right) - x_\xi\left(\tau_{xy} + \tau_{\mathrm{t},xy}\right)\right]_{i,j+1/2} = \left\{J\left(\mu + \mu_\mathrm{t}\right)\left[-\left(\beta + \frac{y_\xi y_\eta}{3}\right)u_\xi\right.\right.$$

$$\left.\left. + \left(\alpha + \frac{y_\xi^2}{3}\right)u_\eta + \left(\varepsilon + \frac{x_\xi y_\eta}{3}\right)v_\xi - \frac{x_\xi y_\xi}{3}v_\eta + \frac{2}{3}\frac{y_\xi v}{yJ}\right] + \frac{2}{3}y_\xi \rho k\right\}_{i,j+1/2}. \tag{3.92}$$

and

$$\left[y_\eta \left(\tau_{yx} + \tau_{\mathrm{t},yx} \right) - x_\eta \left(\tau_{yy} + \tau_{\mathrm{t},yy} \right) \right]_{i+1/2,\,j} = \left\{ J \left(\mu + \mu_{\mathrm{t}} \right) \left[-\frac{x_\eta y_\eta}{3} u_\xi \right. \right.$$

$$\left. \left. + \left(\varepsilon + \frac{x_\eta y_\xi}{3} \right) u_\eta + \left(\gamma + \frac{x_\eta^2}{3} \right) v_\xi - \left(\beta + \frac{x_\xi x_\eta}{3} \right) v_\eta + \frac{2}{3} \frac{x_\eta v}{yJ} \right] + \frac{2}{3} x_\eta \rho k \right\}_{i+1/2,\,j}, \qquad (3.93)$$

$$\left[-y_\xi \left(\tau_{yx} + \tau_{\mathrm{t},yx} \right) + x_\xi \left(\tau_{yy} + \tau_{\mathrm{t},yy} \right) \right]_{i,\,j+1/2} = \left\{ J \left(\mu + \mu_{\mathrm{t}} \right) \left[-\left(\varepsilon - \frac{x_\xi y_\eta}{3} \right) u_\xi \right. \right.$$

$$\left. \left. - \frac{x_\xi y_\xi}{3} u_\eta - \left(\beta + \frac{x_\xi x_\eta}{3} \right) v_\xi + \left(\alpha + \frac{x_\xi^2}{3} \right) v_\eta - \frac{2}{3} \frac{x_\xi v}{yJ} \right] - \frac{2}{3} x_\xi \rho k \right\}_{i,\,j+1/2}, \qquad (3.94)$$

where

$$\alpha = x_\xi^2 + y_\xi^2, \qquad (3.95)$$

$$\beta = x_\xi x_\eta + y_\xi y_\eta, \qquad (3.96)$$

$$\gamma = x_\eta^2 + y_\eta^2, \qquad (3.97)$$

$$\varepsilon = x_\xi y_\eta - x_\eta y_\xi. \qquad (3.98)$$

Then, diffusion fluxes and heat fluxes are given by

$$J_{s,x} = -\rho D_s \frac{\partial X_s}{\partial x} = -J \rho D_s [y_\eta X_{s,\xi} - y_\xi X_{s,\eta}], \qquad (3.99)$$

$$J_{s,y} = -\rho D_s \frac{\partial X_s}{\partial y} = -J \rho D_s [-x_\eta X_{s,\xi} + x_\xi X_{s,\eta}], \qquad (3.100)$$

$$q_{e,x} = -\lambda_e \frac{\partial T_e}{\partial x} = -J \lambda_e [y_\eta T_{e,\xi} - y_\xi T_{e,\eta}], \qquad (3.101)$$

$$q_{e,y} = -\lambda_e \frac{\partial T_e}{\partial y} = -J \lambda_e [-x_\eta T_{e,\xi} + x_\xi T_{e,\eta}]. \qquad (3.102)$$

Hence,

$$(-y_\eta J_{s,x} + x_\eta J_{s,y})_{i+1/2,\,j} = (J \rho D_s)_{i+1/2,\,j} [\gamma X_{s,\xi} - \beta X_{s,\eta}]_{i+1/2,\,j}, \qquad (3.103)$$

$$(y_\xi J_{s,x} - x_\xi J_{s,y})_{i,\,j+1/2} = (J \rho D_s)_{i,\,j+1/2} [-\beta X_{s,\xi} + \alpha X_{s,\eta}]_{i,\,j+1/2}, \qquad (3.104)$$

$$(y_\eta q_{e,x} - x_\eta q_{e,y})_{i+1/2,\,j} = -(J \lambda_e)_{i+1/2,\,j} [\gamma T_{e,\xi} - \beta T_{e,\eta}]_{i+1/2,\,j}, \qquad (3.105)$$

$$(-y_\xi q_{e,x} + x_\xi q_e, y)_{i,\,j+1/2} = -(J \lambda_e)_{i,\,j+1/2} [-\beta X T_{e,\xi} + \alpha T_{e,\eta}]_{i,\,j+1/2}. \qquad (3.106)$$

The rotational and vibrational heat fluxes are evaluated in the same fashion. Similarly, the energy fluxes in the total energy equation are given by

$$(y_\eta \beta_x - x_\eta \beta_y)_{i+1/2,j} = \left\{ u\left[y_\eta \left(\tau_{xx} + \tau_{\mathrm{t},xx} \right) - x_\eta \left(\tau_{xy} + \tau_{,\mathrm{t},xy} \right) \right] \right\}_{i+1/2,j}$$

$$+ \left\{ v\left[y_\eta \left(\tau_{yx} + \tau_{\mathrm{t},yx} \right) - x_\eta \left(\tau_{yy} + \tau_{\mathrm{t},yy} \right) \right] \right\}_{i+1/2,j}$$

$$+ (J\lambda_{tr})_{i+1/2,j} [\gamma T_{tr} - \beta T_{tr}]_{i+1/2,j} + (J\lambda_{rot})_{i+1/2,j} [\gamma T_{rot} - \beta T_{rot}]_{i+1/2,j}$$

$$+ (J\lambda_{vib})_{i+1/2,j} [\gamma T_{vib} - \beta T_{vib}]_{i+1/2,j} + (J\lambda_e)_{i+1/2,j} [\gamma T_e - \beta T_e]_{i+1/2,j}$$

$$+ (J\lambda_{\mathrm{t}})_{i+1/2,j} [\gamma T_{tr} - \beta T_{tr}]_{i+1/2,j} + \sum_{s=1}^{ns} (J\rho D_s)_{i+1/2,j} [\gamma X_{s,\xi} - \beta X_{s,\eta}]_{i+1/2,j}, \quad (3.107)$$

$$(-y_\xi \beta_x + x_\xi \beta_y)_{i,j+1/2} = \left\{ u\left[-y_\xi \left(\tau_{xx} + \tau_{\mathrm{t},xx} \right) + x_\xi \left(\tau_{xy} + \tau_{\mathrm{t},xy} \right) \right] \right\}_{i,j+1/2}$$

$$+ \left\{ v\left[-y_\xi \left(\tau_{yx} + \tau_{\mathrm{t},yx} \right) + x_\xi \left(\tau_{yy} + \tau_{\mathrm{t},yy} \right) \right] \right\}_{i,j+1/2}$$

$$+ (J\lambda_{tr})_{i,j+1/2} [-\beta T_{tr} + \alpha T_{tr}]_{i,j+1/2} + (J\lambda_{rot})_{i,j+1/2} [-\beta T_{rot} + \alpha T_{rot}]_{i,j+1/2}$$

$$+ (J\lambda_{vib})_{i,j+1/2} [-\beta T_{vib} + \alpha T_{vib}]_{i,j+1/2} + (J\lambda_e)_{i,j+1/2} [-\beta T_e + \alpha T_e]_{i,j+1/2}$$

$$+ (J\lambda_{\mathrm{t}})_{i,j+1/2} [-\beta T_{tr} + \alpha T_{tr}]_{i,j+1/2} + \sum_{s=1}^{ns} (J\rho D_s)_{i,j+1/2} [-\beta X_{s,\xi} + \alpha X_{s,\eta}]_{i,j+1/2}. \quad (3.108)$$

In the present calculation, the derivatives for the computational domain are defined by

$$(u_\xi)_{i+1/2,j} = u_{i+1,j} - u_{i,j}, \quad (3.109)$$

$$(u_\eta)_{i+1/2,j} = \frac{1}{4}\left(u_{i,j+1} - u_{i,j-1} + u_{i+1,j+1} - u_{i+1,j-1} \right), \quad (3.110)$$

$$(u_\xi)_{i,j+1/2} = \frac{1}{4}\left(u_{i+1,j} - u_{i-1,j} + u_{i+1,j+1} - u_{i-1,j+1} \right), \quad (3.111)$$

$$(u_\eta)_{i,j+1/2} = u_{i,j+1} - u_{i,j}. \quad (3.112)$$

The average variables at the cell interface are simply evaluated as follows:

$$\mu_{i+1/2,j} = \frac{\mu_i + \mu_{i+1}}{2}, \quad (3.113)$$

$$\mu_{i,j+1/2} = \frac{\mu_j + \mu_{j+1}}{2}, \quad (3.114)$$

$$(D_s)_{i+1/2,j} = \frac{(D_s)_i + (D_s)_{i+1}}{2}, \quad (3.115)$$

$$(D_s)_{i,j+1/2} = \frac{(D_s)_j + (D_s)_{j+1}}{2}. \quad (3.116)$$

On the other hand, the heat conductivity at the cell interface is calculated by the following harmonic average:

$$\frac{1}{\lambda_{i+1/2,j}} = \frac{1}{2}\left(\frac{1}{\lambda_{i,j}} + \frac{1}{\lambda_{i+1,j}}\right), \tag{3.117}$$

$$\frac{1}{\lambda_{i,j+1/2}} = \frac{1}{2}\left(\frac{1}{\lambda_{i,j}} + \frac{1}{\lambda_{i,j+1}}\right). \tag{3.118}$$

The average Jacobian between two cells is evaluated as

$$\frac{1}{J_{i+1/2,j}} = \frac{1}{2}\left(\frac{1}{J_{i,j}} + \frac{1}{J_{i+1,j}}\right), \tag{3.119}$$

$$\frac{1}{J_{i,j+1/2}} = \frac{1}{2}\left(\frac{1}{J_{i,j}} + \frac{1}{J_{i,j+1}}\right). \tag{3.120}$$

3.4 Time Integration

In this section, integration procedure in time direction is described. As is known, compared with the explicit time integration, the implicit scheme has the advantage that the numerical computation can unconditionally converge. The numerical instability can be avoid by using it. Therefore, in this study we adopt the implicit scheme for time integration procedure.

In the equation system, because of the considerably smaller values of electronic mass and energy compared with those of the other species, numerical stiffness tended to arise when solving the electron-energy equation. To avoid this stiffness, we uncoupled the electron-energy equation from the other flow-field equations and then solved the electron temperature instead of the electron energy.

On the other hand, the coupling between flow field and turbulence transport equations is relatively weak [93]. Though solving all equations simultaneously tends to result in rapid convergence, the turbulence transport equations are also separated from the flow-field equation solver to be implemented simply. The electron energy equation (E_e) and the turbulence transport equations (ρk, $\rho\varepsilon$) solvers are separately denoted later.

3.4.1 Implicit Scheme

We rewrite the Navier-Stokes equation system Eq. (3.29) except for the electron energy and the turbulence transport equations as

$$\frac{V_{i,j}}{\Delta t}\Delta \boldsymbol{Q}_{i,j}^{n} = \boldsymbol{R}_{i,j}^{n+1}, \tag{3.121}$$

where $\Delta \boldsymbol{Q}_{i,j}^{n} = \boldsymbol{Q}_{i,j}^{n+1} - \boldsymbol{Q}_{i,j}^{n}$ and the vector of the residuals $\boldsymbol{R}_{i,j}$ is given by

$$\begin{aligned}\boldsymbol{R}_{i,j} = &-\left[2\bar{y}\left(\tilde{\boldsymbol{F}} - \tilde{\boldsymbol{F}}_v\right)\right]_{i+1/2,j} + \left[2\bar{y}\left(\tilde{\boldsymbol{F}} - \tilde{\boldsymbol{F}}_v\right)\right]_{i-1/2,j} \\ &-\left[2\bar{y}\left(\tilde{\boldsymbol{G}} - \tilde{\boldsymbol{G}}_v\right)\right]_{i,j+1/2} + \left[2\bar{y}\left(\tilde{\boldsymbol{G}} - \tilde{\boldsymbol{G}}_v\right)\right]_{i,j-1/2} - \left(\boldsymbol{H}\right)_{i,j} + \left(V\boldsymbol{W}\right)_{i,j},\end{aligned} \tag{3.122}$$

The residuals vector is evaluated in time direction by:

$$\boldsymbol{R}_{i,j}^{n+1} \approx \boldsymbol{R}_{i,j}^{n} + \Delta t \left(\frac{\partial \boldsymbol{R}_{i,j}}{\partial t} \right)^{n}$$

$$= \boldsymbol{R}_{i,j}^{n} + \Delta t \left(\frac{\partial \boldsymbol{R}_{i,j}}{\partial \boldsymbol{Q}} \right)^{n} \left(\frac{\partial \boldsymbol{Q}_{i,j}}{\partial t} \right)^{n}$$

$$= \boldsymbol{R}_{i,j}^{n} + \left(\frac{\partial \boldsymbol{R}_{i,j}}{\partial \boldsymbol{Q}} \right)^{n} \Delta \boldsymbol{Q}_{i,j}^{n} . \tag{3.123}$$

where the term ($\partial \boldsymbol{R}_{i,j} / \partial \boldsymbol{Q}$) is the Jacobian matrix.

Substituting Eq. (3.123) into Eq. (3.121), the following expression yields

$$\left[\frac{V_{i,j}}{\Delta t} - \left(\frac{\partial \boldsymbol{R}_{i,j}}{\partial \boldsymbol{Q}} \right)^{n} \right] \Delta \boldsymbol{Q}^{n} = \boldsymbol{R}_{i,j}^{n} , \tag{3.124}$$

$$\left[\boldsymbol{I} - \frac{\Delta t}{V_{i,j}} \left(\frac{\partial \boldsymbol{R}_{i,j}}{\partial \boldsymbol{Q}} \right)^{n} \right] \Delta \boldsymbol{Q}^{n} = \frac{\Delta t}{V_{i,j}} \boldsymbol{R}_{i,j}^{n} . \tag{3.125}$$

Here, the most accurate method to get the solution $\Delta \boldsymbol{Q}$ is to inverse the left-hand-side matrix of Eq. (3.125) directly. However, since the direct inversion of the matrix requires enormous computation cost and complicated. Therefore it seems very difficult to solve Eq. (3.125) without any modification. On the other hand, because we are only interested in steady-state solutions, it is reasonable to use iterative methods to find approximate solutions for $\Delta \boldsymbol{Q}$ though a time-marching method. In this study, the point implicit method and the lower-upper symmetric Gauss-Seidel method are employed to solve the Eq. (3.125).

3.4.2 Point Implicit Method

As for a simulation of chemical nonequilibrium plasma flow, the computation tends to be stiff due to great difference of characteristic times between flow field τ_f and chemical reaction τ_c. The time scale of the chemical reaction is drastically smaller than that of the flow field. In addition, since the left-hand-side of Eq. (3.125) is roughly evaluated, e.g., LU-decomposition and approximate factorization, numerical error with the matrix inversion causes computation to be unstable. Thus, if the time step Δt is close to the time scale of flow field, it is difficult to treat the chemical reaction accurately. On the other hand, if set $\Delta t \approx \tau_c$, we have to spend enormous computational cost on the flow-field calculation. To overcome the stiffness, the point implicit method which is developed by Bussing and Murman [94] is used in this study. The source term of the chemical species is separated from others and the coefficient matrix is approximately factorized as

$$\boldsymbol{I} - \frac{\Delta t}{V_{i,j}} \left(\frac{\partial \boldsymbol{R}_{i,j}}{\partial \boldsymbol{Q}} \right)^{n} = \boldsymbol{I} - \frac{\Delta t}{V_{i,j}} \left[\cdot \frac{\partial (\boldsymbol{R}_{i,j} - V_{i,j} \boldsymbol{W}_{i,j})}{\partial \boldsymbol{Q}} + \frac{\partial (V_{i,j} \boldsymbol{W}_{i,j})}{\partial \boldsymbol{Q}} \right]$$

$$\approx \left(\boldsymbol{I} - \Delta t \boldsymbol{H}_{i,j} \right) \left[\boldsymbol{I} - \frac{\Delta t}{V_{i,j}} \frac{\partial (\boldsymbol{R}_{i,j} - V_{i,j} \boldsymbol{W}_{i,j})}{\partial \boldsymbol{Q}} \right]. \tag{3.126}$$

where $\boldsymbol{H}_{i,j} = \dfrac{\partial (V_{i,j} \boldsymbol{W}_{i,j})}{\partial \boldsymbol{Q}}$. The Jacobian matrix $\widehat{\boldsymbol{H}} = \partial \boldsymbol{W} / \partial \boldsymbol{Q}$ of the chemical source term is directly inversed. The variable *V* denotes the volume of a control volume.

3.4.3 LU-SGS Method

Lower-Upper Symmetric Gauss-Seidel (LU-SGS) method which was developed by Jameson and Yoon [95] is widely used because of its low numerical complexity and modest memory requirements. It can be implemented easily on parallel computers for structured or unstructured grid system. In the present study, in order to achieve rapid convergence and stable calculation, the LUSGS scheme is used to solve the flow-field equations. The LU-SGS procedure with the point implicit method aforementioned is described in this section. Primarily, we rewrite Eq. (3.125) in detail as follows:

$$\left(I - \Delta t \boldsymbol{H}_{i,j} \right) \left\{ \boldsymbol{I} + \frac{\Delta t}{V_{i,j}} \left(\left[2\bar{y} \left(\tilde{\boldsymbol{A}} - \tilde{\boldsymbol{A}}_v \right) \right]^n_{i+1/2,j} - \left[2\bar{y} \left(\tilde{\boldsymbol{A}} - \tilde{\boldsymbol{A}}_v \right) \right]^n_{i-1/2,j} \right. \right.$$

$$\left. \left. + \left[2\bar{y} \left(\tilde{\boldsymbol{B}} - \tilde{\boldsymbol{B}}_v \right) \right]^n_{i,j+1/2} - \left[2\bar{y} \left(\tilde{\boldsymbol{B}} - \tilde{\boldsymbol{B}}_v \right) \right]^n_{i,j-1/2} \right) \right] \Delta \boldsymbol{Q}^n = \frac{\Delta t}{V_{i,j}} \boldsymbol{R}^n_{i,j}, \tag{3.127}$$

where $\tilde{\boldsymbol{A}}$, $\tilde{\boldsymbol{B}}$, $\tilde{\boldsymbol{A}}_v$, and $\tilde{\boldsymbol{B}}_v$ denote the Jacobian matrices of the inviscid and viscous fluxes, i.e., $\tilde{\boldsymbol{F}}$, $\tilde{\boldsymbol{G}}$, $\tilde{\boldsymbol{F}}_v$, and $\tilde{\boldsymbol{G}}_v$ that is:

$$\tilde{\boldsymbol{A}} = \frac{\partial \tilde{\boldsymbol{F}}}{\partial \boldsymbol{Q}} = y_\eta \boldsymbol{A} - x_\eta \boldsymbol{B}, \tag{3.128}$$

$$\tilde{\boldsymbol{A}}_v = \frac{\partial \tilde{\boldsymbol{F}}_v}{\partial \boldsymbol{Q}} = y_\eta \boldsymbol{A}_v - x_\eta \boldsymbol{B}_v, \tag{3.129}$$

$$\tilde{\boldsymbol{B}} = \frac{\partial \tilde{\boldsymbol{G}}}{\partial \boldsymbol{Q}} = -y_\xi \boldsymbol{A} + x_\xi \boldsymbol{B}, \tag{3.130}$$

$$\tilde{\boldsymbol{B}}_v = \frac{\partial \tilde{\boldsymbol{G}}_v}{\partial \boldsymbol{Q}} = -y_\xi \boldsymbol{A}_v + x_\xi \boldsymbol{B}_v \, . \tag{3.131}$$

The numerical fluxes at the cell interface (i+1/2 and j+1/2, etc.) are roughly evaluated with the first-order upwind difference manner:

$$(\boldsymbol{A})_{i+1/2,j} = (\boldsymbol{A})^+_{i,j} + (\boldsymbol{A})^-_{i+1,j}, \tag{3.132}$$

$$(\boldsymbol{A})_{i-1/2,j} = (\boldsymbol{A})^-_{i,j} + (\boldsymbol{A})^+_{i-1,j}, \tag{3.133}$$

$$(\boldsymbol{B})_{i,j+1/2} = (\boldsymbol{B})^+_{i,j} + (\boldsymbol{B})^-_{i,j+1}, \tag{3.134}$$

$$(\boldsymbol{B})_{i,j-1/2} = (\boldsymbol{B})^-_{i,j} + (\boldsymbol{B})^+_{i,j-1}. \tag{3.135}$$

Then, the fluxes $\boldsymbol{A}^\pm, \boldsymbol{B}^\pm$ are approximately calculated with the spectral radius by

$$\boldsymbol{A}^{\pm} = \frac{1}{2}[\boldsymbol{A} \pm \beta\sigma(\boldsymbol{A})\boldsymbol{I}], \tag{3.136}$$

$$\boldsymbol{B}^{\pm} = \frac{1}{2}[\boldsymbol{B} \pm \beta\sigma(\boldsymbol{B})\boldsymbol{I}], \tag{3.137}$$

$$\sigma(\boldsymbol{X}) = \max[|\lambda_i|], \tag{3.138}$$

where λ denotes the eigenvalue of the matrix $\boldsymbol{A}$ or $\boldsymbol{B}$ and β is a constant. Since the scheme is unconditionally stable if β is larger than unity, it is set to be β =1.1 in the present calculations. On the other hand, the Jacobian matrices of viscous fluxes are evaluated as follows:

$$\boldsymbol{A}_v \approx \frac{\partial}{\partial x^j}\left(\frac{\partial \boldsymbol{F}_v}{\partial \boldsymbol{Q}_{x^j}}\right) \approx \frac{\partial \boldsymbol{P}}{\partial x}, \tag{3.139}$$

$$\boldsymbol{B}_v \approx \frac{\partial}{\partial x^j}\left(\frac{\partial \boldsymbol{G}_v}{\partial \boldsymbol{Q}_{x^j}}\right) \approx \frac{\partial \boldsymbol{P}}{\partial y}, \tag{3.140}$$

$$\boldsymbol{P} = \frac{2\mu}{\rho}\boldsymbol{I}. \tag{3.141}$$

Here, $\tilde{\boldsymbol{A}}_v$, and $\tilde{\boldsymbol{B}}_v$ are expressed by

$$\tilde{\boldsymbol{A}}_v \approx y_\eta \boldsymbol{P}_x - x_\eta \boldsymbol{P}_y, \tag{3.142}$$

$$\tilde{\boldsymbol{B}}_v \approx -y_\xi \boldsymbol{P}_x + x_\xi \boldsymbol{P}_y. \tag{3.143}$$

The Jacobian fluxes are evaluated by the central difference manner in a same fashion to the viscous fluxes:

$$(\tilde{\boldsymbol{A}}_v)_{i+1/2,j} = (J\gamma \boldsymbol{P}_\xi)_{i+1/2,j} = (J\gamma)_{i+1/2,j}(\boldsymbol{P}_{i+1,j} - \boldsymbol{P}_{i,j}), \tag{3.144}$$

$$(\tilde{\boldsymbol{B}}_v)_{i,j+1/2} = (J\alpha \boldsymbol{P}_\eta)_{i,j+1/2} = (J\alpha)_{i,j+1/2}(\boldsymbol{P}_{i,j+1} - \boldsymbol{P}_{i,j}). \tag{3.145}$$

Denotation with subscripts *i* and *j* is the diagonal element of the matrices $\boldsymbol{A}$ or $\boldsymbol{B}$, while ones with *i*+1 or *j*+1 and *i*-1 or *j*-1 are respectively the upper element and the lower element. Consequently, Eq. (3.127) is transformed into the following expression:

$$\left(\boldsymbol{I} - \Delta t \boldsymbol{H}_{i,j}\right)\left(\boldsymbol{D} + \boldsymbol{L} + \boldsymbol{U}\right)\Delta \boldsymbol{Q}^n = \Delta t \boldsymbol{R}^n_{i,j}. \tag{3.146}$$

where

$$\boldsymbol{D} = V_{i,j} + \Delta t\Big[\frac{\overline{y}_{i+1/2,j} + \overline{y}_{i-1/2,j}}{2}\{\beta\sigma(\boldsymbol{A}_{i,j}) + 2(J\gamma \boldsymbol{P})_{i,j}\}$$

$$+ \frac{\overline{y}_{i,j+1/2} + \overline{y}_{i,j-1/2}}{2}\{\beta\sigma(\boldsymbol{B}_{i,j}) + 2(J\alpha \boldsymbol{P})_{i,j}\}\Big], \tag{3.147}$$

$$\boldsymbol{L} = -\Delta t\left[\overline{y}_{i-1/2,j}\left(\tilde{\boldsymbol{A}}^+ + J\gamma \boldsymbol{P}\right)_{i-1,j} + \overline{y}_{i,j-1/2}\left(\tilde{\boldsymbol{B}}^+ + J\alpha \boldsymbol{P}\right)_{i,j-1}\right], \tag{3.148}$$

$$\boldsymbol{U} = \Delta t\left[\bar{y}_{i+1/2,j}\left(\tilde{\boldsymbol{A}}^{-} + J\gamma\boldsymbol{P}\right)_{i+1,j} + \bar{y}_{i,j+1/2}\left(\tilde{\boldsymbol{B}}^{-} + J\alpha\boldsymbol{P}\right)_{i,j+1}\right], \tag{3.149}$$

The term ($\boldsymbol{D} + \boldsymbol{L} + \boldsymbol{U}$) in Eq. (3.146)is factorized by

$$\left(\boldsymbol{D}+\boldsymbol{L}+\boldsymbol{U}\right) = \left(\boldsymbol{D}+\boldsymbol{L}\right)\boldsymbol{D}^{-1}\left(\boldsymbol{D}+\boldsymbol{U}\right) - \boldsymbol{L}\boldsymbol{D}^{-1}\boldsymbol{U} \approx \left(\boldsymbol{D}+\boldsymbol{L}\right)\boldsymbol{D}^{-1}\left(\boldsymbol{D}+\boldsymbol{U}\right). \tag{3.150}$$

If time step Δt is sufficiently small, the approximate factorization is valid. This is because the term $\boldsymbol{L}\boldsymbol{D}^{-1}\boldsymbol{U}$ has an order of Δt. In the present simulation of an arc-heated flow, the time step is limited to be small value due to the strong nonlinearity of the chemical source terms. Thus, the approximation is expected to work well. Substituting Eq. (3.146) into Eq. (3.150) one obtains the following expression:

$$\left(\boldsymbol{I} - \Delta t\boldsymbol{H}_{i,j}\right)\left(\boldsymbol{D}+\boldsymbol{L}\right)\boldsymbol{D}^{-1}\left(\boldsymbol{D}+\boldsymbol{U}\right)\Delta\boldsymbol{Q}^{n} \approx \Delta t\boldsymbol{R}^{n}_{i,j}. \tag{3.151}$$

The presently-used LU-SGS procedure with the point implicit method is described in Algorithm 3.1. The solution is updated iteratively.

Algorithm 3.1: LU-SGS procedure

Point Implicit $\left(\boldsymbol{I} - \Delta t\boldsymbol{H}\right)\Delta\boldsymbol{Q}^{*} = \Delta t\boldsymbol{R}^{n}$

```
for i = 1, imax, step = 1 do
    for j = 1, jmax, step = 1 do
        ΔQ*_{i,j} = (I − Δt H_{i,j})^{-1} Δt R^n_{i,j}
    end for
end for
```

Lower Sweep $(\boldsymbol{D}+\boldsymbol{L})\Delta\boldsymbol{Q}^{**} = \Delta\boldsymbol{Q}^{*}$

```
for i = 1, imax, step = 1 do
    for j = 1, jmax, step = 1 do
        ΔQ**_{i,j} = D^{-1}_{i,j} (ΔQ*_{i,j} − L ΔQ**_{i−1,j} − L ΔQ**_{i,j−1})
    end for
end for
```

Upper Sweep $(\boldsymbol{D}+\boldsymbol{U})\Delta\boldsymbol{Q}^{n} = \boldsymbol{D}\Delta\boldsymbol{Q}^{**}$

```
for i = 1, imax, step = 1 do
    for j = 1, jmax, step = 1 do
        ΔQ^n_{i,j} = ΔQ**_{i,j} − D^{-1}_{i,j} (U ΔQ**_{i+1,j} + U ΔQ**_{i,j+1})
    end for
end for
```

3.5 Electron Energy Equation

In the simulation of a thermal nonequilibrium flow, commonly we must solve the electron energy equation to obtain the electron energy distribution. However, because of the considerably smaller values of electronic mass and energy compared with those of

the other species, numerical stiffness tended to arise when solving the electron-energy equation. To avoid this stiffness, we introduce the method uncoupling the electron energy equation and the other flow-field equations, and then solved the electron temperature instead of the electron energy. In the present study, we express the electron energy equation in steady form and rewrite the equation in delta form as follows:

$$\boldsymbol{A}_e \Delta T_e = \boldsymbol{R}_e . \tag{3.152}$$

where $\boldsymbol{R}_e$ is the residual vector of the electron-energy equation which is given by

$$\left(R_e\right)_{i,j} = -\left[2\bar{y}\left(\tilde{F}_e - \tilde{F}_{e,v}\right)\right]_{i+1/2,j} + \left[2\bar{y}\left(\tilde{F}_e - \tilde{F}_{e,v}\right)\right]_{i-1/2,j} - \left[2\bar{y}\left(\tilde{G}_e - \tilde{G}_{e,v}\right)\right]_{i,j+1/2}$$

$$+\left[2\bar{y}\left(\tilde{G}_e - \tilde{G}_{e,v}\right)\right]_{i,j-1/2} + \left[V_{i,j}\left(-p_e \frac{\partial u_j}{\partial x_j} + S_{\text{int},e} + S_{\text{joule}}\right)\right], \tag{3.153}$$

The Jacobian matrix $\boldsymbol{A}_e$ is defined as $\boldsymbol{A}_e = \partial \boldsymbol{R}_e / \partial T_e$. We split the Jacobian matrix into three contributions named convection, viscosity and source terms. Instead of directly inverting the matrix, Eq. (3.153) is approximately solved with a standard line-relaxation method and the electron temperature is obtained at each time step. We split the Jacobian matrix into three contributions: convection, viscous and source and estimate separately. The convection terms are calculated as the first-order upwind difference manner, that is:

$$\boldsymbol{A}_e \Delta T_e)^{\text{adv}}_{i,j} = (A^+_e \Delta T_e)_{i,j} - (A^+_e \Delta T_e)_{i-1,j} + (A^-_e \Delta T_e)_{i+1,j} - (A^-_e \Delta T_e)_{i,j}$$

$$+(B^+_e \Delta T_e)_{i,j} - (B^+_e \Delta T_e)_{i,j-1} + (B^-_e \Delta T_e)_{i,j+1} - (B^-_e \Delta T_e)_{i,j} \ . \tag{3.154}$$

where

$$A^{\pm}_e = \frac{3}{2}\rho_e R_e V \frac{U' \pm |U'|}{2},\ B^{\pm}_e = \frac{3}{2}\rho_e R_e V \frac{V' \pm |V'|}{2}, \tag{3.155}$$

$$U' = \xi_x u + \xi_y v,\ V' = \eta_x u + \eta_y v . \tag{3.156}$$

Considering the heat conduction term only for simplicity, the viscous terms of the Jacobian matrix are evaluated as follows:

$$(\boldsymbol{A}_e \Delta T_e)^{\text{vis}}_{i,j} = -\bar{A}^{\xi}_{i+1/2,j}(\Delta T_{e,i+1,j} - \Delta T_{e,i,j}) + \bar{A}^{\xi}_{i-1/2,j}(\Delta T_{e,i,j} - \Delta T_{e,i-1,j})$$

$$-\bar{A}^{\eta}_{i,j+1/2}(\Delta T_{e,i,j+1} - \Delta T_{e,i,j}) + \bar{A}^{\eta}_{i,j-1/2}(\Delta T_{e,i,j} - \Delta T_{e,i,j-1}) . \tag{3.157}$$

Finally, each contribution of the source term is differentiated with respect to the electron temperature:

$$(A_e \Delta T_e)^{\text{source}}_{i,j} = A^{\text{source}}_{i,j} \Delta T_{e,i,j}, \tag{3.158}$$

where

$$A^{\text{source}}_{i,j} = \rho_e R_e \frac{\partial u_j}{\partial x_j} + \frac{Q_{\text{T-e}}}{T_{tr} - T_e} + \frac{Q_{\text{R-e}}}{T_{rot} - T_e} - 3\rho_e (T_{tr} - T_e)\sum_{s}^{ns} R_s \frac{\partial \nu_{e,s}}{\partial T_e}$$

$$-3\rho_e (T_{rot} - T_e)\sum_{s=M}^{nm} g_{rot,s} R_s \frac{\partial \nu_{e,s}}{\partial T_e} + \frac{1}{\tau_{\text{N}_2,e}}\left(\rho_{\text{N}_2} C^{\text{eq}}_{\text{vib,N}_2} - Q_{\text{e-V}} \frac{\partial \tau_{\text{N}_2,e}}{\partial T_e}\right)$$

$$-E_{\mathrm{D,N_2}}\frac{\partial \dot{w}^e_{\mathrm{N_2}}}{\partial T_e}-E_{\mathrm{I,N}}\frac{\partial \dot{w}^e_{\mathrm{N}}}{\partial T_e}-E_{\mathrm{I,O}}\frac{\partial \dot{w}^e_{\mathrm{O}}}{\partial T_e}\,. \tag{3.159}$$

Substituting Eqs. (3.154) - (3.159) into Eq. (3.152), one obtains the following expression:

$$A\Delta T_{e,i,j-1}+B\Delta T_{e,i,j}+C\Delta T_{e,i,j+1}=R_{e,i,j}-D\Delta T_{e,i-1,j}-E\Delta T_{e,i+1,j}\,, \tag{3.160}$$

where

$A=-B^{+}_{i,j-1}-\bar{A}^{\eta}_{i,j-1/2}$,

$B=A^{+}_{i,j}-A^{-}_{i,j}+B^{+}_{i,j}-B^{-}_{i,j}+\bar{A}^{\xi}_{i+1/2,j}+\bar{A}^{\xi}_{i-1/2,j}+\bar{A}^{\eta}_{i,j+1/2}+\bar{A}^{\eta}_{i,j-1/2}+A^{\mathrm{source}}_{i,j}$,

$C=B^{+}_{i,j+1}-\bar{A}^{\eta}_{i,j+1/2}$,

$D=-A^{+}_{i-1,j}-\bar{A}^{\xi}_{i-1/2,j}$,

$E=A^{-}_{i+1,j}-\bar{A}^{\xi}_{i+1/2,j}$.

The coefficient matrix of Eq. (3.160) is tridiagonal and the system of linear equation can be solved by standard line relaxation method with Thomas algorithm.

3.6 Turbulent Transport Equations

To numerically solve the turbulence transport equations, we first rewrite Eqs. (2.243) and (2.244) in the following vector form [27]:

$$\frac{\partial \boldsymbol{Q}_{\mathrm{t}}}{\partial t}+\frac{\partial \boldsymbol{F}_{\mathrm{t}}}{\partial x_j}=\frac{\partial \boldsymbol{F}_{\mathrm{t},v}}{\partial x_j}+\boldsymbol{P}_{\mathrm{t}}-\boldsymbol{D}_{\mathrm{t}}, \tag{3.161}$$

where $\boldsymbol{Q}_{\mathrm{t}}=[\rho k,\rho\varepsilon]^t$ and

$$\boldsymbol{F}_t=\begin{bmatrix}\rho k u_j\\ \rho\varepsilon u_j\end{bmatrix},\ \boldsymbol{F}_{t,\upsilon}=\begin{bmatrix}\left(\mu+\dfrac{\mu_t}{\sigma_k}\right)\dfrac{\partial k}{\partial x_j}\\ \left(\mu+\dfrac{\mu_t}{\sigma_\varepsilon}\right)\dfrac{\partial \varepsilon}{\partial x_j}\end{bmatrix},\ \boldsymbol{P}_t=\begin{bmatrix}\tau^t_{ij}\dfrac{\partial u_j}{\partial x_j}\\ C_{\varepsilon 1}f_1\dfrac{\varepsilon}{k}\tau^t_{ij}\dfrac{\partial u_j}{\partial x_j}\end{bmatrix},\ \boldsymbol{D}_t=\begin{bmatrix}\rho\varepsilon\\ C_{\varepsilon 2}f_2\rho\dfrac{\varepsilon^2}{k}\end{bmatrix}. \tag{3.162}$$

Here, $\boldsymbol{F}_t$, $\boldsymbol{F}_{t,\upsilon}$ are the advection and viscous fluxes, respectively. Additionally, $\boldsymbol{P}_t$ and $\boldsymbol{D}_t$ are the production and destruction terms in the source, respectively.

The turbulence transport equations are discretized by the finite volume formulation in the same manner as the other flow-field equations. Similarly, the numerical fluxes of the inviscid and viscous terms are evaluated by the SLAU scheme and the second-order central difference method, respectively. The production term is also calculated by the second-order central difference method. Consequently, Eq. (3.161) is linearized as follows:

$$\frac{V_{i,j}}{\Delta t}\Delta\boldsymbol{Q}^n_{t,i,j}=\boldsymbol{R}^{n+1}_{t,i,j}, \tag{3.163}$$

where $\Delta\boldsymbol{Q}^n_{t,i,j}=\boldsymbol{Q}^{n+1}_{t,i,j}-\boldsymbol{Q}^n_{t,i,j}$ and the vector of the residuals $\boldsymbol{R}_{t,i,j}$ is given by

$$\left(\boldsymbol{R}_t\right)_{i,j} = -\left[2\bar{y}\left(\tilde{\boldsymbol{F}}_t - \tilde{\boldsymbol{F}}_{t,v}\right)\right]_{i+1/2,j} + \left[2\bar{y}\left(\tilde{\boldsymbol{F}}_t - \tilde{\boldsymbol{F}}_{t,v}\right)\right]_{i-1/2,j}$$
$$-\left[2\bar{y}\left(\tilde{\boldsymbol{G}}_t - \tilde{\boldsymbol{G}}_{t,v}\right)\right]_{i,j+1/2} + \left[2\bar{y}\left(\tilde{\boldsymbol{G}}_t - \tilde{\boldsymbol{G}}_{t,v}\right)\right]_{i,j-1/2} + \left[V\left(\boldsymbol{P}_t - \boldsymbol{D}_t\right)\right]_{i,j}, \qquad (3.164)$$

The time integration is performed implicitly. In contrast to the other flow-field equations solver, the delta form is not used in solving the turbulence equations. The destruction term $\boldsymbol{D}_t$ tends to cause high numerical stiffness. Thus, a special numerical treatment is needed for the source terms to guarantee the computational stability (see Ref. [96]):

$$\left[\boldsymbol{P}_\mathrm{t} - \boldsymbol{D}_\mathrm{t}\right]^{n+1} \approx \boldsymbol{P}_\mathrm{t}^{n+1} - \boldsymbol{D}_\mathrm{t}^{n} - \left(\frac{\boldsymbol{D}_\mathrm{t}}{\boldsymbol{Q}_\mathrm{t}}\right)^n \left(\boldsymbol{Q}_\mathrm{t}^{n+1} - \boldsymbol{Q}_\mathrm{t}^{n}\right) = \boldsymbol{P}_\mathrm{t}^{n+1} - \left(\frac{\boldsymbol{D}_\mathrm{t}}{\boldsymbol{Q}_\mathrm{t}}\right)^n \boldsymbol{Q}_\mathrm{t}^{n+1}. \qquad (3.165)$$

Furthermore, linearizing the residual vector (except for the destruction term $\boldsymbol{D}_\mathrm{t}$) in the source at the (n+1)th step, we obtain

$$\left[\boldsymbol{I} + \Delta t\left(\frac{\boldsymbol{D}_{\mathrm{t},i,j}}{\boldsymbol{Q}_\mathrm{t}}\right)^n - \frac{\Delta t}{V_{i,j}}\left(\frac{\partial \boldsymbol{R}^*_{\mathrm{t},i,j}}{\partial \boldsymbol{Q}_\mathrm{t}}\right)^n\right]\boldsymbol{Q}^{n+1}_{\mathrm{t},i,j} = \left[\boldsymbol{I} - \frac{\Delta t}{V_{i,j}}\left(\frac{\partial \boldsymbol{R}^*_{\mathrm{t},i,j}}{\partial \boldsymbol{Q}_\mathrm{t}}\right)^n\right]\boldsymbol{Q}^{n}_{\mathrm{t},i,j} + \frac{\Delta t}{V_{i,j}}(\boldsymbol{R}^*_\mathrm{t})^n_{i,j}, \quad (3.166)$$

where

$$\left(\boldsymbol{R}^*_t\right)_{i,j} = -\left[2\bar{y}\left(\tilde{\boldsymbol{F}}_t - \tilde{\boldsymbol{F}}_{t,v}\right)\right]_{i+1/2,j} + \left[2\bar{y}\left(\tilde{\boldsymbol{F}}_t - \tilde{\boldsymbol{F}}_{t,v}\right)\right]_{i-1/2,j}$$
$$-\left[2\bar{y}\left(\tilde{\boldsymbol{G}}_t - \tilde{\boldsymbol{G}}_{t,v}\right)\right]_{i,j+1/2} + \left[2\bar{y}\left(\tilde{\boldsymbol{G}}_t - \tilde{\boldsymbol{G}}_{t,v}\right)\right]_{i,j-1/2} + \left(V \cdot \boldsymbol{P}_t\right)_{i,j}, \qquad (3.167)$$

Since the destruction terms are always positive, the diagonal dominance in Eq. (3.166) results in an increase, by treating the destruction terms implicitly. Hence, this procedure ensures that the scheme is stable. Finally, the system of linear equations is solved by the GMRES method with the preconditioning technique.

3.7 Boundary Conditions

3.7.1 Flow Field Equations

Inflow

At the inlet of the inductively coupled plasma facilities, the flow is subsonically injected. The static pressure p_{in} is extrapolated from the interior point i.e., $p_{0,j} = p_{1,j}$, while the other flow properties are calculated by the specified total temperature T_0 and mass-flow rate $\dot{m}$ that is:

$$C_p T_{in} + \frac{1}{2}U_{in}^2 = C_p T_0 \;\Rightarrow\; U_{in} = -\frac{C_p p_{in} A_{in}}{\dot{m}R} + \sqrt{\left(\frac{C_p p_{in} A_{in}}{\dot{m}R}\right)^2 + 2C_p T_0}\,, \quad (3.168)$$

$$\dot{m} = \rho_{in} U_{in} A_{in} \;\Rightarrow\; \rho_{in} = \frac{\dot{m}}{U_{in} A_{in}}, \qquad (3.169)$$

$$p_{in} = \rho_{in} T_{in} R \;\Rightarrow\; T_{in} = \frac{p_{in}}{\rho_{in} R}. \tag{3.170}$$

The area A_{in} at the inflow part is obtained by

$$A_{\text{in}} = \pi \sum_{j=1}^{jmax} (y_{i,j} + y_{i,j+1}) \sqrt{x_\eta^2 + y_\eta^2}\,. \tag{3.171}$$

The injected mass concentration is set to be the composition of air, that is, $\text{N}_2 : \text{O}_2$ = 0.765 : 0.235 for ratio of mass in the present simulation. The total temperature is set to be 300 K.

Note that for the 110-kW ICP wind tunnel, the working gas was arranged to be injected from a 2.4 mm slot near the torch wall in the experiment, so the same inflow manner is used for it in the simulation. Beneath y=35.1 mm at the inlet, a wall boundary condition was used there. The wall temperature was set to be 300 K.

Outflow

At the torch or chamber exit, the working pressure in the vacuum chamber is specified, the other flow properties are determined from the zeroth extrapolation as follows:

$$Q_{i\max} = Q_{i\max-1} \tag{3.172}$$

Wall

The wall boundary was assumed to be no-slip for velocity and the wall surface had basically no catalytic effect. Furthermore, in order to determine the wall temperature T_w properly, the whole wall boundary for the 10-kW ICPWT was divided into four parts: the torch and extended tube walls, orifice wall, the vertical wall ($R_{torch}<y_{wall}<2R_{torch}$), and the chamber wall, which are denoted as $T_{w,T}$, $T_{w,O}$, $T_{w,V}$, $T_{w,C}$, respectively. These temperatures were determined at each time step as follows:

(i) $T_{w,T}$ was determined by a radiative equilibrium equation:

$$\varepsilon\sigma T_{w,T} = q_{cond}\,, \tag{3.173}$$

where ε=0.3 and σ=5.67×10^{-8} W/(K^4. m^2) are the emissivity of the quartz tube and Stefan-Boltzmann constant, respectively. Here, q_{cond} represents the conductive heat flux transferred to the wall. By considering the melting temperature of a quartz tube, $T_{w,T}$ was limited to be less than 1000 K. In addition, no pressure gradient normal to the wall was imposed.

(ii) Because of severe deformation of the grids near the orifice wall, numerical error seems easy to occur here. Therefore, a constant wall temperature was used at the orifice exit, i.e., $T_{w,O}$ was set 1000 K at x=340 mm.

(iii) The temperature at the chamber wall was supposed to be identical to the temperature of ambient gas. Therefore, $T_{w,C}$ was fixed to be 300 K.

(iv) The boundary condition on the vertical wall was determined in a different manner according to the temperature of its inner adjacent point T_{jmax-1}. If T_{jmax-1} was higher than 300 K, its boundary condition was determined in the same way as for the torch wall. Otherwise, it was treated as the chamber wall.

The wall boundary for the 110-kW ICPWT was divided into three parts: the torch wall, vertical wall, and chamber wall. The wall temperature in each section is determined by the same manner as it is used for the 10-kW ICPWT.

Center Axis

Along the center axis, an axisymmetric condition is imposed. This is given by

$$Q_{i,0} = Q_{i,1}, \tag{3.174}$$

$$Q_{i,-1} = Q_{i,2}. \tag{3.175}$$

For the y-direction momentum,

$$Q_{i,0} = -Q_{i,1}, \tag{3.176}$$

$$Q_{i,-1} = -Q_{i,2}. \tag{3.177}$$

3.7.2 Electron Energy Equation

All the boundary conditions except for the inflow part of the electron energy equation are set to be adiabatic, that is:

$$\frac{\partial T_e}{\partial n} = 0. \tag{3.178}$$

At the inflow, the electron temperature is assumed to be equal to the inflow temperature T_0 as

$$T_{e,\mathrm{in}} = T_{\mathrm{in}}. \tag{3.179}$$

3.7.3 Turbulent Equations

Treatments at the outflow and the center axis are the same to those of the flow field equation. Here, boundary conditions at the inflow and the wall are denoted.

At the inflow part, the turbulence energy and its dissipation rate are respectively given by

$$k_{in} = 1.5\left(k_{cof}U\right)^2, \tag{3.180}$$

$$\varepsilon_{in} = \frac{10}{\varepsilon_{cof}}\frac{\rho_{in}k_{in}^2}{\mu_{in}}. \tag{3.181}$$

where k_{cof} is set to be 0.02, ε_{cof} is set to be 200.

The boundary conditions of k and ε on the wall surface are determined as

$$k = 0,\ \varepsilon = \frac{2\mu}{\rho}\frac{k_{\mathrm{jmax\text{-}1}}}{\left(y_{\mathrm{jmax}} - y_{\mathrm{jmax\text{-}1}}\right)^2}. \tag{3.182}$$

where the subscript *jmax* indicates the variables on the wall surface. The boundary conditions of k and ε on the center axis and at the exit are extrapolated.

3.7.4 Electromagnetic-Field Equations

As for the boundary conditions for solving the far-field magnetic vector-potential equations, the outer boundaries are set far enough from the coil position so that the intensity of the electromagnetic field is sufficiently small to be given as zero along these boundaries. For the 10-kW ICPWT, the our boundaries locate at x= -100; x=320 mm; y=187 mm in Fig. 4.1(a). For the 110-kW ICPWT, the our boundaries locate at x= -120; x=360 mm; y=206 mm in Fig. 4.2(a). The effects of different positions of these far field boundaries are tested and avoided before the beginning of the calculation.

The axisymmetric boundary condition was imposed on the center axis.

3.8 Electromagnetic Field Solver

The far-field electromagnetic equations were discretized by the finite difference method. The numerical flux was evaluated by the second-order central difference formulation. The under-relaxation iterative method was used to solve the magnetic vector-potential equations. For example, at the nth iterative step the vector potential is evaluated by:

$$A_{\theta,i,j}^{\ n} = A_{\theta,i,j}^{\ n-1} + \alpha\left(\overline{A}_{\theta,i,j}^{\ n} - A_{\theta,i,j}^{\ n-1}\right). \tag{3.183}$$

The relaxation coefficient α was set to be 0.1 and 0.7 for the 10-kW and 110-kW ICPWT, respectively. The relative residual of the vector-potential equations was set to be less than 10^{-5} at each time step for all the computation cases.

To control the total discharge power dissipated into the plasma, the computational input power defined as $P_c = \oint S_{joule} dV$ is integrated over control volumes in the flow field of the torch. The coil current is updated at each time step to govern the computational input power P_c to be equal with the total experimental input power P (e.g., P=10 kW). To achieve a stable calculation, we introduced the following method to update the coil current at the (n+1)th time step:

$$I^{n+1} = I^n + \Delta I^n, \tag{3.184}$$

$$\Delta I^n = \beta\left(P / P_c^n - 1\right) I^n. \tag{3.185}$$

where the relaxation factor β is defined in the program flow chart Fig. 3.3

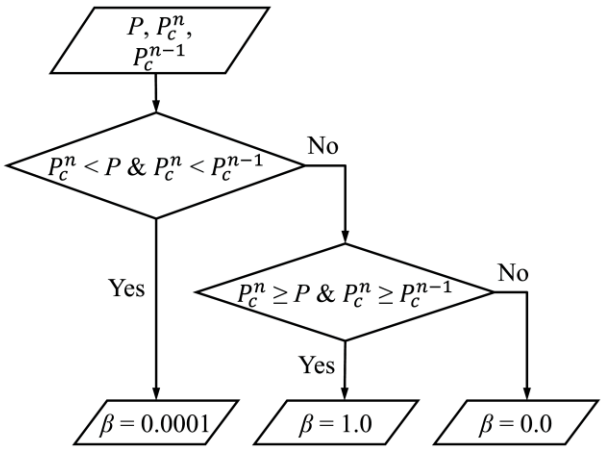

Fig. 3.3 Definition of the relaxation factor β

3.9 Other Implementations

3.9.1 Local Time Stepping

In this study, the time integration scheme was used to update flow-field results at each time step. It is known for chemically reacting flow computations the time step Δt is severely limited due to the strong nonlinearity of the thermochemical source terms. So in order to achieve stable and fast-convergent calculations, attention should be paid to the time integration step Δt . Usually, If the interest of a calculation is the computational stability or temporal evolution of the solution for an equation, then the time step Δt can be set to be smallest value in the whole flow field (Global time stepping technique). However, this technique will cost long time to get convergent solutions of the equation. On the other hand, if the interest is fast convergence or steady state solution of a flow, then local time-stepping technique can be used in the calculation. In this study we adopt the local time-stepping technique to determine the time step Δt. Δt is set to be different for each cell. Specifically, the local time step $(\Delta t)_{i,j}$ at a cell (i, j) is determined as follows:

$$(\Delta t)_{i,j} \le C_{\mathrm{CFL}} \left(\frac{\sqrt{x_\xi^2 + y_\xi^2}}{|U| + c}, \frac{\sqrt{x_\eta^2 + y_\eta^2}}{|V| + c} \right)_{i,j} . \tag{3.186}$$

where C_{CFL} represents the Courant-Friedrichs-Lewy number.

3.9.2 Treatment of Multi-Temperature Model

In the four-temperature model, T_{rot} and T_{vib} denote the rotational and vibrational energy modes of molecules. If there is no or very few molecules in a plasma flow, which is resulted by severe dissociation reactions. Numerical instability of the rotation or the vibration energy tends to arise due to lack of the molecules if the four-temperature model is applied. To overcome this difficulty, we combine a two-temperature model (i.e., the heavy-particle ($T_{tr} = T_{rot} = T_{vib}$) and the electron temperatures (T_e) and a four-temperature model by a degree of the molecular-species mole fraction. In the present calculation, in the region where the molecule mole fraction is less than a small value ε_{mole}, the two-temperature model is adopted instead of the four-temperature model. In this study, ε_{mole} is set to be 1%. On the other hand, because severe recirculation flow appeared near the torch inlet, the multi-temperature model tended to be unstable at the inlet. To keep the stability, a one-temperature model ($T_{tr} = T_{rot} = T_{vib} = T_e$) was used at the inlet section (x≤20 mm) for simplicity.

3.10 Matrix Solver

In order to numerically solve system of linear equations such as the electron energy equation and turbulence transport equations mentioned above, it is necessary to introduce efficient mathematical method to obtain their solutions at each time step. As

for solving the system of linear equations, in most instances it results in the following relation:

$$\boldsymbol{A}\boldsymbol{x} = \boldsymbol{b}. \tag{3.187}$$

where $\boldsymbol{A}$ represents a $n \times n$ coefficient matrix, and $\boldsymbol{x}$ and $\boldsymbol{b}$ are n-dimensional vectors. To get the analytical solution $\boldsymbol{x}$ of this equation, we need to invert $\boldsymbol{A}$ exactly. However, the direct inversion is enormously expensive. It tends to spend much computational time and computer memory storage for system of linear equations. Hence a series of relaxation scheme such as Gauss-Seidel Line Relaxation method, Generalized Minimum RESidual (GMRES) method etc. were commonly used to find an approximate solution of Eq. (3.187) iteratively. In this section, each relaxation scheme used in the present calculation is denoted as follows.

3.10.1 Gauss-Seidel Line Relaxation Method

For the electron energy equation discussed in the previous section, the Gauss-Seidel line relaxation method was used to solve this equation. Here, we rewritten the Eq. (3.160) at a cell (i, j) as

$$A\Delta T_{e,i,j-1} + B\Delta T_{e,i,j} + C\Delta T_{e,i,j+1} = R_{e,i,j} - D\Delta T_{e,i-1,j} - E\Delta T_{e,i+1,j}\,. \tag{3.160}$$

It can be treated as a tridiagonal system of linear equations, and thus can be solved implicitly for ΔT_e by using a line relaxation method with Thomas algorithm.

The line relaxation method can be further divided into Gauss-Seidel and non- Gauss-Seidel methods. For the Gauss-Seidel method, $\Delta T_{e,i-1,j}$ and $\Delta T_{e,i+1,j}$ in the right hand side of Eq. (3.160) are evaluated using the latest available values. It is preferable and efficient to use the Gauss-Seidel method. Since changes in the solution propagate quickly, it can improve convergence speed for an iterative process by using the latest solutions of equations. In contrast, $\Delta T_{e,i-1,j}$ and $\Delta T_{e,i+1,j}$ in the non- Gauss-Seidel method are computed by using previous time step values even if values of the current level are available for some lines. In this case, more iterations are required to obtain ΔT_e for all points.

3.10.2 GMRES Method

To solve the system of turbulent transport equations Eq. (3.166), GMRES (Generalized Minimal RESidual) method [97] was employed in this study. It can be used for solving a linear system where the coefficient matrix is not symmetric or positive. The use of GMRES combined preconditioning technique is widely used in many fields. The basic procedure of the GMRES method is described below.

Considering the system of linear equations Eq. (3.187), generally, the final purpose is to look for an approximate solution $\boldsymbol{x}$ for this equation:

$$\boldsymbol{x} = \boldsymbol{x_0} + \boldsymbol{z}\,. \tag{3.188}$$

where $\boldsymbol{x_0}$ represents an initial gauss and $\boldsymbol{z}$ is a member of the Krylov subspace:

$$\boldsymbol{z} \in \Re_{\boldsymbol{m}}, \Re_{\boldsymbol{m}} \equiv \{\boldsymbol{r}_0, \boldsymbol{A}\boldsymbol{r}_0, \boldsymbol{A}^2\boldsymbol{r}_0, \boldsymbol{A}^3\boldsymbol{r}_0, \ldots \boldsymbol{A}^{\boldsymbol{m}-1}\boldsymbol{r}_0, \}\,. \tag{3.189}$$

where $\boldsymbol{r}_0 = \boldsymbol{b} - \boldsymbol{A}\boldsymbol{x}_0$, and m being the dimension of $\Re$. The parameter m is also termed as the number of search directions. The GMRES algorithm is used to determine $\boldsymbol{z}$ in such a way that the 2-norm of the residual, i.e.,

$$\left\| \boldsymbol{b} - \boldsymbol{A}(\boldsymbol{x}_o + \boldsymbol{z}) \right\|. \tag{3.190}$$

is minimized. In the following, we present the particular steps of the GMRES algorithm.

1) Computation of the orthonormal basis of $\Re_m$

We employ the modified Gram-Schmidt procedure to get the orthonormal vectors:

$\boldsymbol{r}_0 = \boldsymbol{b} - \boldsymbol{A}\boldsymbol{x}_0$

$\boldsymbol{v}_1 = \boldsymbol{r}_0 / \left\| \boldsymbol{r}_0 \right\|$

Do j=1, m

  $\boldsymbol{v}_{j+1} = \boldsymbol{A}\boldsymbol{v}_j$

  Do i=1, j

    $\boldsymbol{h}_{i,j} = \boldsymbol{v}_{j+1}\boldsymbol{v}_i$

    $\boldsymbol{v}_{j+1} = \boldsymbol{v}_{j+1} - \boldsymbol{h}_{i,j}\boldsymbol{v}_i$

  End do

  $\boldsymbol{h}_{j+1,j} = \left\| \boldsymbol{v}_{j+1} \right\|$

  $\boldsymbol{v}_{j+1} = \boldsymbol{v}_{j+1} / \boldsymbol{h}_{j+1,j}$

End do

where $\boldsymbol{h}_{i,j}$ denotes the coefficients of the upper Hessenberg matrix (*i*=line, *j*=column). However, the matrix is extended by the elements $\boldsymbol{h}_{j+,j}$. Therefore, the dimension becomes (m+1) ×m.

2) Generation of the upper Hessenberg matrix

The Hessenberg matrix is expressed as:

$$\boldsymbol{H}_m^* = \begin{bmatrix} \boldsymbol{h}_{1,1} & \boldsymbol{h}_{1,2} & \cdots & \boldsymbol{h}_{1,m-1} & \boldsymbol{h}_{1,m} \\ \boldsymbol{h}_{2,1} & \boldsymbol{h}_{2,2} & \cdots & \boldsymbol{h}_{2,m-1} & \boldsymbol{h}_{2,m} \\ \boldsymbol{0} & \boldsymbol{h}_{3,2} & \ddots & \vdots & \vdots \\ \vdots & \boldsymbol{0} & \ddots & \boldsymbol{h}_{m-1,m-1} & \boldsymbol{h}_{m-1,m} \\ \vdots & \vdots & \ddots & \boldsymbol{h}_{m,m-1} & \boldsymbol{h}_{m,m} \\ \boldsymbol{0} & \boldsymbol{0} & \cdots & \boldsymbol{0} & \boldsymbol{h}_{m+1,m} \end{bmatrix}_{(\boldsymbol{m}+1)\times\boldsymbol{m}} . \tag{3.191}$$

It will be further used below to formulate and solve the minimization problem for the residual Eq. (3.190).

3) Minimization of the residual

The correction of the start solution $\boldsymbol{x}_0$ is defined as:

$$\boldsymbol{z} = \sum_{j=1}^{m} y_j \, \boldsymbol{v}_j \,, \tag{3.192}$$

where y_j are the components of the vector $\vec{\boldsymbol{y}} = \left[y_1, y_2, \cdots, y_m \right]^T$. Furthermore, it can be shown that $\boldsymbol{A}\boldsymbol{V}_m = \boldsymbol{V}_{m+1}\boldsymbol{H}_m^*$, where $\boldsymbol{V}_m = \left[\boldsymbol{v}_1, \boldsymbol{v}_2, \cdots, \boldsymbol{v}_m \right]^T$ being a matrix with $\boldsymbol{v}_j$ as columns. Let us introduce the notation:

$$\boldsymbol{e} = \left[\left\| \boldsymbol{r}_0 \right\|, 0, \cdots, 0 \right]^T, \tag{3.193}$$

where the unit vector $\boldsymbol{e}$ has (*m*+1) elements. Using the definition of Eq. (3.193), we observe that

$$\boldsymbol{r}_0 = \boldsymbol{b} - \boldsymbol{A}\boldsymbol{x}_0 = \boldsymbol{V}_{m+1}\boldsymbol{e}\,, \tag{3.194}$$

Hence, we obtain for the residual Eq. (3.190)

$$\|\boldsymbol{b} - \boldsymbol{A}(\boldsymbol{x}_o + \boldsymbol{z})\| = \left\|\boldsymbol{r}_0 - \boldsymbol{A}(\sum_{j=1}^{m} \boldsymbol{y}_j \boldsymbol{v}_j)\right\| = \|\boldsymbol{r}_0 - \boldsymbol{A}\boldsymbol{V}_m \vec{\boldsymbol{y}}\|$$

$$= \|\boldsymbol{V}_{m+1}(\boldsymbol{e} - \boldsymbol{H}_m^* \vec{\boldsymbol{y}})\| = \|\boldsymbol{e} - \boldsymbol{H}_m^* \vec{\boldsymbol{y}}\|\,, \tag{3.195}$$

We employed the orthogonality of $\boldsymbol{V}_{m+1}$ in the last step. Therefore, the problem of the minimization of the residual can be simplified as:

$$\min\|\boldsymbol{b} - \boldsymbol{A}(\boldsymbol{x}_o + \boldsymbol{z})\| = \min\|\boldsymbol{e} - \boldsymbol{H}_m^* \vec{\boldsymbol{y}}\|\ . \tag{3.196}$$

The solution of the minimization problem can be obtained with the help of the Q-R algorithm which is described next.

4) Q-R algorithm

Let us define $\boldsymbol{R}_m = \boldsymbol{Q}_m \boldsymbol{H}_m^*$ with $\boldsymbol{Q}_m = \boldsymbol{F}_m \boldsymbol{F}_{m-1} \ldots \boldsymbol{F}_1$ being the production of the Givens rotation matrix

$$\boldsymbol{F}_j = \begin{bmatrix} \boldsymbol{I}_j & & \\ & \begin{bmatrix} c_j & s_j \\ -s_j & c_j \end{bmatrix} & \\ & & \boldsymbol{I}_{m-j} \end{bmatrix}_{(m+1)\times(m+1)}\,, \tag{3.197}$$

In Eq. (3.197), $\boldsymbol{I}_j$ denotes the identity matrix of dimension j. Further, c_j and s_j ($c_j^2 + s_j^2 = 1$) represents the sine/cosine of the rotational angle. The rotations are chosen such that $\boldsymbol{H}_m^*$ is transformed into an upper triangular matrix $\boldsymbol{R}_m$ which has the dimensions (m+1)×m and which last line contains only zeros. Since $\boldsymbol{Q}_m^T \boldsymbol{Q}_m = \boldsymbol{I}$, we can write it in Eq. (3.196) as

$$\|\boldsymbol{e} - \boldsymbol{H}_m^* \vec{\boldsymbol{y}}\| = \|\boldsymbol{Q}_m^T(\boldsymbol{Q}_m \boldsymbol{e} - \boldsymbol{Q}_m \boldsymbol{H}_m^* \vec{\boldsymbol{y}}\| = \|\vec{\boldsymbol{g}} - \boldsymbol{R}_m \vec{\boldsymbol{y}}\|\,, \tag{3.198}$$

where $\vec{\boldsymbol{g}} = \boldsymbol{Q}_m \boldsymbol{e}$ denotes the transformation of the vector $\boldsymbol{e}$. The last line of $\boldsymbol{R}_m$ consist of zero. Therefore only the term g_{m+1} is nonzero in the low (m+1) of the vector ($\vec{\boldsymbol{g}} - \boldsymbol{R}_m \vec{\boldsymbol{y}}$). If we denote the first m-components of ($\vec{\boldsymbol{g}} - \boldsymbol{R}_m \vec{\boldsymbol{y}}$) as $\boldsymbol{p}_j$ (j=1, 2, …m), then the norm in Eq. (3.198) becomes

$$\|\vec{\boldsymbol{g}} - \boldsymbol{R}_m \vec{\boldsymbol{y}}\| = \sqrt{g_{m+1}^2 + \sum_{j=1}^{m} p_j^2}\,, \tag{3.199}$$

If we chose the components y_j of $\vec{\boldsymbol{y}}$ in such a way that $\boldsymbol{p}_j^2 = 0$ for all j=1, 2, …m, we obtain for the minimization problem in Eq. (3.196)

$$\min\|\boldsymbol{b} - \boldsymbol{A}(\boldsymbol{x}_o + \boldsymbol{z})\| = \|\vec{\boldsymbol{g}} - \boldsymbol{R}_m \vec{\boldsymbol{y}}\| = g_{m+1}\,, \tag{3.200}$$

The components y_j results from the solution of the following system of linear equations by back-substitution

$$\begin{bmatrix} R_{1,1} & \cdots & R_{1,m-1} & R_{1,m} \\ 0 & \ddots & \vdots & \vdots \\ \vdots & \ddots & R_{m-1,m-1} & R_{m-1,m} \\ 0 & \cdots & 0 & R_{m,m} \end{bmatrix} \begin{bmatrix} y_1 \\ \vdots \\ y_{m-1} \\ y_m \end{bmatrix} = \begin{bmatrix} g_1 \\ \vdots \\ g_{m-1} \\ g_m \end{bmatrix}, \tag{3.201}$$

The solution of the system of equations Eq. (3.187) is then obtained with known y_j from Eq. (3.192). It is important to remark that

$$\|\boldsymbol{r}_m\| = \|\boldsymbol{b} - \boldsymbol{A}(\boldsymbol{x}_o + \boldsymbol{z})\| = \|\boldsymbol{e} - \boldsymbol{H}_m^* \vec{\boldsymbol{y}}\| = \|\vec{\boldsymbol{g}} - \boldsymbol{R}_m \vec{\boldsymbol{y}}\| = g_{m+1}. \tag{3.202}$$

This means that actual residual can be easily determined as g_{m+1}.

In addition, GMRES can work best when the eigenvalues of matrix $\boldsymbol{A}$ is clustered [98]. To achieve this, a preconditioning technique was applied to accelerate the calculation. With a given preconditioning matrix $\boldsymbol{P}$, Eq. (3.187) is expressed as

$$\left(\boldsymbol{A}\boldsymbol{P}^{-1}\right)\left(\boldsymbol{P}\boldsymbol{x}\right) = \boldsymbol{b}, \tag{3.203}$$

where the preconditioning matrix $\boldsymbol{P}$ is referred to as right preconditioner so that $\boldsymbol{P}$ is multiplied from the right side. Rewriting Eq. (3.203):

$$\left(\boldsymbol{A}\boldsymbol{P}^{-1}\right)\boldsymbol{x}' = \boldsymbol{b}. \tag{3.204}$$

where $\boldsymbol{P}\boldsymbol{x} = \boldsymbol{x}'$. The preconditioning matrix $\boldsymbol{P}$ is an approximation of the coefficient matrix $\boldsymbol{A}$, and clusters the eigenvectors of $\boldsymbol{A}$ around unity. Thus, in GMRES loop with the preconditioning technique, we need to solve $\boldsymbol{A}\boldsymbol{x} = \boldsymbol{x}'$ as the inner loop. GMRES loop corresponds to the outer loop. In this study, the matrix in the inner loop is inverted by the Gauss-Seidel method.

3.11 Summary

In this chapter, the numerical methods used to solve the flow-field and electromagnetic-field equations were discussed. Specifically, the flow field equations were discretized by a finite volume method. Exploiting the advantages of arbitrary body-fitted grids, we transformed the Cartesian coordinate system into a generalized coordinate system in the computational domain. The convective terms were evaluated by the SLAU (Simple Low-dissipation Advection Upwind splitting method), and the viscous terms were calculated using the second-order central difference method. To achieve higher order accuracy, Van Leer's MUSCL (Monotonic Upstream-centered Scheme for Conservation Laws) limiter was used for the inviscid numerical fluxes. In addition, when the chemical kinetic model is considered, a robust and effective time integration method is needed to overcome the stiffness in time scale between the chemical reactions and fluid motion. Thus, the point-implicit LUSGS (Lower and Upper Symmetric Gauss-Seidel method) was employed to achieve stable calculation and rapid convergence. To avoid numerical stiffness, we uncoupled the electron-energy equation and turbulent transport equations from the other flow-field equations. The electron energy equation was approximately solved by a standard line relaxation method to

obtain the electron temperature at each time step. The turbulent equations were solved by the GMRES (Generalized Minimal RESidual) method.

The electromagnetic equations were discretized by a finite difference method, and solved by the under-relaxation iterative method. The Lorentz force and Joule heating rate were used to bridge the flow-field and electromagnetic-field. The coil current was controlled by a relaxation parameter β to update the electromagnetic field at each time step. The OpenMP technique was used to accelerate all calculations. Finally, to give a clear view the numerical methods mentioned above are summarized in Table 3.1 as following:

Table 3.1 Numerical methods used in this study

Discretization	Finite Volume Method
Viscous term	2nd order Central Difference
Inviscid term	SLAU + MUSCL
Time integration	LUSGS + Point Implicit Method
Electron Energy Equation	Gauss-Seidel Line Relaxation Method
Turbulent Transport Equations	GMRES
Electromagnetic Equations	Under-Relaxation Iteration Method

Chapter 4 Results and Discussion

First, the computational grid system and working conditions used in the present study are given and summarized.

Second, the comparisons of numerical results with experimental data are primarily performed for the 10-kW and 110-kW ICPWTs, respectively.

Third, the basic flow properties of nitrogen and air inductively coupled plasma flows in each facility are discussed in detail.

Fourth, the interactions between the electromagnetic and flow fields of ICP flows in the 10-kW and 110-kW ICPWTs are studied and compared.

Fifth, the comparison of numerical results obtained under the assumptions of local thermal equilibrium and thermal nonequilibrium is performed. The effects of thermal equilibrium and nonequilibrium model on the flow properties are analysed.

Finally, the effects of different accuracy electron transport properties on the flow fields are examined and discussed.

4.1 Computational Mesh and Condition

The geometry and computational mesh of the 10-kW ICPWT are illustrated in Fig. 4.1. Fig. 4.1(a) shows the far-field grid system used for solving the electromagnetic equations; Fig. 4.1(b) shows the flow-field mesh of the ICP torch that is used to bridge the electromagnetic and entire flow fields of this ICPWT; Fig. 4.1(c) illustrates the geometry and mesh of the whole flow field including an ICP torch, extended tube and vacuum chamber. For the electromagnetic field calculation, the far-field grid that consists of 126×66 nodes covers in the region of $-100 \le x \le 320$ mm and $0 \le y \le 187$ mm. The inductive coil turns 3 times around the discharge torch with a diameter of 8 mm, and locates in $90 \le x \le 125$ mm, y=52.5 mm with an interval of 17.5 mm. The non-uniform grid is used with the mesh being concentrated in the coil region to take care of the coupling between electromagnetic and flow fields. The driving frequency of the coil current for this 10-kW ICPWT is 4.0 MHz.

As for the mesh of the flow field, the computational domain is constructed as same as the structure designed in the experiment [6]. A thin orifice plate with an inner radius of 25 mm and wall thickness of 1.5 mm is positioned at x=320 mm. Because of difficulties in constructing the computational grid in such a narrow space, the wall thickness of the orifice was enlarged and specified from x=320 – 340 mm in the computation. The influence of this enlargement on the flow field is thought to be negligible. The total axial length of the computational domain is kept identical with that in the corresponding experiment.

The geometry and computational mesh of the 110-kW ICPWT considered in this study is illustrated in Fig. 4.2. For the electromagnetic field calculation, the region of the far-field domain that consists of 101×66 node covering the region of $-120 \le x \le 360$ mm and $0 \le y \le 206$ mm. The inductive coil turns 3 times around the discharge torch with a diameter of 8 mm and locates at y=51.0 mm, $51 \le x \le 84$ mm with an interval of 16.5 mm. The non-uniform grid is used with the mesh being concentrated in the coil region. The driving frequency of the coil current for this 110-kW ICPWT is 1.78 MHz.

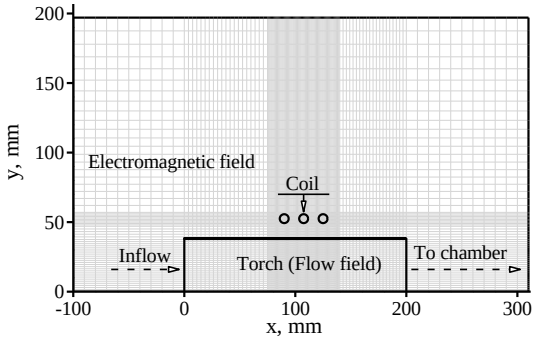

(a) Far-field grid for electromagnetic field

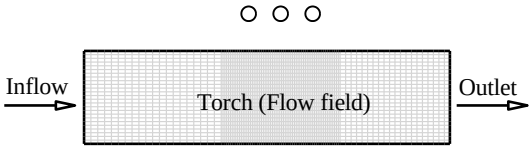

(b) Torch

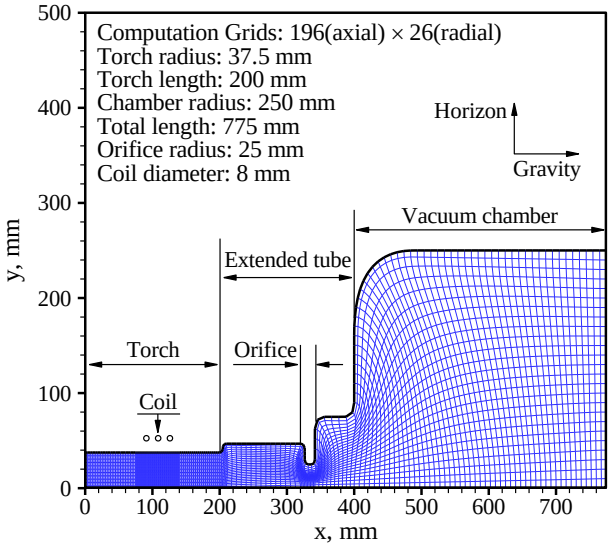

(c) Entire flow field grid

Fig. 4.1 Geometry and grids of the 10-kW ICPWT: (a) Far-field grid for electromagnetic field; (b) Torch; (c) Entire flow field grids

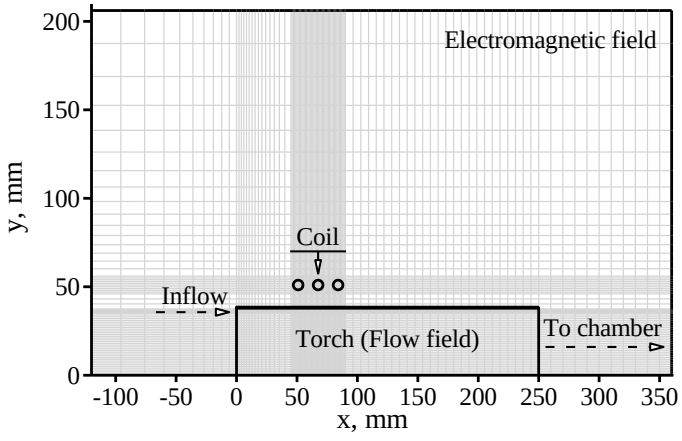

(a) Far-field mesh

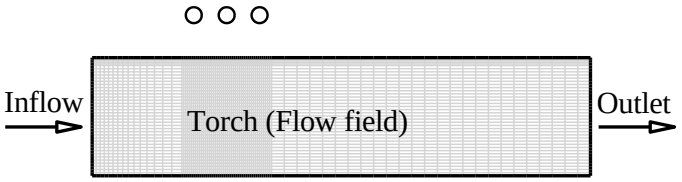

(b) Torch

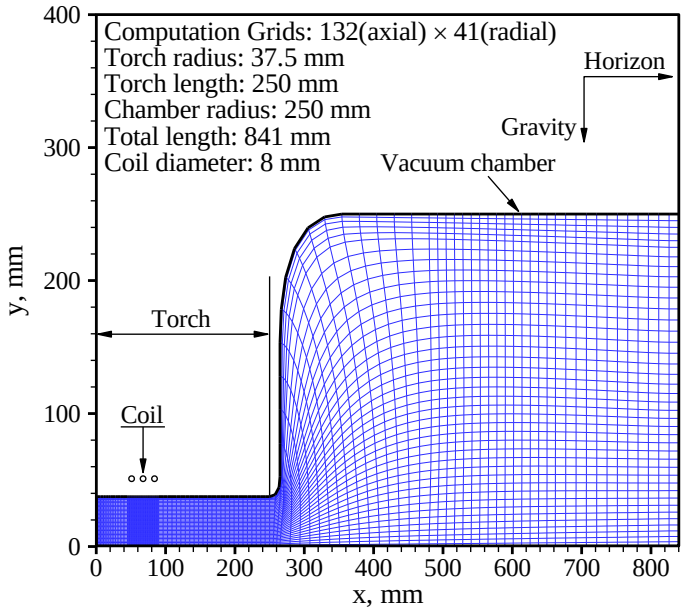

(c) whole flow field

Fig. 4.2 Computational mesh and geometry of the 110-kW ICP wind tunnel, (a) Far-field mesh; (b) Torch; (c) Entire flow field grids

The computational conditions performed for these two ICP wind tunnels in the present study are summarized in Table 4.1. To make comparison between the numerical and experimental results, these operating conditions are mainly referred from corresponding experimental studies, and set identical with the experimental conditions.

Note that for the high-power inductively coupled plasma heater, because of several thermal energy loss (e.g., heat loss caused by cooling water, energy loss caused by electrical impedance on electric circuit, and radiation loss), the net input power dissipated into plasma flow usually is quite different from the plate input power read from the electric supply system [20, 99]. For the 110-kW ICPWT, according to the relevant studies [5, 99], its heat efficiency was evaluated to be about 0.33. Hence, in this study, the heat efficiency of the 110-kW wind tunnel was set as 0.33 for all the computational case. For low-power ICP wind tunnels, because the low-power flow has relatively low temperature and coil current, its radiation loss and electric energy loss on the circuit are usually much smaller than those of high-power ICPWTs. Therefore, the heat efficiency of the low-power ICPWT would be higher than the high-power ICPWT. Furthermore, because there exist minimum input-power for sustaining plasma in the low-power plasma generation experiments, the heat efficiency of some low-power plasma flows (e.g., low-power arc-heated and ICP flows) may be very high in some working conditions [100, 101]. As well, because this minimum power for sustaining plasma is indefinite and different in each working condition, it is difficult to judge the heat efficiency for the low-power ICPWT. Therefore, for simplicity, in this study the heat efficient of the 10-kW ICPWT is assumed to be 1.0 for all the computational cases.

The computational input power i.e., net input-power dissipated into plasmas in all simulations was estimated by multiplying the heat efficiency η to the total input power as the computational heat source. The sum of the Joule heating rate in the computational region amounts to the product of the heat efficiency and total input power. The mass flow rate was specified as the entrance parameter. The vacuum chamber pressure, which is controlled by vacuum pumps to realize a constant pressure environment as required in an experiment, was specified as the outflow condition.

Table 4.1 Computational conditions

ICP Type	10-kW ICPWT					110-kW ICPWT			
Cases	Baseline	Case 1	Case 2	Case 3	Case 4	Case 5	Case 6	Case 7	Case 8
P, kW	10.0	10.0	10.0	10.0	10.0	90.0	70.0	90.0	90.0
p_{ch}, kPa	3.90	3.50	4.30	7.20	8.00	10.0	10.0	10.0	10.0
$\dot{m}$, g/s	0.625	0.65	0.82	0.625	0.625	1.8	2.0	2.0	1.8
Test gas	N_2					N_2	Air		
f, MHz	4.0					1.78			
Efficiency η	1.0					0.33			

4.2 Comparison of Numerical and Experimental Results

In this section, the simulated results are compared with the experimental data such as the photograph of visible plasma, measured temperature, and enthalpy for the 10 kW and 110 kW ICP wind tunnels, respectively.

4.2.1 10-kW ICPWT

Recently, the optical emission spectroscopies of excited molecules $N_2(1+)$, $N_2(2+)$ and $N_2^+(1-)$ were measured and fitted with the theoretical spectra to determine flow temperature in the 10-kW ICPWT [102, 103]. In this section, we make qualitative and quantitative comparisons between the numerical and experimental results, respectively.

First of all, we give qualitative comparison between the simulated high-temperature column and the bright visible plasma in the experiment [103] for the baseline case. Fig. 4.3(a) shows the comparison between the computed translational temperature (left) and the experimental plasma core (right) in the torch. It is seen that the computed high-temperature region ($T \geq 5500$ K) shows a similar shape to that of the bright visible plasma in the experiment. Both in the simulation and in the experiment, the plasma flames seem broaden a little in the radial direction near the third turn of the coil. Fig. 4.3(b) shows the comparison between the computed translational temperature (left) and the experimental plasma column (right) in the chamber. Similar shape of high-temperature columns can also be seen in the chamber between the simulation and experiment.

Second, the quantitative comparisons between the simulated and measured temperatures along the radial and axial directions are given, respectively. (1) Along the radial direction, Fig. 4.4 shows the comparison of the simulated and measured temperatures at x=135 mm for case 1. The operating conditions of case 1 were defined as same as the experimental conditions [102]: P=10 kW, $\dot{m}$=0.65 g/s, p_{ch} =3.5 kPa, f = 4.0 MHz. As can be seen from Fig. 4.4, the computed and measured temperatures show good agreements with each other within $y \leq 15$ mm. (2) Along the axial direction, Fig.

4.5 compares the simulated and measured temperatures on the center axis for baseline case and case 2. The operating conditions of case 2 were defined as [102]: P=10 kW, $\dot{m}$=0.82 g/s, p_{ch} =4.3 kPa, f = 4.0 MHz in the experiment and simulation. For case 2, the simulated temperatures agree well with the measured ones at x=117, 135 mm, but the disagreement is seen at the position x=99 mm on the center axis. For baseline case, the agreement can be observed at x=99 mm. While at x=117, 135 mm the simulated temperatures seem about 1500 K higher than the measured ones there. Generally, on the center axis the maximum relative errors between the simulated and measured temperatures are within 28.5% for these two cases. Because the effect of radiative heat transfer in the coil region was not considered in the present study, they may be the reasons for these discrepancies on the center axis.

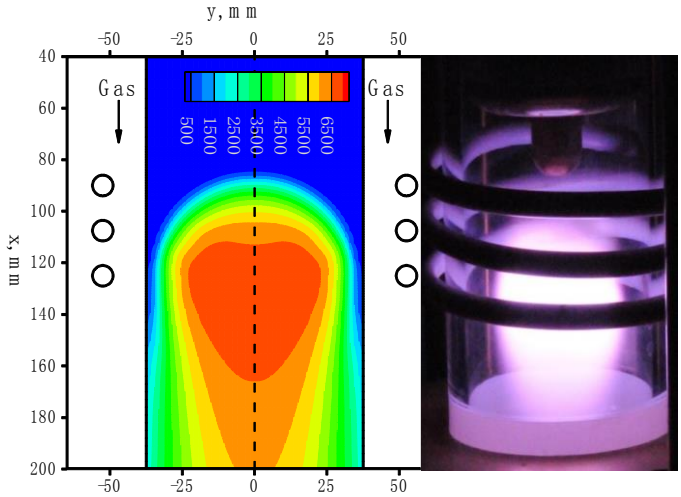

(a)

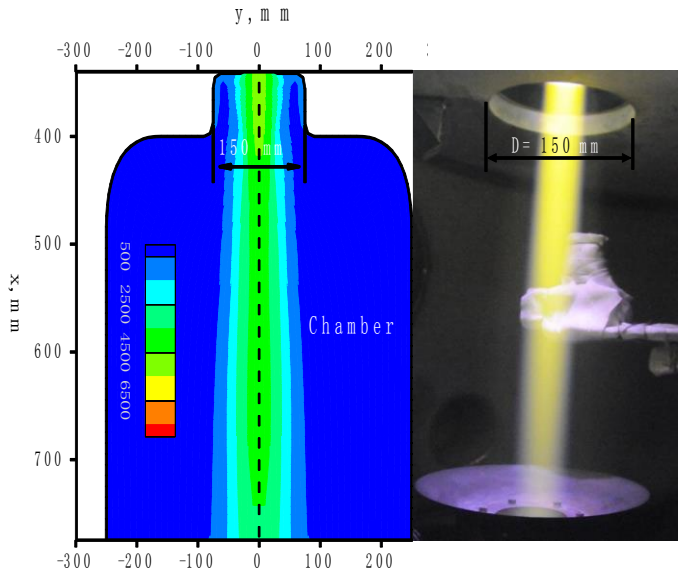

(b)

Fig. 4.3 Comparisons between the computed translational temperature (left) and experimental plasma column (right), (a) in the torch; (b) in the chamber

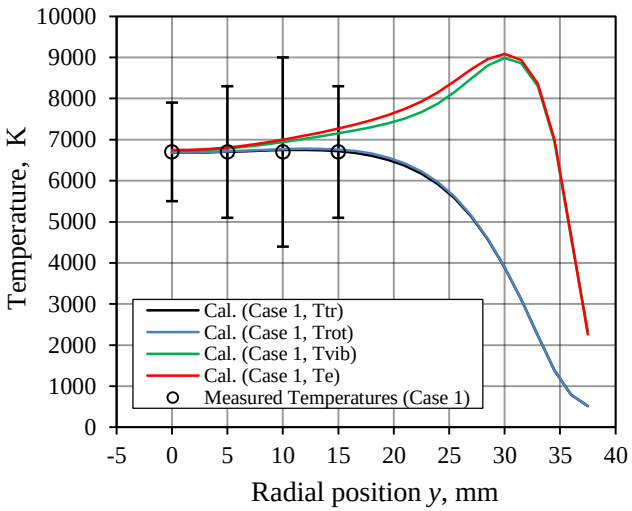

Fig. 4.4 Comparison of the simulated and measured temperatures for case 1 at x=135 mm

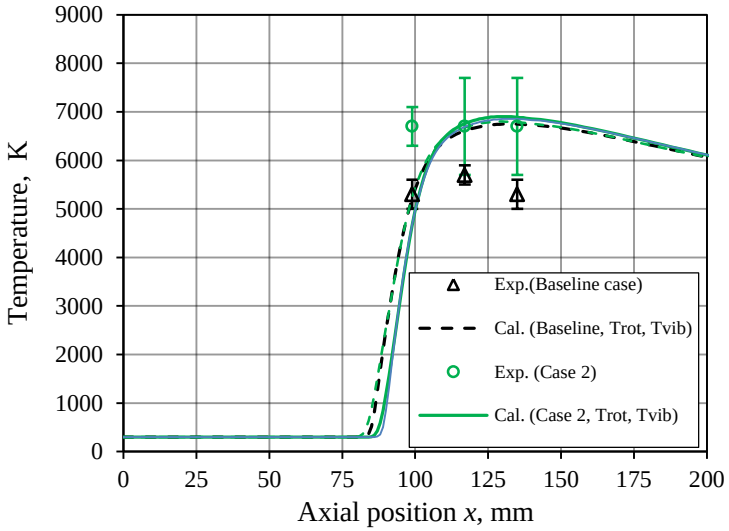

Fig. 4.5 Comparison of the simulated and measured temperatures for baseline case and case 2 along the center axis

4.2.2 110-kW ICPWT

To further validate the numerical methods, simulations were carried out using the 110-kW ICP wind tunnel at JAXA. The total length of the computational domain was extended beyond 816 mm, at which the test pieces were set up in the spectroscopic experiments performed by Fujita et al [99, 104]. They conducted one-dimensional imaging spectroscopy at x=662 mm in the vacuum chamber to obtain the radial distribution of the emission spectrum of the test flow [99, 104]. The spectrum fitting method was employed to determine particle temperature. Finally, the radial temperature distribution at x=662 mm was obtained.

Fig. 4.6 compares the measured and computed radial temperatures at x=662 mm under the conditions of P=90 kW, $\dot{m}$=1.8 g/s and p_{ch} =10 kPa with nitrogen and air as working gases. The simulated translational temperature T_{tr} agrees well with the determined temperature in the radial direction. For example, the measured and

simulated maximum temperature for air plasma at the center axis are 5600±100 and 5510 K, respectively, so the error between the measured and simulated maximum temperature is less than 5%. In addition, the average specific enthalpy of air flow within 25 mm from the center axis are 13.7±1.1 and 14.4 MJ/kg for the experimental and numerical results, respectively.

Furthermore, Fujita et al also performed imaging spectroscopy associated with the line-by-line spectrum analysis by SPRADIAN2 to measure flow temperature and enthalpy under the conditions of P=90 kW, $\dot{m}$=2.0 g/s and p_{ch} =10 kPa with air in the 110-kW ICP wind tunnel [105]. Radial distributions of the flow temperature and enthalpy were obtained in the vacuum chamber [99, 105]. Fig. 4.7 and Fig. 4.8 show comparisons of the measured and computed temperature and enthalpy at x=811 mm under these operating conditions, respectively. As can be seen from these two figures, the simulated temperature and enthalpy show similar variation tendencies with the measured ones. Agreement between the computed and measured temperature and enthalpy can be observed in the radial location $y \geq 14$ mm. While near the center axis the simulated temperature and enthalpy are a few percent smaller than the measured ones within $y <$ 14 mm. The maximum relative errors between the simulated the measured temperature and enthalpy are within 5.2% and 14.4% there, respectively.

Following the work of Fujita et al [106], the rotational and vibrational temperatures of molecular nitrogen and nitric oxide were determined by optical spectroscopy measurements. Therefore, an additional calculation was carried out under the same conditions as used experimentally: P=70 kW, $\dot{m}$=2.0 g/s and p_{ch} =10 kPa. Fig. 4.9 compares numerical and experimental temperature data along the center axis under two different input-power conditions: P=70 and 90 kW, $\dot{m}$ =2.0 g/s and p_{ch} =10 kPa respectively. For the 90-kW computational case, the simulated rational temperature shows good agreement with the measured one at x=460 mm in the vacuum chamber. Near the chamber exit (x=811 mm), the simulated temperature roughly agree with the measured temperature, although it is about 290 K lower than the measured one there. For the 70-kW case, the computed vibrational temperature at x=110 mm is consistent with the measured rotational temperature of molecular nitrogen.

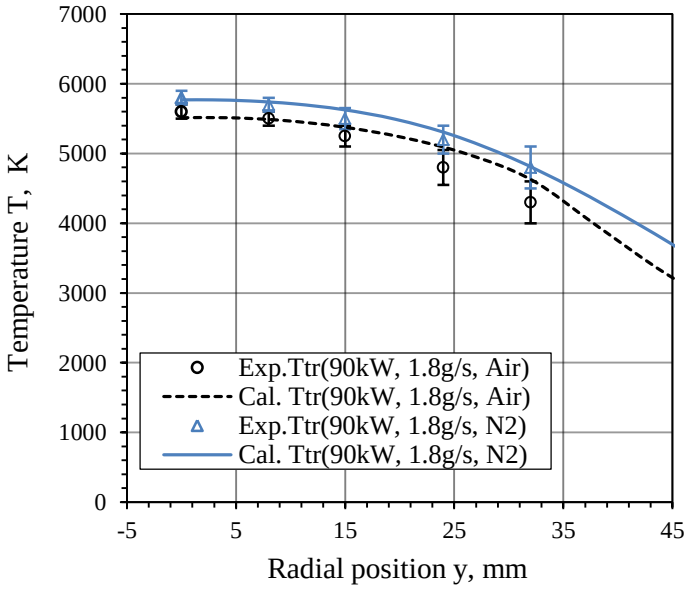

Fig. 4.6 Comparison of the measured and computed temperatures at x=662 mm in the vacuum chamber

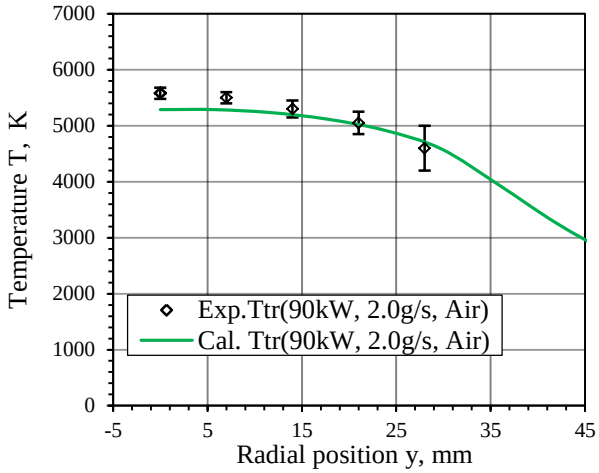

Fig. 4.7 Comparison of the measured and computed temperatures at *x*=811 mm in the vacuum chamber

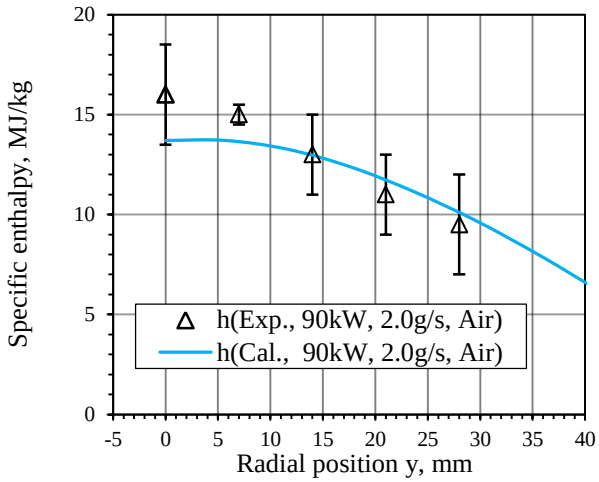

Fig. 4.8 Comparison of the measured and computed specific enthalpy at *x*=811 mm in the vacuum chamber

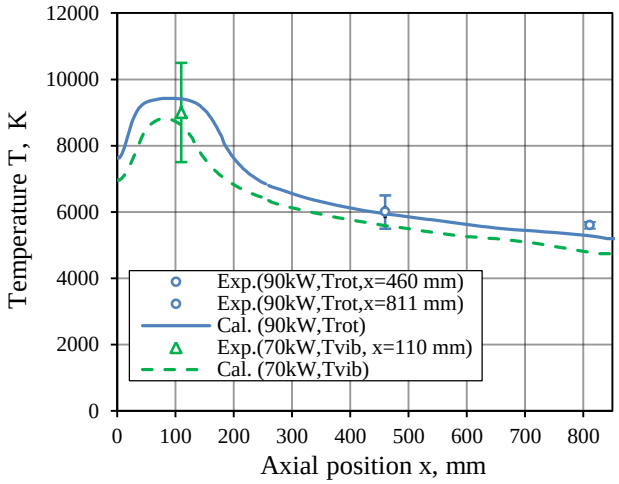

Fig. 4.9 Comparison of the measured and computed temperature along the center axis

4.3 Flow Characteristics in 10-kW and 110-kW ICPWTs

In this section, thermochemical nonequilibrium ICP flows with the test gas being nitrogen and air were modeled and studied in the 10-kW and 110-kW ICPWTs, respectively. First of all, the flow properties of the nitrogen ICP flow in the 10-kW ICPWT are discussed. The numerical results for the baseline case defined as an input power P=10 kW, mass flow rate $\dot{m}$=0.625 g/s, and chamber pressure p_{ch}=3.9 kPa, f=4.0 MHz are shown and discussed. Second, a nonequilibrium air ICP flow under the typical operating conditions: P=90.0 kW, $\dot{m}$=2.0 g/s, p_{ch} =10.0 kPa, f=1.78 MHz is modeled and studied in the 110-kW ICPWT.

4.3.1 10-kW ICPWT

Fig. 4.10 shows the temperature distributions of the computational results for the baseline case. Fig. 4.10(a) shows the distributions of the translational and electron temperatures; Fig. 4.10(b) shows the rotational and vibrational temperatures in the ICP torch; Fig. 4.10(c) shows the distribution of the translational temperature in the whole flow field for the baseline case. As is shown in Fig. 4.10(a), the maximum electron temperature (10563 K) appearing at the position (x, y) = (114, 28.5) mm is about 6163 K higher than the translational temperature there. Similar temperature difference between the vibrational and rotational temperatures is found in Fig. 4.10. The four temperatures do not equilibrate with each other in the coil region. It is confirmed that in the coil region the plasma flow is in thermal nonequilibrium. The maximum nonequilibrium degree $\theta = T_e/T_{tr}$ is about 2.40 there. The mechanism that leads to the differences between the electron and the translational, rotational temperatures are as follows. The electrical energy transferred to the plasma is primarily absorbed by the lightest and most mobile charged particles, i.e., the electrons. Due to relative small input power and stable property of nitrogen, only a few electrons were found under these working conditions (see Fig. 4.13). Therefore the total momentum and energy of electrons are small. So the energy exchange between electrons and heavy species in elastic collisions is inefficient under these working conditions. Thus, it is possible that the electron temperature stays different from the temperatures of atoms and molecules.

Fig. 4.11 shows the radial profiles of the four temperatures at x=114 mm in the coil region. Due to the dense electric field induced by the RF coil current and a negative radial Lorentz force in the coil region, large Joule heating was deposited in the region of x=110-118 mm, y=26-30 mm. Thus, the maximum electron temperature appears in this region. From the center axis to y=28.5 mm, the electron and vibrational temperatures increase gradually and separate from the translational, rotational temperatures. From y=28.5 mm to the torch wall, because the cooling water always flows on the quartz-tube wall, much heat flux is transferred to the wall and brought away by the cold water. Therefore, near the torch wall the four temperatures rapidly decrease.

Furthermore, as is also seen from Fig. 4.11, the vibrational temperature seems almost equal with the electron temperature in the high temperature region, but differs a lot from the translational and rotational temperatures. The reasons that lead to this phenomenon are as follows: for a diatomic molecular gas, because the cross section of diatomic molecule is larger than that of an atom, the electrons will preferentially transfer some energy to the heavy molecules through elastic collisions. On the other hand, due to the relatively small mole fraction of the electron under these working conditions (see Fig. 4.13), collisions between the molecules and electrons do not lead to rotational excitation,

because small amount of electrons possess small momentum. The rotational transitions occur preferentially when colliding particles have similar mass or the electrons possess sufficient large energy and momentum [26]. However, the vibrational excitation can be achieved because the vibrational excitation requires only the transfer of energy. According to the investigations of cross section and rate coefficients for such electron-impact vibrational excitation, Lee [34] has revealed that the relaxation time for equalization between the vibrational temperature of N_2 and electron temperature, which is shown in Fig. 2.11, is very short in the electron-temperature range 5000 -15000 K. The translational temperature, which was controlled by the total energy equation, denotes mean kinetic energy. Only a few electrons hardly cause large variations of the translational temperature. Therefore, in the high temperature region, the vibrational temperature almost equals the electron temperature, but differs from the translational and rotational temperatures.

Fig. 4.12 shows the axial profiles of the four temperatures at y=28.5 mm in the torch. As can be seen, the electron temperature rises rapidly from the torch inlet and reaches a peak value between the second and third coils. In the coil region, the thermal nonequilibrium degree of the flow dramatically increases first and then decreases from x=114 mm. On the other hand, near the torch exit, because of thermal diffusion and energy transfer in the region downstream of the coil, the four temperatures begin to equilibrate with each other. The flow tends to be in local thermal equilibrium from x=190 mm in the torch.

The mole fraction of chemical species at the axial position of x=114 mm is illustrated in Fig. 4.13. Because of high ionization energy of atomic nitrogen, few electron-impact ionization reactions occur in the coil region. The mole fraction of electron remains small even if at the highest temperature position. Atomic nitrogen is the dominant chemical species before y=27 mm at this axial position. 65.3% molecular nitrogen has been dissociated to form atoms and ions near the center axis. Few electrons and ionic species such as N^+ and N_2^+ are found in this case. In the region of y=20-27 mm, because of the increment of electron temperature depicted as Fig. 4.11, the electron-impact ionization reactions $N+e^- \rightarrow N^+ + e^- + e^-$ and $N+N \rightarrow N_2^+ + e^-$ proceed forward fast and cause a temporary increment of the electron mole fraction. Near the torch wall, with the rapid decrease of the four temperatures, the atomic nitrogen recombines to be molecular nitrogen quickly.

Recently, for the arc-heated flow simulation it was reported that turbulence model played an important role in the heat transfer process [27]. Therefore, in this study we tried to consider AKN k-ε turbulence model to take into account the turbulent energy transfer in an ICP simulation. Fig. 4.14(a) and (b) show distributions of turbulent energy k and dissipation rate ε in the torch for the baseline case. As can be seen, the maximum turbulent energy is about 0.15 J/kg beneath the first coil. Compared with the Joule heating rate, it is very small. Because the computed maximum Renolds number is 4045 for this computational case, the flow is thought to approximate laminar. Based on these, for this 10-kW ICPWT there seems no necessary to consider the turbulence model in the future study.

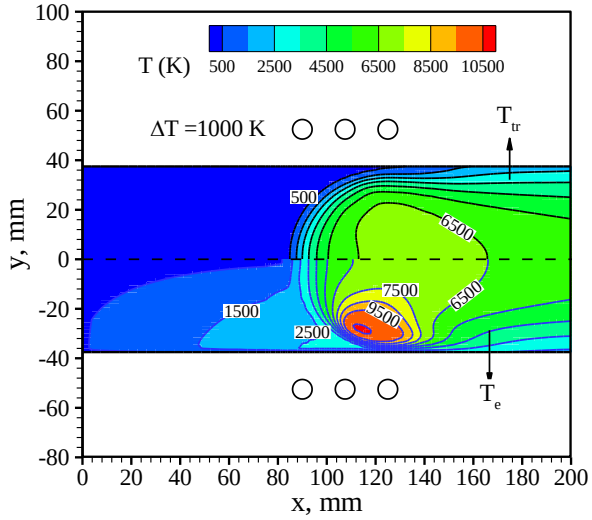

(a) Translational temperature T_{tr} (upper) and electron temperature T_e (lower) in the torch

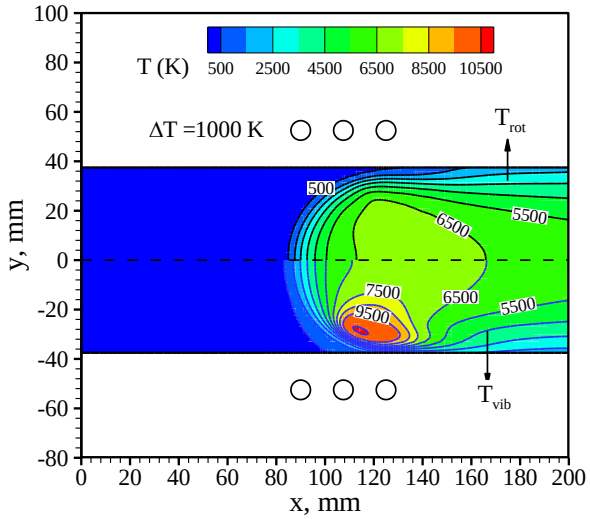

(b) Rotational temperature T_{rot} (upper) and vibrational temperature T_{vib} (lower) in the torch

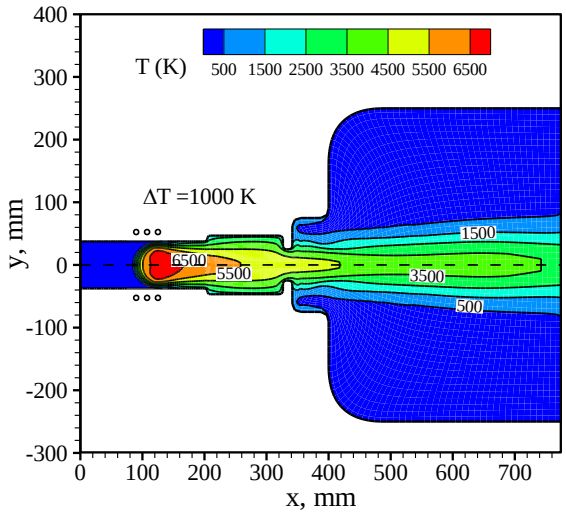

(c) Translational temperature in the whole flow field

Fig. 4.10 Distributions of the four temperatures

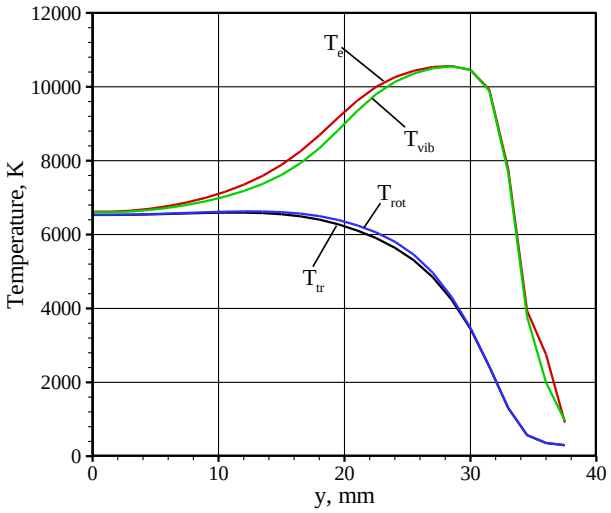

Fig. 4.11 Radial profiles of the four temperatures at *x*=114 mm in the coil region

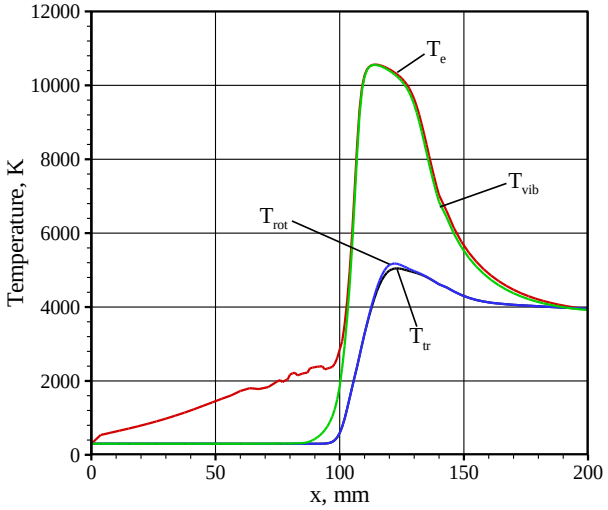

Fig. 4.12 Axial profiles of the four temperatures at *y*=28.5 mm in the torch

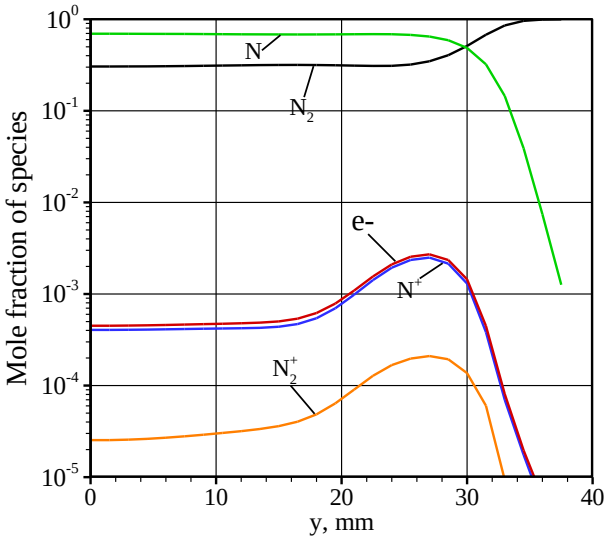

Fig. 4.13 Mole fraction of chemical species along the radial direction at *x*=114 mm

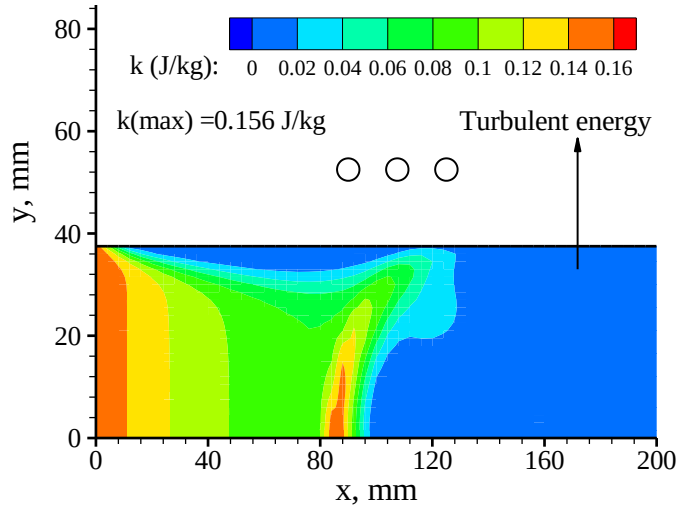

(a) turbulent energy

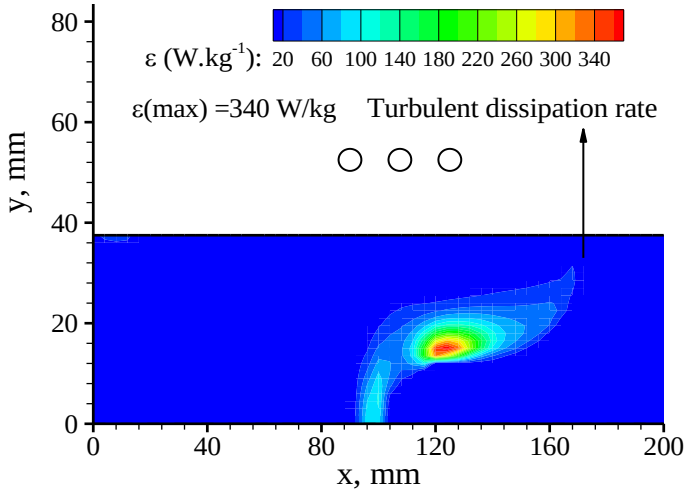

(b) turbulent dissipation rate

Fig. 4.14 Distribution of turbulent energy and dissipation rate

4.3.2 110-kW ICPWT

In this part, flow properties of the air ICP flow under the operating conditions: P=90.0 kW, $\dot{m}$=2.0 g/s, chamber pressure p_{ch} =10.0 kPa, f=1.78 MHz are shown and discussed. The distributions of mole fraction of chemical species and temperature are shown as follows.

The mole fraction of chemical species at the axial position of x=68 mm is illustrated in Fig. 4.15. Atomic nitrogen and atomic oxygen are the dominant chemical species before y ≤ 18 mm. Because of the relatively high input-power for this computational case, molecular oxygen and nitrogen have been almost completely dissociated to form atoms and ions along this radial direction. However, few amount electrons and ionic species such as ionized atomic nitrogen and oxygen are found there. It suggests that the dissociation reactions of molecular oxygen and nitrogen proceeds rapidly in this region, and are the major reactions there. The ionization degree of air species is still small in this high power case. In addition, the mole fractions of all chemical species are almost

not change at the position $y \leq 18$ mm. Local chemical equilibrium seems occur in this region. In the region of $y \geq 18$ mm, as the translational temperature gradually decrease (Fig. 4.21), the molecular nitrogen and monoxide nitrogen increase. Due to relatively low temperature near the torch wall ($y > 30$ mm), dissociation of molecular nitrogen hardly occur. The molecular nitrogen and molecular oxygen are dominant species near the wall.

The mole fractions of chemical species on the center axis for this computational case are illustrated in Fig. 4.16. Before the position of x=140 mm, atomic nitrogen and oxygen are the dominant chemical species on the center axis. In the region of x=140 - 500 mm, atoms and charged species begin to combine together. The recombination reactions of ionic and atomic nitrogen become dominant, and cause the mole fractions of molecular nitrogen gradually increase along the center line. In the vacuum chamber, as the flow approaches the position x=500 mm, most atomic nitrogen has compounded to be molecules. The major components become molecular nitrogen and atomic oxygen after this point. In the discharge ICP torch, before the position of x=140 mm, the mole fractions of all chemical species show a flat distribution along the center axis. Such flat distribution is in accordance with the flat temperature distribution shown in Fig. 4.17 along the center axis. Combining with the flow characteristics discussed on Fig. 4.15, These results indicate that the air ICP flow approximate not only local thermal equilibrium but also local chemical equilibrium near the center axis in the inductive discharge region for this 110-kW ICPWT.

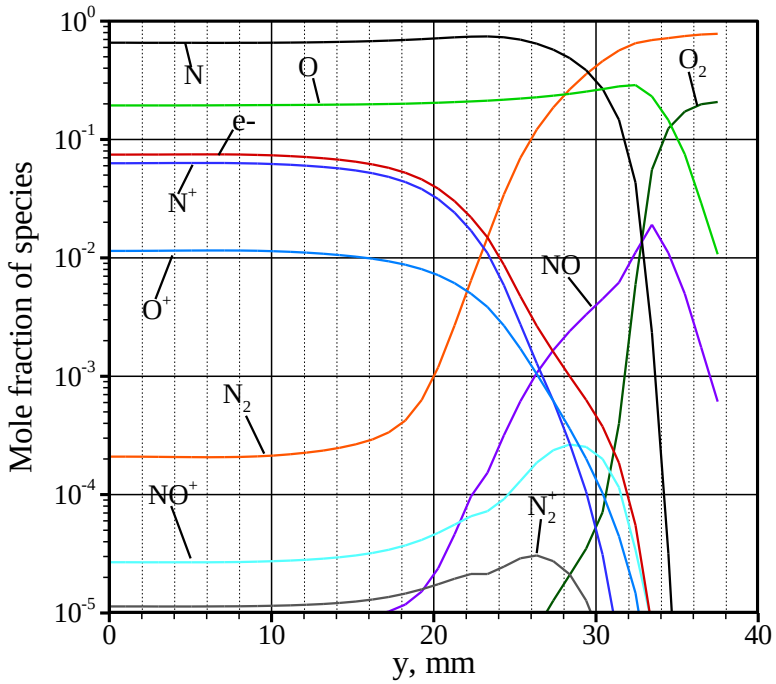

Fig. 4.15 Mole fraction of chemical species along the radial direction at x=68 mm

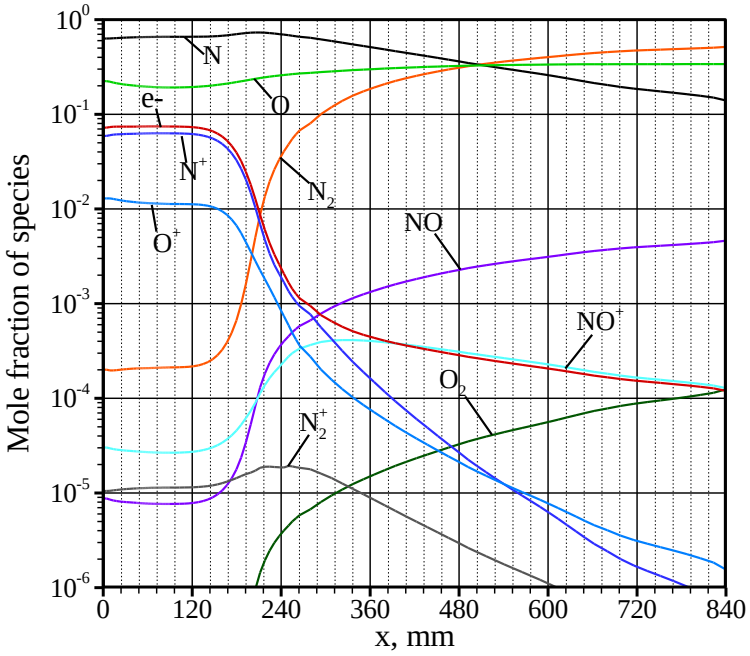

Fig. 4.16 Mole fraction of chemical species along the center axis

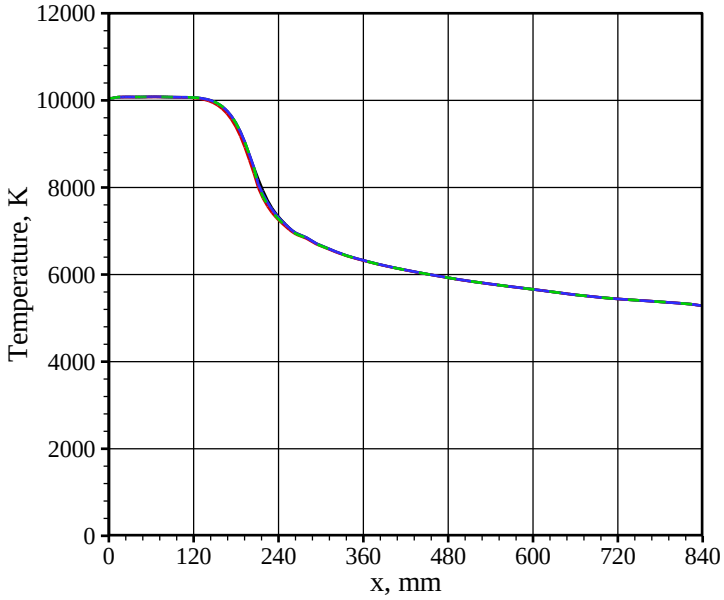

Fig. 4.17 Axial profiles of the four temperatures on the center axis

Fig. 4.18 and Fig. 4.19 show the temperature distributions of the computational results for the abovementioned computational case. Fig. 4.18 shows the distributions of the translational and electron temperatures. As is shown in the figure, the maximum electron temperature is almost equal with the maximum translational temperature (10110 K) near the position (x, y) = (68, 26) mm. While the area of high electron temperature (e.g., the region of $8500 \leq T \leq 9500$ K) is wider than the area of high translational temperature. The distribution of electron temperature seems identical with that of the translational temperature near center axis, while it does not equilibrate with the translational temperature near the torch wall in the coil region. It indicates that the air ICP flow tends to be thermal nonequilibrium along the radial direction. Specifically,

the flow become thermal nonequilibrium after $y \geq 26$ mm; in the region of $y < 26$ mm the flow also approximates local thermal equilibrium for this high power 110 kW ICPWT. The reason for this wide thermal-equilibrium region is thought to be the high working pressure condition for this computational case. Because a high pressure or density working condition will lead to frequent collisions between electrons and heavy particles, and then result in sufficient energy exchanges between electronic and other energy modes.

Fig. 4.19 shows distribution of translational temperature in the whole flow field. As is shown in Fig. 4.19, because of large energy dissipation in coil region, the translational temperature of the gas increases dramatically there. In vacuum chamber, we can see that a relatively wide area is involved in the temperature range from 5000 to 6000 K. An almost uniform temperature environment was achieved in this zone. The plasma column (high-temperature flow region) keeps almost same width until outlet boundary.

Fig. 4.20 shows axial profiles of the four temperatures at y=26 mm in the torch. As can be seen, the electron temperature rises rapidly from torch inlet and reaches a peak value between the second and third coils. In the coil region, the thermal nonequilibrium degree of the flow dramatically increases first and then decreases from x=68 mm. On the other hand, after x=120 mm, because of thermal diffusion and energy transfer between internal energy modes the four temperatures begin to equilibrate with each other. The flow tends to be in local thermal equilibrium from x=120 mm in the torch.

Fig. 4.21 shows the radial profiles of the translational and electron temperatures at x=68 mm in the coil region. Due to the severe inductive discharge in the coil region, large Joule heating was deposited in the region of x=51-84 mm, y=20-30 mm. Thus, the maximum electron temperature appears in this region. From the center axis to y=18 mm, the electron and translational temperatures are equal with each other, and show a flat distribution along the radial direction. From y=18 mm to the torch wall, the electron temperature begin to separate from the translational temperature. Thermal nonequilibrium phenomenon is visible in this region. Near the torch wall e.g., $y > 30$ mm, both of the electron and translational temperatures rapidly decrease.

Fig. 4.22 (a) and (b) show distributions of turbulent energy k and dissipation rate ε in the 110-kW ICPWT for case 8. As can be seen, the maximum turbulent energy is 81 J/kg and appearing in the vacuum chamber. Compared with the flow kinetic energy there ($0.5U^2 \approx 10000$ J/kg, see Fig. 4.30(b)), the turbulent energy is also very small.

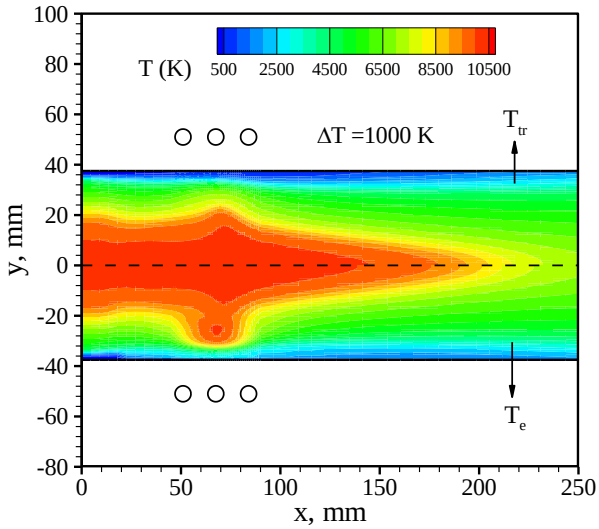

Fig. 4.18 Translational temperature (upper) and electron temperature (lower) in the torch

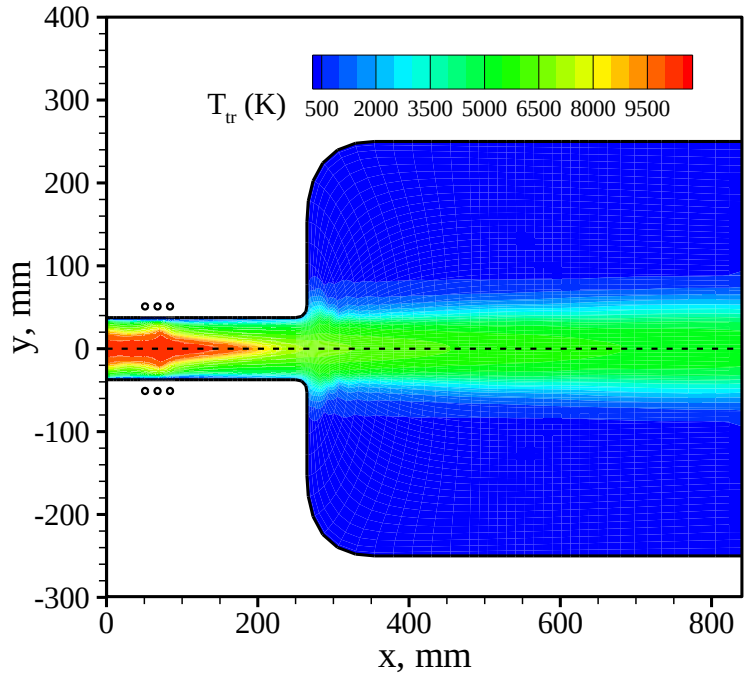

Fig. 4.19 Translational temperature distribution in the whole flow field

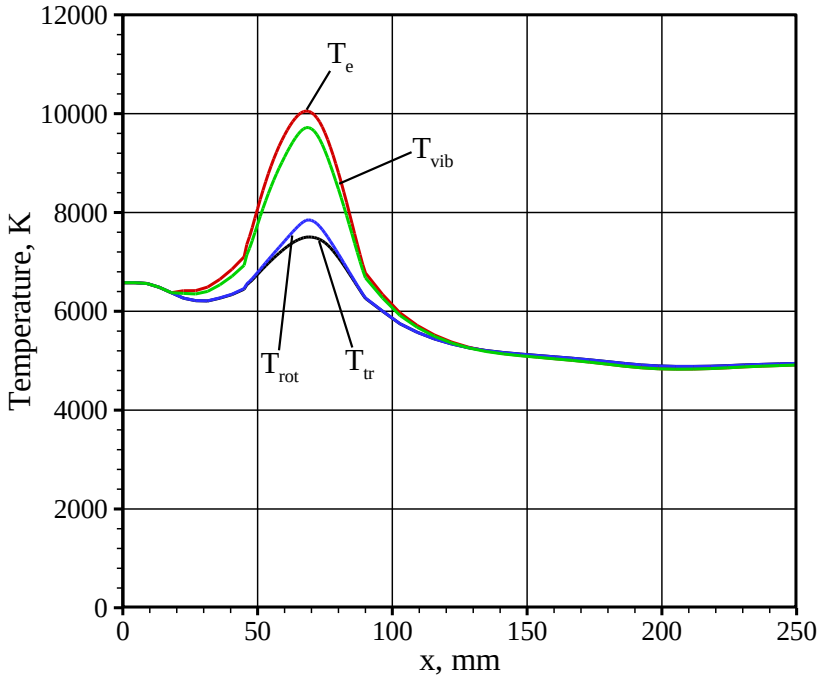

Fig. 4.20 Axial profiles of the four temperatures at *y*=26 mm in the torch

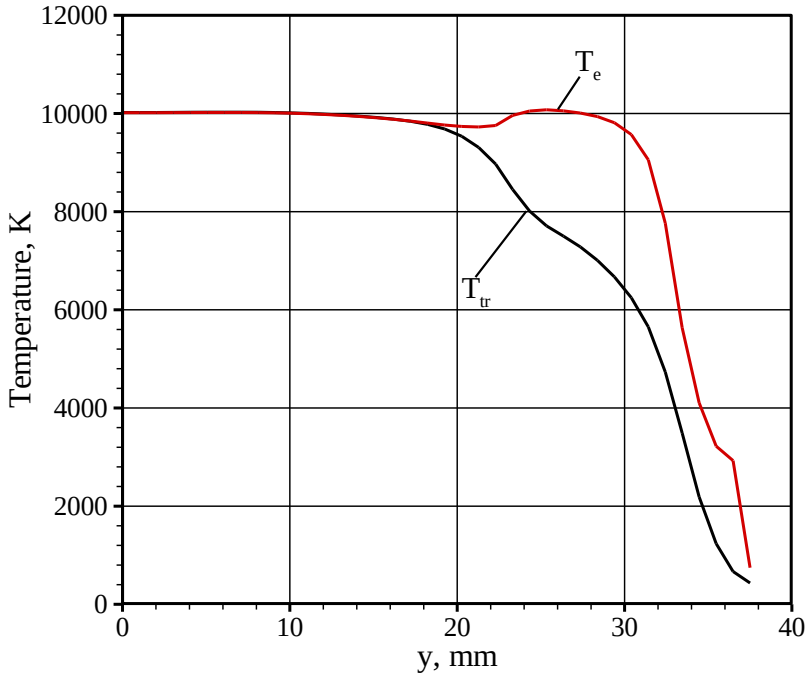

Fig. 4.21 Radial profiles of the translational and electron temperatures at *x*=68 mm in the coil region

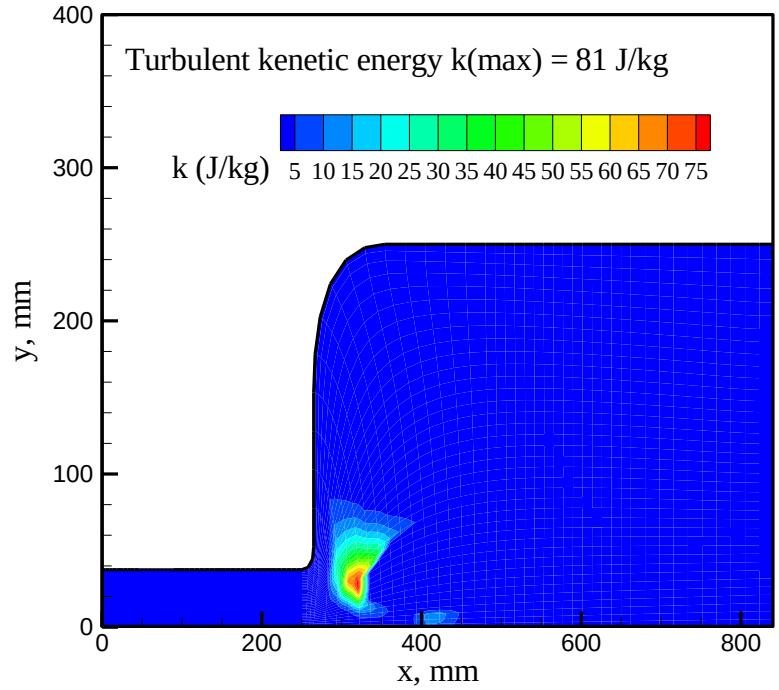

(a) turbulent energy

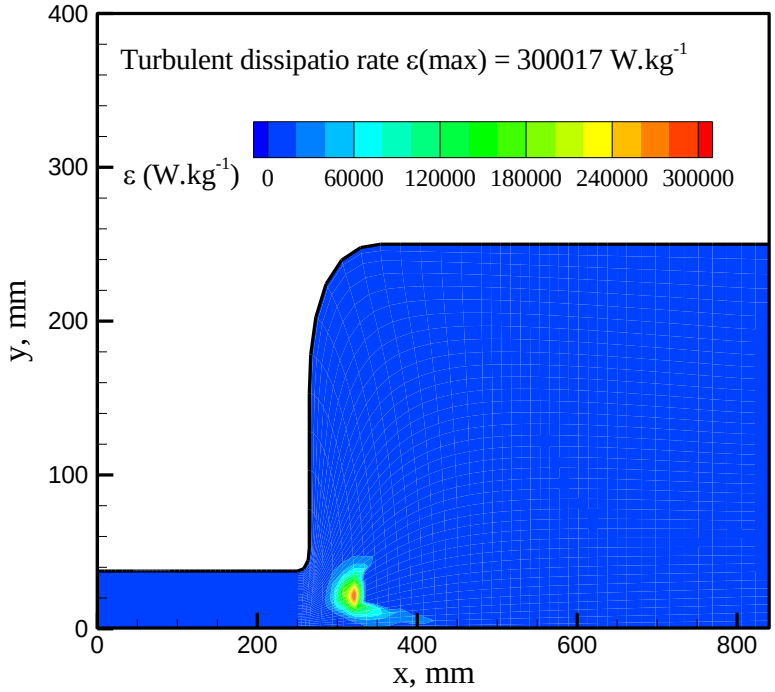

(b) turbulent dissipation rate

Fig. 4.22 Distribution of turbulent energy and dissipation rate

4.4 Interactions between Electromagnetic and Flow Fields

In this section, the interactions between the electromagnetic and flow fields of nitrogen and air ICP flows in the 10-kW and 110-kW ICPWTs are discussed, respectively. The distributions of flow velocity, Lorentz forces, Joule heating rate, electric field intensity etc. for each facility are discussed and analysed in detail.

4.4.1 10-kW ICPWT

The interactions between the electromagnetic and flow fields of a nitrogen ICP flow are investigated in the 10-kW ICPWT. The operating conditions for the 10-kW ICPWT are identical with the baseline case.

Fig. 4.23 shows the distributions of streamlines, vector plot and axial velocity *u* in the torch for the baseline case. Because of a strong inductive discharge, a large part of the Joule heating energy is dissipated in the coil region and results in the increase of the gas velocity and temperature there. Through the distribution of streamlines, we can see that a recirculation flow occurs beneath the first and second turns of the coil. This recirculation is thought to be caused by the comprehensive effects of pressure, the Joule heating and Lorentz forces generated by the electric and magnetic field in the coil region. Similar vortex was also found in the argon ICP flow [16].

Fig. 4.24 shows the distributions of streamlines and pressure in the torch. As can been seen from the figure, The maximum pressure appears between the second and the third coil. The recirculation flow occurs ahead of the maximum pressure position. The negative pressure gradient between the second and third coil seems the direct reason for the recirculation flow from the Fig. 4.24. Because the distributions of velocity and pressure are both affected by the Lorentz forces in the momentum equations. Moreover, flow velocity is also affected by the Joule heating rate in energy equations. Therefore,

this recirculation flow is thought to be caused by the comprehensive interactions among the pressure, Lorentz forces and Joule heating rate.

Fig. 4.25 shows the distributions of axial and radial Lorentz forces which were added in the corresponding momentum equations. Lorentz forces can affect the momentum transfer in both the axial and radial directions. The axial Lorentz force shows a positive direction first, while changes to the inverse direction beneath the 3rd turn of the coil. Additionally, in this study both the gravity and the axial Lorentz force were considered and added in the axial momentum equation as the source terms. Although the gravity was considered, its maximum value was much smaller than that of the axial Lorentz force in the flow field (F_{Lx}(max)=986 N, G(max) =0.5 N). Therefore, the axial Lorentz force played the main role in the axial momentum transfer, the influence of gravity on the flow properties was very small. On the other hand, the radial Lorentz force is always negative and its peak value is several times bigger than the axial Lorentz force. The negative radial Lorentz force indicates that the plasma flow will be pushed to approach the center axis by it. In addition, under the effect of the radial Lorentz force the Joule heating rate distribution which is illustrated in Fig. 4.26 is similar to that of the radial Lorentz force.

Fig. 4.26 shows the distributions of Joule heating rate (upper) and electron temperature (lower). Because of inductive discharge by the coil current, several Joule heating will appear in the coil region; On the other hand, because the Joule heating rate is expressed as: $S_{joule} = \frac{1}{2}\sigma E^2 = \frac{1}{2}\sigma\left(E_R^2 + E_I^2\right)$. It means the Joule heating rate will be controlled by the distributions of electrical conductivity and electric field E together. Although the maximum E^2 appears near the torch wall. Because the wall temperature is limited to be less than 1000 K due to cooling water on the wall, it causes the flow temperature near the wall is low i.e., the electrical conductivity is small there. So the maximum Joule heating rate do not appear on the wall but determined by the electrical conductivity and electric field together. Because of the light mass and active property of electrons, the electrical power (i.e., Joule heating rate) is primarily absorbed by the electrons. So the high electron-temperature area appears in the similar region where the large Joule heating rate appears.

Fig. 4.27 shows the distribution of electric field intensity: imaginary part E_I (upper) and real part E_R (lower) in the torch. The imaginary part of electric field intensity E_I determined by vector potential $E_I = -\omega A_R$ is the main part of the electric field intensity E. Its peak value is about 3 times bigger than the E_R. E_R is always negative in the torch, but E_I shows negative values first and turns to positive beneath the third coil near the center axis. The negative electric field is mainly induced by the coil current, the positive electric field is thought to be generated by plasma current.

Fig. 4.28 shows the distribution of electric field intensity E_I (upper) and electron number density n_e (lower) in the torch. As can be seen from the figure, electrons gathered in the region where the positive E_I appeared. It indicates that the positive electric field intensity E_I is probably generated by these electrons which form the plasma current in the torch.

Fig. 4.29 show the distribution of magnetic vector potential in the far-field region, (a) real part A_R; (b) imaginary part A_I. The real part of magnetic vector potential A_R shows high intensity near the coils. The maximum A_R also appears in the coils. It indicates that the vector potential A_R is mainly induced by the coil current. Because the vector potential is different from the electric field by the angular frequency $\omega = 2\pi f = 2.5 \times 10^7$. So the value of the vector potential is small.

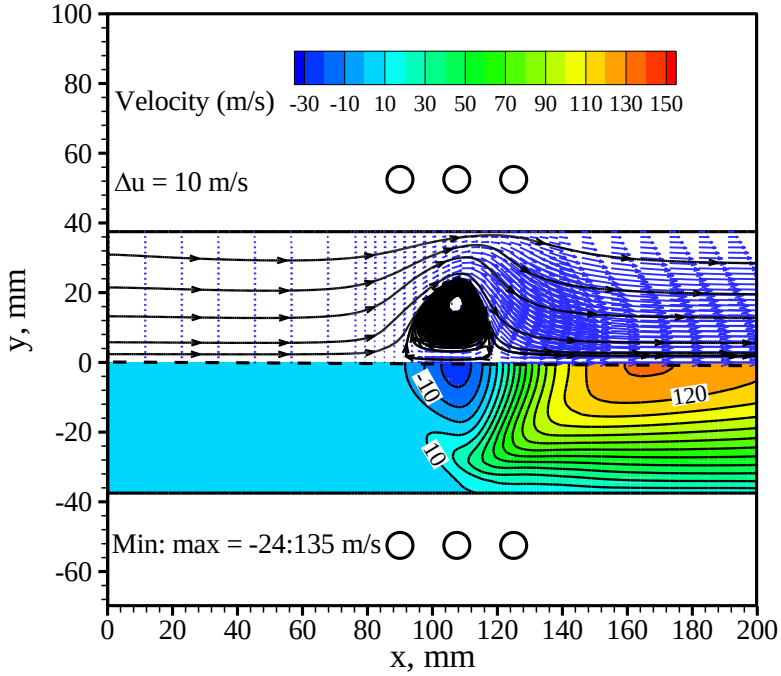

Fig. 4.23 Distributions of streamlines & vector plot (upper) and axial velocity u (lower)

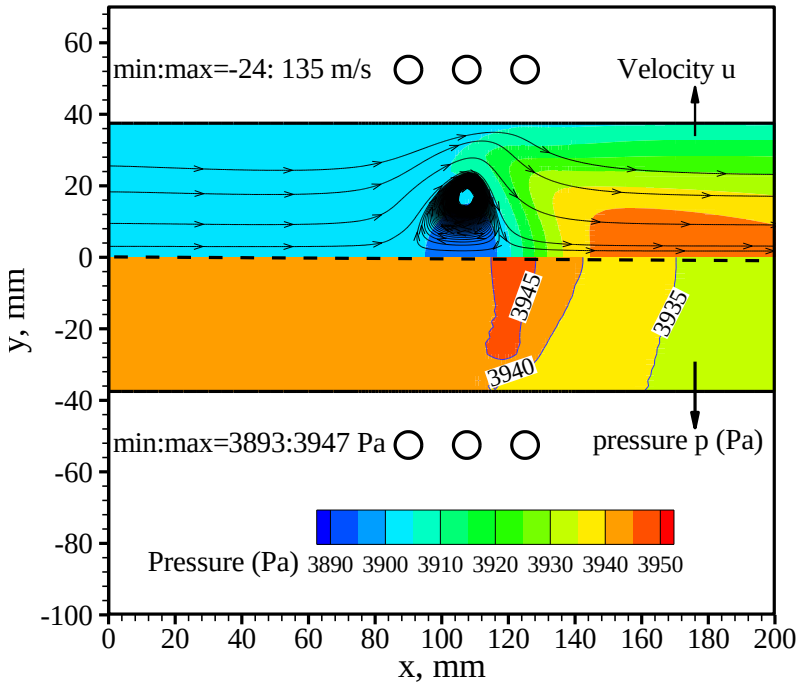

Fig. 4.24 Distributions of streamlines (upper) and pressure (lower)

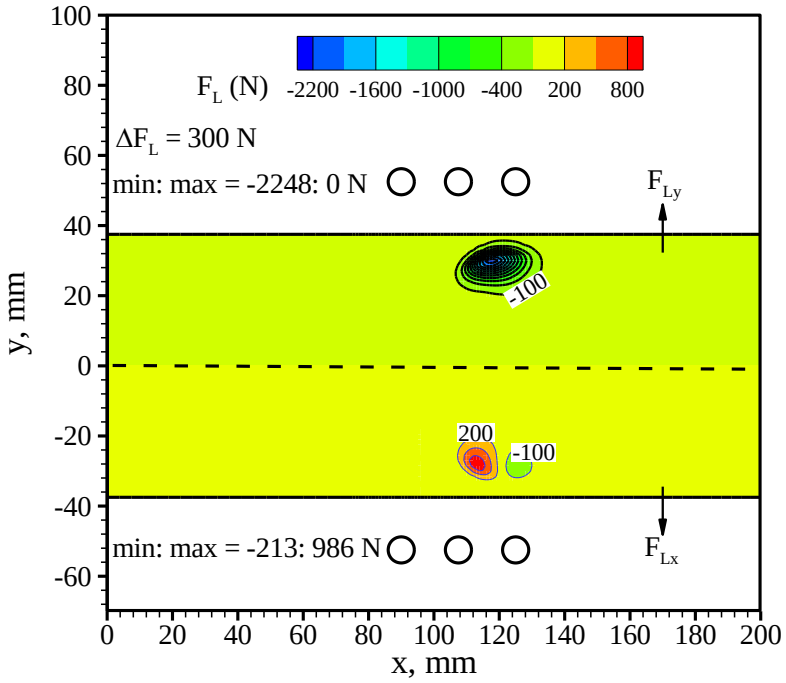

Fig. 4.25 Distributions of axial Lorentz force (upper) and radial Lorentz force (lower)

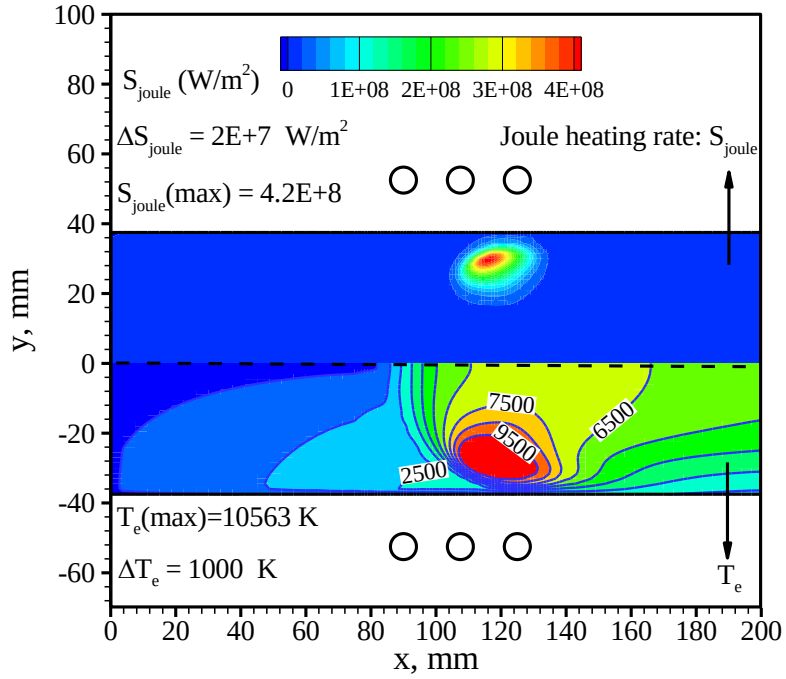

Fig. 4.26 Distributions of Joule heating rate and electron temperature

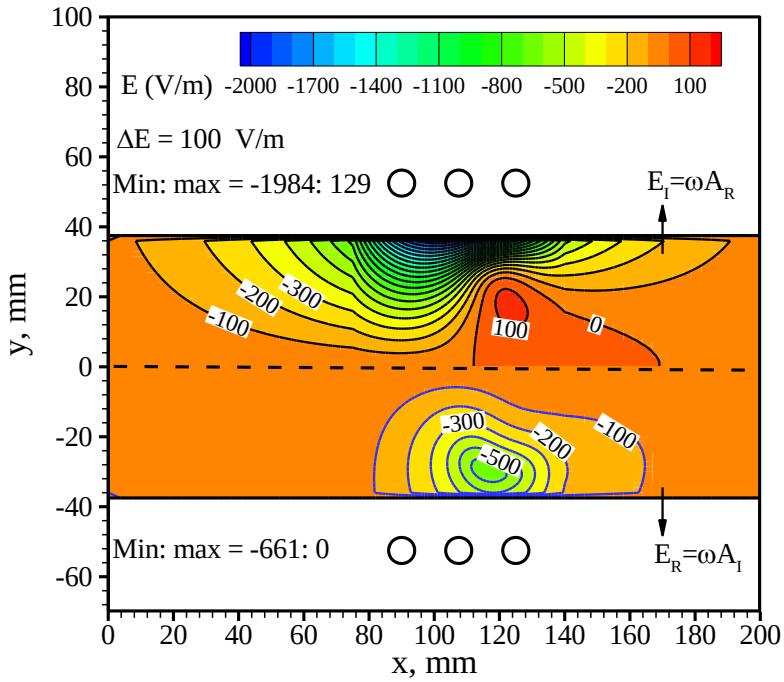

Fig. 4.27 Distribution of electric field intensity: imaginary part E_I (upper) and real part E_R (lower)

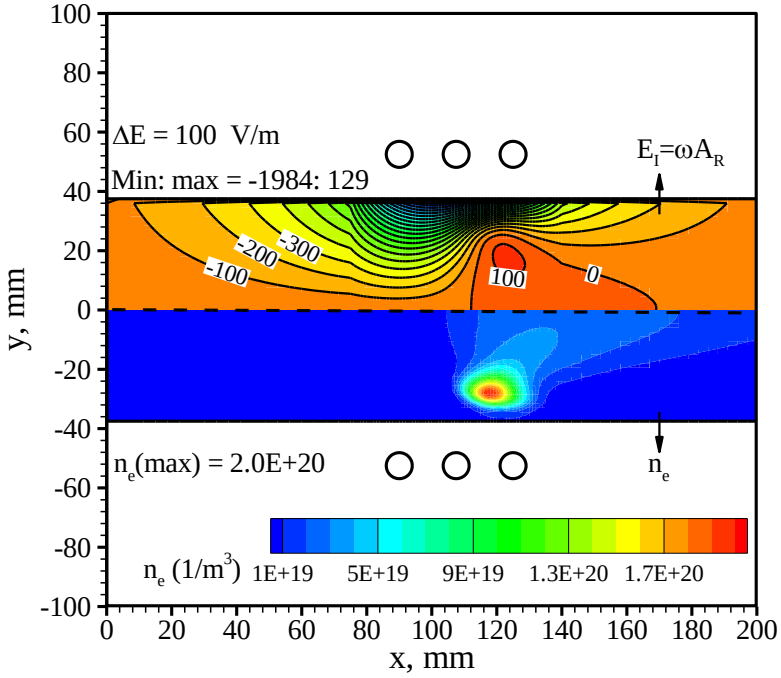

Fig. 4.28 Distribution of electric field intensity E_I (upper) and electron number density n_e (lower)

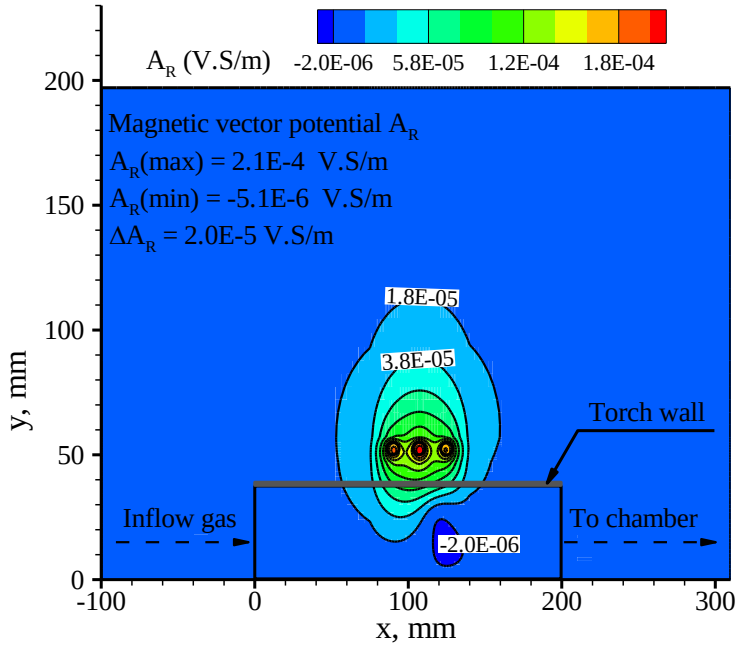

(a) Real part of the magnetic vector potential A_R

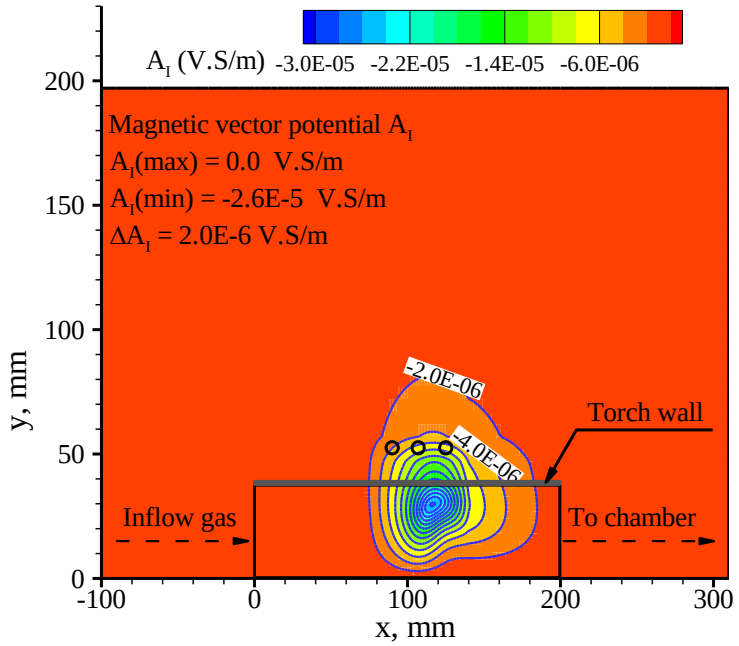

(b) Imaginary part of the magnetic vector potential A_I

Fig. 4.29 Distribution of the magnetic vector potential in the far-field, (a) A_R; (b) A_I

4.4.2 110-kW ICPWT

In this section, the interactions between the electromagnetic and flow fields of the air ICP flow are investigated in the 110-kW ICPWT. The operating conditions of the computational case are as following: P=90.0 kW, $\dot{m}$=2.0 g/s, p_{ch} =10.0 kPa, f=1.78 MHz. Fig. 4.30 shows the distributions of streamlines, vector plot and axial velocity u in the torch. Because of the different inflow manner for this large power ICPWT, a strong

recirculation flow is observed at the inlet. The negative pressure gradient as well as the narrow gas inlet (inlet width is 2.4 mm) is the main reason for the recirculation flow. As can be seen from the distribution of streamlines, the recirculation flow occurs beneath the first and second turns of the coil. Sumi et al. also revealed a similar vortex in their numerical study [5].

Fig. 4.31 shows the distribution of streamlines and pressure in the torch. For this 110-kW ICPWT, the maximum pressure appears between the first and second coil rather than between the second and third coils. While the recirculation flow also occurs ahead of the maximum pressure position. Fig. 4.32 shows the distributions of axial and radial Lorentz forces. A pair of axial Lorentz forces with an inverse direction appears in the coil region. But this time, the value of the negative axial Lorentz force is bigger than the positive one, which is different from the trend of the axial Lorentz force in the 10-kW ICPWT. Because the negative axial Lorentz force acts as the obstructive force for the ICP flow, so the strong recirculation flow appears in this computation.

Fig. 4.33 shows the distributions of radial Lorentz force (upper) and Joule heating rate (lower). As can be seen from the figure, the distribution and location of Joule heating rate is very similar to those of radial Lorentz force. It implies that the distribution and location of Joule heating rate is controlled by radial Lorentz force for this air ICP flow. Furthermore, it is to say that the positions of peak temperature and velocity of this air ICP flow were indirectly affected by the radial Lorentz force.

Fig. 4.34 shows the distribution of electric field intensity: imaginary part E_I (upper) and real part E_R (lower) in the torch. A high-intensity electric field is seen in the coil region. The peak value of E_I is about 4.5 times bigger than maximum E_R. E_R is always negative in the torch, but E_I shows negative values first and turns to positive beneath the third coil near the center axis. Fig. 4.35 shows the distribution of electric field intensity E_I (upper) and electron number density n_e (lower) in the torch. As can be seen from the figure, under the effect of intense electric field, electrons moves downward to the center axis. A lot of electrons gathered in the coil region. Due to the strong recirculation near the inlet, electrons were also transferred to the vicinity of the inlet. Fig. 4.36 show the distribution of magnetic vector potential in the far-field region, (a) imaginary part A_I; (b) real part A_R. The peak value of A_R is much bigger than maximum A_I. The real part of magnetic vector potential A_R shows a high intensity around the coil position.

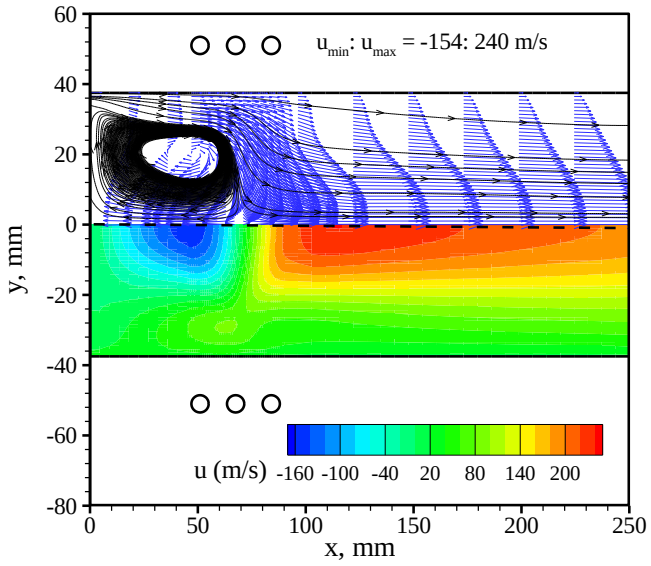

(a) in the torch

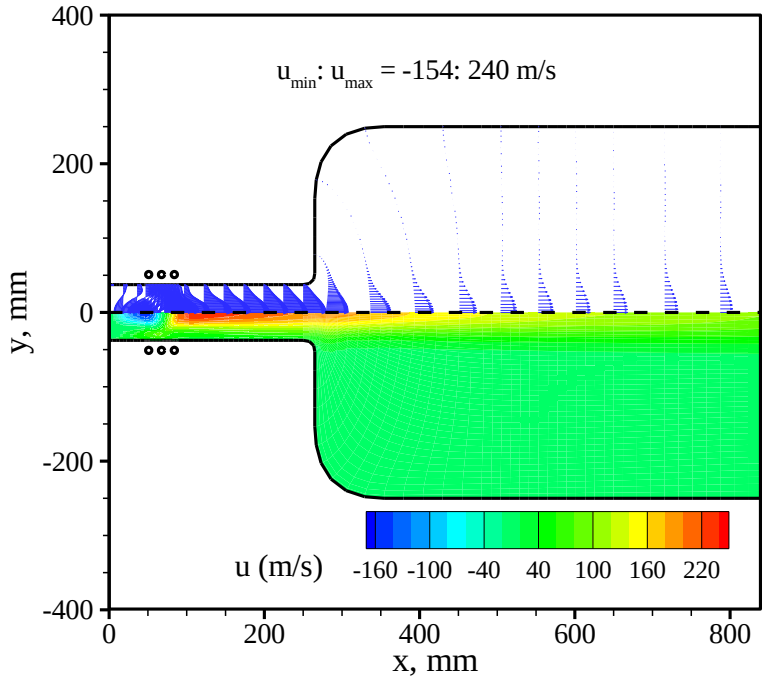

(b) in the whole flow-field

Fig. 4.30 Distributions of streamlines & vector plot (upper) and axial velocity u (lower)

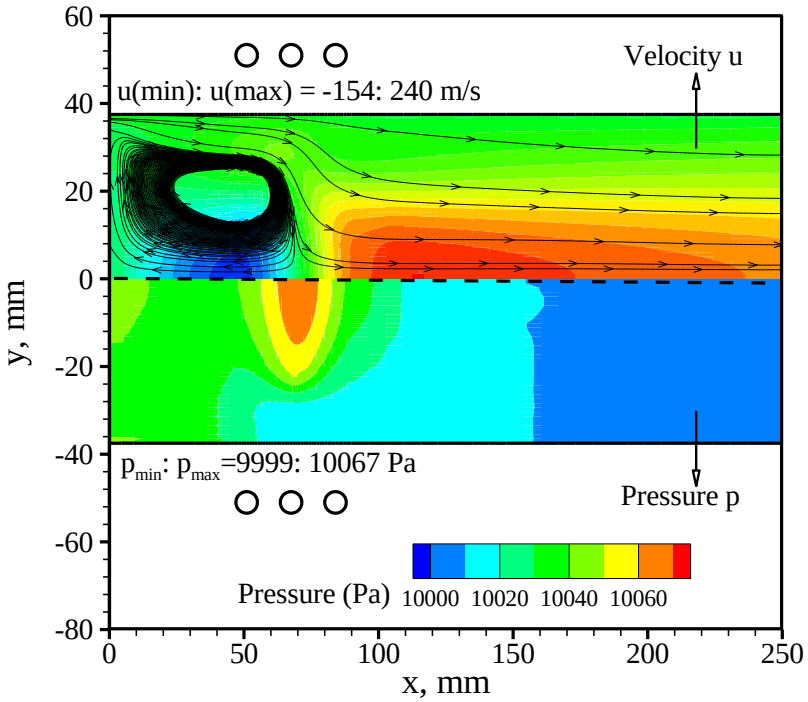

Fig. 4.31 Distributions of streamlines (upper) and pressure (lower)

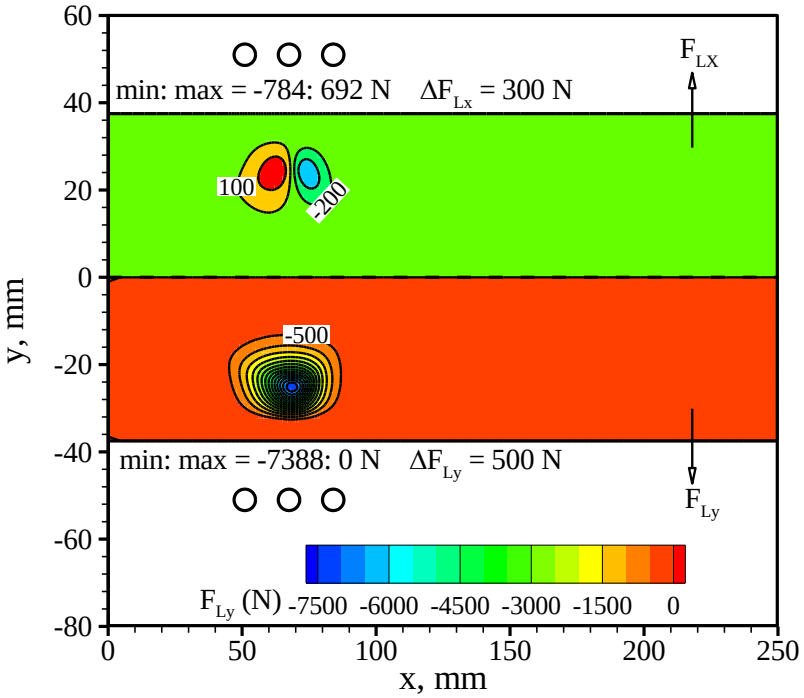

Fig. 4.32 Distributions of axial Lorentz force (upper) and radial Lorentz force (lower)

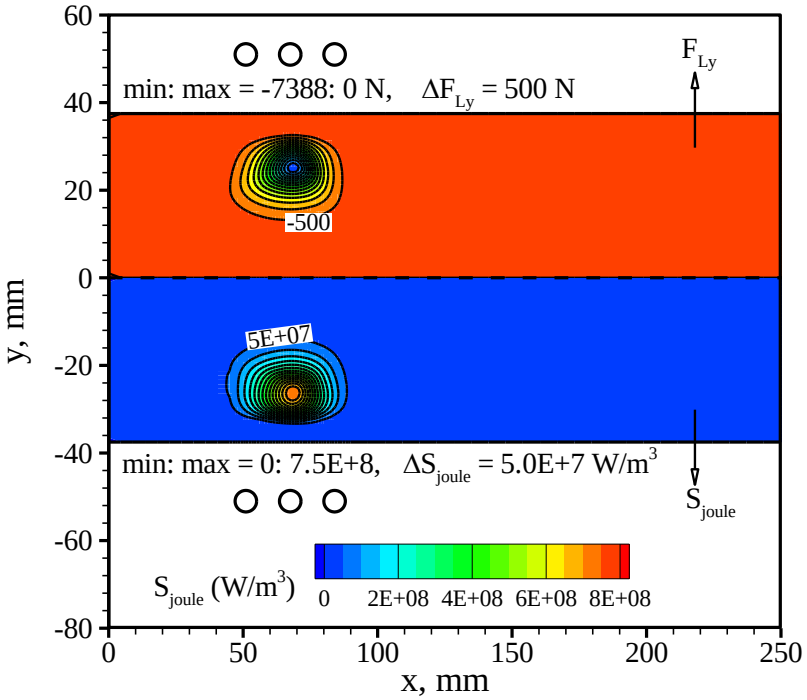

Fig. 4.33 Distributions of Joule heating rate and radial Lorentz force

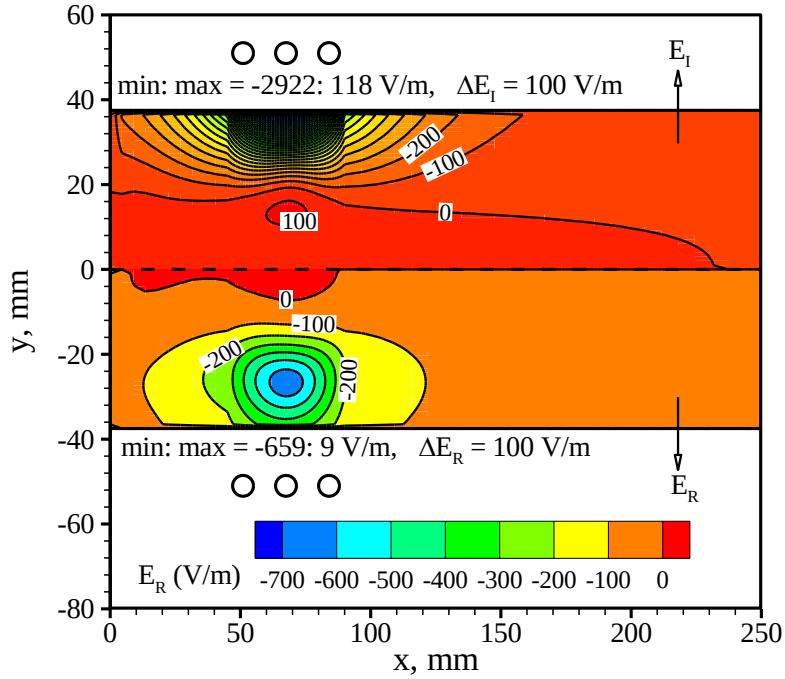

Fig. 4.34 Distribution of electric field intensity: imaginary part E_I (upper) and real part E_R (lower)

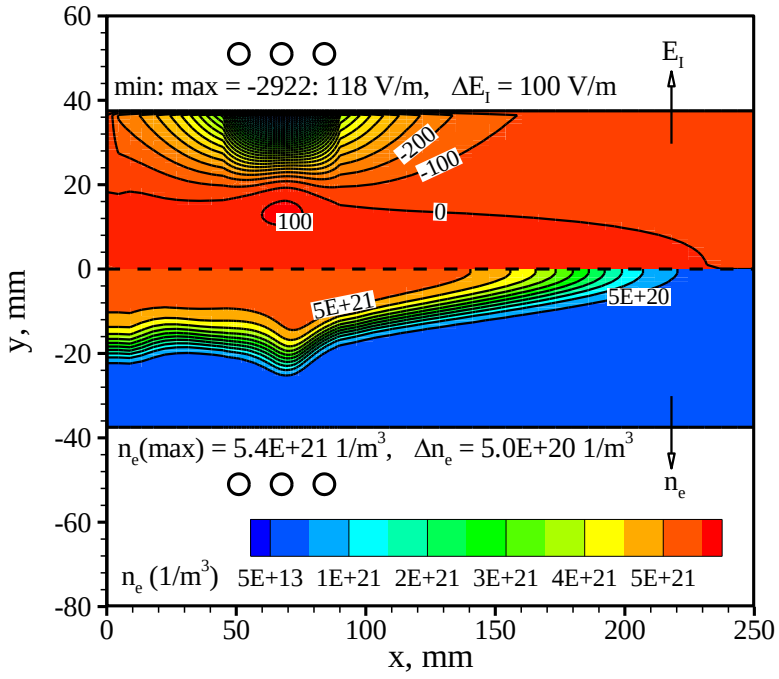

Fig. 4.35 Distribution of electric field intensity E_I (upper) and electron number density n_e (lower)

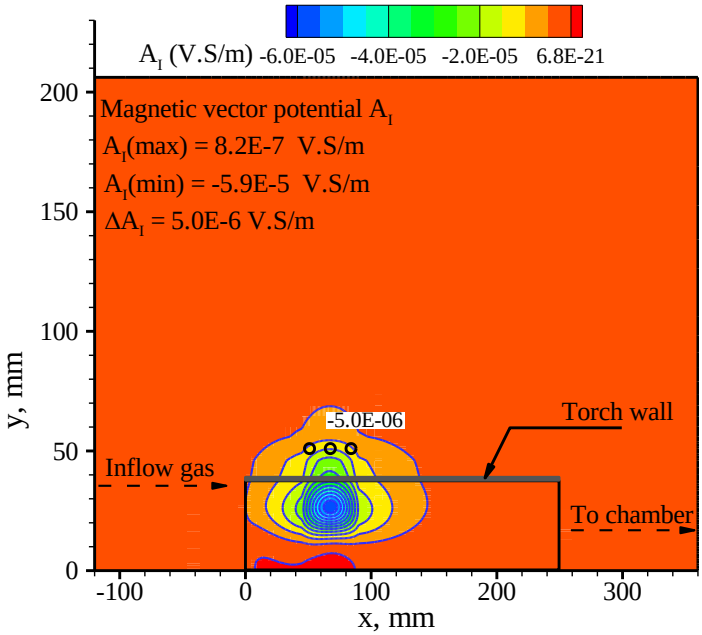

(a) Imaginary part of the magnetic vector potential A_I

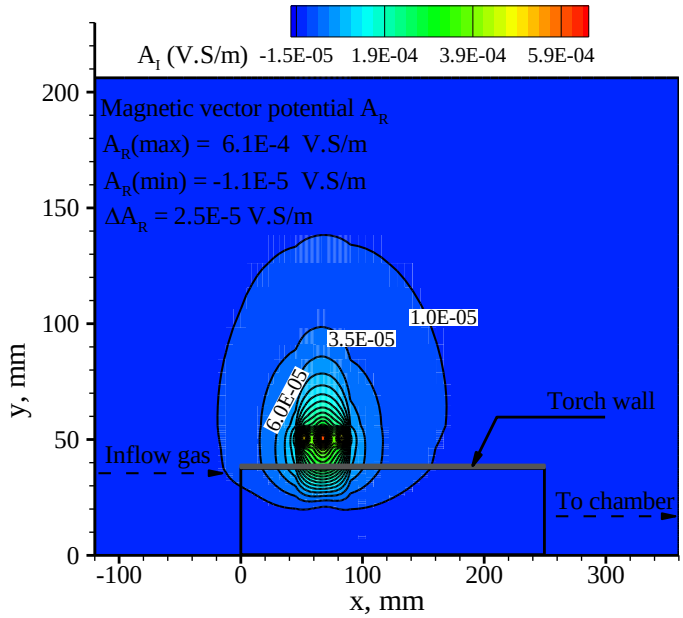

(b) Real part of the magnetic vector potential A_R

Fig. 4.36 Distribution of the magnetic vector potential in the far-field, (a) A_R; (b) A_I

4.5 Effects of Thermal Equilibrium and Nonequilibrium Model

In this section, we give a comparison between the numerical results obtained under the assumption of local thermal equilibrium (one-temperature model i.e., 1T model) and thermal nonequilibrium (four-temperature model i.e., 4T model) under the operating conditions of an input power P=10 kW, mass flow rate $\dot{m}$=0.625 g/s, and chamber pressure p_{ch} =7.2 kPa in the 10-kW ICPWT.

Fig. 4.37(a) and (b) shows the comparison of temperatures obtained by the 1T and 4T models. We can see that as the result of 1T model, the plasma flow moves much

downward in the coil region when it is compared with the temperature distribution obtained by using the 4T model. This is caused by the bigger axial Lorentz force for the 1T model case. Table 4.2 shows the comparisons of the computed maximum temperatures, Lorentz forces, electric field, etc. The relative deviation is defined as $\left(z^{1T}-z^{4T}\right)/z^{4T}$ where z denotes temperatures, Lorentz forces, and electric field parameters, etc. As is shown in the table, when the 1T model was used, the maximum axial Lorentz force is larger than the force obtained by using the 4T model. Therefore, under the 1T model the plasma flow was pushed to the much downward position in the coil region. Furthermore, regarding to the 1T model, because the electron temperature was assumed to be identical with the heavy particle's average temperature T_{tr}. This assumption is valid in high-pressure conditions e.g., atmospheric pressure condition, in which the internal energy exchange between electron and other species can sufficiently carry on through frequent elastic collisions. Compared with the atmospheric pressure, the working pressure of the 1T-model case (p_{ch}=7.2 kPa) is low. Therefore the assumption of local thermal equilibrium for this low pressure case would result in big numerical error on the evaluation of temperature field. Because the chemical reaction rates and magnetic vector potential equations were highly related to the electron and translational temperatures, the numerical errors caused by the 1T model would be accumulated on the computations of chemical reactions and electromagnetic equations, and then transferred to the whole flow field. As is illustrated in Table 2, the relative errors of T_{tr}, F_{Lx}, and E_{I} between the 1T and 4T model cases are as large as 21.8%, 28.0%, and 96.6%.

Fig. 4.38 shows the comparison of T_{tr} obtained by the 1T and 4T models for case 4: (a) in the whole flow field; (b) at x=700 mm in vacuum chamber. (1) From the figure (a) we can see that in the coil region the maximum T_{tr} obtained by the 1T model is about 1000 K higher than the one calculated by the 4T model. As flow proceeds downward, the temperature difference becomes smaller and smaller along the radial direction. On the other hand, combining with the Fig. 4.37 we can see that the temperature difference in the coil region seems decrease with the increase of working pressure. (2) Seen from Fig. 38(b), the temperature simulated by the 1T model at x=700 mm in the vacuum chamber is about 200 K higher than the one computed by the 4T model within y≤60 mm. The temperature difference seems small in the test chamber.

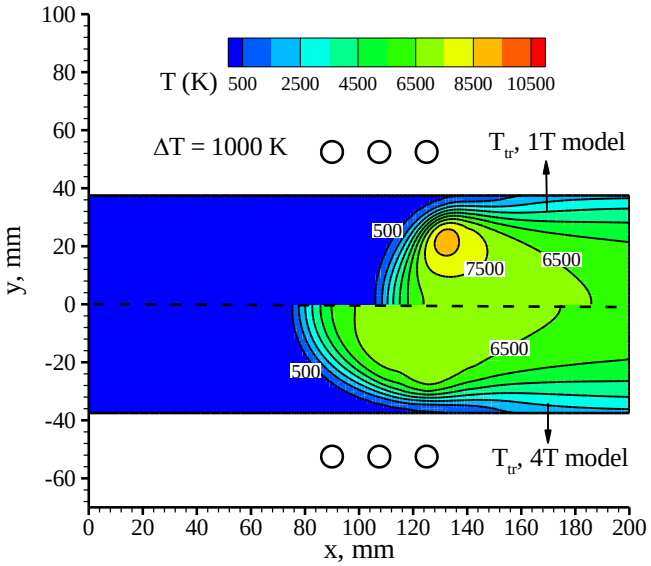

(a) Translational temperature (1T model) – Translational temperature (4T model)

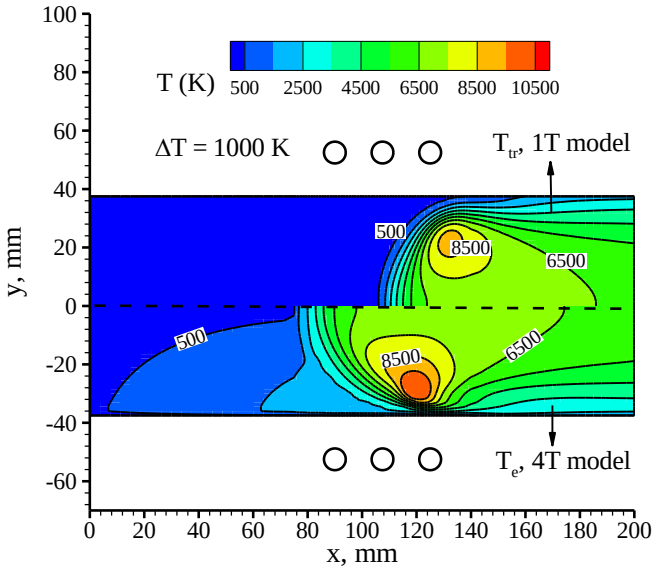

(b) Translational temperature (1T model) – Electron temperature (4T model)

Fig. 4.37 Comparison of temperature obtained by the 1T (upper) and 4T (lower) models

Table 4.2 Comparison of numerical results between the 1T and 4T models

	T_{tr} (K)	T_e (K)	F_{Lx} (N)	$-F_{Ly}$ (N)	$-E_R$ (V/m)	$-E_I$ (V/m)	σ (S/m)
1T model, z^{1T}(max)	8947.7	8947.7	936.3	1288.2	767.8	4907.8	937.9
4T model, z^{4T}(max)	7348.7	10449.4	731.6	1981.1	727.7	2494.4	1072.9
Relative deviation	+21.8%	-14.4%	+28.0%	-35.0%	+5.5%	+96.6%	-5.4%

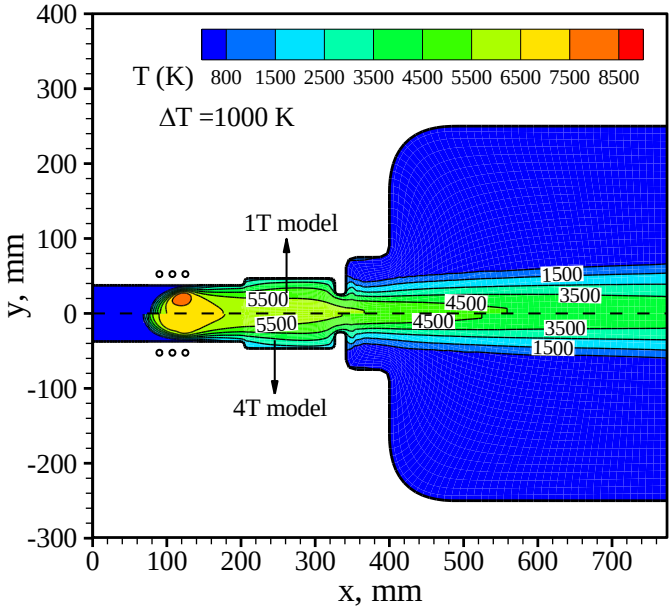

(a) in the whole flow field

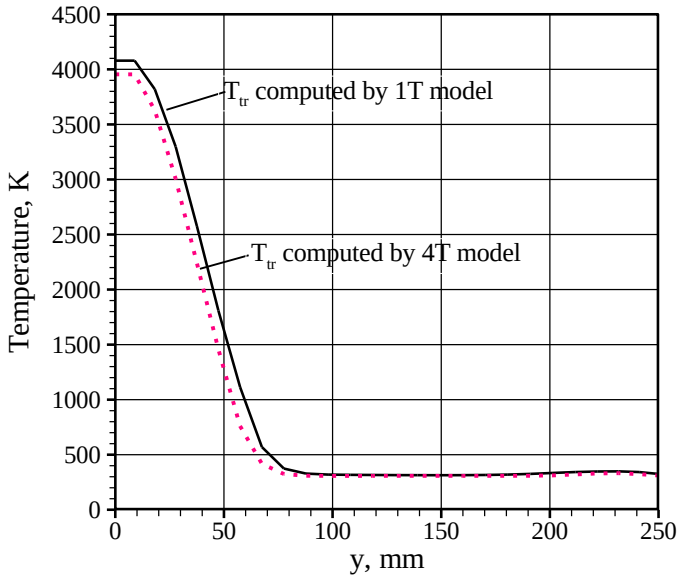

(b) at x=700 mm in the vacuum chamber

Fig. 4.38 Distribution of translational temperature obtained by the 1T and 4T models for case 4

4.6 Effects of High-order Electron Transport Properties

In this section, the effects of different accuracy electron transport properties on the flow fields are investigated in the 10-kW ICPWT. Fig. 4.39(a) and (b) show the distributions of the first- and third-order electrical conductivities and electron thermal conductivities on the center axis for the baseline case. Note that, for the baseline case, the third-order accuracy electron transport properties (σ^{3rd} and λ_e^{3rd}) were used to calculate the electromagnetic and flow fields such as the computations of vector potential equations, Joule heating rate, Lorentz forces, etc. Here the first-order electrical conductivity (σ^{1st}) and electron thermal conductivity (λ_e^{1st}) were computed by (2.153) and (2.192) according to the methods described in Ref. [28]. However, they did not participate in the calculations of the electromagnetic and flow fields.

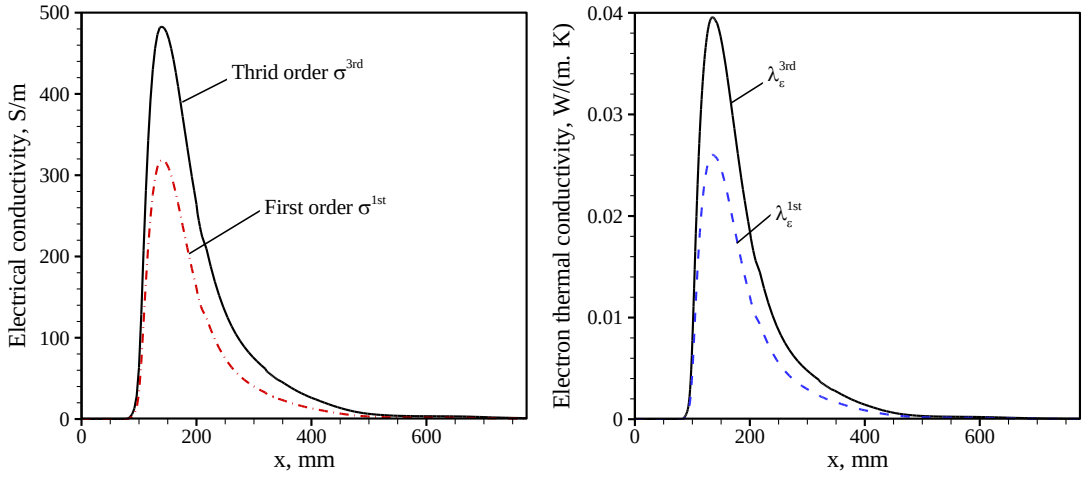

Fig. 4.39 Distributions of the first and third order electron transport properties on the center axis, (a) electrical conductivity; (b) electron thermal conductivity

As can be seen from Fig. 4.39, the maximum σ^{1st} and λ_e^{1st} are about 160 S/m, 0.014 W/(m·K) smaller than the maximum σ^{3rd}, λ_e^{3rd} at the axial position of x=140 mm, although the same pressure, electron temperature, and number density of chemical species were used to evaluate the electrical conductivity and electron thermal conductivity. Because the first-order formulas of electron transport properties were derived under the chemical equilibrium assumption [107], and only the first-order ordinary diffusion coefficient was used in these equations [40]. Thus, in chemical nonequilibrium or high temperature conditions the first-order formulas of electron transport properties seem apt to lose the accuracy.

In order to examine the effects of different accuracy electron transport properties on the flow fields, we take the electrical conductivity as an example to illustrate this issue. Based on the results of baseline case, we performed a simulation marked as test case. The operating conditions of test case were identical with those of the baseline case, but the first-order electrical conductivity as described in Ref. [28] was used in the test case. The other transport parameters of test case such as electron thermal conductivity were computed in the same way as they were calculated in the baseline case. Fig. 4.40 compares the simulated temperatures for baseline case and test case along the center axis. As can be seen in the figure, on one hand, the computed four temperatures (T_{tr}, T_{rot}, T_{vib} and T_e) seem to equilibrate with each other for these two cases along the center axis. It implies that the plasma flow tends to be local thermal equilibrium there; On the other hand, the maximum T_{tr} calculated by the third-order electrical conductivity (baseline case) is about 661.5 K lower than the one calculated by the first-order electrical conductivity (test case). The reason for this result can be explained by the total energy conservation law i.e., the fixed total computational input power dissipated into the plasma flow. From Fig. 4.39, we knew that the Eq. (26) possessing a first-order accuracy usually underestimates the electrical conductivity. Moreover, because the computational input power is functions of the electric field and electrical conductivity that is related to the translational and electron temperatures, in test case the maximum electric field and electrical conductivity would be forced to increase to keep the total energy conservation. Therefore, the maximum translational and electron temperatures obtained by the first-order electrical conductivity for test case became higher than the temperatures obtained for baseline case under the same input power condition.

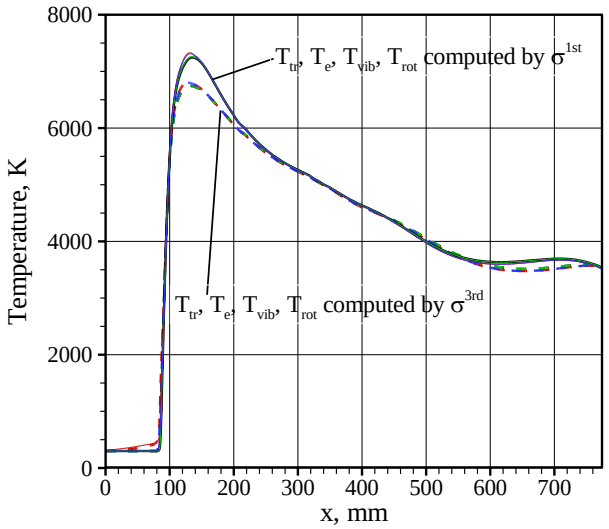

Fig. 4.40 Comparison of the temperatures simulated by the third and first order electrical conductivities along the center axis

Table 4.3 shows comparisons of the numerical results for baseline case and case 3. The relative deviation is defined as $\left(z^{1st}-z^{3rd}\right)/z^{3rd}$. The superscript 3rd and 1st indicate the baseline case and case 3, respectively. As shown in the table, the obtained flow-field and electric-field variables such as the maximum translational temperature, radial Lorentz force, and imaginary part of the electric field for case 3 are 9.6%, 14.2 % and 26.1% higher than those of the baseline case. These results imply that may be necessary to adopt the third-order accuracy electrical conductivity to improve the prediction accuracy for the nitrogen ICP simulation.

To examine the effects of different accuracy electrical conductivity on the flow field with the experimental data, we compare the simulated temperatures for case 1 (3rd EC) and a comparative case (1st EC) with the measured temperature in the Fig. 4.41. Note that about the case 1 and the comparative case, their operating conditions were identical, but the first-order electrical conductivity was used in the calculations of electromagnetic fields for the comparative case. As can be seen from Fig. 4.41, the simulated temperatures by using the first-order electrical conductivity (1st EC) are about 800 Kelvin higher than the temperatures measured in the experiment and simulated in case 1 within $y \leq 15$ mm. This result proved that it is necessary to use the third- rather than the first-order electrical conductivity in an ICP simulation to improve prediction accuracy.

Table 4.3 Comparison of the numerical results between baseline case and case 3

	T_{tr} (K)	T_e (K)	F_{Lx} (N)	$-F_{Ly}$ (N)	$-E_R$ (V/m)	$-E_I$ (V/m)	σ (S/m)
Baseline Case, Z_{max}^{3rd}	6912.3	10562.9	986.0	2248.5	661.1	1983.4	1494.6
Case 3, Z_{max}^{1st}	7573.8	10728.5	1169.2	2568.1	701.4	2501.5	1614.1
Relative deviation	+9.6%	+1.6%	+18.6%	+14.2%	+6.1%	+26.1%	+8.0%

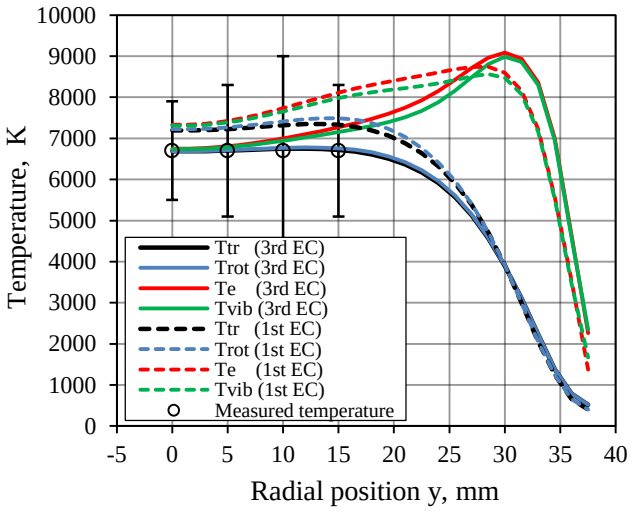

Fig. 4.41 Comparisons of simulated temperatures for case 1 and comparative case with the experimental data at x=135 mm

Fig. 4.42 shows the comparison of T_{tr} obtained by using σ^{1st} and σ^{3rd} for the baseline case: (a) in the whole flow field; (b) at x=700 mm in vacuum chamber. As can be seen from the figures, the simulated temperatures are about several hundred Kelvin different in the coil region. While in the vacuum chamber, temperature difference is very small. Although at x=700 mm the temperature simulated by σ^{1st} is about 100 K

higher than the one computed by σ^{3rd} within y≤15 mm. The deviation of the temperature is within 2.8% there (100K/3600K =2.8%). It may indicates that the different accuracy electron transport properties can affect flow-field results notably in the coil region, but hardly cause big variation of the flow temperature in the test chamber.

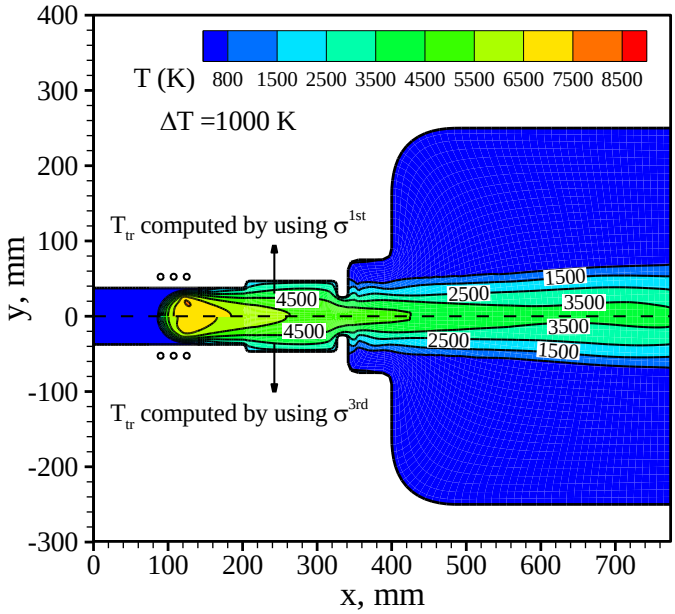

(a) in the whole flow-field

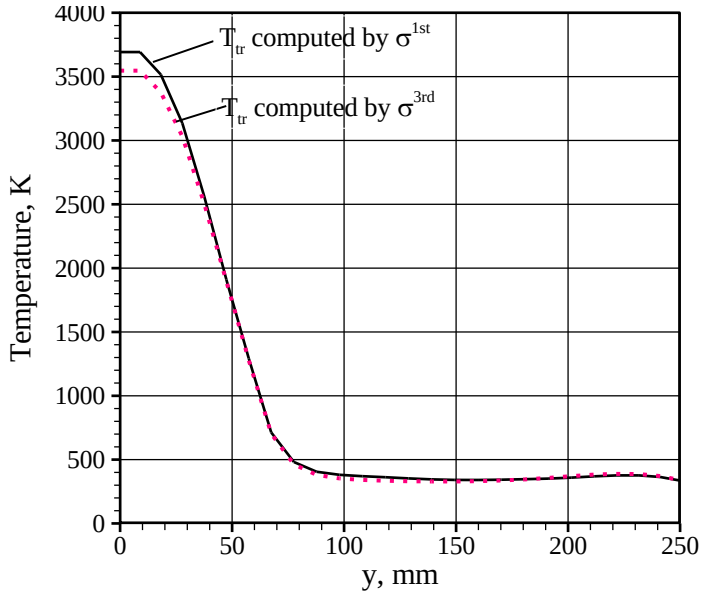

(b) at *x*=700 mm in the vacuum chamber

Fig. 4.42 Distributions of the translational temperatures obtained by using σ^{1st} and σ^{3rd}

Chapter 5 Conclusions

Numerical simulations of inductively coupled plasma flows were carried out to study physical properties of the flow inside the 10-kW and 110-kW ICPWTs with nitrogen and air as the working gases. Two-dimensional compressible axisymmetric Navier-Stokes (N-S) equations that took into account chemical-kinetic models were solved. Far-field magnetic vector potential equations were tightly coupled with the flow field equations to describe the heating process of an radio-frequency inductive discharge. The high-order-accuracy electron transport properties were computed with the latest available collision integral data, and applied to the present simulations. The low-Renolds number AKN k-ε turbulence model was employed in the calculations to estimate the state of the flow and turbulent heat transfer. A four-temperature model including the improved electron-vibration relaxation time was used to study thermochemical states of the plasma flows in the induction torch and spacious vacuum chamber. Through the present numerical simulations, detailed distributions of the flow and electromagnetic fields for the nitrogen and air ICP flows in these two ICPWTs were obtained and analysed.

The numerical results were compared with corresponding experimental data for the 10-kW and 110-kW ICPWTs, respectively. The computational results generally agree with the experimental results. Through the present study, following matters were made clear:

(1) The fundamental flow structures such as high-temperature plasma core, Joule heating phenomenon and chemical components of the ICP flow were successfully reproduced and obtained through present numerical simulations.

(2) For the 10-kW nitrogen ICP flow, due to the insufficient energy exchange between electrons and heavy particles, the plasma flow tends to be in thermal nonequilibrium in the discharge region, while near the center axis, in the downstream of the torch, and in the vacuum chamber, the flow approximates local thermal equilibrium. In the inductive coil region, collisions of molecules with only a few electrons do not lead to rotational excitation but results in vibrational excitation. Short vibrational-electron relaxation time leads to equalization of vibrational temperature and electron temperature in the high temperature region. Dissociation of molecular nitrogen was the dominant reaction in the heating region, along with few ionization reactions. In the vacuum chamber, recombination of atomic oxygen and atomic nitrogen played an important role.

(3) In the 110-kW ICPWT, thermal nonequilibrium phenomenon was also observed near the torch wall in the coil region for the air plasma flow. Because of the relatively high input-power, molecular oxygen and nitrogen have been almost completely dissociated to form atoms and ions near the center axis. While the ionization degree of air species is still small under the high-pressure condition. The mole fractions of all chemical species are almost not change near the center axis in the coil region. Local chemical equilibrium seemed achieved there. In the vacuum chamber, as the flow approaches the position x=500 mm, most atomic nitrogen has compounded to be molecules. The major components became molecular nitrogen and atomic oxygen after this position.

(4) Due to the comprehensive effects of pressure, Lorentz force and severe Joule heating in the coil region, recirculation flows were detected in both of these two ICP wind tunnels. In the 10-kW ICPWT, the position of the recirculation appears beneath the second and third turns of the coil. Because of a stronger negative axial Lorentz force in the 110-kW ICPWT, the recirculation appears beneath the first and second turns of the coil. The common characteristics in these two ICPWT are as following: The axial and radial Lorentz forces play important roles in the momentum transfer in the coil region. The radial Lorentz force is always negative and its peak value is several times bigger than the axial Lorentz force. The distribution and position of the Joule heating rate are mainly affected by the radial Lorentz force.

(5) Through the comparisons of the numerical results obtained under the local thermal equilibrium and thermal nonequilibrium assumptions, the four-temperature model was observed to play an important role in predicting the flow field properly for the 10-kW ICPWT.

(6) According to the comparison of the numerical results obtained using the first- and third-order electrical conductivities used in the electromagnetic field calculation, it was clarified that the electron transport properties with the third-order accuracy are necessary and useful to improve the modeling accuracy for ICP simulations.

Although progress has been made to develop reliable and high-accuracy numerical techniques for the nonequilibrium simulations of ICP flows. Some discrepancies between the simulated and measured temperature are seen at few positions in the present study. Because the effects of radiation and energy loss on the electric circuit were not considered in the simulations, they may be the reasons for these discrepancies. This issue will be studied further in the future.

Acknowledgement

The author is supported by the State Scholarship Fund organized by China Scholarship Council during this doctoral course. Computation was mainly carried out using the computer facilities at the Research Institute for Information Technology, Kyushu University.

I would like to express my sincere appreciation to the supervisor Professor Ken-ichi Abe for his valuable advice and guidance on the research throughout these years. I learned and benefited a lot from his precious advice and profound CFD knowledge. He is kind, generous and gentle in the daily life. I am also grateful for his help and encouragement in the daily life.

I am sincerely grateful to Professor Shigeru Aso (Kyushu University) and Associate Professor Naoji Yamamoto (Kyushu University) for their helpful suggestions and comments to improve the thesis.

My genuine appreciation goes to Assistant Professor Hisashi Kihara (Kyushu University) for his excellent advice and helpful discussion on the study. He is amiable and humorous in the daily life. It is relaxed and enjoyable to communicate with him every time.

My special appreciation goes to Assistant Professor Yusuke Takahashi (Hokkaido University) for supplying me his computational code for the arc-heated flow. His valuable advice and insightful discussions on the numerical computation helped me a lot to improve my study.

I would like to express my genuine appreciation to Professor Takashi Abe (Japan Aerospace Exploration Agency), Assistant Professor Kazuhiko Yamada (Japan Aerospace Exploration Agency) and Mr. Satoshi Miyatani (The University of Tokyo) for supplying me this opportunity to study the facility in their laboratory. I am grateful for their support with using experimental data.

I thank all the members in the Fluid Mechanics laboratory in Kyushu University. The friendly study environment and interesting activities in this laboratory is enjoyable and memorable.

Finally, I express my sincere appreciation to my parents for their great encouragement and care during these years.

Appendix A

A. 1 Derivation of Magnetic Vector Potential Induced by Coil-Current

For a radio-frequency alternative coil-current, it can generate magnetic field in a free space. If the amplitude *I* and radius *a* of the current are known, the induced magnetic field *B* can be figured out according to Biot-Savart law [49]. Using equation $\vec{B} = \nabla \times \vec{A}$, then the magnetic vector potential *A* induced by the coil-current at an arbitrary position P can be obtained. In the following part, the detailed derivations of the magnetic field B and vector potential *A* induced by a circular coil-current are given. Fig. A. 1 shows the illustration of a coil-current ring and an arbitrary position P.

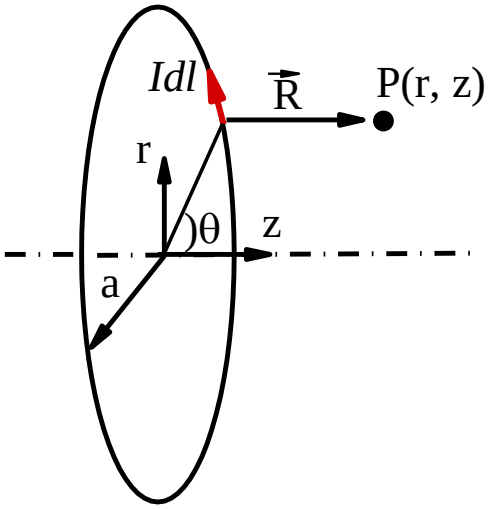

Fig. A. 1 Illustration of a current ring and an arbitrary position P

(1) Magnetic field $\vec{B}$

First, the coil-induced magnetic field B_r and B_z at the position P are derived. To keep the coordinate of the magnetic field in accordance with N-S equations used in this study. We select Cartesian coordinate to derive the analytical solution of the vector potential induced by an coil current. But instead of [x, y, z], the coordinate notation [z, y, r] is used here. This approach is valid because θ component of the *B* field is not considered. From the designated coordinate system the following vectors are presented:

$$OP = \begin{Bmatrix} z \\ 0 \\ r \end{Bmatrix}, \quad OQ = \begin{Bmatrix} 0 \\ a\cos\theta \\ a\sin\theta \end{Bmatrix}, \quad \vec{R} = OP - OQ = \begin{Bmatrix} z \\ -a\cos\theta \\ r - a\sin\theta \end{Bmatrix}. \tag{A.1}$$

where $R^2 = z^2 + a^2\cos^2\theta + (r - a\sin\theta)^2 = z^2 + a^2 + r^2 - 2ar\sin\theta$. The Biot-Savart law controlling the current-induced magnetic field is

$$d\vec{B}(P) = \frac{\mu_0}{4\pi}\frac{Id\vec{l} \times \vec{e}_R}{R^2}, \tag{A.2}$$

where

$$d\vec{l} = \begin{Bmatrix} 0 \\ -ad\theta\sin\theta \\ ad\theta\cos\theta \end{Bmatrix} \text{ and } \vec{e}_R = \begin{Bmatrix} \frac{z}{R} \\ \frac{-a\cos\theta}{R} \\ \frac{r-a\sin\theta}{R} \end{Bmatrix} . \tag{A.3}$$

Substitute the vector notations Eq. (A.3) into Eq. (A.2) to get

$$d\vec{B}(P) = \frac{\mu_0}{4\pi}\frac{I}{R^2} \begin{Bmatrix} 0 \\ -a\sin\theta d\theta \\ a\cos\theta d\theta \end{Bmatrix} \times \begin{Bmatrix} \frac{z}{R} \\ \frac{-a\cos\theta}{R} \\ \frac{r-a\sin\theta}{R} \end{Bmatrix}$$

$$= \frac{\mu_0}{4\pi}\frac{I}{R^2} \begin{Bmatrix} -a\sin\theta d\theta\left(\frac{r-a\sin\theta}{R}\right) + a\cos\theta d\theta\left(\frac{a\cos\theta}{R}\right) \\ \frac{z}{R}a\cos\theta d\theta \\ \frac{z}{R}a\sin\theta d\theta \end{Bmatrix}$$

$$= \frac{\mu_0}{4\pi}\frac{I}{R^3} \begin{Bmatrix} -ar\sin\theta + a^2\sin^2\theta + a^2\cos^2\theta \\ za\cos\theta \\ za\sin\theta \end{Bmatrix} d\theta$$

$$= \frac{\mu_0}{4\pi}\frac{I}{R^3} \begin{Bmatrix} -ar\sin\theta + a^2 \\ za\cos\theta \\ za\sin\theta \end{Bmatrix} d\theta . \tag{A.4}$$

Substitute $R = \sqrt{z^2 + a^2 + r^2 - 2ar\sin\theta}$ into Eq. (A.4), it becomes

$$d\vec{B}(P) = \frac{\mu_0 I}{4\pi} \begin{Bmatrix} \frac{a(a - r\sin\theta)}{\left(z^2 + a^2 + r^2 - 2ar\sin\theta\right)^{\frac{3}{2}}} \\ \frac{za\cos\theta}{\left(z^2 + a^2 + r^2 - 2ar\sin\theta\right)^{\frac{3}{2}}} \\ \frac{za\sin\theta}{\left(z^2 + a^2 + r^2 - 2ar\sin\theta\right)^{\frac{3}{2}}} \end{Bmatrix} d\theta . \tag{A.5}$$

Integrate Eq. (A.5) to get

$$\vec{B}(P)=\begin{Bmatrix}B_z(P)\\B_y(P)\\B_r(P)\end{Bmatrix}=\frac{\mu_0 I}{4\pi}\int_0^{2\pi}\begin{Bmatrix}\dfrac{a(a-r\sin\theta)}{\left(z^2+a^2+r^2-2ar\sin\theta\right)^{\frac{3}{2}}}\\ \textit{not considered}\\ \dfrac{za\sin\theta}{\left(z^2+a^2+r^2-2ar\sin\theta\right)^{\frac{3}{2}}}\end{Bmatrix}d\theta\,. \tag{A.6}$$

Note that:

$$\frac{\partial}{\partial a}\left[\frac{1}{\left(z^2+a^2+r^2-2ar\sin\theta\right)^{\frac{1}{2}}}\right]=\frac{a-r\sin\theta}{\left(z^2+a^2+r^2-2ar\sin\theta\right)^{\frac{3}{2}}}, \tag{A.7}$$

$$\frac{\partial}{\partial z}\left[\frac{1}{\left(z^2+a^2+r^2-2ar\sin\theta\right)^{\frac{1}{2}}}\right]=\frac{z}{\left(z^2+a^2+r^2-2ar\sin\theta\right)^{\frac{3}{2}}}. \tag{A.8}$$

and then, the equations for B_r, B_z are arrived

$$B_r=\frac{-\mu_0 Ia}{2\pi}\frac{\partial}{\partial z}\int_{-\frac{\pi}{2}}^{\frac{\pi}{2}}\frac{\sin\theta d\theta}{\left(z^2+a^2+r^2-2ar\sin\theta\right)^{\frac{1}{2}}}, \tag{A.9}$$

$$B_z=\frac{-\mu_0 Ia}{2\pi}\frac{\partial}{\partial a}\int_{-\frac{\pi}{2}}^{\frac{\pi}{2}}\frac{d\theta}{\left(z^2+a^2+r^2-2ar\sin\theta\right)^{\frac{1}{2}}}. \tag{A.10}$$

In order to verify the derived equations, take the position (r, z) = (0, 0) as an example ($B_r=0$ and $B_z=\dfrac{\mu_0 I}{2a}$ were known) . Indeed,

$$B_{z(0,0)}=\frac{-\mu_0 Ia}{2\pi}\frac{\partial}{\partial a}\int_{-\frac{\pi}{2}}^{\frac{\pi}{2}}\frac{d\theta}{a}=\frac{-\mu_0 Ia}{2\pi}\left(\frac{-1}{a^2}\right)=\frac{\mu_0 I}{2a}. \tag{A.11}$$

Thus, the derivation process is thought to be no mistake.

(2) Magnetic vector potential $\vec{A}$

Second, the analytic form of vector potential $\vec{A}$ is derived here according to the relation $\vec{B}=\nabla\times\vec{A}$. Here Because axisymmetric assumption was used in this study, so the only interest is in tangential component of the vector potential A_θ. There are two methods that A_θ can be derived as the curl of $\vec{A}$ yields two equations: $-\dfrac{\partial A_\theta}{\partial z}=B_r$ and $\dfrac{1}{r}\dfrac{\partial}{\partial r}(rA_\theta)=B_z$. The former is chosen here. Then, the equation of B_r is primarily transformed into analytical form. The procedure is as following. Set

$$m = \frac{4ar}{z^2 + (a+r)^2} \text{ and } \varphi = \frac{\theta + \pi/2}{2}. \tag{A.12}$$

$$B_r = \frac{-\mu_0 Ia}{2\pi} \frac{\partial}{\partial z} \int_0^{\frac{\pi}{2}} \frac{1 - 2\sin^2\varphi}{\sqrt{z^2 + (a+r)^2}\sqrt{1 - \frac{4ar}{z^2 + (a+r)^2}\sin^2\varphi}} 2d\varphi$$

$$= \frac{\mu_0 Ia}{2\pi\sqrt{z^2 + (a+r)^2}} \frac{\partial}{\partial z} \int_0^{\frac{\pi}{2}} \frac{2 - 4\sin^2\varphi}{\sqrt{1 - m\sin^2\varphi}} d\varphi. \tag{A.13}$$

Note that:

$$D = 1 - m\sin^2\varphi \Rightarrow \sin^2\varphi = \frac{1-D}{m}, \tag{A.14}$$

$$2 - 4\sin^2\varphi = 2 - 4\left(\frac{1-(1-m\sin^2\varphi)}{m}\right) = 2 - \frac{4}{m} + \frac{4}{m}(1 - m\sin^2\varphi). \tag{A.15}$$

Rearrangement Eq. (A.13) with Eqs. (A.14) and (A.15) to obtain

$$B_r = \frac{\mu_0 Ia}{2\pi\sqrt{z^2 + (a+r)^2}} \frac{\partial}{\partial z} \int_0^{\frac{\pi}{2}} \left[\frac{2 - \frac{4}{m}}{\sqrt{1 - m\sin^2\varphi}} + \frac{4}{m}\sqrt{1 - m\sin^2\varphi} \right] d\varphi$$

$$= \frac{\mu_0 Ia}{2\pi\sqrt{z^2 + (a+r)^2}} \frac{\partial}{\partial z} \left[\left(2 - \frac{4}{m}\right) \int_0^{\frac{\pi}{2}} \frac{d\varphi}{\sqrt{1 - m\sin^2\varphi}} + \frac{4}{m} \int_0^{\frac{\pi}{2}} \sqrt{1 - m\sin^2\varphi} d\varphi \right]$$

$$= \frac{\mu_0 Ia}{2\pi\sqrt{z^2 + (a+r)^2}} \frac{\partial}{\partial z} \left[\left(2 - \frac{4}{m}\right) K(m) + \frac{4}{m} E(m) \right]. \tag{A.16}$$

where

$$K(m) = \int_0^{\frac{\pi}{2}} \frac{d\varphi}{\sqrt{1 - m\sin^2\varphi}}, \; E(m) = \int_0^{\frac{\pi}{2}} \sqrt{1 - m\sin^2\varphi} d\varphi. \tag{A.17}$$

$K(m)$ and $E(m)$ are the complete elliptic integral of the first and second kinds. With this result, go back to the differential equation $-\frac{\partial A_\theta}{\partial z} = B_r$ to find the analytical form of A_θ. Finally, analytical form of the magnetic vector potential in a Cartesian coordinate can be expressed as:

$$A_\theta = \frac{-\mu_0 Ia}{2\pi\sqrt{z^2 + (a+r)^2}} \left[\left(2 - \frac{4}{m}\right) K(m) + \frac{4}{m} E(m) \right], \tag{A.18}$$

where $m = \dfrac{4ar}{z^2 + (a+r)^2}$, which is defined zero at the center axis. Suppose $k = \sqrt{m} = \sqrt{\dfrac{4Rr}{z^2 + (R+r)^2}}$, then Eq. (A.18) becomes:

$$A_\theta == \frac{\mu_0 I}{2\pi}\sqrt{\frac{a}{r}}\left[\left(\frac{2}{k} - k\right)K(k) - \frac{2}{k}E(k)\right], \tag{A.19}$$

where $K(k) = \int_0^{\frac{\pi}{2}} \dfrac{d\varphi}{\sqrt{1 - k^2 \sin^2 \varphi}}$, $E(k) = \int_0^{\frac{\pi}{2}} \sqrt{1 - k^2 \sin^2 \varphi}\, d\varphi$

$K(k)$ and $E(k)$ are the complete elliptic integrals of the first and second kinds.

Appendix B

B. 1 Jacobian Matrix of Inviscid Term

The inviscid Jacobian matrices $\boldsymbol{A}$ and $\boldsymbol{B}$ that are mentioned in Eqs. (3.128) and (3.130) are derived as follows. Primarily, the conservative vector $\boldsymbol{Q}$ and numerical fluxes $\boldsymbol{F}$, $\boldsymbol{G}$ are rewritten here as:

$$\boldsymbol{Q}=\begin{bmatrix}\rho\\ m\\ n\\ E\\ \rho_1\\ \vdots\\ \rho_{ns}\\ E_{rot}\\ E_{vib}\\ E_e\end{bmatrix},\quad \boldsymbol{F}=\begin{bmatrix}\rho u\\ \rho u^2+p\\ \rho u\upsilon\\ (E+p)u\\ \rho_1 u\\ \vdots\\ \rho_s u\\ E_{rot}u\\ E_{vib}u\\ E_e u\end{bmatrix},\quad \boldsymbol{G}=\begin{bmatrix}\rho\upsilon\\ \rho u\upsilon\\ \rho\upsilon^2+p\\ (E+p)\upsilon\\ \rho_1\upsilon\\ \vdots\\ \rho_s\upsilon\\ E_{rot}\upsilon\\ E_{vib}\upsilon\\ E_e\upsilon\end{bmatrix}. \tag{B.1}$$

where $m=\rho u$ and $n=\rho v$. The Jacobian matrices $\boldsymbol{A}$ and $\boldsymbol{B}$ can be evaluated by:

$$\boldsymbol{A}=\frac{\partial \boldsymbol{F}}{\partial \boldsymbol{Q}}, \tag{B.2}$$

$$\boldsymbol{B}=\frac{\partial \boldsymbol{G}}{\partial \boldsymbol{Q}}. \tag{B.3}$$

Here, each element of $\boldsymbol{A}$ and $\boldsymbol{B}$ is evaluated as a partial derivative of $\boldsymbol{F}$ and $\boldsymbol{G}$ with respect to $\boldsymbol{Q}$. For example, the fourth column and the first row of $\boldsymbol{A}$ is derived by:

$$\frac{\partial (E+p)u}{\partial \rho}=\frac{\partial}{\partial \rho}[(E+p)m/\rho]=u(p_\rho-h). \tag{B.4}$$

Therefore, the Jacobian matrices $\boldsymbol{A}$ and $\boldsymbol{B}$ can be given by:

$$\boldsymbol{A}=\begin{bmatrix}
0 & 1 & 0 & 0 & 0 & \cdots & 0 & 0 & 0 & 0\\
-u^2+p_\rho & 2u+p_m & p_n & p_E & p_{\rho_1} & \cdots & p_{\rho_{ns}} & p_{E_{rot}} & p_{E_{vib}} & p_{E_e}\\
-u\upsilon & \upsilon & u & 0 & 0 & \cdots & 0 & 0 & 0 & 0\\
-u(p_\rho-h) & h+up_m & up_n & u(1+p_E) & up_{\rho_1} & \cdots & up_{\rho_{ns}} & up_{E_{rot}} & up_{E_{vib}} & up_{E_e}\\
-u\rho_1/\rho & \rho_1/\rho & 0 & 0 & u & \cdots & 0 & 0 & 0 & 0\\
\vdots & \vdots & \vdots & \vdots & \vdots & \ddots & \vdots & \vdots & \vdots & \vdots\\
-u\rho_{ns}/\rho & \rho_{ns}/\rho & 0 & 0 & 0 & \cdots & u & 0 & 0 & 0\\
-uE_{rot}/\rho & E_{rot}/\rho & 0 & 0 & 0 & \cdots & 0 & u & 0 & 0\\
-uE_{vib}/\rho & E_{vib}/\rho & 0 & 0 & 0 & \cdots & 0 & 0 & u & 0\\
-uE_e/\rho & E_e/\rho & 0 & 0 & 0 & \cdots & 0 & 0 & 0 & u
\end{bmatrix}, \tag{B.5}$$

$$\boldsymbol{B}=\begin{bmatrix} 0 & 0 & 1 & 0 & 0 & \cdots & 0 & 0 & 0 & 0 \\ -u\upsilon & \upsilon & u & 0 & 0 & \cdots & 0 & 0 & 0 & 0 \\ -\upsilon^2+p_\rho & p_m & 2\upsilon+p_n & p_E & p_{\rho_1} & \cdots & p_{\rho_{ns}} & p_{E_{rot}} & p_{E_{vib}} & p_{E_e} \\ -\upsilon(p_\rho-h) & \upsilon p_m & h+\upsilon p_n & \upsilon(1+p_E) & \upsilon p_{\rho_1} & \cdots & \upsilon p_{\rho_{ns}} & \upsilon p_{E_{rot}} & \upsilon p_{E_{vib}} & \upsilon p_{E_e} \\ -\upsilon\rho_1/\rho & 0 & \rho_1/\rho & 0 & \upsilon & \cdots & 0 & 0 & 0 & 0 \\ \vdots & \vdots & \vdots & \vdots & \vdots & \ddots & \vdots & \vdots & \vdots & \vdots \\ -\upsilon\rho_{ns}/\rho & 0 & \rho_{ns}/\rho & 0 & 0 & \cdots & \upsilon & 0 & 0 & 0 \\ -\upsilon E_{rot}/\rho & 0 & E_{rot}/\rho & 0 & 0 & \cdots & 0 & \upsilon & 0 & 0 \\ -\upsilon E_{vib}/\rho & 0 & E_{vib}/\rho & 0 & 0 & \cdots & 0 & 0 & \upsilon & 0 \\ -\upsilon E_e/\rho & 0 & E_e/\rho & 0 & 0 & \cdots & 0 & 0 & 0 & \upsilon \end{bmatrix} \tag{B.6}$$

where the partial derivatives of pressure e.g., p_ρ, p_m, p_n are expressed as:

$$p_\rho=(\hat{\gamma}-1)\frac{q^2}{2}, \tag{B.7}$$

$$p_m=-(\hat{\gamma}-1)u, \tag{B.8}$$

$$p_n=-(\hat{\gamma}-1)\upsilon, \tag{B.9}$$

$$p_E=(\hat{\gamma}-1), \tag{B.10}$$

$$p_{\rho_s}=\begin{cases} -(\hat{\gamma}-1)\Delta h_s^0+\dfrac{p-p_e}{\hat{\gamma}-1}, & (s\neq e) \\ 0, & (s=e) \end{cases}, \tag{B.11}$$

$$p_{E_{rot}}=-(\hat{\gamma}-1), \tag{B.12}$$

$$p_{E_{vib}}=-(\hat{\gamma}-1), \tag{B.13}$$

$$p_{E_e}=-(\hat{\gamma}-1), \tag{B.14}$$

From Eqs. (B.5) and (B.6), the Jacobian matrix $\tilde{\boldsymbol{P}}=k_x\boldsymbol{A}+k_y\boldsymbol{B}$ can be expressed by

$$\tilde{\boldsymbol{P}}=\begin{bmatrix} 0 & k_x & k_y & 0 & 0 & \cdots & 0 & 0 & 0 & 0 \\ k_x p_\rho-uU & -k_x u(p_E-1) & k_y u-k_x\upsilon p_E & k_x p_E & k_x p_{\rho_1} & \cdots & k_x p_{\rho_{ns}} & k_x p_{E_{rot}} & k_x p_{E_{vib}} & k_x p_{E_e} \\ k_y p_\rho-\upsilon U & k_x\upsilon-k_y u p_E & U-k_y\upsilon(p_E-1) & k_y p_E & k_y p_{\rho_1} & \cdots & k_y p_{\rho_{ns}} & k_y p_{E_{rot}} & k_y p_{E_{vib}} & k_y p_{E_e} \\ (p_\rho-h)U & k_x h-uUp_E & k_y h-\upsilon U p_E & U(1+p_E) & Up_{\rho_1} & \cdots & Up_{\rho_{ns}} & Up_{E_{rot}} & Up_{E_{vib}} & Up_{E_e} \\ -U\rho_1/\rho & k_x\rho_1/\rho & k_y\rho_1/\rho & 0 & U & \cdots & 0 & 0 & 0 & 0 \\ \vdots & \vdots & \vdots & \vdots & \vdots & \ddots & \vdots & \vdots & \vdots & \vdots \\ -U\rho_{ns}/\rho & k_x\rho_{ns}/\rho & k_y\rho_{ns}/\rho & 0 & 0 & \cdots & U & 0 & 0 & 0 \\ -UE_{rot}/\rho & k_x E_{rot}/\rho & k_y E_{rot}/\rho & 0 & 0 & \cdots & 0 & U & 0 & 0 \\ -UE_{vib}/\rho & k_x E_{vib}/\rho & k_y E_{vib}/\rho & 0 & 0 & \cdots & 0 & 0 & U & 0 \\ -UE_e/\rho & k_x E_e/\rho & k_y E_e/\rho & 0 & 0 & \cdots & 0 & 0 & 0 & U \end{bmatrix} \tag{B.15}$$

where $U = k_x u + k_y \upsilon$, $(k_x, k_y) = (y_\eta, -x_\eta)$ for $\tilde{\boldsymbol{A}}$ and $(k_x, k_y) = (-y_\xi, x_\xi)$ for $\tilde{\boldsymbol{B}}$.

B. 2 Jacobian Matrix of Source Term

In the present study, the Jacobian matrix with regard to the thermochemical source term $\hat{\boldsymbol{H}} = \partial \boldsymbol{W} / \partial \boldsymbol{Q}$ in Eq. (3.126) can be expressed as follows:

$$\hat{\boldsymbol{H}} = \begin{bmatrix} 0 & 0 & 0 & 0 & 0 & \cdots & 0 \\ 0 & 0 & 0 & 0 & 0 & \cdots & 0 \\ 0 & 0 & 0 & 0 & 0 & \cdots & 0 \\ 0 & 0 & 0 & 0 & 0 & \cdots & 0 \\ \dfrac{\partial \dot{\omega}_1}{\partial \rho} & \dfrac{\partial \dot{\omega}_1}{\partial m} & \dfrac{\partial \dot{\omega}_1}{\partial n} & \dfrac{\partial \dot{\omega}_1}{\partial E} & \dfrac{\partial \dot{\omega}_1}{\partial \rho_1} & \cdots & \dfrac{\partial \dot{\omega}_1}{\partial \rho_{ns}} \\ \vdots & \vdots & \vdots & \vdots & \vdots & \ddots & \vdots \\ \dfrac{\partial \dot{\omega}_{ns}}{\partial \rho} & \dfrac{\partial \dot{\omega}_{ns}}{\partial m} & \dfrac{\partial \dot{\omega}_{ns}}{\partial n} & \dfrac{\partial \dot{\omega}_{ns}}{\partial E} & \dfrac{\partial \dot{\omega}_{ns}}{\partial \rho_1} & \cdots & \dfrac{\partial \dot{\omega}_{ns}}{\partial \rho_{ns}} \end{bmatrix}. \tag{B.16}$$

Each element of $\hat{\boldsymbol{H}}$ can be obtained by differentiating the mass production rate $\dot{\omega}_s$ with respect to each conservative variable. For example, the differential equation $\partial \dot{\omega}_s / \partial Q_l$ for species *s* can be expressed as:

$$\frac{\partial \dot{\omega}_s}{\partial Q_l} = M_i \sum_{r=1}^{nr} (\nu'_{s,r} - \nu_{s,r}) \times \left[\left\{ \varepsilon_l \frac{\nu_{l,r}}{\rho_l} + \frac{1}{T_{\mathrm{f},r}} \left(s_r + \frac{\theta_r}{T_{\mathrm{f},r}} \right) \frac{\partial T_{\mathrm{f},r}}{\partial q_l} \right\} L_{\mathrm{f},r} - \left\{ \varepsilon_l \frac{\nu'_{l,r}}{\rho_l} + \frac{1}{T_{\mathrm{b},r}} \frac{\partial T_{\mathrm{b},r}}{\partial q_l} \times \left(s_r + \frac{\theta_r}{T_{\mathrm{b},r}} - A_{1,r} / Z_{\mathrm{P}} + A_{3,r} + A_{4,r} Z_{\mathrm{P}} + A_{5,r} Z_{\mathrm{P}}^2 \right) \right\} L_{\mathrm{b},r} \right],$$

$$\varepsilon_l = \begin{cases} 0, & l = 1, \cdots, 4 \\ 1, & l = 4+1, \cdots, 4+ns \end{cases}. \tag{B.17}$$

For the charge exchange reaction (*r*=49) in Table 2.3, the following equations are used:

$$\frac{\partial \dot{\omega}_s}{\partial Q_l} = M_i \sum_{r=1}^{nr} (\nu'_{s,r} - \nu_{s,r}) \times \left[\left\{ \varepsilon_l \frac{\nu_{l,r}}{\rho_l} + \frac{1}{T_{\mathrm{f},r}} \left(s_r + \frac{\theta_r}{T_{\mathrm{f},r}} \right) \frac{\partial T_{\mathrm{f},r}}{\partial q_l} \right\} L_{\mathrm{f},r} - \left\{ \varepsilon_l \frac{\nu'_{l,r}}{\rho_l} + \frac{1}{T_{\mathrm{b},r}} \frac{\partial T_{\mathrm{b},r}}{\partial q_l} \times \left(s_r + \frac{\theta_r}{T_{\mathrm{b},r}} + 5B_{1,r} Z_{\mathrm{G}}^4 + 4B_{2,r} Z_{\mathrm{G}}^3 + 3B_{3,r} Z_{\mathrm{G}}^2 + 2B_{4,r} Z_{\mathrm{G}} + B_{5,r} \right) \right\} L_{\mathrm{b},r} \right],$$

$$\varepsilon_l = \begin{cases} 0, & l = 1, \cdots, 4 \\ 1, & l = 4+1, \cdots, 4+ns \end{cases}. \tag{B.18}$$

where $Z_{\mathrm{P}} = 10^4 / T_{\mathrm{b},r}$ and $Z_{\mathrm{G}} = \ln(10^4 / T_{\mathrm{b},r})$. Then, partial derivatives of the temperature, for example, the translational temperature T_{tr} are given by:

$$\frac{\partial T_{tr}}{\partial \rho} = \frac{\frac{1}{2}q^2}{\rho \hat{C}_v}, \tag{B.19}$$

$$\frac{\partial T_{tr}}{\partial m} = -\frac{u}{\rho \hat{C}_v}, \tag{B.20}$$

$$\frac{\partial T_{tr}}{\partial n} = -\frac{\upsilon}{\rho \hat{C}_v}, \tag{B.21}$$

$$\frac{\partial T_{tr}}{\partial E} = \frac{1}{\rho \hat{C}_v}, \tag{B.22}$$

$$\frac{\partial T_{tr}}{\partial \rho_s} = \begin{cases} -\dfrac{C_{v,s} T_{tr} + \Delta h_s}{\rho \hat{C}_v}, & (s \neq e) \\ 0, & (s = e) \end{cases}. \tag{B.23}$$

For the ionization reactions such as r=17, 37, 38 in Table 2.3, partial derivatives of the electron temperature $\partial T_e / \partial Q_l$ will be used instead of $\partial T_{tr} / \partial Q_l$. Since the electron energy equation is solved separately from other equations, for simplicity a local thermal equilibrium is assumed here. $\partial T_e / \partial Q_l$ is set to be identical with $\partial T_{tr} / \partial Q_l$ to obtain the Jacobian matrix source term in a ionization reaction.

References

[1] M. Auweter-Kurtz and T. Wegmann. "Overview of IRS Plasma Wind Tunnel", *Research and Technology Organization Notes RTO-EN-8-2A*, Von Karman Institute for Fluid Dynamics, Belgium, pp. 1-20, 1999.

[2] T. Watanabe and H. Okumiya, "Formation mechanism of silicide nanoparticles by induction thermal plasmas", *Science and Technology of Advanced Materials*, Vol. 5, No. 5-6, pp. 639-646, 2004.

[3] F. Gitzhofer, "Induction plasma synthesis of ultrafine SiC", *Pure and Applied Chemistry*, Vol. 68, No. 5, pp. 1113-1120, 1996.

[4] B. Bottin, M. Carbonaro, S. Zemsch, et al., "Aerothermodynamic design of an inductively coupled plasma wind tunnel", *AIAA Paper 97 - 2498*, 1997.

[5] T. Sumi, K. Fujita, T. Kurotaki, et al., "Numerical simulation of inductively coupled air plasmas", *Transactions of the Japan Society for Aeronautical and Space Sciences*, Vol. 48, No. 159, pp. 40-45, 2005.

[6] K. Yamada, S. Miyatani, H. Maeno, et al. "The Development of 10 kW and φ75 mm large diameter ICP Heater," *Symposium on Flight Mechanics and Astrodynamics*, Yonago, pp. 1-6. 2013.

[7] Y. Takama and K. Suzuki, "Spectroscopic Diagnostics of Thermochemical Nonequilibrium Hydrogen Plasma Flow", *Journal of Thermophysics and Heat Transfer*, Vol. 21, No. 3, pp. 630-637, 2007.

[8] S. V. Utyuzhnikov, A. V. Konyukhov, D. V. Rudenko, et al., "Simulation of subsonic and supersonic flows in inductive plasmatrons", *AIAA Journal*, Vol. 42, No. 9, pp. 1871-1877, 2004.

[9] http://www.cardc.cn/html/Facility/cgs/Plasma/64.html.

[10] B. Wu, L. Lin, X.-j. Zhang, et al., "Numerical Investigation on the Flow and Temperature Fields in an Inductively Coupled Plasma Reactor", *Plasma Science and Technology*, Vol. 2, No. 6, pp. 565-572, 2000.

[11] G. Herdrich, M. Auweter-Kurtz, H. L. Kurtz, et al., "Operational behavior of inductively heated plasma source IPG3 for entry simulations", *Journal of Thermophysics and Heat Transfer*, Vol. 16, No. 3, pp. 440-449, 2002.

[12] T. Panagopoulos, D. Kim, V. Midha, et al., "Three-dimensional simulation of an inductively coupled plasma reactor", *Journal of Applied Physics*, Vol. 91, No. 5, pp. 2687-2696, 2002.

[13] S. S. Kim, C. S. Chang, N. S. Yoon, et al., "Inductively coupled plasma heating in a weakly magnetized plasma", *Physics of Plasmas*, Vol. 6, No. 7, p. 2926, 1999.

[14] J. Cheng, Y. Zhu and L. Ji, "Modeling Approach and Analysis of the Structural Parameters of an Inductively Coupled Plasma Etcher Based on a Regression Orthogonal Design", *Plasma Science and Technology*, Vol. 14, No. 12, pp. 1059-1068, 2012.

[15] D. Bernardi, V. Colombo, E. Ghedini, et al., "Comparison of different techniques for the FLUENT$^{@}$ - based treatment of the electromagnetic field in inductively coupled plasma torches", *The European Physical Journal D - Atomic, Molecular and Optical Physics*, Vol. 27, No. 1, pp. 55-72, 2003.

[16] X. Chen, "Heat-Transfer and Flow in a Radio-Frequency Plasma Torch - a New Modeling Approach", *International Journal of Heat and Mass Transfer*, Vol. 33, No. 5, pp. 815-826, 1990.

[17] S. Xue, P. Proulx and M. I. Boulos, "Effect of the Coil Angle in an Inductively Coupled Plasma Torch: A Novel Two-Dimensional Model", *Plasma Chemistry and Plasma Processing,* Vol. 23, No. 2, pp. pp. 245-263, 2003.

[18] J. Mostaghimi, P. Proulx and M. I. Boulos, "A two-temperature model of the inductively coupled rf plasma", *Journal of Applied Physics,* Vol. 61, No. 5, p. 1753, 1987.

[19] D. Vanden Abeele and G. Degrez, "Efficient computational model for inductive plasma flows", *AIAA Journal,* Vol. 38, No. 2, pp. 234-242, 2000.

[20] S. Lenzner, M. Auweter-Kurtz, J. Heiermann, et al., "Energy partitions in inductively heated plasma sources for reentry simulations", *Journal of Thermophysics and Heat Transfer,* Vol. 14, No. 3, pp. 388-395, 2000.

[21] R. M. Barnes and S. Nikdel, "Temperature and velocity profiles and energy balances for an inductively coupled plasma discharge in nitrogen", *Journal of Applied Physics,* Vol. 47, No. 9, pp. 3929-3935, 1976.

[22] S. B. Punjabi, N. K. Joshi, H. A. Mangalvedekar, et al., "A comprehensive study of different gases in inductively coupled plasma torch operating at one atmosphere", *Physics of Plasmas,* Vol. 19, No. 1, pp. 1-13, 2012.

[23] Y. Tanaka and T. Sakuta, "Chemically non-equilibrium modelling of thermal ICP at atmospheric pressure using reaction kinetics", *Journal of Physics D: Applied Physics,* Vol. 35, pp. 468-476, 2002.

[24] M. G. Dunn and J. A. Lordi, "Measurement of $N_2^+ + e^-$ dissociative recombination in expanding nitrogen flows", *AIAA Journal,* Vol. 8, No. 2, pp. 339-345, 1970.

[25] M. G. Dunn and S.-W. Kang. "Theoretical and experimental studies of reentry plasmas", *NASA CR-2232,* National Aeronautics and Space Administration, pp. 1-115, 1973.

[26] C. Park, *Nonequilibrium Hypersonic Aerothermodynamics,* Wiley, New York, 1990.

[27] Y. Takahashi, H. Kihara and K. Abe, "Turbulence and radiation behaviours in large-scale arc heaters", *Journal of Physics D: Applied Physics,* Vol. 44, No. 8, pp. 1-19, 2011.

[28] R. N. Gupta, J. M. Yos, R. A. Thompson, et al. "A review of reaction rates and thermodynamic and transport properties for an 11-species air model for chemical and thermal nonequilibrium calculations to 30000 K", *NASA Reference Publication 1232,* Washington DC, U.S.A., pp. 1-91, 1990.

[29] S. A. Vasil'eviskii and A. F. Kolesnikov, "Numerical simulation of equilibrium induction plasma flows in a cylindrical plasmatron channel", *Fluid Dynamics,* Vol. 35, No. 5, pp. 769-777, 2000.

[30] G. Degrez, D. V. Abeele, P. Barbante, et al., "Numerical simulation of inductively coupled plasma flows under chemical non-equilibrium", *International Journal of Numerical Methods for Heat & Fluid Flow,* Vol. 14, No. 4, pp. 538-558, 2004.

[31] T. Suzuki, K. Fujita and T. Sakai, "Experimental Study of Graphite Ablation in Nitrogen Flow, Part II: Further Numerical Analysis", *Journal of Thermophysics and Heat Transfer,* Vol. 24, No. 3, pp. 589-597, 2010.

[32] N. Hirata, S. Nozawa, Y. Takahashi, et al., "Numerical Study of Pyrolysis Gas Flow and Heat Transfer inside an Ablator", *Computational Thermal Science,* Vol. 4, No. 3, pp. 225-242, 2012.

[33] Y. Takahashi, H. Kihara and K. Abe, "Numerical Investigation of Nonequilibrium Plasma Flows in Constrictor- and Segmented-Type Arc Heaters", *Journal of Thermophysics and Heat Transfer,* Vol. 24, No. 1, pp. 31-39, 2010.

[34] J.-H. Lee, "Electron-impact vibrational relaxation in high-temperature nitrogen", *Journal of Thermophysics and Heat Transfer,* Vol. 7, No. 3, pp. 399-405, 1993.
[35] A. Bourdon and P. Vervisch, "Electron-vibration energy exchange models in nitrogen plasma flows", *Physical Review E,* Vol. 55, No. 4, pp. 4634-4641, 1997.
[36] M. Kim, A. Gülhan and I. D. Boyd, "Modeling of Electron Energy Phenomena in Hypersonic Flows", *Journal of Thermophysics and Heat Transfer,* Vol. 26, No. 2, pp. 244-257, 2012.
[37] J. Mostaghimi and M. I. Boulos, "Two-Dimensional electromegnetic field effects in induction plasma modeling", *Plasma Chemistry and Plasma Processing,* Vol. 9, No. 1, pp. 25-44, 1989.
[38] S. W. Xue, P. Proulx and M. I. Boulos, "Extended-field electromagnetic model for inductively coupled plasma", *Journal of Physics D-Applied Physics,* Vol. 34, No. 12, pp. 1897-1906, 2001.
[39] Y. Tanaka, "Two-temperature chemically non-equilibrium modelling of high-power Ar–N2 inductively coupled plasmas at atmospheric pressure", *Journal of Physics D: Applied Physics,* Vol. 37, No. 8, pp. 1190-1205, 2004.
[40] R. S. Devoto, "Simplified expressions for the transport properties of ionized monatomic gases", *Physics of Fluids,* Vol. 10, No. 10, pp. 2105-2112, 1967.
[41] S. Ghorui and A. K. Das, "Collision integrals for charged-charged interaction in two-temperature non-equilibrium plasma", *Physics of Plasmas,* Vol. 20, No. 9, p. 093504, 2013.
[42] A. Laricchiuta, D. Bruno, M. Capitelli, et al., "High temperature Mars atmosphere. Part I: transport cross sections", *The European Physical Journal D,* Vol. 54, No. 3, pp. 607-612, 2009.
[43] T. Ito, K. Ishida, M. Mizuno, et al. "110kW new high enthaply wind tunnel heated by inductively-coupled-plasma," *12th AIAA International Space Planes and Hypersonic Systems and Technologies,* Norfolk, Virginia. 2003.
[44] M. A. Lieberman and A. J. Lichtenberg, *Principles of plasma discharges and materials processing,* Wiley, 2005.
[45] Y. Raizer, M. Shneider and N. Yatsenko, *Radio-frequency capacitive discharge,* CRC Press, Florida, 1995.
[46] J.-H. Lee, "Basic governing equations for the flight regimes of aeroassisted orbital transfer vehicles", AIAA Paper 84-1729, 1985.
[47] J. O. Hirschfelder, C. F. Curtiss and R. B. Bird, *Molecular theory of gases and liquids,* Wiley New York, 1954.
[48] K. Abe, T. Kondoh and Y. Nagano, "A new turbulence model for predicting fluid flow and heat transfer in separating and reattaching flows-I. Flow field calculations", *International Journal of Heat and Mass Transfer,* Vol. 37, No. 1, pp. 139-151, 1994.
[49] M. M.-T. Tsay, *Two-dimensional numerical modeling of Radio-Frequency ion engine discharge,* Massachusetts Institute of Technology, Ph. D Thesis, 2010.
[50] M. Yu, Y. Takahashi, H. Kihara, et al., "Numerical simulation of nonequilibrium inductive plasma flow coupled with electromagnetic field calculation", *American Institute of Physics Conference Proceedings,* Vol. 1628, pp. 1124-1131, 2014.
[51] C. Park, "Review of chemical-kinetic problems of future NASA missions. I-Earth entries", *Journal of Thermophysics and Heat Transfer,* Vol. 7, No. 3, pp. 385-398, 1993.
[52] C. Park, R. L. Jaffe and H. Partridge, "Chemical-kinetic parameters of hyperbolic earth entry", *Journal of Thermophysics and Heat Transfer,* Vol. 15, No. 1, pp. 76-90, 2001.

[53] G. Colonna, F. Esposito and M. Capitelli, "The role of rotation in state-to-state vibrational kinetics", *AIAA Paper -3423*, 2006.
[54] M. Capitelli, C. M. Ferreira, A. I. Osipov, et al., *Plasma kinetics in atmospheric gases*, Springer, 2000.
[55] M. Nagulapally, G. V. Candler, C. O. Laux, et al. "Numerical simulation of a constant current density discharge in a flowing air plasma," *30th AIAA Plasmadynamics and Lasers Conference AIAA 99-3477*, Norfolk, VA. 1999.
[56] S. Chapman and T. G. Cowling, *The mathematical theory of non-uniform gases*, Cambridge University Press, Cambridge, 1952.
[57] M. Capitelli, C. Gorse, S. Longo, et al., "Collision integrals of high-temperature air species", *Journal of Thermophysics and Heat Transfer*, Vol. 14, No. 2, pp. 259-268, 2000.
[58] B. Bottin, D. V. Abeele, M. Carbonaro, et al., "Thermodynamic and transport properties for inductive plasma modeling", *Journal of Thermophysics and Heat Transfer*, Vol. 13, No. 3, pp. 343-350, 1999.
[59] J. M. Yos. "Transport properties of nitrogen, hydrogen, oxygen, and air to 30,000 K", *Technique Memorandum RAD-TM-63-7*, Massachusetts, 1963.
[60] M. Fertig, A. Dohr and H.-H. Fruacute. "Transport Coefficients for High Temperature Nonequilibirum Air Flows," *7th AIAA/ASME Joint Thermophysics and Heat Transfer Conference*. 1998.
[61] M. Fertig, A. Dohr and H. H. Fruhauf, "Transport coefficients for high-temperature nonequilibrium air flows", *Journal of Thermophysics and Heat Transfer*, Vol. 15, No. 2, pp. 148-156, 2001.
[62] C. F. Curtiss and J. O. Hirschfelder, "Transport Properties of Multicomponent Gas Mixtures", *Journal of Chemical Physics*, Vol. 17, No. 6, pp. 550-555, 1949.
[63] T. Sakai and O. T., "Improvements in a Navier-Stokes code for arc heater flows", *AIAA Paper - 3782*, 2003.
[64] M. van de Sanden, P. Schram, A. Peeters, et al., "Thermodynamic generalization of the Saha equation for a two-temperature plasma", *Physical Review A*, Vol. 40, No. 9, pp. 5273-5276, 1989.
[65] V. Rat, A. B. Murphy, J. Aubreton, et al., "Treatment of non-equilibrium phenomena in thermal plasma flows", *Journal of Physics D: Applied Physics*, Vol. 41, No. 18, p. 183001, 2008.
[66] G. Colonna and A. D'Angola, "A hierarchical approach for fast and accurate equilibrium calculation", *Computer Physics Communications*, Vol. 163, No. 3, pp. 177-190, 2004.
[67] G. Colonna, "Improvements of hierarchical algorithm for equilibrium calculation", *Computer Physics Communications*, Vol. 177, No. 6, pp. 493-499, 2007.
[68] V. Colombo, E. Ghedini and P. Sanibondi, "Thermodynamic and transport properties in non-equilibrium argon, oxygen and nitrogen thermal plasmas", *Progress in Nuclear Energy*, Vol. 50, No. 8, pp. 921-933, 2008.
[69] E. I. Asinovsky, A. V. Kirillin, E. P. Pakhomov, et al., "Experimental investigation of transport properties of low-temperature plasma by means of electric arc", *Proceedings of the Institute of Electrical and Electronics Engineers*, Vol. 59, No. 4, pp. 592-601, 1971.
[70] M. Capitelli and R. S. Devoto, "Transport coefficients of high-temperature nitrogen", *Physics of Fluids*, Vol. 16, No. 11, pp. 1835-1841, 1973.
[71] A. B. Murphy, "Transport-Coefficients of Air, Argon-Air, Nitrogen-Air, and Oxygen-Air Plasmas", *Plasma Chemistry and Plasma Processing*, Vol. 15, No. 2, pp. 279-307, 1995.

[72] M. Capitelli, G. Colonna, C. Gorse, et al., "Transport properties of high temperature air in local thermodynamic equilibrium", *European Physical Journal D*, Vol. 11, No. 2, pp. 279-289, 2000.
[73] A. D'Angola, G. Colonna, C. Gorse, et al., "Thermodynamic and transport properties in equilibrium air plasmas in a wide pressure and temperature range", *European Physical Journal D*, Vol. 46, No. 1, pp. 129-150, 2008.
[74] M. J. Wright, D. Bose, G. E. Palmer, et al., "Recommended collision integrals for transport property computations part 1: air species", *AIAA Journal*, Vol. 43, No. 12, pp. 2558-2564, 2005.
[75] A. B. Murphy and C. J. Arundell, "Transport-Coefficients of Argon, Nitrogen, Oxygen, Argon-Nitrogen, and Argon-Oxygen Plasmas", *Plasma Chemistry and Plasma Processing*, Vol. 14, No. 4, pp. 451-490, 1994.
[76] W. G. Vincenti and C. H. Kruger, *Introduction To Physical Gas Dynamics*, Krieger, Malabar, 1965.
[77] C. Park and S.-H. Lee, "Validation of multitemperature nozzle flow code", *Journal of thermophysics and heat transfer*, Vol. 9, No. 1, pp. 9-16, 1995.
[78] J. Parker, "Rotational and vibrational relaxation in diatomic gases", *Physics of Fluids*, Vol. 2, No. 4, pp. 449-462, 1959.
[79] C. Park, "Rotational relaxation of N_2 behind a strong shock wave", *Journal of Thermophysics and Heat Transfer*, Vol. 18, No. 4, pp. 527-533, 2004.
[80] R. C. Millikan and D. R. White, "Systematics of vibrational relaxation", *The Journal of chemical physics*, Vol. 39, No. 12, pp. 3209-3213, 1963.
[81] C. Park, "Problems of rate chemistry in the flight regimes of aeroassisted orbital transfer vehicles", *AIAA paper*, pp. 511-537, 1985.
[82] J. Appleton and K. Bray, "The conservation equations for a non-equilibrium plasma", *Journal of Fluid Mechanics*, Vol. 20, No. 4, pp. 659-672, 1964.
[83] M. Mitchner and C. H. Kruger, *Partially ionized gases*, Wiley New York, 1973.
[84] P. A. Gnoffo, R. N. Gupta and J. L. Shinn. "Conservation equations and physical models for hypersonic air flows in thermal and chemical nonequilibrium", USA, 1989.
[85] S. a. a. S. Lazdinis, "Free electron and vibrational temperature nonequilibrium in high temperature nitrogen", *Physics of Fluids*, Vol. 17, No. 8, pp. 1539-1546, 1974.
[86] M. Vinokur, "An analysis of finite-difference and finite-volume formulations of conservation laws", *Journal of computational physics*, Vol. 81, No. 1, pp. 1-52, 1989.
[87] S. K. Godunov, "A difference method for numerical calculation of discontinuous solutions of the equations of hydrodynamics", *Matematicheskii Sbornik*, Vol. 89, No. 3, pp. 271-306, 1959.
[88] M.-S. Liou and C. J. Steffen Jr, "A new flux splitting scheme", *Journal of Computational physics*, Vol. 107, No. 1, pp. 23-39, 1993.
[89] E. Shima and K. Kitamura, "Parameter-free simple low-dissipation AUSM-family scheme for all speeds", *AIAA Journal*, Vol. 49, No. 8, pp. 1693-1709, 2011.
[90] K. Kitamura, "Performance of low-dissipation Euler fluxes and preconditioned LU-SGS at low speeds", *Communications in Computational Physics*, Vol. 10, No. 1, pp. 90-119, 2011.
[91] B. Van Leer, "Towards the ultimate conservative difference scheme. V. A second-order sequel to Godunov's method", *Journal of Computational Physics*, Vol. 32, pp. 101-136, 1979.

[92] B. Van Leer, "Towards the ultimate conservative difference scheme. IV. A new approach to numerical convection", *Journal of computational physics,* Vol. 23, No. 3, pp. 276-299, 1977.
[93] D. C. Wilcox, *Turbulence modeling for CFD,* DCW industries La Canada, CA, 1998.
[94] T. R. A. Bussing and E. M. Murman, "Finite-volume method for the calculation of compressible chemically reacting flows", *AIAA Journal,* Vol. 26, No. 9, pp. 1070-1078, 1988.
[95] A. Jameson and S. Yoon, "Lower-upper implicit schemes with multiple grids for the Euler equations", *AIAA Journal,* Vol. 25, No. 7, pp. 929-935, 1987.
[96] J. Bardina, P. Huang and T. Coakley, "Turbulence modeling validation, testing, and development", *NASA Technical Memorandum-110446,* 1997.
[97] J. Blazek, *Computational Fluid Dynamics: Principles and Applications*, Elservier, Baden-Daettwil, Switzerland, 2001.
[98] V. Venkatakrishnan, "Preconditioned conjugate gradient methods for the compressible Navier-Stokes equations", *AIAA Journal,* Vol. 29, No. 7, pp. 1092-1100, 1991.
[99] K. Fujita, M. Mizuno, K. Ishida, et al., "Spectroscopic flow evaluation in inductively coupled plasma wind tunnel", *Journal of Thermophysics and Heat Transfer,* Vol. 22, No. 4, pp. 685-694, 2008.
[100] B. W. Yu and S. L. Girshick, "Modeling inductively coupled plasmas: The coil current boundary condition", *Journal of Applied Physics,* Vol. 69, No. 2, p. 656, 1991.
[101] Y. Takahashi, "*Numerical study of thermochemical nonequilibrium flow in arc-heated plasma wind tunnel*", Master Thesis, Kyushu University, 2007.
[102] S. Miyatani, "Spectroscopic measurement of plasma flow generated by 10 kW and 75 mm ICP heater", *58th Space Science and Technology Union Symposium, JSASS-2014-4534*, 2014.
[103] S. Miyatani, K. Yamada and T. Abe, "Spectroscopic measurement of plasma flow generated by 10kW and Φ75mm ICP heater", *8th European Symposium on Aerothermodynamics for Space Vehicles*, 2015.
[104] T. Suzuki, K. Fujita, K. Ando, et al., "Experimental study of graphite ablation in nitrogen flow", *Journal of Thermophysics and Heat Transfer,* Vol. 22, No. 3, pp. 382-389, 2008.
[105] K. Fujita, T. Suzuki, M. Mizuno, et al., "Comprehensive flow characterization in a 110-Kilowatt inductively-coupled-plasma heater", *Journal of Thermophysics and Heat Transfer,* Vol. 23, No. 4, pp. 840-843, 2009.
[106] K. Fujita, M. Mizuno, K. Ishida, et al. "Spectroscopic measurement of ICP-heated wind tunnel plasmas," *37th AIAA Thermophyscis Conference,* Oregen. 2004.
[107] S. Selle and U. Riedel, "Transport properties of ionized species", *Annals of the New York Academy of Sciences,* Vol. 891, No. 1, pp. 72-80, 1999.